Exploration of Compounds in the LiBr-LiOH Phase Diagram for Energy Storage Applications

Emily Milan

Wolfson College

University of Oxford

A thesis submitted for the degree of

Doctor of Philosophy

Trinity 2025

Declaration of Authorship

The work in this thesis is the result of my research in the Department of Materials at the University of Oxford, conducted between September 2021 and June 2025 under the supervision of Professor Mauro Pasta. No part of this thesis has been submitted for a degree at this or any other university. The results presented are my own unless otherwise stated.

Emily Milan

June 2025

Abstract

The sustainable energy transition demands advancements in energy storage technologies. This thesis investigates materials within the LiBr–LiOH binary system, with potential applications in solid-state batteries and thermal energy storage (TES). However, proposed phase diagrams for the LiBr-LiOH system are characterised by complex peritectic and peritectoid transitions, which may present challenges for the synthesis and performance of these materials. The work in this thesis provides new insights into the phase behaviour, structure, and lithium-ion conductivity of phases in the LiBr–LiOH system, offering indications of their potential suitability for energy storage applications.

The first experimental chapter, Chapter 3, looks to establish a stronger understanding of the LiBr-LiOH system and clarify the impacts of these findings on $Li_4(OH)_3Br$'s potential as a phase change material for TES. The previously uncharacterised high-temperature phase, $Li_3(OH)_2Br$, was identified and structurally characterised using a combination of experimental techniques and supported by theoretical modelling. X-ray diffraction studies indicate that the phase adopts a hexagonal structure in the $P6_3/mmc$ space group. Promising lithium-ion dynamics are found in this phase, however it could not be retained to room temperature metastably. Investigations into $Li_4(OH)_3Br$ revealed that earlier characterisations were compromised by air exposure. A revised $Pmnm$ crystal structure is proposed for the anhydrous stable phase, and strategies to overcoming its non-equilibrium solidification explored. This different crystal structure to previous reports explains why experimental melting enthalpies are significantly lower than initially predicted.

The second experimental chapter, Chapter 4, focuses on two antiperovskites, Li_2OHBr and the lesser reported $Li_5(OH)_2Br_3$, which have been suggested as candidate electrolytes for solid-state batteries. The synthesis of these phases is approached with consideration of the LiBr-

LiOH phase diagram, and the importance of cooling conditions on phase purity is demonstrated. Some success is achieved in designing a strategy to produce large single crystals of Li_2OHBr, albeit with significant porosity. Directional solidification is suggested as a route to improve the microstructure further and produce crystals suitable for fundamental studies.

Finally, vitrification was explored as a strategy to enhance ionic conductivity in Li_2OHBr. Amorphous Li_2OHX (X = Br, Cl) glasses were successfully synthesised using a melt-quenching technique, with solid-state NMR confirming improved lithium dynamics. However, these glasses were prone to crystallisation in initial attempts to press bulk electrolyte pellets, limiting their practical use.

Contents

Acknowledgements

Firstly, I would like to thank my supervisor, Professor Mauro Pasta, for his guidance, optimism and the many opportunities he has provided throughout my DPhil. His support has been instrumental in shaping my research, and I am especially grateful for access to the world-class facilities that have enabled this work. I would also like to give thanks to the EPSRC and Morgan Advanced Materials for funding this work, without whom I would never have had this fantastic opportunity.

It has been a privilege to work in the Pasta group, and I will miss the daily group lunches. I extend special thanks to Prof. Hyeon Jeong Lee and Dr Brigita Darminto for teaching me the ropes of the antiperovskite material system, and to Dr Stephen Turrell, Dr Jack Aspinall and Dr Matthew Burton for their invaluable feedback, discussions and advice. I would like to acknowledge those within my group and the wider university who have contributed to the completion of this work:

- Dr Gregory Rees and Dr Hua Guo for NMR measurements in Chapter 5, and for their help with interpretation.
- Prof. Andrew Goodwin and Dr John Cattermull for generous access to their discretionary I11 beamtime for the data collected in Chapter 3, their advice on refinement approaches, and for valuable and insightful feedback.
- Dr Gareth Hughes and Dr Phani Karamched for their FIB and SEM support and advice.
- Dr Johannes Ihli for facilitating collaborations and assisting with experimental design for the ACT and laser FIB trials at the Hercules Facility in Leicester, and Dr Pranay Shrestha for conducting the subsequent ACT analysis, included in Chapter 4.

- Dr Emma Hedley for the TEM images of glass-ceramic Li_2OHBr in Chapter 5.
- Prof. Robert House for his help running the in-house VT-XRD measurements in Chapter 3.

Beyond the university, I have had the privilege of collaborating with many fantastic researchers whose contributions have greatly elevated this work. I am deeply grateful to:

- Prof. Steve Feller for his glass expertise and enthusiasm, without which we would not have been able to synthesise glasses from such a challenging system. I also thank his students at Coe College- Aaron Phillips, Cristian Cano, Yi Wei and Zachary Pearlman- for their help synthesising the twin-roll quenched glasses reported in Chapter 5, and for their dedication optimising the synthesis procedure such that I was able to complete a thorough characterisation.
- Dr James Quirk and Prof. James Dawson (Newcastle University) for their modelling work, which supported my experimental work in Chapter 3.
- Dr Kenjiro Hashi (NIMS) for the high-temperature NMR measurements in Chapter 3, whose ingenius homemade setup enabled experiments at temperatures not possible elsewhere.
- Dr Daniel Mayoh (University of Warwick) for his assistance with Laue diffraction measurements during the single crystal growth attempts in Chapter 4.
- Gareth Douglas (Hercules Facility, University of Leicester) for the ACT measurements and laser FIB trials on the Li_2OHBr antiperovskite samples in Chapter 4.

I am grateful to everyone who supported me throughout this journey. Thank you to my friends, old and new, for good times and memories made. Thank you to my Dad, Richard, for his help with drawing schematics and building the HDS setup in Chapter 4. Finally, I would like to express my deepest appreciation to my family for their unwavering support, encouragement, and patience over the past four years. They helped me to keep going during some of the most challenging moments. Their steadfast belief has helped me navigate both the highs and the lows of this process, and for that, I am eternally grateful.

Publications and Conference Presentations

This thesis is established based on the following articles and conference presentations:

1. Milan, E. and Pasta, M., The role of grain boundaries in solid-state Li-metal batteries. *Mater. Futures* **2**, 013501 (2023).

2. Milan, E. 5th September 2023. *Glasses as Grain-Boundary-Free Electrolytes for Li-Metal Batteries* [Conference Presentation] Society of Glass Technology Annual Conference 2023. Cambridge, United Kingdom

3. Milan, E., Rees, G., Phillips, A., Cano, C., Wei, Y., Guo, H., Feller, S., Pasta, M., Lithium antiperovskite-derived glass solid electrolytes. *ACS Materials Lett.* **7**, 1187-1194 (2025).

4. Milan, E., Quirk, J.A., Hashi, K., Cattermull, J., Goodwin, A.L., Dawson, J.A., Pasta, M., Filling the gaps in the LiBr-LiOH phase diagram: A study on the high-temperature $Li_3(OH)_2Br$ phase. *Chem. Mater.* **37**, 8, 2899–2906 (2025)

5. Milan, E., Quirk, K., Cattermull, J., Goodwin, A.L., Dawson, J.A., Pasta, M., Synthesis and characterisation of $Li_4(OH)_3Br$ for thermal energy storage. *ACS Appl. Energy Mater.* **8**, 8, 5353–5359 (2025)

6. Milan E. 26th May 2025. *Understanding the LiBr-LiOH Phase Diagram and its Implications for Antiperovskite Solid Electrolyte Synthesis* [Conference Presentation] European Materials Research Society. Strasbourg, France.

Other articles contributed to:

1. Darminto, B., Rees, G., Cattermull, J., Hashi, K., Diaz-Lopez, M., Kuwata, N., Turrell, S.J., Milan, E., Chart, Y., Di Mino, C., Lee, H.J., Goodwin, A.L., Pasta, M. On the Origin of the Non-Arrhenius Na-ion Conductivity in Na_3OBr. *Angew. Chem.*, **62**, e2023144 (2023)

2. Aspinall, J., Sada, K., Guo, H., Kotakadi, S., Narayanan, S., Chart, Y., Jagger, B., Milan, E., Brassart, L., Armstrong, D., Pasta, M. The impact of magnesium content on lithium-magnesium alloy electrode performance with argyrodite solid electrolyte. *Nat Commun*, **15**, 4511 (2024)

Unpublished Manuscripts:

1. Aspinall, J., Shen, F., Burton, B., Shrestha, P., Guo, H., Kotakadi, S., Tu, Y., Milan, E., Autran, P, O., Ihli, J., Aihara, Y., Brassart, L., Martínez-Pañeda, E., Pasta, M. High Diffusivity Lithium Intermetallic in Two-Phase Alloy Negative Electrode for Solid-State Batteries. *Manuscript under consideration in Nature Materials.*

List of Abbreviations

ACT absorption contrast tomography.

AIRSS ab-initio random structure searching.

BPP Bloembergen-Purcell-Pound.

BSE backscattered electrons.

CA chronoamperometry.

CCD critical current density.

CE coulombic efficiency.

CPE constant phase element.

CSP concentration solar plants.

DC direct current.

DFT density functional theory.

DSC differential scanning calorimetry.

DSG direct steam generation.

DTA differential thermal analysis.

EBSD electron backscatter diffraction.

ECM equivalent circuit model.

EDS energy dispersive spectroscopy.

EDX energy dispersive X-ray.

EFG electric field gradient.

EIS electrochemical impedance spectroscopy.

EV electric vehicles.

FTIR fourier transform infrared.

FWHM full width half maximums.

HDS horizontal directional solidification.

HOMO highest occupied molecular orbital.

LAGP $Li_{1.5}Al_{0.5}Ge_{1.5}(PO_4)_3$.

LCO lithium cobalt oxide.

LHTES latent heat thermal energy storage.

LiPON lithium phosphorous oxynitride.

LLTO lithium lanthanum titanate.

LLZO $Li_7La_3Zr_2O_{12}$.

LPS lithium thiophosphates.

LUMO lowest unoccupied molecular orbital.

MAS magic angle spinning.

MD molecular dynamics.

NMR nuclear magnetic resonance.

PCM phase change material.

PECS precision etching coating system.

PEEK polyether ether ketone.

PFG pulsed-field gradient.

PFIB plasma focused ion beam.

RDF radial distribution function.

RF radio frequency.

SE secondary electron.

SEI solid electrolyte interphase.

SEM scanning electron microscopy.

SHE standard hydrogen electrode.

SLR spin-lattice relaxation.

SS stainless steel.

SSB solid-state battery.

TEM transmission electron microscopy.

TES thermal energy storage.

VT variable temperature.

XRD X-ray diffraction.

Chapter 1

Introduction

Contents

1.1 Context

Over recent decades, global energy demand has increased dramatically. Forecasts for global power generation predict demand to increase from 28 TWh in 2023 to 50 TWh in 2040[1]. The harvesting of energy from renewable sources, such as solar and wind, has emerged as an approach to meeting this demand in a sustainable manner. Accounting for 32 % of power generation in 2023, predictions indicate that renewables will reach a 70 % share by 2040, resulting in a decrease from current CO_2 emissions[1]. However, the current drive for society to undergo a transition away from traditional, harmful energy sources, such as coal and oil, is a challenge that will be impossible without reliable and efficient methods for storing energy. Although many renewable energy technologies are improving year-on-year, effective methods of storage are required such that the energy supplied from these often intermittent sources can be stabilised to be available continually and reliably in times of high demand. Additionally, a means of decarbonising transport is required, with additional safety and energy-density prerequisites being of paramount importance.

A broad range of technologies offer routes to storing energy. The work in this thesis considers the use of materials for electrochemical storage applications, specifically batteries, and for thermal energy storage (TES) systems, specifically a phase change material (PCM). The following chapter will introduce these key energy storage technologies, following which, the materials of interest in this thesis shall be presented and the aims of this work established.

1.1.1 Thermal Energy Storage and Phase Change Materials

Increasing demand for efficient energy storage solutions has stimulated research into TES, particularly in the context of renewable energy integration and waste heat recovery. Employing TES for the capture and retention of excess thermal energy enables its use during periods of high demand or low energy production. Currently TES systems can be classified into 3 categories: sensible heat, latent heat, and thermochemical energy storage[2]. Among these, latent heat thermal energy storage (LHTES), which exploits the thermal energy associated with phase changes, is gaining increasing attention for the high energy densities offered and the potential for efficient thermal regulation[2].

Although the phrase "phase change material" could be considered to encompass most materials, the term specifically refers to materials which exhibit high latent heat changes in a useful temperature range, and are able to occur reversibly without degradation. Traditional, organic, low-temperature PCMs such as paraffin wax can be useful in passive temperature regulation in buildings, or as heat sinks in electronics, for example. For high-temperature storage such as power generation applications and waste heat recovery from industrial processes, inorganic alternatives are typically used. Since LHTES systems store energy during the phase transition of a material, most commonly between solid and liquid phases, significant energy storage without a substantial change in temperature is possible[2]. Consistent output temperatures are crucial for power generation applications, such as concentration solar plants (CSP), where systems are optimised to specific operating temperatures, with higher temperatures resulting in a more efficient thermodynamic cycle. Additionally, maintaining constant temperatures reduces thermal stresses on the system's components, helping to prolong their lifetime.

Various PCM systems have been explored for high-temperature LHTES. Inorganic materials such as molten salts (e.g. $NaNO_3$, KNO_3) and eutectic mixtures (e.g. NaCl-KCl, $NaNO_3$-KNO_3) are prominent in research due to their high latent heat capacity, stability at elevated temperatures, and relatively low costs[3–5]. Recently, the peritectic compound $Li_4(OH)_3Br$ has also been proposed as a possible PCM[6–11]. It is this phase which shall be studied in Chapter 3.

1.1.2 Electrochemical Energy Storage and Lithium-Ion Batteries

Batteries are a form of electrochemical storage in which stored chemical energy can be converted to electricity to power devices on demand. In recent years, the greatest battery market growth has corresponded to lithium-ion batteries[12], a chemistry of battery whereby reversible intercalation of Li^+ ions into active electrode materials is utilised. The lithium-ion battery market is predicted to grow by 27 % per annum to reach 4700 GWh by 2030, within which electric vehicles (EV) are a major constituent[13].

Lithium is a highly electropositive element, with the smallest atomic radius and lowest mass of any metal, enabling impressive charge capabilities and power densities not matched by other chemistries. Li-ion batteries are a class of secondary (also known as rechargeable) battery, which operate using principles of electrochemical redox. As shown schematically in Figure

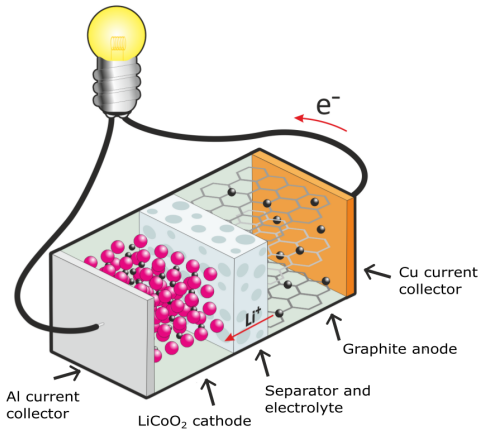

Figure 1.1: *Schematic of an archetypal Li-ion battery connected to an external circuit to discharge.*

1.1, these batteries comprise two electrodes of differing potentials, separated by an electrically-insulating but ionically-conducting electrolyte. Traditionally, the electrolyte consists of a porous separator infiltrated with a liquid organic electrolyte in which ions can solvate to cross between the electrodes. During discharge, simultaneous oxidation and reduction reactions take place at the anode and cathode electrodes respectively. Oxidation of the anode releases lithium ions which pass through the electrolyte and intercalate into the cathode. Simultaneously, the anode releases electrons into an external circuit via current collectors. The movement of these electrons through the external circuit, necessitated to maintain charge neutrality, does electrical work which can be utilised. The reversible intercalation of lithium ions into the anode and cathode materials enables for recharging of batteries through application of a reverse voltage.

Traditionally, the transition metal oxide cathode $LiCoO_2$ has been used with a graphite anode in Li-ion batteries. Various other cathode materials such as $LiMn_2O_4$ (LMO), $LiFePO_4$ (LFP) and $LiNi_xMn_yCo_{1-x-y}O_2$ (NMC), are now in use. The redox reactions for a classic lithium cobalt oxide (LCO) battery are shown in Equations (1.1) to (1.3).

$$\text{Anode: } LiC_6 \rightleftharpoons Li^+ + e^- + C_6 \tag{1.1}$$

$$\text{Cathode: } Li^+ + e^- + CoO_2 \rightleftharpoons LiCoO_2 \tag{1.2}$$

$$\text{Overall: } LiC_6 + CoO_2 \rightleftharpoons LiCoO_2 + C_6 \tag{1.3}$$

To understand the performance of Li-ion batteries, it is necessary to introduce some key metrics.

The theoretical potential (or voltage) of a cell corresponds to the difference in electrochemical potential (μ) of electrons in the two electrodes divided by the elemental charge e (Equation (1.4)). This cell potential varies with the state-of-charge of the cell as a result of the lithium concentration dependence of the phases in the cathode and anode. Internal impedances in the cell mean that some of the voltage is dropped when current is drawn from the cell. This reduces the discharge voltage and means increased voltages are required during charging. To limit these ohmic drop overpotentials, it is desirable to have high electrolyte ionic conductivities[14].

$$V_{OC} = -\frac{\mu_{Li}^{cathode} - \mu_{Li}^{anode}}{e} \tag{1.4}$$

The theoretical capacity of an electrode, q, can be calculated from the number of moles of Li^+ ions that can be stably intercalated into the structure (z), the Faraday constant (F), and its molar mass (M), using Equation (1.5)[14]. In a battery, the capacity of the anode and cathode side are matched using appropriate masses of active material.

$$q(mA\ h\ g^{-1}) = \frac{zF}{3.6M} \tag{1.5}$$

Integrating the cell potential with respect to capacity, as in Equation (1.6), corresponds to the available energy to be stored in a cell[14]. As such, it is desirable for batteries with both large cell potentials and extractable capacities.

$$\text{Energy}_{cell} = \int_0^Q V(q)\ dq \tag{1.6}$$

Values of specific energy or energy density are often quoted, normalised by mass or volume respectively. Here, non-active components such as binders, the electrolyte and current collectors must be accounted for. Inevitable degradation during use will also impact the values achieved in practice.

1.2 Solid-State Batteries

1.2.1 Lithium Metal Batteries

The volumetric and gravimetric energy densities achieved by Li-ion batteries have increased dramatically since their conception, but the physicochemical limit is being approached[15]. Consumers continue to demand more from their EVs, and with hopes for electric aviation growing, transformational rather than incremental improvements are required. By replacing the graphite anode (372 mA h g^{-1}) in which Li^+ ions reversibly intercalate (Equation (1.1)) with a lithium metal anode which is oxidised and reduced upon cycling (Equation (1.7)), the theoretical capacity is increased tenfold (3861 mA h g^{-1}), due to the absence of a host structure. Furthermore, pure lithium metal anodes exhibit the lowest reduction potential (-3.04 V vs a standard hydrogen electrode (SHE)). This combination of large capacity and low reduction potential could offer exceptional energy densities, making lithium metal the holy grail of anodes, and driving forward research into aptly-named lithium metal batteries.

$$Li \rightleftharpoons Li^+ + e^- \tag{1.7}$$

Whether an electrolyte is oxidised/reduced in electrolyte-electrode side reactions can be determined from its electrochemical stability window, defined by the energies of the lowest unoccupied molecular orbital (LUMO) and highest occupied molecular orbital (HOMO) in liquid electrolytes[16].

As shown in Figure 1.2, the potentials of the anode and cathode ideally lie within this window. In reality this is often not the case. Irreversible capacity loss is typically seen in the first charge of a battery, as lithiated graphite reduces the electrolyte to form a layer of products known as the solid electrolyte interphase (SEI), in doing so consuming some of the lithium and preventing it from being cycled. SEIs typically have reduced ionic conductivity compared to the electrolyte, and so also have detrimental impacts on the cell's impedance. An ideal SEI acts as a passivating layer, preventing further electrolyte decomposition upon continued cycling. Although this approach can work well with graphite anodes, lithium metal anodes introduce additional challenges. Specifically, plating of lithium in liquid electrolytes often occurs inhomogeneously,

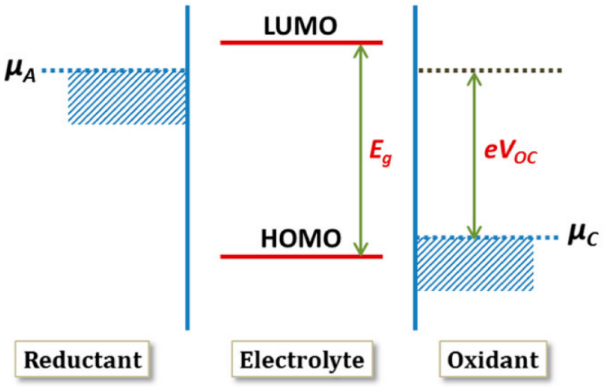

Figure 1.2: *Schematic energy level diagram showing a liquid electrolyte with electrochemical stability window E_g in contact with an anode and a cathode with electrochemical potentials of μ_A and μ_C respectively. The occupied electron states are represented by the blue shaded region. Figure adapted with permission from*[16]*. ©2013 American Chemical Society.*

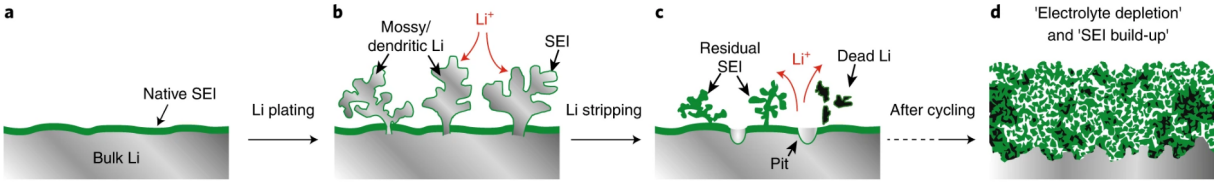

Figure 1.3: *Schematic showing degradation processes at the lithium anode-liquid electrolyte interface during cycling. a) Initially a planar SEI forms on the lithium anode. b) Inhomogeneous plating during charging results in dendrite formation. c) Lithium is stripped upon discharging, leaving residual SEI, dead lithium and pits in the anode. d) Continuous cycling forms a thick porous layer of degradation products. Adapted with permission from*[17]*.*

forming concentrated electric fields which preferentially plate lithium to produce high surface area filaments commonly referred to as dendrites[17]. As well as consuming lithium to generate significant areas of SEI, these dendrites have the potential to grow across the electrolyte and cause an internal short circuit, resulting in cell failure and potentially dangerous thermal runaway which could ignite the organic liquid electrolyte. Additionally, the large volume changes associated with the plating and stripping of lithium metal continually disrupt the SEI. This results in repeated exposure of fresh anode, promoting further lithium-consuming reactions[18,19], and can potentially break off dendrite pieces such that they become electronically-isolated and no longer contribute to the cell's capacity, known as "dead" lithium[17,20,21]. These processes are illustrated schematically in Figure 1.3.

The amount of lithium consumed by reactions, or lost as dead lithium, can be tracked using the coulombic efficiency (CE), η, for any given cycle. This is calculated using Equation (1.8).

$$\eta\ (\%) = \frac{q_{discharge}}{q_{charge}} \times 100 \tag{1.8}$$

For a battery cycle life of 1000 cycles, defined as the number of cycles at which the battery has 80% of its original capacity, a CE above 99.98% is required[16,22]. In spite of significant research directed at creating safe liquid lithium metal batteries, their success is still unrealised.

1.2.2 Motivation for Solid-State Batteries

A promising approach to overcome the challenges associated with liquid electrolyte lithium metal batteries is through use of solid electrolytes. Drawn schematically in Figure 1.4a, this is known as a solid-state battery (SSB). It has been anticipated that several advantages over liquid electrolytes could be offered by SSBs. A primary factor driving early research in the field was the hope that solids would avoid failure and other detrimental behaviour arising from lithium dendrite growth[23]. Furthermore, the safety of cells is expected to be improved by the removal of flammable liquid electrolytes. In a highly-cited piece of theoretical work, Monroe and Newman proposed that dendrite formation could be prevented by use of high stiffness (E > 15 GPa) polymer electrolytes[24]. The model assumes ideal, homogenous and purely elastic interfaces, considering only mechanical stability and ignoring other real-world effects such as electrochemical instability, defects, plasticity and non-linear growth. As such, the use of high stiffness electrolytes alone is insufficient to prevent dendrite formation in practical systems.

Another key motivator for SSBs is the desire to increase energy density through the use of both lithium metal anodes and high voltage (> 5 V) cathodes, which are incompatible with the electrochemical stability windows of current liquid electrolytes[25–27]. The electrochemical stability window in solids, defined by the conduction and valence band energies, has been demonstrated to be wide and stable over a large temperature range for some solid electrolytes[28].

The reduced reaction rates expected between solids may also lead to longer cell lifetimes, and the resistance of solid anionic networks to bulk polarisation could enable greater power capabilities[25]. The ratio of the Li^+ current to the total current, known as the Li^+ transference number, is typically in the range of 0.2 - 0.5 for liquid electrolytes, unlike solid electrolytes which lie close to the ideal value of unity[29]. This enables higher power capabilities for a given

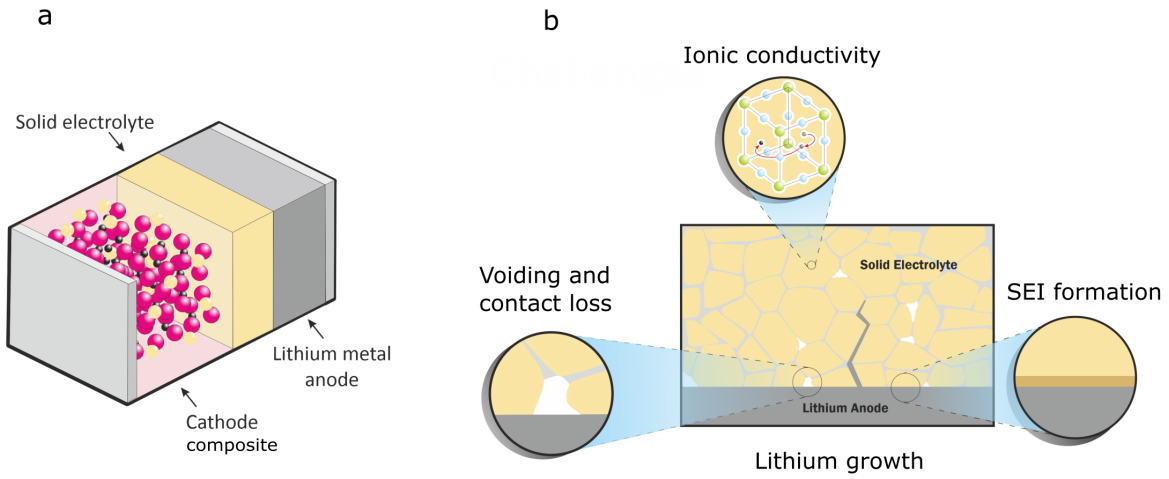

Figure 1.4: *Solid-state batteries. a) Schematic of a SSB which utilises a lithium metal anode. b) Illustration of some key challenges which need to be overcome for successful implementation of SSBs.*

electrolyte conductivity in solids, as the concentration gradients which develop at high cycling rates are shallower, and hence result in less polarisation of the cell voltage[30].

1.2.3 Challenges for Solid-State Batteries

Despite these advantages, the success of all-solid-state batteries has not yet been fully implemented. For a successful solid electrolyte, a range of requirements must be satisfied. In addition to good ionic conductivity and a wide electrochemical stability window, materials must have low electronic conductivity, low cost, good thermal and mechanical stability during cycling, high ion selectivity, and be safe[31–33]. Broadly, Li-ion conductor research is focussed in three areas: inorganic ceramics, organic polymers and composites which combine their properties[34]. Although the flexible nature of polymers offer advantages for interfacial contact, they generally have poorer ionic conductivities, electrochemical stability windows, and temperature stability[35,36]. Inorganic electrolytes encompass a range of crystallographic structures, compositions and processing routes[37]. Two dominant chemistries investigated are oxides, such as garnet $Li_7La_3Zr_2O_{12}$ (LLZO), and sulphides, such as argyrodites and lithium thiophosphates (LPS)[38–40]. However, finding solid electrolyte solutions which simultaneously offer wide electrochemical stability windows and high ionic conductivities is challenging. Despite expectations, many solid electrolytes are not thermodynamically stable with lithium metal. Nonetheless, in instances where the electronic conductivity of the formed SEI is low, the layer can act as passivating, providing kinetic

stabilisation in practice[41]. Ionic conductivity relies on mechanisms such as vacancy diffusion, direct interstitial and correlated interstitial mechanisms in solids, which are typically slower than diffusion processes in liquids. Although ionic conductivities in some sulphide materials are now on the order of commercial organic liquid electrolytes (10^{-2} S cm^{-1}), sulphides typically exhibit poor electrochemical stability windows. On the contrary, oxides generally exhibit good electrochemical stability, but poorer ionic conductivity[26,37].

Furthermore, solids introduce new problems which are not applicable to liquids, specifically relating to the nature of solid-solid interfaces. Liquid electrolytes naturally wet electrode surfaces, whereas solids tend to have poorer physical contact, a problem enhanced by the stresses that develop during the volume changes occurring upon electrochemical cycling[42–44]. This impacts charge transfer for the redox reactions at the electrolyte-electrode interfaces, and can also have detrimental impacts on cycle life, charge rate capability and capacity retention. Additionally, in spite of hopes and predictions, growth of lithium filaments is observed in solid electrolytes operating at high current densities upon charging[45,46]. This is often attributed to defects present in solid electrolytes leading to their fracture[47–49]. Upon discharging, voiding and contact loss between the lithium anode and the electrolyte can occur as a result of slow diffusion kinetics and insufficient creep of lithium metal[46]. These various challenges, illustrated in Figure 1.4b, will all need to be addressed for the success of SSBs. To do this, promising solid electrolyte materials and their processing routes must be studied.

1.3 The Proposed Impacts of Grain Boundaries in Solid Electrolytes

Current state-of-the-art solid electrolytes are inorganic ceramics, typically made from crystalline powders by sintering or pressing. The nature of these synthesis routes mean that the electrolytes produced are polycrystalline and contain a high density of grain boundaries, which can be expected to have consequences on the performance of the electrolyte.

A grain refers to a region of material in which atoms have a continuous periodic arrangement. Grain boundaries are the interfaces between grains of differing orientation, which themselves will have a locally different structure. Grain boundaries are established to have far-

reaching effects on materials, such as the mechanical, electrical, corrosion and thermal properties. Further to this, the degree of misorientation between grains controls the grain boundary structure which can further affect properties. It is generally the case that higher angles result in higher associated grain boundary energies, which can make them preferential sites for reactions, or can control the grain growth, for example.

The following section will consider the current understanding of the impacts grain boundaries have on solid electrolyte performance, specifically ionic conductivity and failure by lithium growth. A large portion of the work in this section was first published in the following article: Milan, E. and Pasta, M., The role of grain boundaries in solid-state Li-metal batteries. *Mater. Futures* **2**, 013501 (2023).

1.3.1 Ionic Conductivity

Although diffusion along grain boundaries is often faster than within the bulk of polycrystalline materials[50,51], it has long been believed that grain boundaries act as a bottleneck to ionic conductivity in superionic conductors[52–55]. Various mechanisms explaining this ion-blocking effect of grain boundaries have been suggested, such as distortions due to grain misalignment[52] and grain boundaries acting as sinks of ionically-blocking impurities[56]. In spite of this, limited experimental work confirming the impact of grain boundaries on conductivity exists in the solid-state battery field.

Wu and Guo synthesised lithium lanthanum titanate (LLTO) samples with the composition $Li_{3x}La_{0.67-x}TiO_3$ with grain sizes varying from 25 nm to 3.11 μm through annealing heat treatments of sintered compacts at temperatures between 900 °C and 1100 °C at 80 MPa pressure under vacuum. Through deconvolution of impedance Nyquist plots into bulk and grain boundary components, they observed not only the dramatically lower grain boundary conductivities ($\sim$4 orders of magnitude lower than the bulk), but also an increase in grain boundary resistance with decreasing grain size, despite the grain boundaries being apparently crystallographically the same[57]. This is shown in Figure 1.5a showing the grain boundary conductivity of different prepared samples. To explain this, they proposed a space-charge model in which the cores of the grain boundaries are positively charged and so repel the mobile cations. They use this concept to define an 'electrical grain boundary' which has greater thickness than the

corresponding crystallographic grain boundary, illustrated in Figure 1.5b. This is an idea which has been well-established in fuel cell literature where extensive research already exists[58–62]. It is worth noting that no comparison of density variations between samples were provided, other than that they were all greater than 94% relative density, meaning the impact of porosity variations cannot be eliminated with certainty. This is an important consideration in experimental research on grain boundaries, which shall be addressed further in Section 1.3.3.

Several theoretical studies using molecular dynamics (MD) to calculate ionic conductivities and activation energies for cation migration across different low-energy grain boundaries, support the conclusion that oxides generally exhibit reduced grain boundary conductivities[52,63,64].

Unlike candidate oxide electrolytes, sulphides appear to have low grain boundary resistances which are comparable to the bulk, making grain boundaries less detrimental to performance[66–69]. Dawson *et al.* modelled a homologous oxide and sulphide (Na_3PO_4 and Na_3PS_4) to directly compare the effect grain boundaries have on each structure. The radial distribution function (RDF) plots which show the average distribution of atoms around a given atom were calculated (Figure 1.5c). It was observed that in the case of the oxide, the grain boundary was over-coordinated. However, in the sulphide, the RDFs calculated for single crystal and polycrystalline simulations were essentially the same, implying the conduction mechanism in the grain boundary is the same as the bulk crystal[64]. They suggested that small differences in conductivity observed in the sulphide can be credited to composition changes and a higher concentration of point defects in the grain boundary region.

Quirk and Dawson looked at modelling four Li-ion conductors - an antiperovskite oxide (Li_3OCl) and hydroxide (Li_2OHCl), a thiophosphate (Li_3PS_4), and a halide (Li_3InCl_6)[65]. The oxides were demonstrated to have higher activation energies across grain boundaries than within the bulk, as expected. The effect was found to be less severe in the halide, much like in sulphides (Figure 1.5d). Electrostatic perturbations in grain boundary regions were shown to be higher in the case of the oxides, which is attributed to be the reason behind the increased activation energies. These results indicate that grain boundaries may not always be limiting from the viewpoint of ionic conductivity, but are expected to be more detrimental in oxide electrolytes where suboptimal ionic conductivity is already considered as a drawback.

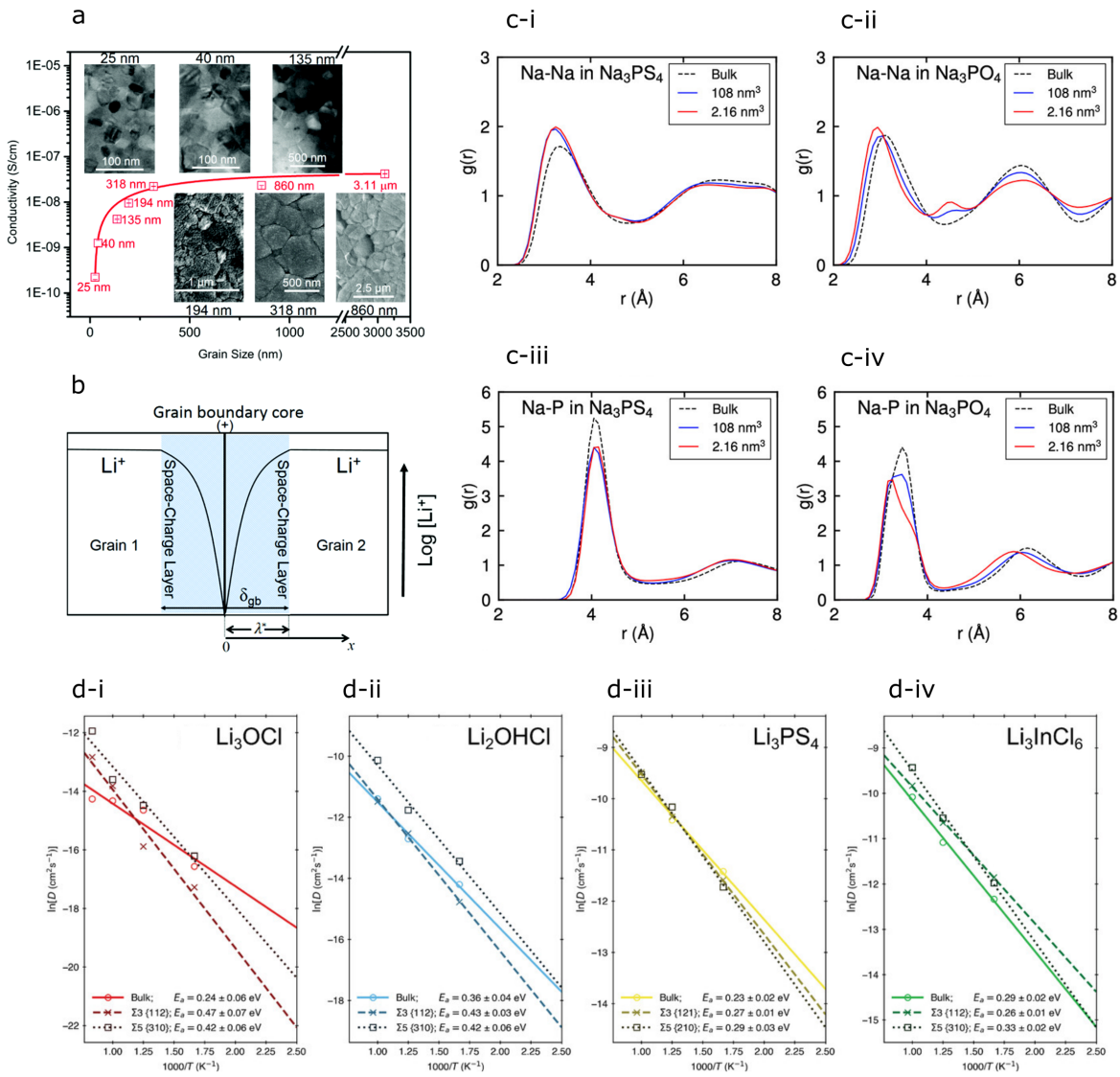

Figure 1.5: *Ionic conductivity of grain boundaries. a) Work by Wu and Guo showing grain boundary conductivity of $Li_{0.3}La_{0.57}TiO_3$ samples at 0 °C with different grain sizes. Reproduced with permission from*[57]*. b) Grain boundary space-charge layer model, reproduced with permission from*[57]*. c) Na-Na and Na-P Radial Distribution Functions calculated for bulk and polycrystalline Na_3PS_4 and Na_3PO_4 with grain volumes of 108 and 2.16 nm^3 at 400 K. Reprinted with permission from*[64] *©2019 American Chemical Society. d) Calculated Li-ion diffusivities for the bulk and grain boundaries of i) Li_3OCl, ii) Li_2OHCl, iii) Li_3PS_4 and iv) Li_3InCl_6. Corresponding activation energies, E_a, for each system are also shown. Reprinted with permission from*[65]*.*

1.3.2 Lithium Growth

The avoidance of filamentary lithium growth was a key motivator in initial investigations into solid-state electrolytes. Theoretical work on lithium-polymer electrolyte interfaces by Monroe and Newman proposed that lithium dendrite growth can be prevented by use of solid electrolytes

with a shear modulus greater than twice that of lithium[24], which is satisfied by most inorganic electrolytes. In spite of this, lithium growth is still a problem. The growth of these filaments is dependent on the rate of electrodeposition, and so critical current density (CCD) is often used as a convenient measure of resistance to failure by filament short-circuiting. Targets of 3-10 mA cm^{-2} for competitive Li-metal batteries are a long way from realisation[25,70].

Cheng *et al.* claimed to demonstrate that lithium filaments propagate intergranularly in polycrystalline samples by providing scanning electron microscopy (SEM) images displaying a web-like structure of lithium on an LLZO surface fractured post cycling (Figure 1.6a)[20]. Another study used X-ray computed tomography to show lithium filaments often take tortuous pathways through LLZO, which are concordant with expected intergranular pathways for the grain size of the sample[71]. These findings may indicate that grain boundaries contribute to solid electrolyte failure by lithium growth, making them detrimental even in material systems where their effect on ionic conductivity is negligible.

Several theories have been suggested to explain the occurrence of intergranular lithium deposition. Much of this existing work is based on LLZO electrolytes, deemed a good choice thanks to its high bulk conductivity and relatively good chemical stability with lithium metal[72,73]. The behaviour of different material systems may vary. Consequently, it would be beneficial to study lithium-growth behaviour across other candidate electrolyte materials as well.

Yu *et al.* proposed that the lower shear modulii of grain boundaries allow for accumulation of lithium in these elastically softer regions. This generates a stronger local electric field, hence promoting further deposition (Figure 1.6b)[74]. Alternatively, if grain boundaries act as fast diffusion pathways such that the rate of lithium arriving at the electrolyte-electrode interface exceeds the lateral diffusion away, the resulting lithium 'pile-up' might lead to deposition of filaments along the grain boundaries (Figure 1.6c). Although density functional theory (DFT) calculations and other studies indicate grain boundaries hinder ionic conductivity, it should be noted that studies have focussed on difficulty crossing between grains, whereas diffusion along grain boundaries themselves may provide fast channels if there is increased free volume, for example.

Han *et al.* proposed an electronic leakage mechanism in which electrons tunnel into the electrolyte and reduce Li^+ ions[31]. This theory is able to explain the occurrence of both

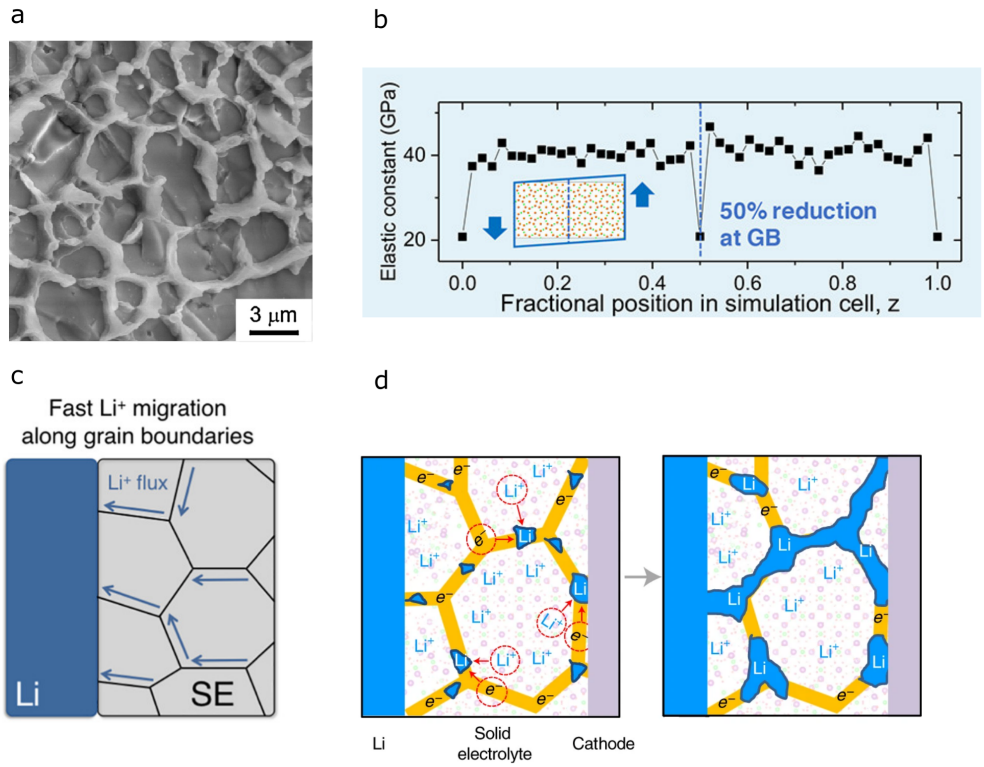

Figure 1.6: ***a)*** *SEM image of the fractured surface of cycled LLZO, showing apparent lithium deposition along grain boundaries. Reprinted from*[20] *with permission from Elsevier.* ***b)*** *Example calculation of the elastic modulus across a grain boundary in LLZO carried out by Yu et al. and used to explain why lithium accumulates along grain boundaries. Reprinted with permission from*[74] *©2018 American Chemical Society.* ***c)*** *Suggested mechanism of intergranular lithium deposition in which grain boundaries act as fast-diffusion pathways, resulting in a 'pile up' of lithium at the anode-electrolyte interface. Reprinted with permission from*[74] *©2018 American Chemical Society.* ***d)*** *Schematic showing how electrons tunnelling into the solid electrolyte can reduce lithium ions and result in lithium deposits which interconnect over time. This is proposed to occur preferentially along grain boundaries thanks to their reduced band gaps. Reprinted with permission from Springer Nature: Nature Materials*[75] *©2021*

growth of lithium occurring at the anode-electrolyte interface, and direct lithium deposition inside of the solid electrolyte. For high ionic conductivity oxide and sulphide electrolytes such as LLZO and LPS, the electronic conductivity is of the order $10^{-9} - 10^{-7}$ S cm^{-1}.[76–78] This was used to explain why lithium phosphorous oxynitride (LiPON), which has very low electronic conductivities between $10^{-15} - 10^{-12}$ S cm^{-1}, may perform better at resisting lithium growth than other solid electrolytes, including those with much higher shear modulii and ionic conductivities[31]. This theory was extended further with the postulation that grain boundaries act as preferential routes for electron leakage[75]. The greatly affected atomic arrangements at grain boundaries can reduce their band gaps relative to the bulk, and when the local potential at grain boundaries exceeds this narrow bandgap, the resulting leakage current acts as a source of

electrons for lithium reduction. These isolated deposits grow with cycling, eventually interconnecting and leading to short-circuits, as demonstrated schematically in Figure 1.6d. LiPON is deposited as an amorphous film free from grain boundaries and so may also perform well for this reason. Further insights into the electronic structures of grain boundaries in oxide, sulphide and halide grain boundaries were obtained from atomistic modelling by Quirk *et al*[65]. Projected density of states were plotted using the hybrid-DFT functional HSE06. In all scenarios, band gap narrowing was found to occur in grain boundaries (by an average of 0.73 eV across the studied materials), indicating higher electronic conduction, as is instrumental to Han's theory for intergranular lithium plating. Not only will these increased leakage currents potentially play a role in failure by lithium-growth-induced short-circuiting, but also have negative consequences on cell efficiency.

Another explanation for grain-boundary plating was proposed by Li and Monroe. This theory suggests grain boundary deposition may be due to the capacitive nature of the electrolyte-electrode interface, which can sustain a space-charge layer under pressure when there is a current[79]. Their chemical deposition energetics argument states that when the compressive stress at the electrolyte-electrode interface exceeds a critical value, it becomes more favourable for lithium to deposit along grain boundaries than the electrolyte-electrode interface. This condition is more likely to occur at high-energy grain boundaries which lead to a less negative critical pressure[79]. The work assumes that the strain energy associated with depositing along the grain boundary is small. Precipitation along grain boundaries is a commonly observed phenomenon, and so it seems reasonable to expect that this strain term would not massively change the excess energy required for grain-boundary plating such that it becomes unfeasible. This theory still requires a source of electrons to reduce the lithium, as well as satisfaction of the free energy requirements, and so does not contradict the theory proposed by Han *et al.*

The Effect of Grain Size on Critical Current Density

Cheng *et al.* reported perhaps counter-intuitive findings of an improved CCD with smaller grain size for sintered LLZO samples. This was attributed to the three-times higher interfacial resistance measured in the case of the large-grained samples[80], which might be explained by noting that control of grain size was obtained through the sintering of different sized particles. Singh

et al. carried out a study which also used variation of particle size to produce cold-pressed Li_6PS_5Cl pellets (referred to in the study as 'small-grain' and 'large-grain' samples) demonstrating the same trend in CCD[81]. Their work showed the samples made from larger particles to have a higher surface roughness, which was used to explain their worse resistance to lithium filament growth[81]. Firstly, current focusing will be enhanced in locations of increased surface roughness, as is demonstrated in Figure 1.7a showing finite element analysis of the current density distribution at the interfaces between small- and large-grained samples with the lithium metal anode[81]. Various studies have considered non-uniform current distributions at the lithium anode-solid electrolyte interface, such as these, to be important in lithium filament nucleation[72,82,83].

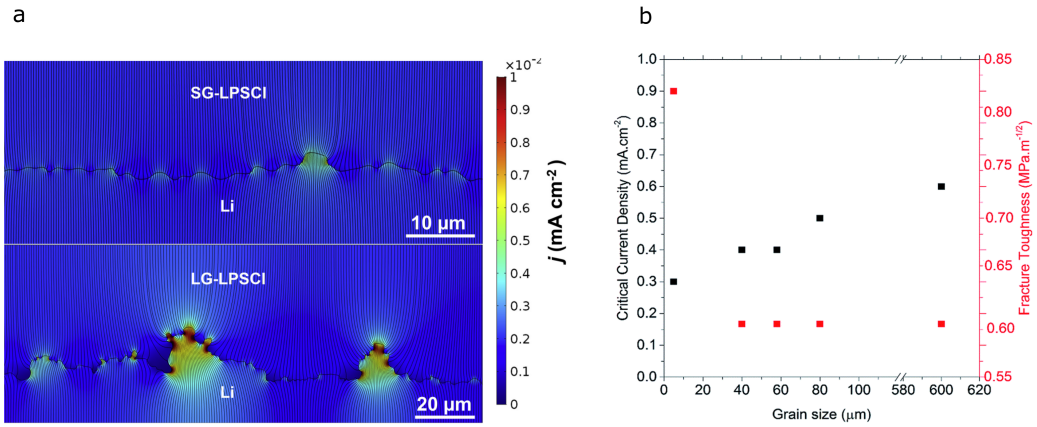

Figure 1.7: *a) Finite element analysis of the current density distribution at Li|SG-LPSCl and Li|LG-LPSCl interfaces obtained via digitisation of plasma focused ion beam (PFIB)-SEM images. Sharper and deeper flaws are observed in the LG case. (SG - small grain, LG - large grain). Adapted from[81] with permission from Elsevier. b) Critical current density and fracture toughness of LLZO samples as a function of grain size. Reprinted from[84] with permission from RSC.*

Secondly, when conformal contact is made between the lithium anode and solid electrolyte, the lithium which fills the pits in the solid electrolyte surface exerts a force on the electrolyte. This can be considered as a crack in a mode I opening geometry. Hence, the higher the surface roughness, the larger the effective crack size, the higher the stress concentration factor (K_c) at the 'crack' tip, and the lower the loads required to propagate the 'crack'. In the case of both of these papers, the interfacial properties attributed to control the lithium growth are not strictly a result of the grain boundaries, but the surface roughness and interfaces produced by synthesis approaches used to control the grain size. This is an important distinction, and some of the experimental challenges which exist in deconvoluting the effects of different microstruc-

tural features shall be addressed further in Section 1.3.3. In addition to improving the CCD through decreased surface roughness, Singh *et al.* propose that resistance to lithium propagation is also improved in their small-grained samples thanks to a stress-shielding effect. They argue that the high density of grain boundary triple junctions in samples with smaller grains results in continuous deflection of the lithium protrusion such that it takes a more tortuous path and hence increases the fracture toughness, K_{IC}, of the material[81].

Other work carried out by Sharafi *et al.* used hot pressing to yield samples with very small interfacial resistances. In this work, the grain size was controlled by varying the hot pressing temperature, and the grain structure was characterised using electron backscatter diffraction (EBSD) spectroscopy. A CCD increasing with grain size was demonstrated in this research, unlike the above findings from Cheng *et al.* and Singh *et al.*[84]. Supporting characterisation allowing for a dependency on fracture toughness to be eliminated was provided (Figure 1.7b, Table 1.1). Although the relative density and average grain misorientation angle were found to increase in conjunction with grain size in their samples synthesised through different hot-pressing temperatures, a further sample with yet larger grains was produced through the addition of an annealing step (50 hours, 1300 °C) post hot-press (at 1100 °C). This material exhibited the same relative density and a similar misorientation as the sample hot-pressed at 1300 °C (Table 1.1), indicating that the observed differences between these two measurements are indeed a result of the grain size. Sharafi *et al.* postulate that the contradictory findings by Cheng *et al.* could be a result of the nature of the grain boundaries produced in sintered compared to hot-pressed pellets differing. The impacts of grain boundaries extend beyond simply the grain boundary density, and may depend on other factors such as grain boundary energies, thicknesses, grain shapes and texture. This in turn will depend on the synthesis routes used to produce them, and is not something which has been sufficiently addressed in literature. For example, applying pressure during sintering, known as hot pressing, adds an additional driving force for densification without impacting the grain coarsening behaviour. It is also shown to produce mechanically stronger grain boundaries, evident from transgranular rather than intergranular fracture of $Li_{6.19}Al_{0.27}La_3Zr_2O_{12}$ hot-pressed when compared to traditional sintering[85].

Table 1.1: Summary of microstructural, mechanical and electrochemical properties of different LLZO samples investigated by Sharafi *et al.* HP-XX^{o}C refers to a sample hot pressed at XX^{o}C for 1 hour. A-1300 ^{o}C refers to a HP-1100 ^{o}C sample which was subsequently annealed at 1300 ^{o}C for 50 hours. Reprinted from[84] with permission from RSC.

	Microstructural Properties				Mechanical Properties		Electrochemical Properties	
Pellet	Phase purity	Relative density (%)	d_{ave} (μm)	Misorientation angle (^{o})	H (GPa)	K_{IC} (MPa m$^{-1/2}$)	σ_{total} (mS cm^{-1})	CCD (mA cm^{-2})
HP-1100 ^{o}C	Cubic LLZO	96.0 ± 0.5	5 ± 2	20	9.88 ± 0.49	0.82 ± 0.07	0.46	0.3
HP-1200 ^{o}C	3 vol% pyrochlore	97.7 ± 0.5	40 ± 13	35	8.05 ± 0.52	0.61 ± 0.05	0.52	0.4
HP-1250 ^{o}C	1 vol% pyrochlore	98.1 ± 0.5	60 ± 20	40	7.74 ± 0.46	0.60 ± 0.06	0.54	0.4
HP-1300 ^{o}C	Cubic LLZO	99.4 ± 0.5	80 ± 20	40	7.42 ± 0.48	0.61 ± 0.04	0.56	0.5
A-1300 ^{o}C	Cubic LLZO	99.4 ± 0.5	600 ± 200	41	6.80 ± 0.49	0.60 ± 0.05	0.57	0.6

1.3.3 Decoupling the Effects of Grain Boundaries from Other Microstructural Features

Many inorganic solid-state electrolytes have high melting temperatures, meaning that processing is not typically carried out by melt-casting[86]. Instead, nanoscale powders are often synthesised, which can then be sintered or pressed into pellets. These powder particles can constitute of single crystals, polycrystals, amorphous materials or even multiple phases. Differing sinter temperatures or subsequent heat treatments can then be used to control the grain size. During sintering, various diffusion mechanisms take place, some of which contribute to densification to a greater extent than others. As such, the conditions chosen for sintering (temperature, time, particle size) have effects on the densification of the final sample as well as the grain coarsening behaviour. Additionally, depending on the rate of grain growth, remaining porosity may be either isolated inside of grains, or interconnected along grain boundaries, which may further influence plating behaviour. For example, in a sample with a high degree of associated grain boundary porosity, it is conceivable that plating lithium would deposit along the boundaries with significantly less stress than in a 'perfect' grain boundary with a much sharper interface and less steric space. These considerations bring into question whether studies investigating the effect of grain boundaries, which often dismiss the small density variations arising from the different synthesis conditions, can be taken at face value, or whether it is in fact the porosity which is responsible for observations. Prudence is especially important in instances where sintering of different sized particles is used to control grain size[87,88], as there will also be implications on the sinter quality resulting from a combination of different diffusion distances, initial packing efficiency and driving forces for densification.

In addition to the intrinsic difficulties with controlling grain size, it is sometimes the case that minimal microstructural characterisation is provided in literature. SEM is an essential

tool for gaining insights into the microstructure of solid electrolytes, but care must be taken not to mistake "particle size" for "grain size". SEM should ideally be used in conjunction with EBSD mapping, also providing information on texture and misorientation in samples. It may also be desirable to capture cross-sectional images since grain structure and porosity visible in surface images might not be representative of the bulk.

When navigating research on the role of grain size in solid-state electrolytes, it is important to consider whether the effects of grain size can be isolated from other variables. Whether grain boundaries in electrolytes are detrimental to the CCD is still not fully understood. Many mechanisms explaining the nucleation and growth of lithium have been proposed, but the reality is probably a complex interplay of factors. In order to address this, it is desirable to deconvolute the effects of porosity and grain boundaries, rather than dismissing small density variations which occur when using different sintering and heat treatment conditions to control grain growth, as well as surface roughness, interfacial contact and other microstructural features. An effective method of producing very dense samples will be required to do this, such as melt-casting. Lithium hydroxyhalide antiperovskites (Li_2OHX, X = Cl, Br) may be an ideal model system for this thanks to their low melting points ($< 300\,^{\circ}C$), which allow for both easy synthesis and control of grain size through cooling rate[86]. Another potential method of investigation might be controlled nucleation and growth of crystals from a glassy matrix through heat treatments. Typically, crystal nucleation and crystal growth dominate at different temperatures[89], and so the number of nucleated grains (and consequently grain size) can be controlled through the time held in the nucleation temperature range[90].

In spite of an incomplete understanding of the mechanisms governing grain boundary behaviour, early indications of increased electronic leakage and the reduced ionic conductivity in some systems imply that the removal of grain boundaries may benefit the performance of electrolytes regardless. Some of the questions and challenges associated with grain boundaries are shown in Figure 1.8, along with potential routes to removing them from electrolytes. One approach to eliminating grain boundaries is the creation of glasses. A lot of the work in this area has been focused on sulphide glasses. However, in view of the low grain boundary resistances exhibited by crystalline sulphides[91], they may not be a material system in which a particularly large benefit is gained from amorphisation. Additionally, the preference of glass-ceramics over glasses in sulphide work means that the focus in research is not actually on grain-boundary-free

systems. The potential performance improvements which could be gained from amorphisation should be investigated for other material systems. This is not limited to established solid electrolyte candidates, but could also encompass new chemistries such as borate glasses doped with lithium ions[92]. Successful materials must have good ionic conductivity and wide electrochemical stability windows. Additionally, in a bid to replicate the lithium-filament resistance of LiPON, it might be beneficial to pursue materials demonstrating high fracture toughness, low defect density and low electronic conductivity.

Another solution to removing grain boundaries is to make single crystal electrolytes. For these to be practically useful, a scalable and reproducible method of making single crystals with smooth surfaces is required. Previously, LLZO single crystals free from voids and grain boundaries have been demonstrated. However, defects were introduced during mechanical polishing of the samples, visible in SEM images[47,93]. Lithium filament growth was observed, proposed to be a result of nucleation from pre-existing flaws such as these at the interface[47]. As well as yielding the benefits of grain boundary removal, having access to atomically-smooth, bulk single crystals will enable other factors impacting the CCD, such as surface roughness, to be investigated without the influence of grain boundaries.

1.4 The LiBr-LiOH System

Recently, materials in the LiBr-LiOH system have received significant attention in energy storage research: Li_2OHBr as a potential solid-state electrolyte for lithium-metal batteries, and $Li_4(OH)_3Br$ as a PCM for TES[6–10,86,94–97]. This section introduces these two compounds, following which the current understanding of the LiBr-LiOH system more widely will be considered.

1.4.1 Lithium Hydroxyhalide Antiperovskites as Solid Electrolytes

Antiperovskites are a class of inorganic materials which have the perovskite crystal structure with inverted cation and anion sites. The crystal structure for antiperovskite Li_3OBr is shown in Figure 1.9a. The ideal antiperovskite structure is cubic, although lower symmetry distortions can occur depending on the composition, temperature and pressure[98]. Antiperovskites have been demonstrated to exhibit a wide range of interesting properties, including instances

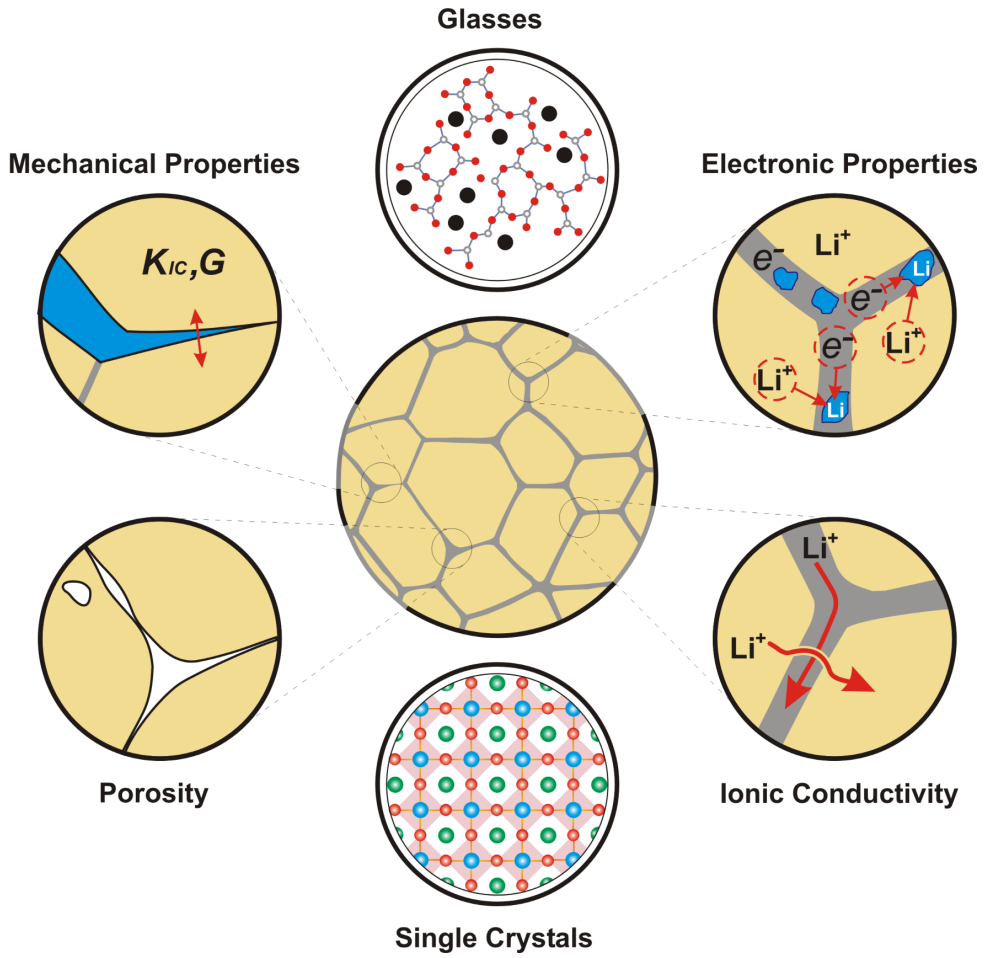

Figure 1.8: *Diagram showing key impacts of grain boundaries in solid-state electrolytes and potential research routes for removing them.*

of superconductivity (Ni_3MgC)[99], negative thermal expansion (Mn_3GaC)[100] and non-Arrhenius behaviour (K_3OI)[101]. One application for which they have received research attention, is as solid electrolytes in SSBs, and for some time, the antiperovskite Li_2OHBr has attracted significant interest[86,94,96,97,102–108]. Its low density, low processing temperatures, moderate ionic conductivity and high stability with lithium metal makes it a desirable candidate[109].

Interest in antiperovskite solid electrolytes first grew in 2012 when Zhao and Daemen reported the synthesis of Li_3OX (X = Cl, Br) antiperovskites, with ionic conductivities of $> 10^{-3}$ S cm^{-1} at room temperature and an activation energy of 0.2 - 0.3 eV for Li_3OCl[95]. In the following years, a wide range of conductivities have been reported, between 1.26×10^{-7} S cm^{-1} and 8.5×10^{-4} Scm^{-1} for Li_3OCl[53,54,110]. Subsequently, a strong case has been built that these studies are not in fact reporting synthesis of Li_3OX (X = Cl, Br) compounds as intended[102,109,111,112]. Firstly, Li_3OCl is predicted to be thermodynamically-unstable at room temperature, instead decomposing to Li_2O and LiCl[113–117]. Secondly, Li_3OCl is extremely hy-

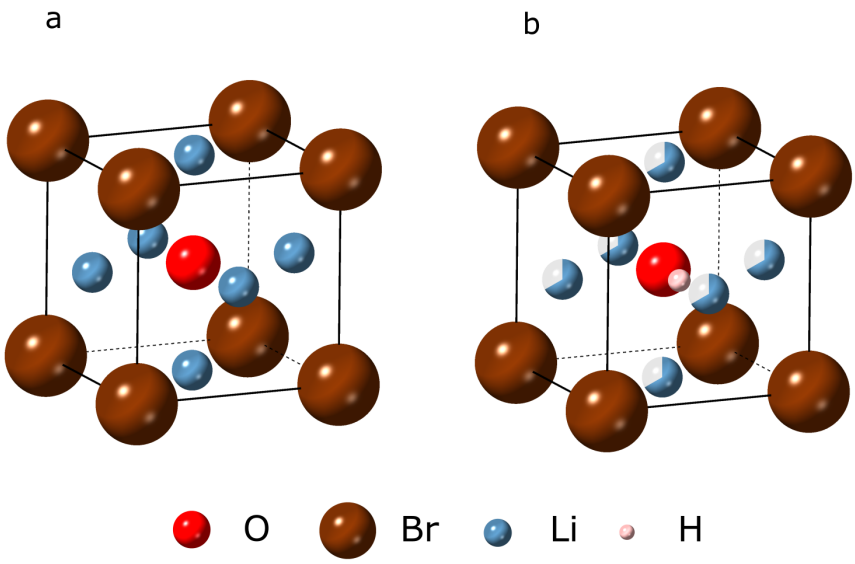

Figure 1.9: *Crystallographic structures of antiperovskites a) Li_3OBr and b) Li_2OHBr, generated using Crystalmaker software. In Li_3OBr the Li^+ cation sites are fully occupied, whereas in Li_2OHBr a third of the sites are unoccupied and the O^{2-} site is replaced with OH^-.*

groscopic, reacting with moisture to form the lithium hydroxyhalide antiperovskite Li_2OHCl via Equation (1.9) in the presence of any moisture or sources of OH[113,118].

$$Li_3OCl + H_2O \longrightarrow Li_2OHCl + LiOH \tag{1.9}$$

Solid-state synthesis using Li_2O and LiCl precursors is challenging due to the poor interdiffusion between these high melting point reactants (1438 °C and 605 °C respectively)[95,119]. Melt processing using the lower melting point precursor LiOH (462 °C) is often targeted instead[54,95,110], producing a water by-product (via Equation (1.10)) which is likely to hydrate the Li_3OCl even with attempts to remove it as it forms. Furthermore, lithium oxyhalide antiperovskites are indistinguishable from their hydroxyhalide counterparts by X-ray diffraction (XRD) due to their similar crystal structures. In spite of this, studies fail to provide additional characterisation which would provide discrimination between the two, such as the presence of -OH bonding in fourier transform infrared (FTIR) spectroscopy or Raman spectroscopy. It is therefore expected that a range of purities and hydration occur in previous Li_3OX studies. Regardless, people continue to report its synthesis without addressing the associated challenges.

$$2\,\mathrm{LiOH} + \mathrm{LiCl} \longrightarrow \mathrm{Li_3OCl} + \mathrm{H_2O} \tag{1.10}$$

In spite of the controversy surrounding Li_3OX reports, the lithium hydroxyhalide antiperovskites, such as Li_2OHCl and Li_2OHBr, appear to be promising electrolyte candidates. These differ from the Li_3OX antiperovskite structure by replacing the O^{2-} anion with a hydroxyl OH^- anion, and consequently introducing vacancies onto a third of the Li^+ sites to maintain charge neutrality, as shown in Figure 1.9b of the Li_2OHBr crystal structure. These vacancies are then available for a vacancy conduction mechanism. Additionally, rotation of the OH^- anions has been observed in numerous theoretical and experimental (pulsed-field gradient (PFG)-nuclear magnetic resonance (NMR) and ^{1}H NMR) studies[102,113,118,120–122]. This is believed to facilitate Li^+ migration via a "paddlewheel" mechanism. These thermodynamically-stable antiperovskites can be synthesised from LiOH and the corresponding lithium halide salt (Equation (1.11)) through a melt synthesis approach at relatively low temperatures ($< 350\,^\circ$C), enabling low cost synthesis and processing. In studies investigating interfaces between lithium hydroxyhalide antiperovskites and lithium metal, passivating SEIs with good stability are formed[86,96], as with other oxide electrolytes. The density of Li_2OHBr (~ 2.78 g cm^{-3}) and Li_2OHCl (~ 2.23 g cm^{-3}), however, are significantly reduced compared to other oxide electrolytes, such as LLZO (5.07 g cm^{-3}), $Li_{0.34}La_{0.56}TiO_3$ (5.01 g cm^{-3}) and $Li_{1.5}Al_{0.5}Ge_{1.5}(PO_4)_3$ (LAGP) (3.56 g cm^{-3})[123], offering an additional advantage. Other envisaged benefits include low electronic conductivity[105] and non-toxicity. Limiting lithium hydroxyhalide antiperovskites, are their sub-optimal ionic conductivities. Furthermore, a large range of room temperature values have been reported for Li_2OHBr (1×10^{-7} S cm^{-1} – 7×10^{-6} S cm^{-1})[86,102–105,108] and Li_2OHCl (6.8×10^{-9} S cm^{-1} – 4×10^{-5} S cm^{-1})[86,96,102,105], making it unclear what the true conductivities are. This variation has often been attributed to detrimental impacts of grain boundaries[52,65,86,107,108,124]. Another factor may be the presence of impurities, which can be seen frequently in reports[96,97,102,105,108]. To establish the bulk conductivity of these materials, microstructure and purity optimisation will be necessary.

$$\mathrm{LiOH} + \mathrm{LiX} \longrightarrow \mathrm{Li_2OHX} \tag{1.11}$$

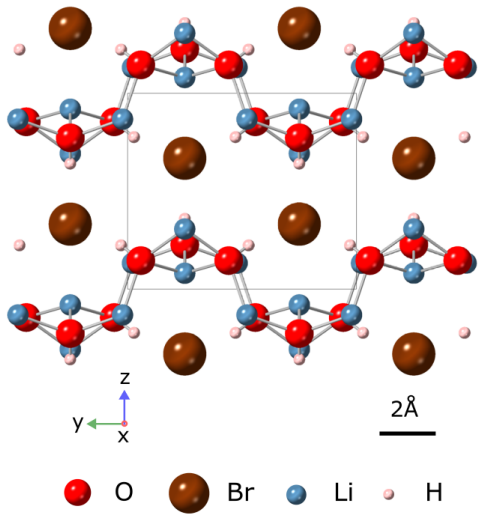

Figure 1.10: *Layered crystallographic structure of $Li_4(OH)_3Br$ proposed by Hönnerscheid et al.*[127] *drawn using CrystalMaker software.*

1.4.2 $Li_4(OH)_3Br$ for Latent Heat Storage

$Li_4(OH)_3Br$ is a compound found in the LiBr-LiOH phase diagram with a melting point around 290 °C, believed to form from the peritectic solidification of "liquid + LiOH"[9,125–128]. The crystal structure of $Li_4(OH)_3Br$, determined by Hönnerscheid *et al.*, belongs to the $P2_1/m$ space group and is shown in Figure 1.10[127].

In 2017, Achchaq considered the use of peritectic compounds for application as PCMs, conducting an extensive search of 635 binary systems in the temperature range 300 °C to 700 °C using FactSage software[129,130]. Calculations found an impressive transition enthalpy as high as 804 J g^{-1} (425 kW h m^{-3}) for the peritectic formation of $Li_4(OH)_3Br$ at ∼ 300 °C. By comparison, steam accumulators, which are the predominant technology currently used in industry for the temperature range 250 °C to 300 °C, exhibit low storage capacities of 20 - 30 kW h m^{-3}.[9,131] This, and the relatively low cost of LiBr and LiOH salts, makes the use of $Li_4(OH)_3Br$ in TES applications appealing, particularly for use in direct steam generation (DSG) CSP where isothermal storage capacity at 300 °C is desirable[132]. Consequently, $Li_4(OH)_3Br$ has attracted attention in research for potential application in LHTES[6–11].

Despite the promising calculations, experimental melting enthalpies above 250 J g^{-1} have not been obtained to date[6–9]. A possible factor contributing to this is the slow kinetics of

peritectic reactions, often leading to incomplete formation of the peritectic phase. Mahroug *et al.* used XRD to argue that this is not the case, and that complete reaction occurs in samples cooled at rates between 0.5 K min^{-1} to 50 K min^{-1}. This could suggest that a direct transformation in which the peritectic phase directly nucleates in the liquid upon cooling occurs instead, as has been reported in various other binary systems[133–137]. However, it should be noted that they chose to disregard transmission electron microscopy (TEM) and energy dispersive spectroscopy (EDS) images which showed inhomogeneities in composition, indicating that there could be multiple phases present[8]. Legros *et al.* proposed a polymorph may sometimes form depending on the synthesis precursors used, and suggested that the presence of this phase may explain the lower storage capacities observed experimentally[7].

In spite of the sub-theoretical values obtained experimentally, $Li_4(OH)_3Br$ still demonstrates excellent melting enthalpies for PCMs in the range 280 °C to 310 °C[3–5]. When compared to $NaNO_3$, the most highly researched option of TES for DSG CSP, $Li_4(OH)_3Br$ demonstrates improved energy density and reduced volume changes, which could potentially offer infrastructure savings and improved lifetimes[8,138]. It is apparent that, despite showing promising thermal storage behaviour, a complete understanding of $Li_4(OH)_3Br$ is missing.

1.4.3 Proposed LiBr-LiOH Phase Diagrams

In early work by Scarpa, it was believed that Li_2OHBr and $Li_4(OH)_3Br$ were the only phases existing in the LiBr-LiOH binary phase diagram[125]. In 1953, a high-temperature phase with stoichiometry $Li_3(OH)_2Br$ was mentioned by Reshetnikov[139], however information about the phase is unavailable, and subsequent publications doubted its existence[126,128]. Based on differential thermal analysis (DTA) measurements, Hartwig *et al.* proposed the phase diagram shown in Figure 1.11a, in which both Li_2OHBr and $Li_4(OH)_3Br$ are peritectic phases[126]. More recently, Sangster employed a computer-coupled phase diagram/thermodynamic analysis to calculate an updated phase diagram[128]. As shown in Figure 1.11b, here Li_2OHBr is proposed to be peritectoid, forming from $Li_4(OH)_3Br$ and LiBr.

In 2022, Mahroug *et al.* investigated to substantiate claims of a $Li_3(OH)_2Br$ phase[9]. Crucially, differential scanning calorimetry (DSC) measurements taken across a range of compositions indicated a phase transition at $\sim$ 230 °C which had not previously been identified,

with a maximum transition enthalpy for the composition 67 mol % LiOH, indicating that the stoichiometry of the unknown phase lies at this LiBr-LiOH ratio. They additionally conducted *in-situ* and *ex-situ* XRD measurements which showed the formation of new diffraction reflections upon heating samples from the room-temperature "Li_2OHBr + $Li_4(OH)_3Br$" phase field. Based on these findings, Mahroug *et al.* developed the existing phase diagram to include $Li_3(OH)_2Br$. As shown in Figure 1.11c, these alterations would introduce $Li_3(OH)_2Br$ as a peritectic phase (liquid + $Li_4(OH)_3Br \rightarrow Li_3(OH)_2Br$)[9]. This phase diagram is shown more clearly in Figure 1.11d in which the phase fields are labelled. In Mahroug's proposal, undefined phase transitions are drawn for compositions with greater than 75 mol % LiOH at $\sim 230\,^{\circ}C$ and $\sim 280\,^{\circ}C$. These transitions are plotted as a result of observed DSC peaks (shown by red circles in Figure 1.11c), but are not permitted by the Gibbs phase rule. It is therefore important that future work on the LiBr-LiOH phase diagram addresses this issue.

Each of these phase diagrams rely heavily on thermal analysis techniques such as DSC and DTA. Although these techniques provide a strong starting point to understanding systems, the peritectic and peritectoid reactions proposed are likely to suffer from poor kinetics, meaning that equilibrium conditions may be difficult to achieve in these studies. Anneals may be used to systematically study the phase diagram, although the presence of high-temperature phase fields and narrow temperature range fields make verifying the phase diagram still far from trivial. Furthermore, it is possible that there are still unidentified phases in the LiBr-LiOH binary system which have not been included in the diagram. One such phase is the Ruddlesden-Popper antiperovskite $Li_5(OH)_2Br_3$, which it has not yet been established whether is equilibrium or non-equilibrium.

1.4.4 Ruddlesden-Popper Antiperovskites

Recently, it has been speculated that Ruddlesden-Popper antiperovskites with the composition $Li_5(OH)_2Br_3$, or $LiBr(Li_2OHBr)_2$, could be promising solid electrolytes[140–142]. This structure differs from a regular antiperovskite in that it is a 2-dimensional networked material consisting of Li_2OHBr antiperovskite-like double layers which alternate with rocksalt-like layers, as shown in Figure 1.12. A primary motivation for using this alternative to Li_2OHBr would be if improvements to lithium ion dynamics, which have been indicated in theoretical studies, were observed

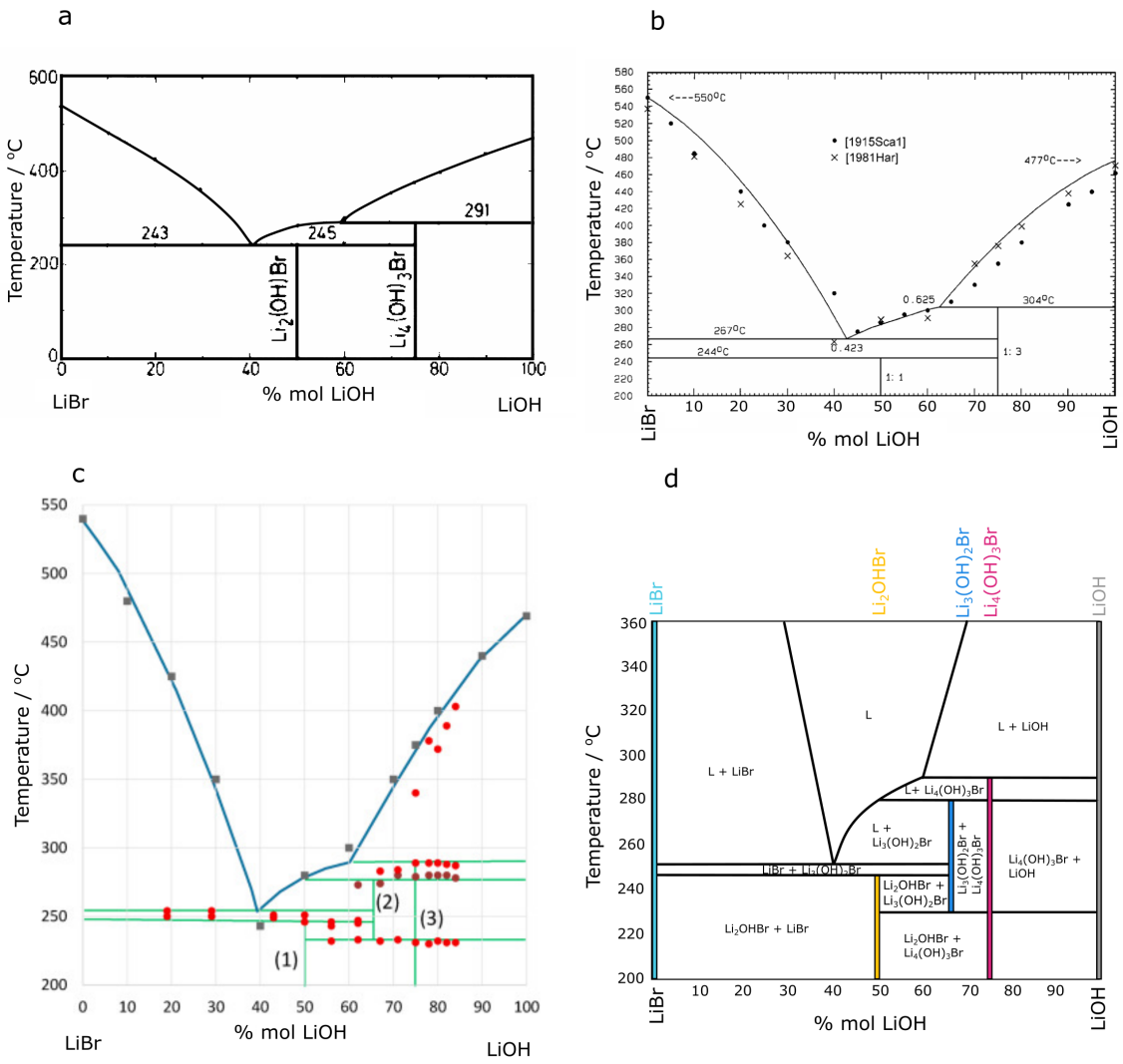

Figure 1.11: *Progression of proposed LiBr-LiOH phase diagrams. a) By Hartwig et al. in 1981, adapted from*[126] *with permission from Elsevier. b) By Sangster in 2000, using thermal analysis carried out by Scarpa and Hartwig, adapted from*[128] *with permission. c) By Mahroug et al. in 2022, introducing $Li_3(OH)_2Br$ at 66.7 mol % LiOH. DSC peak positions are plotted as red points. Adapted from*[9] *with permission. d) Mahroug's phase diagram redrawn to clearly show phase field labels. Forbidden phase transitions were plotted in Mahroug's diagram, which results in the undefined phase fields shown here. Note that the stoichiometric ranges of each pure phase are unknown and not represented by the line thicknesses.*

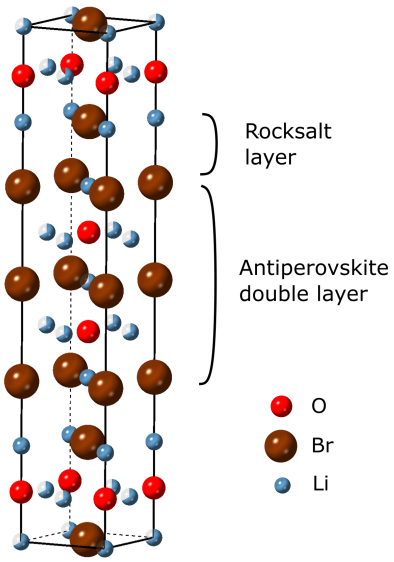

Figure 1.12: *Crystallographic structure of $Li_5(OH)_2Br_3$ as reported by Koedtruad et al.*[141] *visualised using CrystalMaker software. Rocksalt layers are seen to alternate with antiperovskite double layers.*

experimentally. Computational work on the closely related Ruddlesden-Popper phase $Li_7O_2Br_3$, or $LiBr(Li_3OBr)_2$, found a reduced activation energy for lithium-ion hopping when compared to the parent antiperovskite, Li_3OBr. This was attributed to the weaker interactions experienced by lithium ions at the edges of layers in the $Li_7O_2Br_3$ lattice[143]. Other modelling work has also demonstrated a relationship between network dimensionality and lithium-ion dynamics. One study on the chloride counterpart, Li_3OCl, indicated progressively improved room-temperature ionic conductivities and lowered activation energies for lithium-ion hopping as the network dimensionality of the material is decreased to 2DN-Li_4OCl_2, 1DN-Li_5OCl_2 and 0DN-Li_6OCl_4. This was proposed to be due to larger geometric bottlenecks and softer structural frameworks in the layered phases[144]. This relationship was further supported in simulations by Dutra *et al.*, who showed that the formation of defects is easier in lower-dimension antiperovskite materials, and additionally suggested that the increased polarisability of Br anions over Cl anions results in weaker Li-halide interactions in bromide analogue low-dimensional antiperovskites, which results in superior lithium-ion diffusion[145]. These findings suggest that experimental improvements in ionic conductivity may be achieved by lowering the dimensionality of Li_2OHBr to $Li_5(OH)_2Br_3$.

In spite of the promising computational work, synthesis of $Li_5(OH)_2Br_3$ remains challenging. $Li_5(OH)_2Br_3$ is not present in any current models of the LiBr-LiOH phase diagram, and its phase-pure synthesis has not been reported using the starting precursors LiBr and LiOH.

Despite theoretically lying in the LiBr-LiOH binary system at 40 mol % LiOH, synthesis attempts using stoichiometric LiBr and LiOH contained high fractions of both Li_2OHBr (38%) and LiBr (4%)[140,141]. The only report of single-phase $Li_5(OH)_2Br_3$ (as determined by XRD), used a combination of Li_2O, LiBr and LiOH in the stoichiometry $LiBr(Li_{2.5}OH_{0.5}Br)$[141]. This could suggest a large fraction of amorphous material may be present. It is apparent that the synthesis route, and subsequent characterisation, of this Ruddlesden-Popper antiperovskite is not yet well established.

1.5 Thesis Outline and Objectives

The content of this thesis spans applications of LiBr-LiOH compounds as PCMs for LHTES, and as solid electrolytes for SSBs, the latter being the primary focus. So far, we have encountered the key technologies and phases of interest in this work. The initial objectives of this DPhil were to investigate approaches of making "grain boundary-free" lithium hydroxyhalide antiperovskite electrolytes, and subsequently assess their performance. Section 1.3 outlined the motivations behind this, discussing the negative impacts believed to arise from the presence of grain boundaries in solid electrolytes.

To achieve these "grain boundary-free" systems, the problem will be approached from two angles. The first is to make single crystals, in which the sample consists of a single grain orientation, typically achieved through slow cooling of a seed crystal. The second is to make glasses: amorphous structures often synthesised by rapidly cooling molten liquids to freeze-in the disordered structure. In essence, these synthesis routes lie on opposite extremes of the "cooling rate spectrum". Impurity problems in the lithium hydroxyhalide antiperovskites are a common challenge for anyone working in the field. However, during initial studies it became evident that impurity formation observed in Li_2OHBr and similar stoichiometries, were arising not due to chemical impurities, but phase impurities, which in turn were highly dependent on the cooling conditions used. This is particularly problematic in attempts to synthesise single crystals from Li_2OHBr. Further to this, upon investigating slightly LiOH-rich antiperovskites, observed impurities did not correspond to $Li_4(OH)_3Br$ as anticipated, indicating a discrepancy with the current understanding of the LiBr-LiOH material system which needs to be understood further. These results shifted some of the focus in this work to generating a greater understanding of the

LiBr-LiOH phase diagram, and hence this behaviour, before returning to the original aims of grain boundary-free antiperovskites.

In Chapter 2, the fundamentals of the experimental techniques employed in this thesis to answer these questions will be introduced.

The first experimental chapter, Chapter 3, will investigate the LiOH-rich phases in the LiBr-LiOH phase diagram, $Li_3(OH)_2Br$ and $Li_4(OH)_3Br$. Misunderstandings in literature are clarified and current knowledge built on to characterise $Li_3(OH)_2Br$ and what is herein proposed to be the thermodynamically-stable $Li_4(OH)_3Br$ phase, for the first time. These findings are applied to understand previous surprising reports, including the sub-theoretical experimental melting enthalpies of $Li_4(OH)_3Br$ when considered for TES.

Following this, Chapter 4 will return to one of the original objectives: to grow Li_2OHBr single crystals. Building on the understanding gained in Chapter 3, it is apparent that this is an extremely challenging goal, which is not fully attained in this work. Nonetheless, significant progress is made into understanding the relationships between synthesis conditions, microstructure and phase purity in Li_2OHBr. The phase behaviour, synthesis and suitability of $Li_5(OH)_2Br_3$ as an alternative solid electrolyte candidate are also considered, offering new insights into a largely unknown phase, and completing our exploration of the equilibrium LiBr-LiOH system.

In the final experimental chapter, Chapter 5, lithium hydroxyhalide antiperovskite glasses are synthesised and characterised. Following controversial previous attempts at antiperovskite glass synthesis[112,146–151], there has been speculation as to whether vitrification of these compounds will benefit ionic conductivity[152–155]. In this chapter, it is demonstrated that glasses yield improvements in lithium dynamics, but currently lack the stability against crystallisation required for practical use.

The key discoveries and conclusions established in this thesis are concisely revisited in Chapter 6, and future work which would progress understanding and performance of these materials further are considered. I hope this thesis is valuable to anyone embarking on research with this challenging material system.

Chapter 2

Experimental Methods

Contents

This chapter aims to provide an outline of the important synthetic and characterisation techniques employed in this thesis. In instances where the measurement details are chapter specific, further information is provided in the corresponding chapter's experimental methods section.

Due to the highly hygroscopic nature of the compounds of interest, all work was carried out under inert conditions unless specifically stated otherwise. Samples were handled in argon-filled gloveboxes (MBraun, $H_2O < 0.5$ ppm, $O_2 < 0.5$ ppm) and were transferred between gloveboxes in sealed glass vials with Parafilm tape around joints. When samples had to be transported significant distances, sample vials were sealed in heat-sealable pouches under vacuum as an extra layer of protection. Utensils and consumables were dried in a vacuum oven ($\sim$1 mbar, 70 °C) for a minimum of 3 hours prior to use, and were transferred directly from the oven to the glovebox antechamber.

2.1 Synthetic Techniques

Synthesis investigations are a big focus in this thesis and shall be covered in detail in each results chapter. Brief introductions to the general approaches employed are provided here.

2.1.1 Melt Casting Synthesis

A melt-casting synthesis is employed throughout this thesis, using lithium hydroxide and lithium halide precursors. The use of these relatively inexpensive and abundant precursors, and the moderately low combined melting temperatures (< 350 °C), makes this a desirable synthesis approach. Additionally, the production of dense, continuous membranes upon solidification can be exploited in microstructure studies.

For synthesis of the bromide compounds, anhydrous LiOH (98%, Sigma-Aldrich) and LiBr ($\geq$ 99%, Sigma-Aldrich) salts were weighed out in the correct molar ratio for the desired stoichiometry, accounting for the purity of the precursors. The same is true for the Li_2OHCl and $Li_2OHCl_{0.5}Br_{0.5}$ samples in Chapter 5, using anhydrous LiCl ($\geq$ 98%, Alfa Aesar) where

appropriate.

The weighed-out samples were then ground together using an agate mortar and pestle for ∼10 minutes to ensure a homogeneous mixture and short diffusion distances. The resulting mixture was placed into alumina crucibles and heated in an MTI compact muffle furnace to the molten state. The heating protocols chosen greatly impact the phases and purity achieved, and so shall be addressed in detail in each chapter. After cooling, the samples were either ground into a powder using an agate mortar and pestle, or used in their bulk form.

2.1.2 Quartz Tube Sealing

For single crystal growth, impurities can prevent high quality single crystals from being produced. In growth attempts in Chapter 4, samples were sealed under vacuum in quartz tubes in order to minimise any potential side reactions which may occur during extended periods at elevated temperatures. Sealing in quartz tubes was also adopted in some initial glass synthesis attempts in Chapter 5, to enable quenching of samples into liquid nitrogen outside of a glovebox.

Each quartz tube was cut to an appropriate length using a dremel, closed at one end with a blowtorch, washed with deionised water, and dried overnight in a vacuum oven (∼1 mbar, 70 °C). Powders ground together in the correct LiBr:LiOH stoichiometry were cold-pressed into pellets using a hardened 440C stainless steel (SS) evacuable pellet die, and loaded into the quartz tube. A swagelock with O-rings and a valve were fitted to the open end of the tube, such that it could be removed from the glovebox and connected to a vacuum pump without air exposure. The tube was evacuated to $\sim 10^{-5}$ mbar and sealed using a blowtorch. During sealing, care was taken to ensure the heating was sufficiently far from the sample such as to avoid any sample degradation. To check whether a good vacuum had been maintained during the sealing process, a small region of the tube was reheated to see if the wall bends inwards as the viscosity decreases. After synthesis and heat treatments, samples were removed by breaking the quartz tube.

2.1.3 Ball Milling

Ball milling is a mechanical technique often employed to reduce particle sizes, mix precursors, or synthesise metastable compounds[156–159]. In this thesis, ball milling was briefly explored as an

approach to synthesise metastable $Li_3(OH)_2Br$ in Chapter 3 and antiperovskite-based glasses in Chapter 5. Solid precursors were sealed in zirconia jars with zirconia balls in a ball-to-powder ratio of 13:1 under argon atmosphere. A planetary ball mill (Fritsch Pulverisette 7 Premium) was then used to rapidly rotate the jars. The collisions of the balls with the jar and powder generate highly localised heat and large mechanical stresses, intimately mixing the powders, and in some instances forming metastable phases. In this work, cycles of 3 minutes milling at 500 rpm were used, followed by 7 minutes rest to allow dissipation of heat built up during the milling steps.

2.2 Structural and Chemical Characterisation

2.2.1 X-ray Diffraction

Atoms in a crystal exhibit a long-range periodic arrangement, which can be defined by a single unit cell that repeats throughout space in 3 dimensions. This unit cell, defined by a set of lengths a, b, c and angles α, β, γ, belongs to one of seven crystal systems. These crystal systems range from the highest symmetry case being cubic ($a = b = c, \alpha = \beta = \gamma = 90°$), to the most general case in which each parameter is unique. Further to this, 14 Bravais lattices can be used to describe the ways in which atoms are arranged in space while maintaining the translational symmetry, known as the centring. For the example of a cubic cell with atoms on the unit cell corners, atoms could also be placed in the cell centre or on the centre of each face. Combinations of symmetry operators, such as translations, rotations, reflections, and glide planes, can operate on these lattices, generating 230 unique crystallographic space groups.

XRD is a structural characterisation technique particularly useful for studying crystalline materials. XRD exploits the diffraction of X-rays by planes of atoms in a crystal (Figure 2.1). Bragg's law (Equation (2.1))[160] describes the conditions under which X-rays scattered from planes parallel to the sample surface constructively interfere, where n is an integer, λ is the X-ray wavelength, d is the interplanar spacing and θ is the angle of incidence.

$$2d \sin\theta = n\lambda \tag{2.1}$$

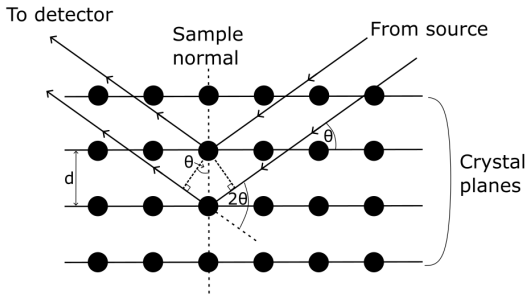

Figure 2.1: *Schematic diagram showing an XRD experiment measuring a monocrystalline cubic sample where the angle θ and interplanar spacing d are defined as in Bragg's law. Typically 2θ is plotted against diffracted intensity in patterns.*

In a typical diffractometer, an X-ray source and detector are positioned on the circumference of a circle with the sample at the centre. The relative angles can be varied to measure intensity as a function of angle. To vary the angle, either a $\theta - 2\theta$ measurement can be taken, whereby the sample and detector are moved relative to a fixed source, or a $\theta - \theta$ measurement, in which it is the sample that is stationary. A series of "Bragg peaks" are generated at angles when sets of crystal planes satisfy Bragg's law. A set of planes hkl produce a peak with intensity I_{hkl} determined by the structure factor F_{hkl} (Equation (2.2)).

$$I_{hkl} \propto |F_{hkl}|^2 \tag{2.2}$$

The structure factor is a mathematical expression describing how X-rays are scattered by a crystal, and depends on the identity and positions of atoms in a unit cell. This structure factor is defined as:

$$F_{hkl} = \sum_{j=1}^{N} f_j(\theta) \cdot \exp[2\pi i(hx_j + ky_j + lz_j)] \tag{2.3}$$

where x_j, y_j and z_j refer to the fractional coordinates of the j^{th} atom in the cell, which has scattering factor f_j. In some instances, destructive interference from symmetry-related atoms may result in the structure factor equalling zero, which produces systematic absences in the diffraction pattern. The scattering factor relates to the scattering amplitude of an atom, with greater values for atoms with high electron densities. To account for thermal vibrations,

an additional term containing an isotropic displacement factor U_j can be incorporated into the structure factor, as in Equation (2.4). Both this term and the scattering factor are angle dependent, falling off in intensity at higher angles.

$$F_{hkl} = \sum_{j=1}^{N} f_j(\theta) \cdot \exp(-8\pi^2 U_j \sin^2\theta/\lambda^2) \cdot \exp[2\pi i(hx_j + ky_j + lz_j)] \tag{2.4}$$

By fitting and indexing the observed peaks in an unknown phase with the help of crystallographic software, the unit cell parameters can be determined. From the systematic absences observed, information about the centring and symmetry of the sample can be found, revealing possible space groups. This process shall be carried out in Chapter 3.

Standard room-temperature XRD measurements were taken on a Rigaku Miniflex diffractometer (Cu Kα) in a nitrogen-filled glovebox (MBraun, $H_2O < 0.5$ ppm, $O_2 < 0.5$ ppm). In this instrument, electrons are accelerated at a copper target, generating X-rays of characteristic discrete wavelengths. Cu $K_{\alpha 1}$ is the most intense with a wavelength of 1.542 Å. A nickel monochromator is used to selectively filter out Cu K_β radiation. Cu $K_{\alpha 2}$ has very similar energy to Cu $K_{\alpha 1}$, making it difficult to separate, and so both are present, leading to peak splitting in XRD patterns at higher angles. Samples were loaded in a recession-style single crystal silicon holder to minimise non-crystalline background contributions. To create a random distribution of crystallite orientations, samples were ground into a fine powder and scattered onto the sample holder using a thin layer of grease to hold the sample in an unbiased orientation. The sampling statistics are improved further by rotating the sample at 10 rpm during data collection. To ensure correct sample alignment, a glass slide was used to level the sample with the top of sample holder.

Several other diffractometers were used in this work. The *in-situ* air-exposure XRD measurements in Chapter 3 were made using a Rigaku Smartlab diffractometer (Cu Kα) on powder samples loaded in a borosilicate capillary. In-house variable temperature (VT) XRD measurements were also made using a Rigaku Smartlab diffractometer (Cu Kα), with the help of Professor Robert House. For these, powder samples were pressed into a 10 mm diameter pellet and loaded onto a heating stage under argon flow. Samples were heated and cooled at a rate of $1\,^{\circ}\mathrm{C\ min^{-1}}$.

Chapter 3 also includes some synchrotron XRD measurements. Synchrotrons offer higher flux X-rays, reduced instrumental broadening, improved detectors and hence better signal-to-noise ratios. Additionally, the high flux means that patterns can be collected in seconds, particularly useful for obtaining *in-situ* VT measurements. Synchrotron powder XRD measurements were carried out on the I11 beamline at Diamond Light Source (λ = 0.82311 Å) thanks to provision of a BAG allocation from Professor Andrew Goodwin. Powders were sealed under argon in 0.5 mm diameter borosilicate glass capillaries (wall thickness 0.01 mm) after sonication using an electric toothbrush to ensure close-packing of the powder particles. An FMB Oxford cyberstar hot air blower was used to apply a continuous heating rate of 6 °C min^{-1}, during which measurements were taken at approximately 2.5 °C intervals. Diffraction patterns were collected in capillary transmission geometry using the Mythen2 Position Sensitive Detector. Two data collections of 5 seconds each were taken at angles 0.25 degrees apart, then summed to account for gaps in the detector coverage.

2.2.2 Refinements

From XRD patterns, useful information about a sample's crystallinity and basic identification of expected phases can be quickly confirmed. Using the theory introduced in Section 2.2.1, much more complex information can be obtained. With a reasonable starting crystal model, a theoretical XRD pattern can be calculated and compared to the observed data. Changes can then be made to the structural model to iteratively improve the fit to the observed data in a least squares refinement. One particularly useful metric for assessing the quality of a fit is the weighted profile R-factor:

$$R_{wp} = \sqrt{\frac{\sum_i w_i (y_i^{obs} - y_i^{calc})^2}{\sum_i w_i (y_i^{obs})^2}} \tag{2.5}$$

where y_i refers to the peak intensity, w_i is the weighting by peak intensity, and R_{wp} values as low as possible are desirable. Refinements in this work were carried out using TOPAS-Academic software[161].

Pawley refinements are used to capture information about a sample's unit cell and symmetry from the observed peak positions in a diffraction pattern. In a Pawley fit, a lattice

parameter and space group model are used to generate allowed *hkl* reflections, which are modelled as peaks with individually-scaled intensity values. In this work, peaks were fit by a common Thompson-Cox-Hasting pseudo-Voigt (TCHZ) peak shape function, which is influenced by instrument and sample effects. A background was defined by a Chebyshev polynomial function, arising due to diffuse scattering effects. By allowing each peak intensity value to freely refine, chemical information about the crystal structure is lost, but excellent fits can be achieved, giving an indication of the "best possible" R_{wp} for a subsequent Rietveld refinement.

Rietveld refinements use a complete structural model of the contents of a unit cell to calculate a theoretical diffraction pattern. Unlike in a Pawley refinement, a single arbitrary scaling factor is used to describe all of the peak intensities. The relative intensities of peaks in a diffraction pattern depend on the atomic positions, types, occupancies, thermal displacements, and in the instance of multi-phase systems, phase fractions, which are all incorporated in the structural model. This can make high quality Rietveld refinements very challenging, and quantitative statements cannot be made about any one parameter without an accurate and full rigorous physical model. Additionally, care must be taken to ensure that different parameters which influence the calculated diffraction pattern in the same way don't become correlated, such as thermal displacement and site occupancy. Other complications may arise from samples exhibiting anisotropic strains (resulting in variable peak width) or texture (skewing the intensity of different peaks). Caution should be employed not to overfit the pattern, and constraints can be imposed during a refinement to ensure physicality, such as known stoichiometries, maximum site occupancies of 1, positive thermal displacement parameters and phase fractions totalling 1.

In the LiBr-LiOH materials, lithium and hydrogen are very poor X-ray scatterers, meaning reliable information about them cannot be obtained from X-ray studies alone. As such, information relating to these elements have been constrained in Rietveld refinements in this work, detailed further when relevant.

2.2.3 Differential Scanning Calorimetry

DSC is a thermal analysis technique which can be used to study thermal events, such as phase transitions and glass transitions, by measuring the heat flow into or out of a sample as it is heated and cooled. A pan containing a sample and an empty reference pan are both heated under con-

trolled conditions and the temperature monitored. The instrument measures the difference in heat flow required to maintain the same temperature for the sample and the reference, which is then plotted as a function of temperature to create a DSC curve. Peaks signify thermal transitions, the area of which corresponds to the event's enthalpy change. High ramping rates may skip through reactions due to insufficient kinetics, whereas slow rates can lead to impractically long experiment lengths.

Most DSC measurements in this work were taken using a Netzsch TGA-MS using ∼5 mg of sample loaded in an alumina pan and covered with an alumina lid. An argon shower was used to protect the sample from air exposure during loading into the instrument. Measurements were taken under argon atmosphere with a heating and cooling rate of 5 °C min^{-1}. Where other equipment was used, details are provided in the relevant chapters.

2.2.4 Solid-state Nuclear Magnetic Resonance Spectroscopy

NMR is a powerful technique which can be used to obtain information about the chemical structure, 3D structure and motion of molecules in materials. NMR measurements were carried out by Dr Gregory Rees, Dr Hua Guo and Dr Kenjiro Hashi for this work. A brief introduction to the theory of solid-state NMR is provided here to help with interpretation and analysis in the rest of the thesis.

Nuclei of different elements have different spin angular momentums. When atoms with non-zero spin are placed in an external magnetic field, the degeneracy of the nuclear spin states is lost, resulting in an energy difference ΔE. The energy difference between spin states is given by Equation (2.6)[162]:

$$\Delta E = \gamma\hbar(1-\sigma)B_0 \tag{2.6}$$

where B_0 is the strength of the static external magnetic field. The gyromagnetic ratio, γ, is a fundamental property corresponding to the ratio of an atom's magnetic moment to its angular momentum. The chemical shielding around a nucleus, σ, depends on the electron distribution around a nucleus, which affects the magnetic field experienced by the nucleus. Chemical shielding

varies between different chemical environments of a given isotope, and is often anisotropic.

Electromagnetic radiation can be used to induce transitions between spin states in a material[162]. For typical NMR magnetic fields (5 - 28 T), these correspond to Larmor frequencies in the radio frequency (RF) range. NMR frequencies are often reported as the fractional difference between the frequency of the studied nucleus and a reference compound, known as the chemical shift δ. As well as chemical shift, various anisotropic couplings modify NMR frequencies, resulting in orientation dependence and 3D structural information. For powder samples, as in this work, crystallites exist in many orientations relative to B_0. This generates shifts from all possible orientations, and hence produces characteristic broad lineshapes. To eliminate anisotropic contributions, magic angle spinning (MAS) can be used. Here, the sample is spun rapidly around an axis at 54.7° to the static magnetic field. This averages the anisotropic interactions to zero, hence retaining only the isotropic centreband component[163].

NMR techniques can also be used to probe information about the dynamics of atoms in materials. When a spin is perturbed by a RF pulse, it decays back to equilibrium over a characteristic timescale. This process is known as spin-lattice relaxation (SLR), and is directly influenced by the interaction of nuclei with the local magnetic environment[164,165]. Using a saturation-recovery or inverse-recovery pulse sequence, a time constant T_1 associated with relaxation along the direction parallel to the applied static magnetic field can be defined as the time taken for 63 % of the magnetisation to return to equilibrium. Slower molecular motions can be captured using a spin-locking sequence, in which a weak continuous RF field is applied transverse to B_0, hence locking the magnetisation in the rotation frame, and giving rise to another relaxation time constant, $T_{1\rho}$. The relaxation rate, $R_{1\rho} = 1/T_{1\rho}$, is sensitive to Li-ion jump rates, particularly when they match the frequency of the applied spin-locking field in the rotating frame (kHz, 10^5 s^{-1}, milliTesla). Consequently, relaxation rates are influenced by fluctuations in the local nuclear environments that occur on timescales inversely proportional to the applied field (10 kHz). The temperature-dependent $R_{1\rho}$ values pass through a maximum when the fluctuation timescales commute with the applied field. The resultant Lorentzian peaks are typically asymmetrical due to correlation effects, such as disorder, affecting the low-temperature flank. The $R_{1\rho}T$ curves can be fitted to the Bloembergen-Purcell-Pound (BPP) model ($J(\omega) \propto C\frac{2\tau}{1+(\omega_0\tau)^\beta}$, where $J(\omega)$ is the spectral density, ω the angular frequency, τ the correlation time (i.e. characteristic timescale of motion) and β an empirical factor between 0 and 2 accounting for asymmetry[166]. In the

high-temperature regime of a three-dimensional isotropic ion conductor, where $\omega_0\tau \ll 1$, the activation energy ($E_{a(HT)}$) for long-range ion motion does not suffer from these adverse effects, and so is typically quoted[167].

A final technique used in this work is PFG-NMR[168]. Here, after an initial 90° excitation RF pulse, a gradient pulse G of duration δ is applied to make a spatially-varying magnetic field, effectively position-encoding the spins in a sample. After a set period of time Δ, a second gradient pulse is applied to reverse the encoding. If no diffusion has occurred, the spins refocus and generate a strong signal, whereas signal loss indicates spin dephasing due to diffusion in the sample, with greater signal loss indicating faster diffusion. By tracking the signal decay with gradient strength, the diffusion coefficient D can be calculated using the Stejskal-Tanner equation:

$$I = I_0 \exp[-(\gamma\delta G)^2 D(\Delta - \frac{\delta}{3})] \tag{2.7}$$

where I is the signal intensity, I_0 being with a gradient strength of zero. The diffusion coefficient describes the rate of random thermal translational motion and is related to the mean squared displacement by $\langle r^2 \rangle = 2Dt$ in 1D. As such, PFG-NMR probes micron-scale displacements for diffusion times Δ on the order of hundreds of milliseconds. In some systems, microstructural restrictions may lower the apparent diffusion coefficient.

2.2.5 Raman Spectroscopy

Raman spectroscopy is a technique used to probe vibrational modes in materials. A high intensity laser is focused onto a sample, which scatters the light. Although most of the incident light is scattered at the same wavelength (Rayleigh Scatter), a small fraction is scattered at different wavelengths (Raman Scatter). This happens when a molecular vibration results in a change in polarisability, and therefore relates to the chemical structure of the sample. A Raman spectrum can be plotted as intensity against the energy shift from the incident laser wavelength. Each peak corresponds to a particular molecular bond vibration, identifiable from its position, and the intensity of which indicates its relative concentration in the analyte. The primary range of interest in LiBr-LiOH compounds lies around 3600 cm^{-1}, corresponding to the Raman-active

O-H bond stretching vibration.

In this work, a Renishaw inVia Reflex laser confocal Raman microscope with a 532 nm laser and 1800 lines mm^{-1} grating was used to measure powder samples. Prior to measurements, the spectrometer was calibrated to a silicon reference to ensure consistency and accuracy. The instrument operates in air, and so samples were sealed in glass vials through which the laser was focused. A 5 times magnification focussing lens was used to take a representative sampling size. Scans were initially measured at low powers and observed to check structural changes weren't occurring as a consequence of the laser, such as by local heating. Presented spectra were recorded for 20 accumulations with a laser power of 150 mW and an exposure time of 1 s. Background removal was conducted using the Renishaw WiRE 5.5 software.

2.3 Microstructural Characterisation

2.3.1 Scanning Electron Microscopy

SEM is a powerful technique enabling characterisation of a material's microstructure, topography and composition using a focussed beam of electrons scanned across the surface of a sample. The wavelength of this beam of electrons is much shorter than that of visible light, enabling significantly higher resolutions than optical microscopy[169,170]. The beam penetrates the sample to interact over a characteristic volume, known as the interaction volume, which typically has a teardrop shape as shown schematically in Figure 2.2a. The interaction of the electrons with the sample generates a variety of signals. These can each be detected using different detectors, yielding a wide range of information.

The images in this work are taken using a secondary electron (SE) detector. Low energy SEs are emitted from inelastic collisions between the incident electrons and the sample's atoms. The low energy of SEs means they are strongly attenuated by the sample and so only SEs emitted near the surface of the sample are able to escape and reach the detector. As such, SE images provide useful information about the surface topography of a sample. Additionally, the small sampling volume from which the SE signal originates mean high resolution images can be obtained. Another signal, backscattered electrons (BSE), can offer information about the average local atomic number ("Z-contrast") and grain orientations in samples. BSEs arise from

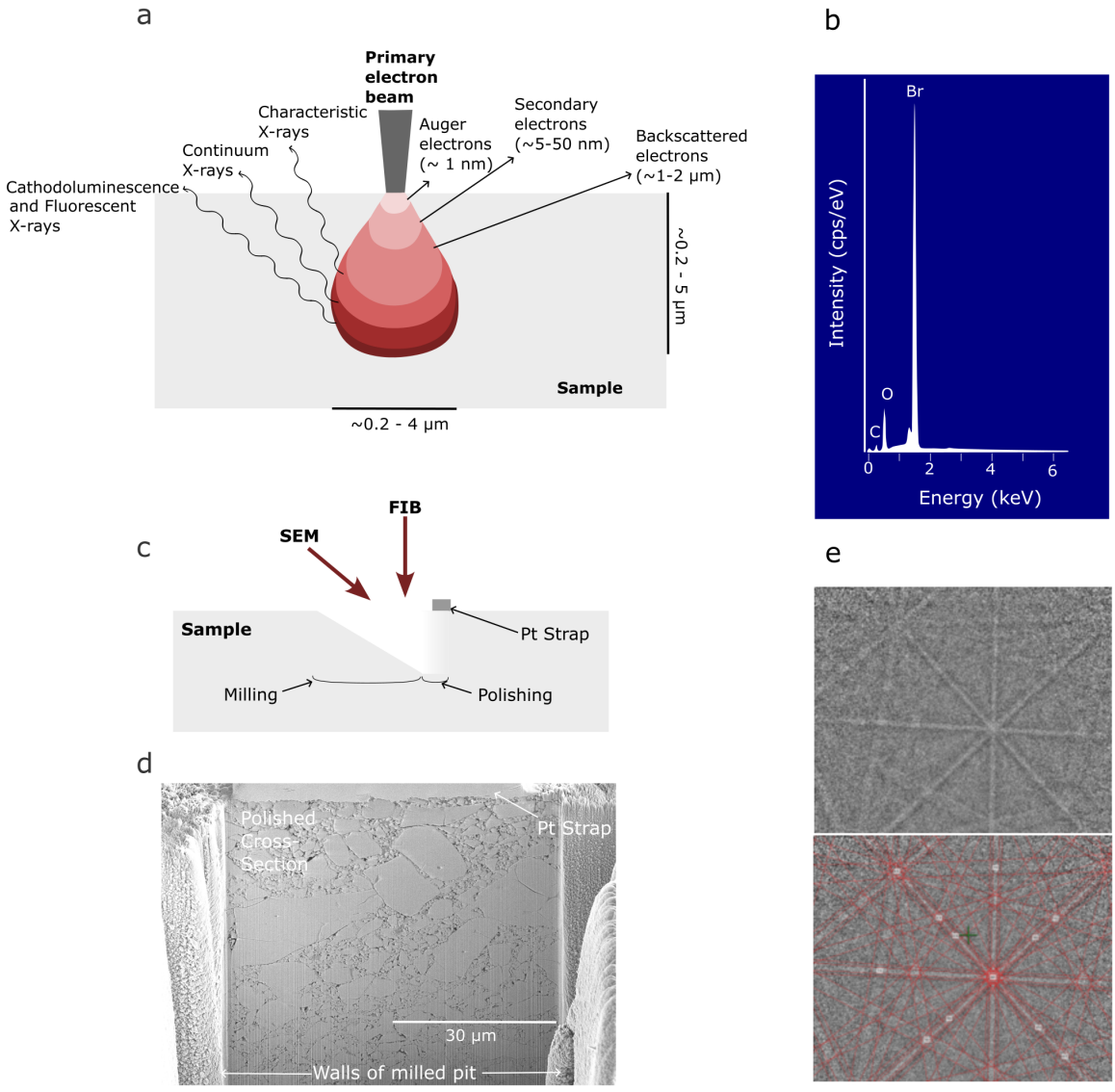

Figure 2.2: *Scanning electron microscopy and related techniques. a) Illustration of the interaction volume of the incident electron beam in an SEM sample, showing the generated signals and their approximate regions. b) Example region of an energy dispersive X-ray (EDX) spectrum showing peaks corresponding to bromine, oxygen and carbon. c) Schematic of PFIB-SEM operation to produce a cross-section. d) Example polished cross-section of a cold-pressed Na_3OBr pellet. e) Kikuchi bands from EBSD of a Li_2OHBr sample without (top) and with (bottom) software band indexing.*

elastic scattering of incident electrons, which travel from a much deeper sampling region.

Challenges imaging the LiBr-LiOH compounds in this work arise from the increased beam damage that light element-containing samples are prone to, and image distortion from charging effects in poor electronic conductors. To overcome this, low probe currents ($\sim$ 0.8 nA) and accelerating voltages (5-10 kV) are necessary for imaging. SEM, EDX and EBSD images in Chapter 4 were taken using a Tescan Mira-3 FEG-SEM with Oxford Instruments EBSD and EDS detectors. This SEM opens into a glovebox, enabling sample loading without air exposure. The other instrument employed in this thesis, used for preparing PFIB cross-sections, SEM images and EDX maps in Chapter 5, is a Thermo Scientific Helios G4 PFIB CXe DualBeam with an Oxford Instruments EDS detector. A Gatan iload vacuum transfer vessel was used to prevent air exposure upon sample loading. The basic principles behind EDS, PFIB-SEM and EBSD spectroscopy shall now be briefly introduced.

2.3.2 Energy Dispersive X-ray Spectroscopy

Another useful signal generated by the incident electron beam in an SEM is characteristic X-ray radiation, produced when an inner shell electron is ejected by the incident beam and subsequently replaced by an outer shell electron, emitting the energy difference as an X-ray photon. The discrete electronic energy levels of different elements mean the energies of the X-rays are characteristic of the elements present, allowing for semi-quantitative composition determination. An example EDX spectrum is shown in Figure 2.2b. By rastering the electron beam across the sample surface, qualitative elemental maps can be created. Although a useful tool, light elements such as hydrogen and lithium produce low intensity and energy X-rays, which are absorbed by components such as the detector window without reaching the detector. Additionally, when lower accelerating voltages are used to reduce beam damage, higher energy transitions are not excited due to insufficient beam energy. As a result, reliable quantitative information is difficult to obtain without complementary characterisation techniques. In this work, an accelerating voltage of 20 kV was used, providing information about oxygen and bromine in microstructures.

2.3.3 Focused Ion Beam Milling

In some instances, it is desirable to acquire cross-sectional images in addition to surface images of a sample. For example, it may be useful to obtain information about the porosity, a microstructure's depth homogeneity or simply to produce flat surfaces in instances where surface images are dominated by topography. To create clean cross-sections with minimal damage, a PFIB can be used to mill a trench in the sample. The PFIB instrument used in this work contains a focussed ion beam column with a xenon ion (Xe^+) source at a 52 ° angle to an SEM column, as shown schematically in Figure 2.2c. To protect samples during the milling stage, a platinum strap layer is first deposited on the sample surface. The trench is then milled parallel to this strap using a relatively high current (0.5 μA, 30 kV). Subsequent polishing steps at progressively finer currents are applied to prepare a smooth and damage-free cross-section. Polishing was terminated at a 30 kV, 4 nA ion beam in this work, beyond which little further improvement was seen. An example cross-section after polishing is shown in Figure 2.2d.

2.3.4 Electron Backscatter Diffraction Spectroscopy

EBSD is another SEM technique, used to determine information about the crystal orientations in a sample. Incident electrons elastically scatter in all directions, meaning all sets of crystal planes in the sample have electrons travelling at their Bragg angle. This diffraction forms intersecting "Kossel cones" of high electron density. In EBSD, some of the electrons exiting the sample (backscatter) are collected by a detector. This signal appears as near straight lines called Kikuchi bands, the location and orientation of which depend on the crystallographic structure and orientation of the measured point. These lines are automatically indexed, in this work using Oxford Instruments' Aztec package. By recording EBSD patterns at discrete points on a sample surface, orientation maps can be built up to reveal the grain structure, phase distribution and texture of a sample.

In this work, EBSD was carried out using a working distance of 25 mm and an accelerating voltage of 20 kV. The sample was tilted to 70 ° to maximise the backscatter signal.

EBSD requires very smooth sample surfaces because the diffraction pattern is formed from a very thin surface layer. To achieve this, samples were prepared by mechanically polishing

with SiC papers to 4000 grit, and then polished using a precision etching coating system (PECS). In the PECS, the sample is mounted such that the top surface of the sample aligns with the intersection of two Ar^+ ion beams. The Ar^+ ion beams polish a small area on the rotating sample, which can then be measured using EBSD. It was found that polishing using a 4 keV beam at a grazing angle of 4 ° for 30 minutes was ideal for preparing Li_2OHBr surfaces for EBSD. These conditions are quite gentle due to the soft nature of the antiperovskite samples being investigated.

2.4 Electrochemical Cell Preparation and Measurements

Two types of electrochemical cell configuration are used in this work, depending on the form of the solid electrolyte being tested. For powdered samples, cold-pressed pellets of solid electrolyte were prepared in a custom 'PEEK' cell. For bulk samples, pouch cells were prepared. Both cell types and their subsequent electrochemical testing shall be described in the following section.

2.4.1 PEEK Cells

The 'PEEK' cell comprises a polyether ether ketone (PEEK) die in which a 5 mm diameter solid electrolyte pellet can be directly pressed. PEEK was chosen as a strong, chemically-inert and electronically-insulating material from which to make this cell body. A hydraulic press was used to densify powders into bulk pellets in the die via SS plungers applying a pressure of 370 MPa for 3 minutes. The pellet's average thickness was measured from the plunger separation using a micrometer, and was typically 400-600 microns thick. In most cases, disks of nickel foil (Advent Materials, 99.95 %, 0.0125mm) blocking electrodes were then placed on either side of the electrolyte pellet. The cell is designed to apply a uniaxial stack pressure via a top screw, controlled using a calibrated torque wrench. Schematics of the PEEK cell setup are shown in Figure 2.3. For measurements taken in this work, a stack pressure of 70 MPa was applied. Since PEEK cell measurements in this work are primarily interested in the bulk solid electrolyte conductivity, this pressure helps to ensure good contact is maintained, minimising interfacial resistance contributions.

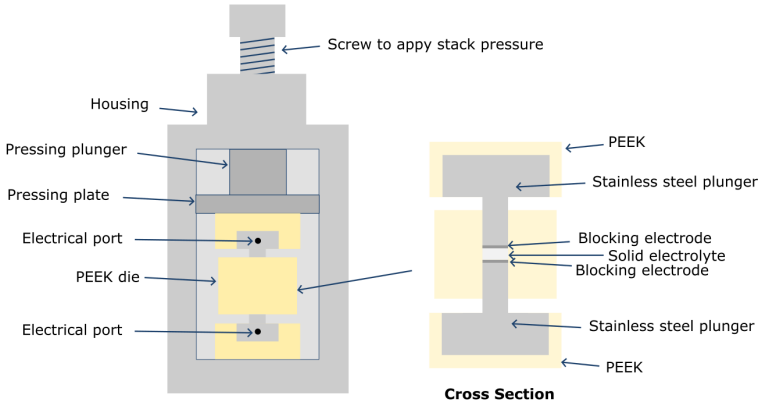

Figure 2.3: *Diagram depicting the PEEK cell setup for electrochemical testing, with an inset illustrating a cross-section of the PEEK die.*

2.4.2 Pouch Cells

Pouch cells provide multiple advantages in terms of the flexibility they offer. Firstly, the geometry is not constrained as it is in the PEEK cells, and the cell can adopt the form factor desirable for the solid electrolyte. Secondly, the cells are sealed under vacuum, meaning that they are protected from air exposure and can be tested outside of the glovebox. However, the construction time and difficulty for pouch cells is substantially higher.

Solid Electrolyte Preparation

To produce solid electrolyte pellets from the rods of samples cast in quartz tubes in Chapter 4, samples first had to be cut into thin parallel-sided slices using a slow saw (Buehler IsoMet Low Speed). To do this, samples were first embedded in an epoxy (Araldite Rapid) and mounted to the slow saw cutting stage. Before each use, the diamond wafering blade was dressed and the catch tray filled with anhydrous hexane as a lubricant. An in-built micrometer was used to control the position of the cut, and the saw was set to cut samples at relatively slow speeds. A counterweight on the gravity-fed arm is adjusted to control the pressure at which the sample is fed to the saw, to optimise the cutting rate whilst minimising damage to the sample. After cutting the pellets, it was possible to debond the epoxy from the circumference of the pellet if desired.

SiC polishing papers from 800 grit to 4000 grit were used to reduce the thickness of the pellets further ($\leq 600\mu$m) and produce a polished finish with minimal scratches. For samples cast in coin cell cases in Chapter 4, the cutting step was not required, but it was still necessary to polish samples to smooth, parallel-sided pellets.

Electrode Preparation

Nickel blocking electrodes were applied to the solid electrolyte pellets in Chapter 4 and glass flakes in Chapter 5 by sputtering. To define the electrode area on the samples, a hole was removed from a piece of Kapton tape using a biopsy punch and applied to the solid electrolyte sample to mask off all but the desired area. The same was repeated on the other side of the solid electrolyte, with care taken to ensure the electrode areas fully overlap. The contact area was accurately determined using optical microscopy.

RF magnetron sputter deposition using a solid Ni target was used to deposit contacts onto the masked electrolytes, after which the masking tape could be removed. A reasonably high Ar flow rate of 20 SCCM was chosen during sputtering to produce smooth and uniform contacts.

Cell Assembly

A photograph and annotated diagram of a pouch cell prepared before assembly is shown in Figure 2.4. To prepare two-electrode pouch cells, two pieces of copper foil were arranged between two sheets of heat-sealable laminated aluminium, such that the copper pieces overlap at a single point within the pouch, between which the solid electrolyte was placed. Both copper current collector foils extend out of the pouch for connecting to an external circuit. Hot-melt adhesive tape was attached on either side of the copper foils so that the pouch could be air-tightly sealed. The cell components were arranged in the dried pouch, with Kapton tape providing electrical insulation where necessary. The pouches were then sealed under vacuum using a vacuum heat sealer in a glovebox. Once the pouch was sealed, contact between the cell components was ensured by gently clamping two glass slides around the cell using a crocodile clip. The cell was then connected to an external circuit for testing.

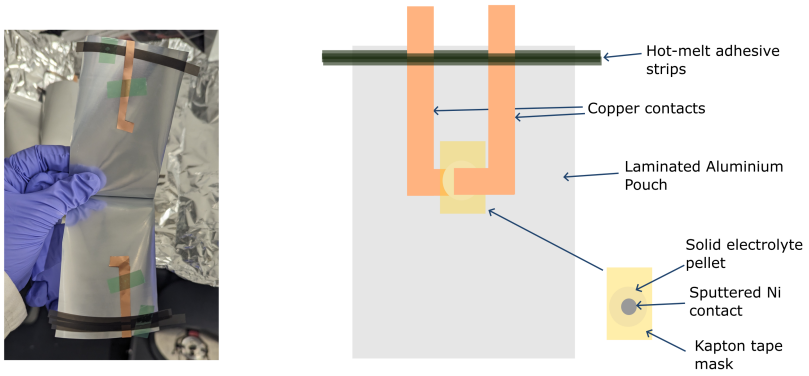

Figure 2.4: *Photograph (left) and schematic (right) of how pouch cells were prepared in this work.*

2.4.3 Potentiostatic Electrochemical Impedance Spectroscopy

The impedance, and hence ionic conductivity, of different solid electrolytes in this work was determined using electrochemical impedance spectroscopy (EIS) [171,172]. For this, PEEK or pouch cells were constructed as described, with Ni or SS blocking electrodes designed to prevent lithium ion transport across the electrolyte-electrode interface. In EIS, a time-varying voltage $E(t)$ is applied to the cell (Equation (2.8)), generating an out-of-phase current $I(t)$ with the same frequency (Equation (2.9)). EIS conditions should ensure that the input and output signals are proportional and of the same frequency (known as linearity), output signals arise only due to input signals (known as causality), and the system returns to equilibrium following perturbations (known as stability). Systems are assumed to be linear for low amplitude applied voltages, such that the impedance Z can be given by an analogous expression to Ohm's law for resistance in direct current (DC) circuits (Equation (2.10)).

$$E(t) = E_0 \exp(j\omega t) \tag{2.8}$$

$$I(t) = I_0 \exp(j[\omega t - \varphi]) \tag{2.9}$$

$$Z(\omega) = \frac{E(t)}{I(t)} = Z_0 \exp(j\varphi) = Z_0(\cos\varphi + j\sin\varphi) \tag{2.10}$$

The complex impedance can be plotted on a Nyquist plot as -Im(Z) against Re(Z), where each point corresponds to a measurement at a specific input frequency. The distance from the origin represents the impedance magnitude, and the angle with respect to the real axis, its phase angle. The impedance changes with frequency, which it is possible to capture with a model. The physical system can be viewed as a combination of analogous circuit elements combined in series and parallel arrangements to make an equivalent circuit model (ECM). Three key components are resistors (R), capacitors (C) and constant phase element (CPE), shown in Equations (2.11) to (2.13).

$$Z_R = R = \frac{V_0}{I_0} \tag{2.11}$$

$$Z_C = \frac{-j}{\omega C} \tag{2.12}$$

$$Z_{CPE} = \frac{1}{T(j\omega)^P} \tag{2.13}$$

A CPE is similar to a capacitor, but incorporates non-ideality parameters T and P to account for the leaky nature of capacitors often seen in real systems, for example due to surface roughness of solid electrodes[173]. ECMs should aim to capture physical processes, which can be challenging.

A simple example ECM is shown in Figure 2.5. The resistor R_0 corresponds to instrument cabling and contacts, and the parallel R_1/CPE_1 element corresponds to the bulk ionic conductivity of the electrolyte. Observed data might not be well-fitted using these elements alone, which could be due to high grain boundary resistances or interfaces, which would need to be captured in additional, lower frequency, R_n/CPE_n elements. In instances where only the total resistance is of interest, the intercept of the data with the real axis can be used, avoiding the challenges of reliably deconvoluting contributions from unresolvable semicircles.

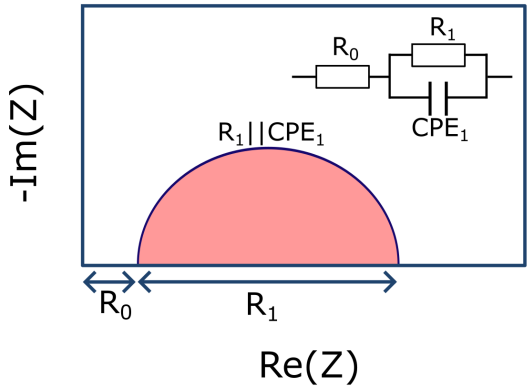

Figure 2.5: *Example ECM and a schematic of its corresponding Nyquist plot.*

An ionic conductivity σ_i can be found from this resistance using Equation (2.14):

$$\sigma_i = \frac{L}{RA} \tag{2.14}$$

where L is the electrode separation and A the area of the current path (covered by the blocking electrodes). From temperature-dependent ionic conductivity measurements, an activation energy for ionic conduction can be found with an Arrhenius plot of $\ln \sigma$ against T^{-1}.

Measurements in this work were taken using a Bio-Logic MTZ35 frequency response analyser in a two-point probe configuration in the frequency range 35 MHz to 0.1 Hz with a voltage amplitude of 10 mV (10 measurements per decade, 20 cycles per measurement). Where ECMs were used, the data was modelled using BioLogic EC lab software. To control the temperature, pouch cells were tested in a temperature-controlled climatic chamber (ITS, BioLogic Science Instruments) and PEEK cells were heated in an MTI compact muffle furnace in a glovebox. The temperature protocols employed in each instance are detailed in the relevant chapters.

Chapter 3

$Li_3(OH)_2Br$, $Li_4(OH)_3Br$ and Thermal Energy Storage

Contents

3.1 Introduction

$Li_4(OH)_3Br$ has been proposed as a PCM for high-temperature LHTES with the potential to offer exceptional energy storage capacity, but reports lack a thorough understanding of observed behaviour. Notably, experimental melting enthalpies (≤ 250 J g^{-1}) differ substantially from those predicted computationally (804 J g^{-1})[6–9,129,130]. Additionally, Mahroug *et al.* suggested that complete formation of the peritectic phase occurs across a wide range of cooling rates, despite unexplained evidence of multiple phases in TEM and EDS images[8]. Furthermore, Legros *et al.* proposed a polymorph may sometimes form depending on the synthesis precursors used, and suggested that the presence of this phase may explain the lower storage capacities observed experimentally[7]. To fully understand these observations, it is also important to establish whether the speculated high-temperature $Li_3(OH)_2Br$ phase exists, and to develop a robust understanding of its behaviour and properties through a thorough characterisation.

Understanding the LiBr-LiOH phase diagram may be critical to understanding impurity formation in Li_2OHBr and solidification phenomena in $Li_4(OH)_3Br$, as well the possibility of exciting properties offered by the discovery of novel materials, such as $Li_3(OH)_2Br$. In this chapter, the existence of a $Li_3(OH)_2Br$ phase is confirmed and the phase is characterised for the first time. A combination of diffraction studies and theoretical modelling are employed to determine a possible crystal structure for $Li_3(OH)_2Br$, and its lithium-ion dynamics evaluated through use of NMR spectroscopy, EIS, and supported by MD. In attempts to retain this phase to room temperature, it is found that an alternative metastable state often forms instead. The properties of this material are also considered, and its implications addressed.

Building on this improved understanding of $Li_3(OH)_2Br$, an in-depth study of the $Li_4(OH)_3Br$ phase is conducted, in which the concerns raised from literature are addressed. Here, it is demonstrated that previous reports of $Li_4(OH)_3Br$ correspond to a hydrated compound rather than the thermodynamically-stable phase, and address the implications of this on its application in TES. Contrary to Mahroug's claims, it is found that $Li_4(OH)_3Br$ cannot easily be obtained phase-pure from direct cooling procedures as a result of non-equilibrium solidification. To overcome this, a synthesis route is designed to obtain the $Li_4(OH)_3Br$ phase with high purity, enabling subsequent characterisation of the structure and its thermal behaviour. Finally, the implications of these findings on the proposed phase diagram are speculated.

3.2 Experimental Methods

3.2.1 Synthesis

To synthesise samples in this chapter, the melt-casting approach was used. "Furnace-cooled" refers to samples which were cooled back to room temperature from the melt at a controlled rate, whereas "quenched" samples were removed from the furnace and placed on the SS floor of the glovebox ($\sim 25\,^{\circ}\mathrm{C}$) to cool quickly to room temperature. For anneals discussed in this chapter, quenched samples were ground into a powder and reheated to the desired temperature with a ramp rate of $5\,^{\circ}\mathrm{C\ min^{-1}}$ for the length of time specified in text.

3.2.2 XRD Refinements

Pawley refinements and constrained Rietveld refinements were carried out on XRD data using TOPAS-Academic software[161]. In all instances, unit cell, background and peak shape parameters were allowed to refine freely. For the Rietveld refinement of $Li_3(OH)_2Br$ at $250\,^{\circ}\mathrm{C}$, the O and Br fractional positions were allowed to refine on their Wyckoff site in addition to three thermal displacement parameters for the Br, O and Li atoms. For $Li_4(OH)_3Br$, the atomic positions were fixed for the lighter atoms (Li, O and H), refining only the Br atoms. For the Rietveld refinement at $250\,^{\circ}\mathrm{C}$, a thermal displacement parameter was introduced, which was constrained to be equal across elements to reduce the number of free parameters.

3.2.3 DSC

For quantitative enthalpy determination (in Figure 3.11), measurements were taken on a TA Instruments DSC25 with ramp rates of $5\,^{\circ}\mathrm{C\ min^{-1}}$. Samples were hermetically-sealed in aluminium crucibles in argon gloveboxes to ensure full protection from air exposure. Peak integration for enthalpy determination was carried out using OriginLab software.

3.2.4 NMR

^{7}Li NMR measurements were performed by Dr Kenjiro Hashi (NIMMS) using an ECZ-500 (JEOL, Japan) spectrometer and a homemade high-temperature PFG-NMR probe[174]. The sample was packed into a quartz NMR tube SP-405 (SHIGEMI, Japan) and sealed in an argon-filled glove box. The resonance frequency of ^{7}Li was 194.4 MHz. NMR spectra were recorded using a single pulse sequence. The chemical shift was referenced to 1.0 M LiCl solution at 0 ppm. SLR times were measured by using a saturation recovery method. The data was fitted to $f(t) = f_{\infty}(1 - H_0 \exp(-t/T_{1\rho}))$. The diffusion coefficients were measured using the STE-PFG sequence.

3.2.5 Electrochemical Measurements

For electrochemical measurements of $Li_4(OH)_3Br$ and quenched $Li_3(OH)_2Br$, PEEK cells were constructed using nickel foil blocking electrodes. For high-temperature measurements of the $Li_3(OH)_2Br$ phase, the cell's SS pistons were used as blocking electrodes due to the reactivity of nickel. Samples were heated to the desired temperature for 30 minutes prior to measurement, followed by a 15 minute ramp period to the next temperature. Total conductivities were obtained from Nyquist plots. For measurements of quenched $Li_3(OH)_2Br$, an ECM comprising R_1 + Q_2/R_2 + Q_3/R_3 was used to model the data, where Q represents a CPE. DC chronoamperometry (CA) measurements were taken for 10 hours at 0.3 V, 0.6 V and 1 V to determine electronic conductivity.

3.3 Results and Discussion

Although investigations into the $Li_3(OH)_2Br$ and $Li_4(OH)_3Br$ phases were conducted in parallel, it has been decided that the most logical presentation of this work is to treat them individually. The first focus in this chapter will be the $Li_3(OH)_2Br$ phase, about which very little is currently known. Following this, the $Li_4(OH)_3Br$ investigations shall be covered. The highly overlapping nature of these studies, however, means that it has occasionally been necessary to reference a future sections' findings, although this has been limited to cases where it is strictly necessary.

3.3.1 Confirming the existence of $Li_3(OH)_2Br$

The first priority is to establish whether a phase with the stoichiometry $Li_3(OH)_2Br$ in fact exists. Anhydrous LiBr and LiOH were ground together in the correct molar stoichiometric ratio, 2/3 LiOH to 1/3 LiBr. This mixture was then heated at 5 °C min^{-1} to its molten state at 350 °C for 30 minutes, before furnace cooling at 3 °C min^{-1} to room temperature. Under equilibrium conditions, this material is expected to contain Li_2OHBr and $Li_4(OH)_3Br$ at room temperature in all proposed LiBr-LiOH phase diagrams[9,126,128]. The XRD pattern of this sample, shown in Figure 3.1a, contains peaks corresponding to Li_2OHBr, however not the $Li_4(OH)_3Br$ phase reported in literature. The remaining peaks instead correspond to what is here believed to be the thermodynamically-stable form of $Li_4(OH)_3Br$, as will be discussed in Section 3.3.5. Ticks beneath the diffraction pattern indicate the positions of Bragg peaks expected from this $Li_4(OH)_3Br$ and the Li_2OHBr phases. Further, Raman spectroscopy, shown in Figure 3.1b, exhibits peaks matching pure Li_2OHBr and $Li_4(OH)_3Br$ (as synthesised in Section 3.3.5). This material was ground into a powder using a mortar and pestle, and investigated by DSC and VT-XRD from room temperature to 300 °C. Figure 3.1c and d show these DSC and VT-XRD measurements, taken at 5 °C min^{-1} and 6 °C min^{-1} respectively. In the DSC, endothermic peaks are observed at $\sim$ 230 °C and $\sim$ 280 °C which indicate phase transitions are occurring at these temperatures. In the VT-XRD, the Li_2OHBr and $Li_4(OH)_3Br$ phases completely disappear at $\sim$ 230 °C to form a new crystalline phase. Mahroug's phase diagram indicates this new phase should correspond to a phase with the stoichiometry $Li_3(OH)_2Br$.

This new phase persists until melting. The first indications of melting onset between 260 °C and 270 °C, where a uniform reduction in XRD peak intensity and rapid narrowing of the ^{7}Li NMR lineshape occurs (Figure 3.2), with the $Li_3(OH)_2Br$ phase fully disappearing by $\sim$ 290 °C. This aligns with the second endothermic peak seen in the DSC upon heating. Unlike indicated on Mahroug's phase diagram (Figure 1.11d), no $Li_4(OH)_3Br$ formation is observed prior to melting. Additionally, on further heating to 300 °C, no LiOH forms as expected from the phase diagram, but instead another peak appears, as yet unidentified. It is difficult to ascertain whether these observations correspond to equilibrium conditions and hence indicate a discrepancy with the phase diagram, or can be attributed to non-equilibrium phenomena. Nevertheless, these findings support the existence of a phase with composition $Li_3(OH)_2Br$ which forms from 225 °C upon heating and melts around 270 °C.

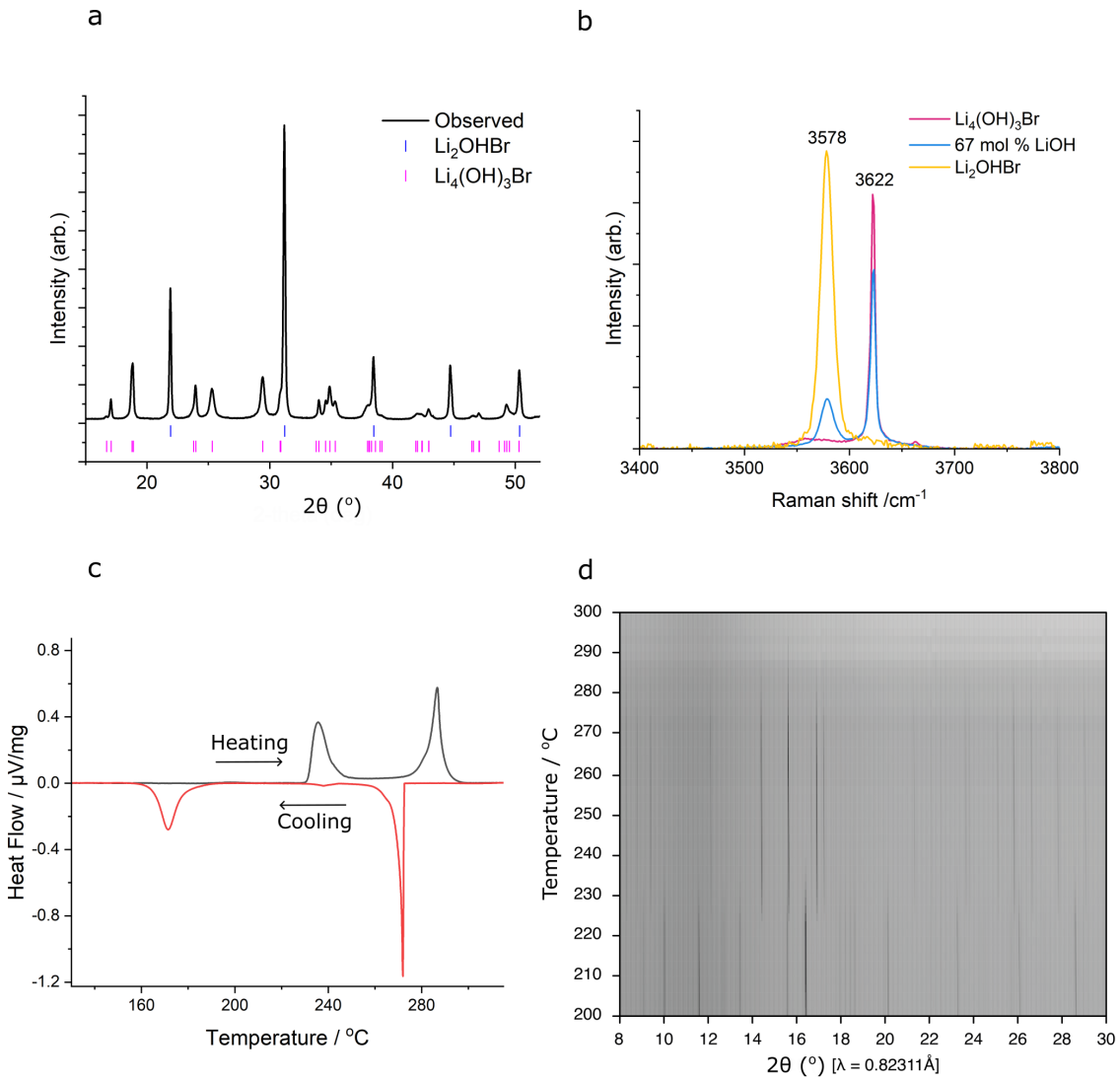

Figure 3.1: *Existence of $Li_3(OH)_2Br$. a) XRD pattern from room-temperature 67 mol % LiOH sample cooled from 350 °C at 3 °C min^{-1}. Bragg peak positions for $Li_4(OH)_3Br$ reported herein and Li_2OHBr phases are indicated by ticks beneath the data. b) Room-temperature Raman spectroscopy measurements in the O-H bond stretching vibration region, showing 67 mol % LiOH sample after cooling from 350 °C at 3 °C min^{-1}. Bonding environments corresponding to Li_2OHBr (3578 cm^{-1}) and $Li_4(OH)_3Br$ (3622 cm^{-1}), are observed, compared with reference measurements. c) Heating and cooling DSC of 67 mol % LiOH sample at a rate of 5 °C min^{-1}. Two peaks are seen in each instance, expected to correspond to the formation and decomposition of $Li_3(OH)_2Br$. d) A film plot showing synchrotron VT XRD measurements (λ = 0.82311 Å) of the 67 mol % LiOH sample shown in part a, heated at 6 °C min^{-1}. A phase transition occurs at $\sim$ 225 °C, followed by melting from $\sim$ 270 °C.*

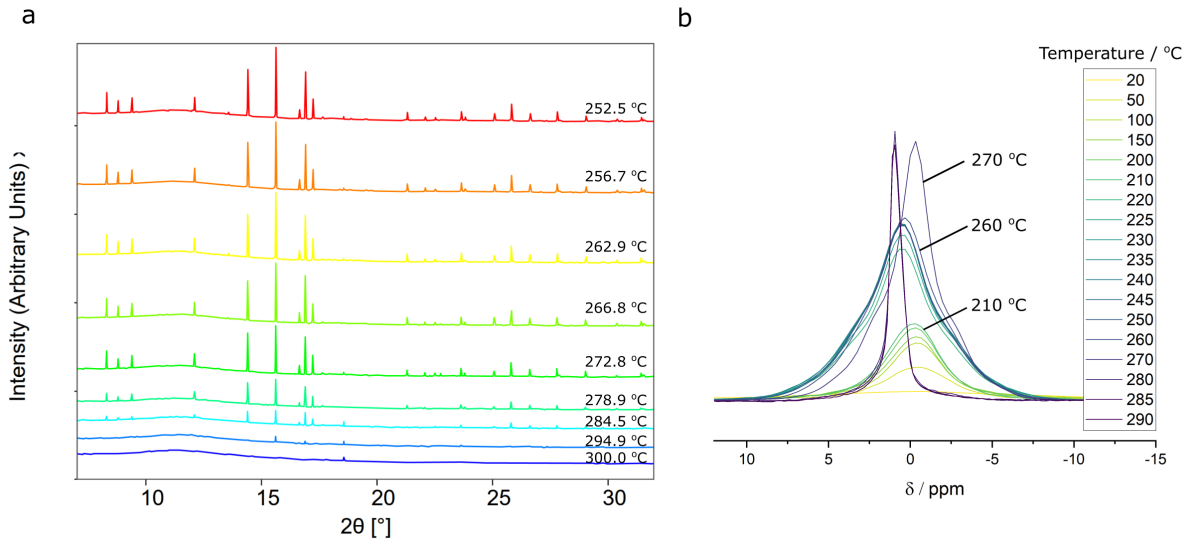

Figure 3.2: *$Li_3(OH)_2Br$ Melting. a) In-situ synchrotron XRD heating of $Li_3(OH)_2Br$ at* 6 °C *min^{-1}. The decrease in peak intensity corresponds to sample melting. The bottom spectrum corresponds to the sample after holding at* 300 °C *for 10 minutes. Residual solid at* 300 °C *is expected to be LiOH in Mahroug's phase diagram, but these peaks correspond to another, unidentified phase. b) ^7Li NMR lineshapes taken at temperatures between* 20 °C *and* 290 °C*, showing phase transitions at* ∼ 220 °C *and* ∼ 270 °C

3.3.2 Structural Characterisation of $Li_3(OH)_2Br$

A cold-pressed pellet of the 67 mol % LiOH sample was heated to 250 °C at 1 °C min^{-1}. To ensure equilibrium conditions, *in-situ* XRD measurements were taken while the sample was held at 250 °C for 1 hour. The diffraction pattern was found to be stable in this time, indicating that equilibrium conditions were being obtained, and what is believed to be a single phase. The observed peak positions for the $Li_3(OH)_2Br$ phase were indexed and space group searching conducted using TOPAS-Academic software[161] (Table A.1). The peaks were found to be well fit by several hexagonal unit cells. A Pawley refinement for the $P6_3$ space group, shown in Figure A.1, fits the diffraction pattern in excellent agreement, giving lattice parameters of $a = b =$ 6.57192(6) Å, $c =$ 10.74643(17) Å.

In a collaboration with Dr James Quirk and Professor James Dawson from Newcastle University, theoretical modelling was used to predict crystal structures for phases in the LiBr-LiOH system. A low-energy structure for $Li_3(OH)_2Br$ was determined through ab-initio random structure searching (AIRSS). To do this, thousands of structures were generated in which the Li-O-Br sublattice was arranged in the $P6_3$ space group, with H ignored in symmetry determination

as it could not be refined in XRD. Each candidate structure was optimised using a CHGNet machine-learned force field fine-tuned for the Li-O-H-Br phase space[175]. A possible structure for $Li_3(OH)_2Br$ was found and equilibrated at 250 °C so that fractional occupations at finite temperature could be determined. The lithium atoms were found to be highly mobile, meaning that precise occupancies could not be determined from MD. As such, the occupancies were assumed to be equal across all sites. Further details of the computational approach employed by Dr Quirk and Professor Dawson are outlined in Appendix A.2. The resultant computational structure is shown in Figure A.3, and detailed in Table A.4.

The pseudo-symmetry observed in the structure and the absence of a clear mechanism for inversion-symmetry breaking, indicate that the phase may belong to a higher symmetry space group than $P6_3$. Specifically, with minor adjustments to the atom positions, the unit cell can be made to include additional mirror planes and a c-axis glide plane. As such, the atomic positions were adjusted to be consistent with the $P6_3/mmc$ space group. For this, the origin of the cell had to be shifted so that mirror planes perpendicular to the c-axis lie at $z = 1/4$ and $z = 3/4$, in accordance with the $P6_3/mmc$ space group. This structure refines well with the observed diffraction data. The refined structural model for this proposed $P6_3/mmc$ structure is shown in Figures 3.3a and b, and compared with the computational starting model in Figure A.3. A combination of network-like lithium sites and distinct "cage" geometries are predicted to exist in the structure, shown with blue and green lithium atoms respectively. An XRD pattern taken at 250 °C, along with a corresponding Rietveld refinement, is shown in Figure 3.3c (Table 3.1). Information from the lithium in the structure was not refined due to its poor X-ray scattering cross-section, to avoid unphysical and inaccurate results. In order to establish information about lithium in the structure accurately, complementary techniques such as neutron diffraction will be necessary in future work.

Table 3.1: Crystallographic parameters from the Rietveld refinement of $Li_3(OH)_2Br$ *in-situ* at 250 °C shown in Figure 3.3c. Errors on refined parameters are indicated in parentheses.

Space Group	$P6_3/mmc$					
$a = b$ (Å)	6.57137(8)					
c (Å)	10.7454(2)					
V (Å^3)	401.851(13)					
Atom	Wyckoff position	x	y	z	Occupancy	U_{iso} (Å^2)
Br1	4f	1/3	2/3	0.9373(2)	1	0.0344(11)
O1	6h	0.1631(7)	0.8369	0.25	1	0.061(3)
O2	2a	0	0	0	1	0.061(3)
Li1	4e	0	0	0.3185	0.24	0.25(4)
Li2	6h	0.1775	0.8225	0.75	0.24	0.25(4)
Li3	12k	0.0938	0.9062	0.6454	0.24	0.25(4)
Li4	12k	0.1456	0.8544	0.0879	0.24	0.25(4)
Li5	4f	1/3	2/3	0.1905	0.24	0.25(4)
Li6	12k	0.0790	0.5395	0.1804	0.24	0.25(4)

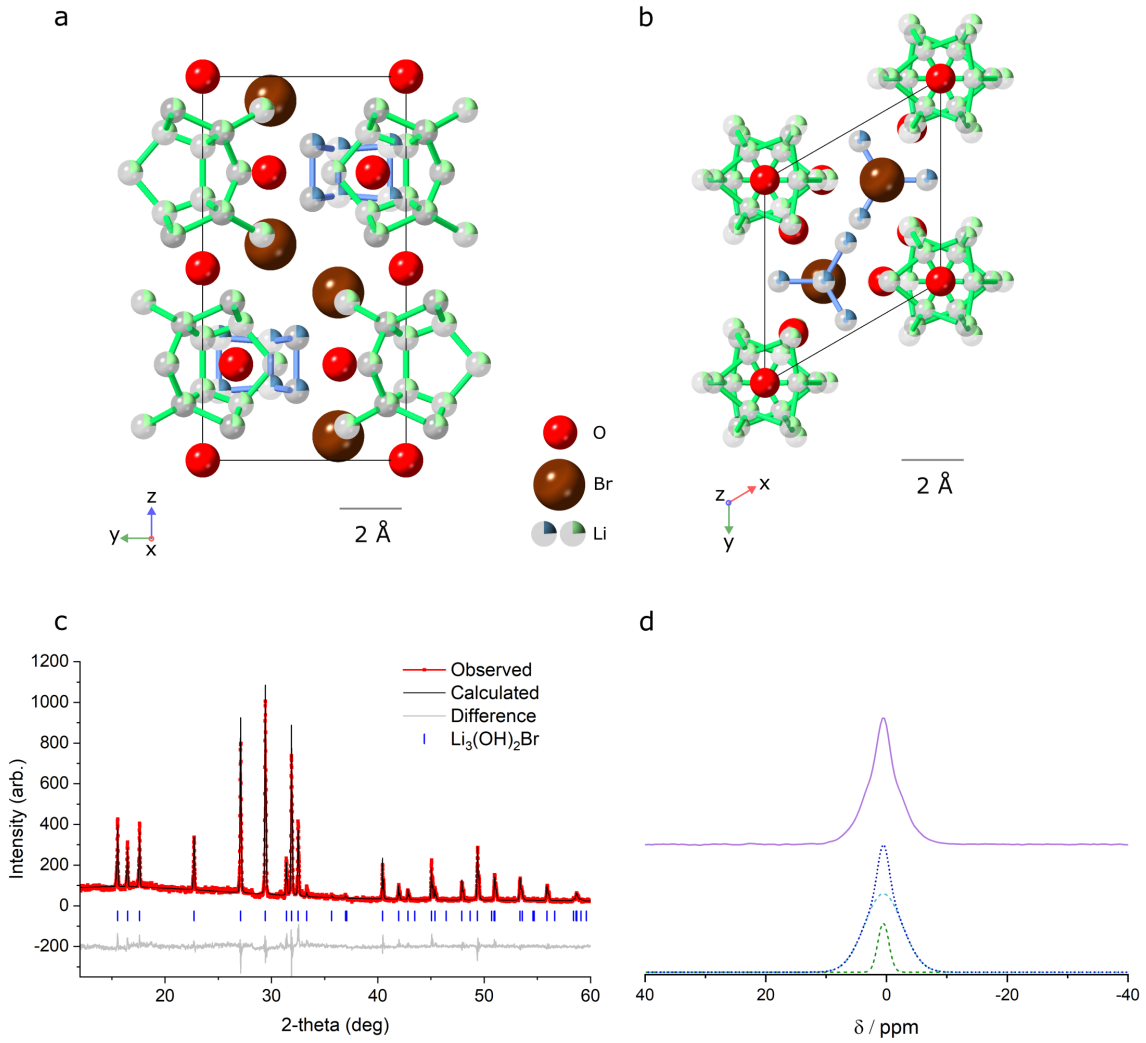

Figure 3.3: *Crystal Structure of $Li_3(OH)_2Br$. Refined $P6_3/mmc$ structure for $Li_3(OH)_2Br$ viewed along a) [100] and b) [001]. Lithium occupancies are represented by pie charts, and are assumed to be equal (0.24) across all sites. Blue and green lithium atoms are used to distinguish between cage-like (green) and network-like (blue) sites in the structure. The green lithium atoms are extended beyond a single unit cell in the a-b plane to emphasise the cage-like structures they form. c) XRD pattern of $Li_3(OH)_2Br$ after 1 hour annealing at 250 °C, with matching Rietveld refinement using the proposed $P6_3/mmc$ structural model of $Li_3(OH)_2Br$ (R_{wp} = 11.9 %). The corresponding difference curve is offset below the data and ticks indicate the positions of the Bragg reflections. d) ^{7}Li NMR spectra of $Li_3(OH)_2Br$ at 230 °C. The lineshape can be deconvoluted into two Gaussian peaks, indicating 2 lithium environments in the structure.*

In addition to diffraction studies, ^{7}Li NMR lineshapes were measured. Between 220 °C and 270 °C, in the temperature range of the $Li_3(OH)_2Br$ phase, a lineshape consisting of a narrow and a broad component is observed. An example spectrum, taken at 230 °C, is shown in Figure 3.3d. The narrow component suggests a highly mobile site, whereas the broad component indicates another, less mobile environment. It is possible that the narrower element arises from

the "cage" lithiums in the structure, in which rapid *intra*-cage hopping may occur.

3.3.3 Lithium Dynamics in $Li_3(OH)_2Br$

Since another LiBr-LiOH compound, Li_2OHBr, is a superionic conductor of interest for solid-electrolyte applications[86,94–97,103,104,106], it is interesting to assess the mobility of lithium ions in $Li_3(OH)_2Br$ to see whether it also exhibits superionic conductivity.

To evaluate the lithium-ion dynamics in the $Li_3(OH)_2Br$ phase, ^7Li SLR-NMR measurements and PFG-NMR measurements were taken across a range of temperatures, as shown in Figure 3.4a. The SLR measurements display three distinct regions. At low temperatures, the low-temperature flank of the rate peak corresponding to the region of mixed Li_2OHBr and $Li_4(OH)_3Br$ can be seen. Around 220 °C, $Li_3(OH)_2Br$ begins to form and data points on the high-temperature flank of the corresponding rate peak can be seen. From 260 °C, another change corresponding to the sample melting is observed. The narrow temperature range in which the $Li_3(OH)_2Br$ phase exists means it is challenging to fit a BPP model to the SLR data. To obtain an estimate of the activation energy for lithium-ion hopping, an approximation can instead be made using an Arrhenius relationship[176,177]. A linear fit between 225 °C and 250 °C suggests a low activation energy of 0.22 eV. PFG-NMR measurements could be obtained from 220 °C (coinciding with the onset of $Li_3(OH)_2Br$ formation). A lithium diffusivity of $1.53 \times 10^{-10}\ m^2\ s^{-1}$ was found for the $Li_3(OH)_2Br$ phase at 250 °C. An activation energy cannot be obtained from the diffusivity measurements due to microscopic changes occurring upon heating. The high temperatures involved result in sintering and grain growth in the powder sample, which impacts PFG diffusivity measurements probing a similar length-scale.

To study ionic conductivity in $Li_3(OH)_2Br$ over macroscopic length-scales, EIS was conducted on cold-pressed pellets. As shown in the Nyquist plots in Figure 3.4b, characteristic semi-circles are observed at lower temperatures that could be fitted using an ECM containing a bulk and an interface component. As the temperature increases, low resistances result in the semicircles disappearing, and so the intersection of the low frequency tail with the real axis was instead used to calculate the total resistance. The temperature dependence of the ionic conductivity is shown in Figure 3.4c. A step change corresponding to the phase transition forming $Li_3(OH)_2Br$ can be seen at 230 °C, with an ionic conductivity of 0.12 S cm^{-1} at 250 °C

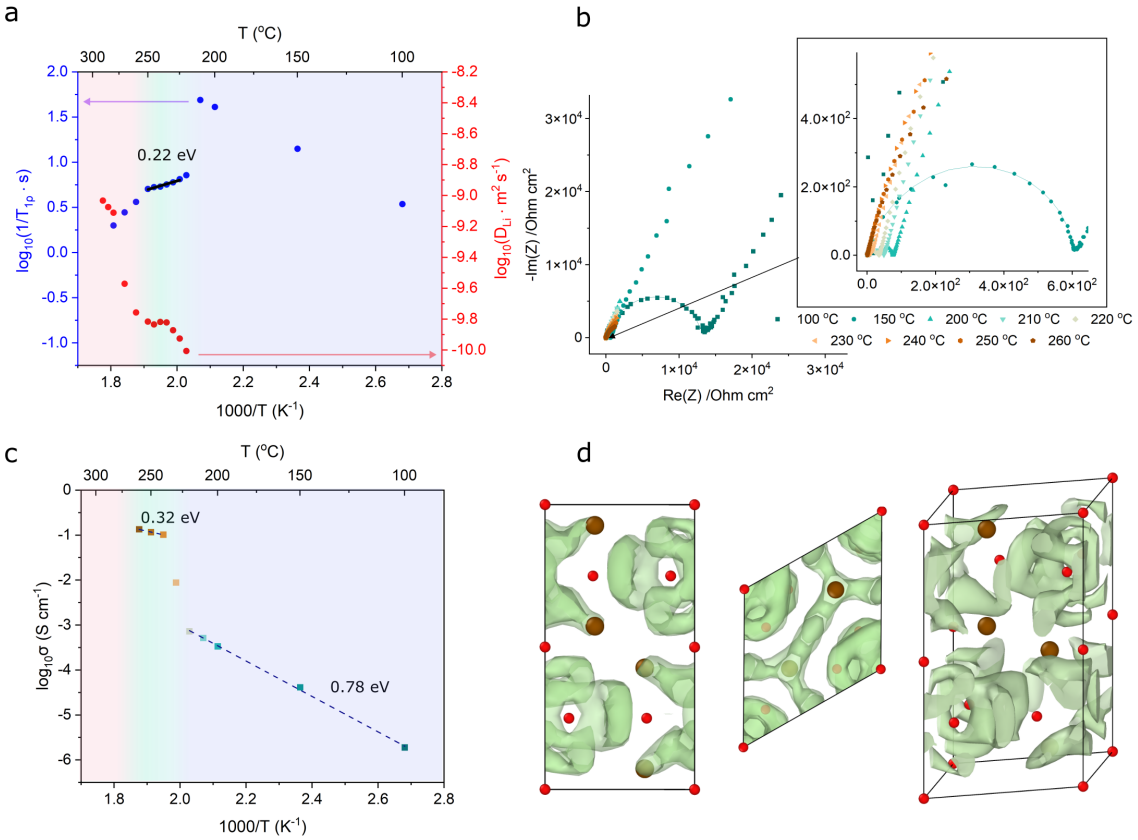

Figure 3.4: *Li-ion Dynamics of $Li_3(OH)_2Br$. a) NMR Relaxometry and Diffusivity measurements of 67 mol % LiOH as a function of temperature. $Li_3(OH)_2Br$ forms from 220 °C and starts to melt from 260 °C. A linear fit to the SLR data is included for what is believed to be the pure $Li_3(OH)_2Br$ phase region, used to calculate an activation energy for Li-ion hopping. b) Nyquist plots from EIS of 67 mol % LiOH as a function of temperature. c) Temperature dependence of ionic conductivity of 67 mol % LiOH. The ionic conductivity increases dramatically when $Li_3(OH)_2Br$ forms above 225 °C. d) Lithium density plots for the $Li_3(OH)_2Br$ phase from MD simulations, overlaid on the $P6_3/mmc$ unit cell and viewed along [100], [001] and at an offset angle. Lithium density is seen to be confined to cages with facile intra-cage hopping.*

and an activation energy of 0.32 ± 0.04 eV found between 240 °C and 260 °C. Upon extrapolating to room temperature, an ionic conductivity of $5.2 \pm 1.6 \times 10^{-4}$ S cm^{-1} is found. It would be desirable to retain this phase, and hence the excellent ionic conductivity, to lower temperatures. $Li_3(OH)_2Br$ could offer several significant advantages over many solid electrolytes currently under consideration. $Li_3(OH)_2Br$ contains inexpensive and abundant precursors, unlike popular options such as doped LLZO and lithium argyrodite sulphides[178]. Li_2OHBr exhibits good stability with lithium metal at room temperature, as is the case with other oxide electrolytes[86,96]. This is anticipated to translate to $Li_3(OH)_2Br$. Furthermore, the density of $Li_3(OH)_2Br$ (2.23 g cm^{-3}) is significantly reduced compared to other oxide electrolytes, such as LLZO (5.07 g cm^{-3}),

$Li_{0.34}La_{0.56}TiO_3$ (5.01 g cm^{-3}) and LAGP (3.56 g cm^{-3})[123].

To identify and eliminate impacts of sintering occurring at high temperatures, EIS measurements were also taken using another heating protocol (see Appendix A.4). Similar behaviour was observed between the $Li_3(OH)_2Br$ phase in both samples, indicating that the obtained conductivity is representative of bulk $Li_3(OH)_2Br$.

MD simulations were carried out on a supercell of the computational $Li_3(OH)_2Br$ structure containing 576 lithium ions across a temperature range of 220 °C to 240 °C. Lithium density plots, shown in Figure 3.4d, reveal that the lithium trajectories are largely confined to 'cages' in which lithium can easily move between sites within the cage (*intra*-cage), but where jumps between the cages (*inter*-cage) are less frequent. The corresponding activation energies for intra-cage and inter-cage jumps were calculated to be 0.18 ± 0.02 eV and 0.35 ± 0.02 eV respectively. Accordingly, the long-range macroscopic activation energy is calculated to be 0.27 ± 0.03 eV, which is in reasonable agreement with the EIS findings. The underestimate in activation energy between MD and EIS is reasonable given the differences between the computational and experimentally-refined structure, and the absence of extended defects such as grain boundaries in MD, which assumes a pristine crystal. Attempts to engineer $Li_3(OH)_2Br$ to improve ionic conductivity may focus on lowering the barriers for inter-cage diffusion to enable long-range transport. Discrepancies between the intra- and inter-cage activation energies are well-studied in the familiar argyrodite family of solid electrolytes Li_6PS_5Cl,[179] where increased disorder is a possible avenue to encouraging macroscopic diffusion.

3.3.4 Metastable Retention of $Li_3(OH)_2Br$

To see whether the $Li_3(OH)_2Br$ phase could be retained to room-temperature metastably, samples were annealed at 250 °C for 4 hours such that $Li_3(OH)_2Br$ fully forms, followed by quenching to room temperature to try and "freeze-in" the phase. Both samples quenched from the liquid state at 350 °C, and from the $Li_3(OH)_2Br$ phase field at 250 °C, exhibited a similar XRD pattern with a different set of reflections to $Li_3(OH)_2Br$, $Li_2(OH)Br$ or $Li_4(OH)_3Br$ (Figure 3.5a). The thermodynamically-unstable nature of the $P6_3/mmc$ phase at low temperatures, coupled with the fast cooling rate inhibiting the necessary atomic rearrangements for attaining equilibrium, result in the metastable state observed here. The ionic conductivity of this metastable state was

assessed using EIS (Figure 3.5b,c), but did not demonstrate the same promising behaviour as the high-temperature phase, yielding an ionic conductivity of 3.6×10^{-8} S cm^{-1} at 30 °C and an activation energy of 0.75 eV in the temperature range 30 °C to 50 °C. DC CA measurements indicated an electronic conductivity of 2.0×10^{-11} S cm^{-1} at 25 °C (Figure 3.5d). This ionic conductivity is lower than that of the related compound and solid electrolyte candidate, Li_2OHBr, which typically exhibits ionic conductivities of 10^{-7} - 10^{-6} S cm^{-1} for cold-pressed pellets at room temperature[86,94–97,103,104,106]. Synthesis of Li_2OHBr from the melt, as is typical in literature, requires cooling through phase fields containing $Li_3(OH)_2Br$ (Figure 1.11d). Consequently, it is important to consider undesirable $Li_3(OH)_2Br$ impurity formation in Li_2OHBr synthesis. Small $Li_3(OH)_2Br$ crystallites formed during cooling, combined with potentially high levels of microstrain from the diffusionless metastable transformation, may mean that it is not obvious in XRD, typically used to screen for impurities. These implications shall be discussed further in Chapter 4, in which the synthesis of Li_2OHBr is considered. Ball milling of LiBr and LiOH precursors in the correct stoichiometric ratio was also tested to see if $P6_3/mmc$ $Li_3(OH)_2Br$ could be synthesised, but was unsuccessful.

3.3.5 Reconsidering $Li_4(OH)_3Br$ and its Synthesis

In Section 3.3.1, it was indicated that the expected $Li_4(OH)_3Br$ phase was not formed from the 67 mol % LiOH samples furnace-cooled into the "Li_2OHBr + $Li_4(OH)_3Br$" phase field at room temperature. The subsequent sections aim to explain this discrepancy and previous misunderstandings about $Li_4(OH)_3Br$, followed by providing an accurate characterisation of the $Li_4(OH)_3Br$ phase. XRD patterns obtained from the different synthesis approaches described in this section are compared in Figure 3.6a. The colour-coded schematic in Figure 3.6b shows the relationship between these different synthesis routes.

To produce $Li_4(OH)_3Br$, a synthesis route representative of those in literature was first carried out. Anhydrous LiBr and LiOH were ground together in the correct stoichiometric ratio, heated to 400 °C for 1 hour with a ramp rate of 5 °C min^{-1}, furnace-cooled at 2 °C min^{-1} inside a glovebox, and ground into a powder using an agate mortar and pestle. An XRD pattern obtained from these samples, also taken under glovebox atmosphere, is shown in Figure 3.6ai. A schematic of the process is shown in Figure 3.6b. The XRD pattern does not match that of

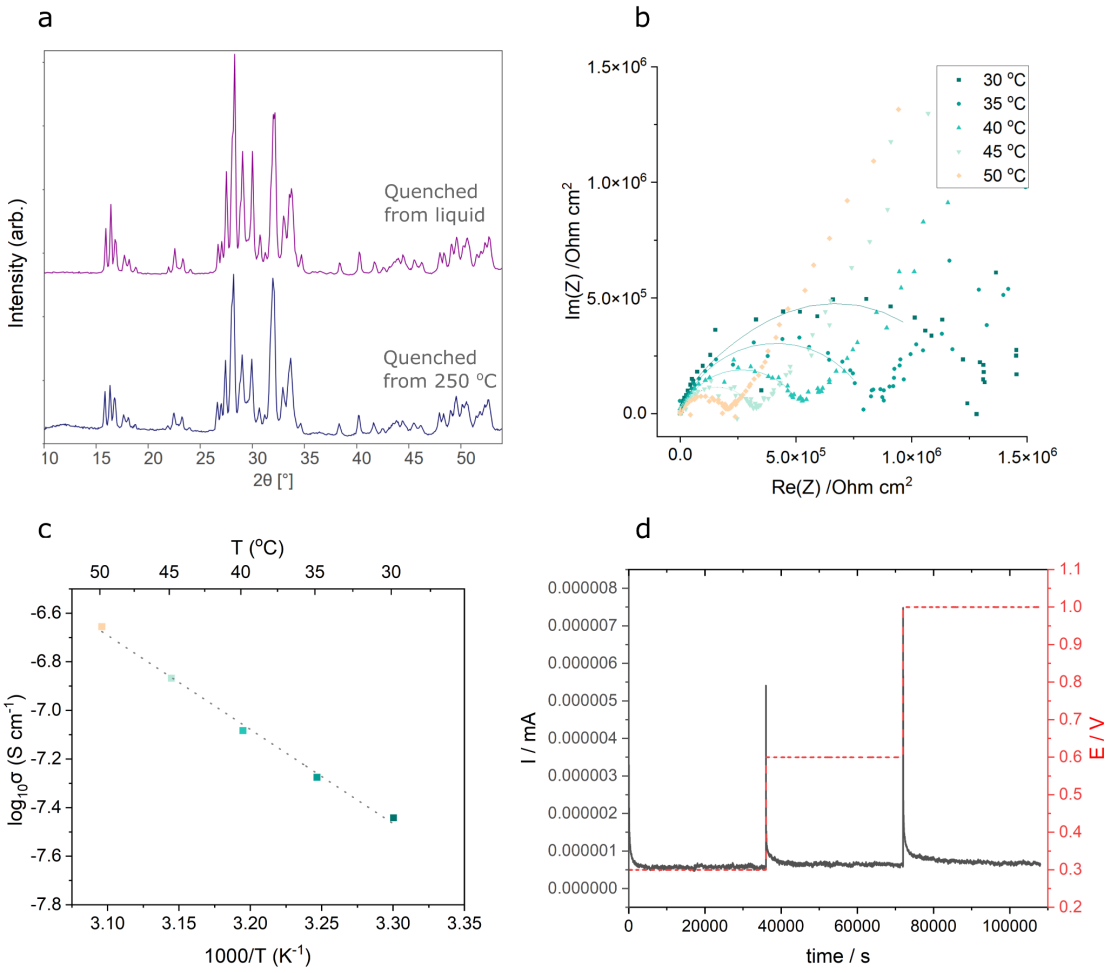

Figure 3.5: *Quenched $Li_3(OH)_2Br$. a) XRD spectra of 67 mol % LiOH after quenching to room temperature from the liquid state (at 350 °C), and from an anneal at 250 °C. The resulting patterns correspond to a metastable state not containing the $P6_3/mmc$ $Li_3(OH)_2Br$ phase, $Li_4(OH)_3Br$ or Li_2OHBr. b) Nyquist plots from EIS of quenched $Li_3(OH)_2Br$ as a function of temperature. b) Temperature dependence of the ionic conductivity. c) Room temperature DC CA used for determination of the electronic conductivity*

previous literature reports of $P2_1/m$ $Li_4(OH)_3Br$[6–9,127], however it has previously been found by Legros *et al.*, who speculated that it might be a polymorph of $Li_4(OH)_3Br$[7]. Here, it is proposed that the pattern observed actually corresponds to a mixture of phases, containing a large fraction of the Li_2OHBr antiperovskite phase, shown for comparison in Figure 3.6avii, and the true thermodynamically-stable $Li_4(OH)_3Br$ phase. The solidification of $Li_4(OH)_3Br$ is proposed to be peritectic through the reaction: liquid + LiOH → $Li_4(OH)_3Br$[9,126,128]. Given the unfavourable kinetics of peritectic reactions, it can be challenging to achieve equilibrium conditions, and so the presence of non-equilibrium phases such as Li_2OHBr in samples at room-temperature is not surprising. The implications of non-equilibrium solidification are an important consideration in the use of peritectic compounds for LHTES, as the enthalpy of melting less energetically-stable

phases differs to that of their equilibrium counterparts.

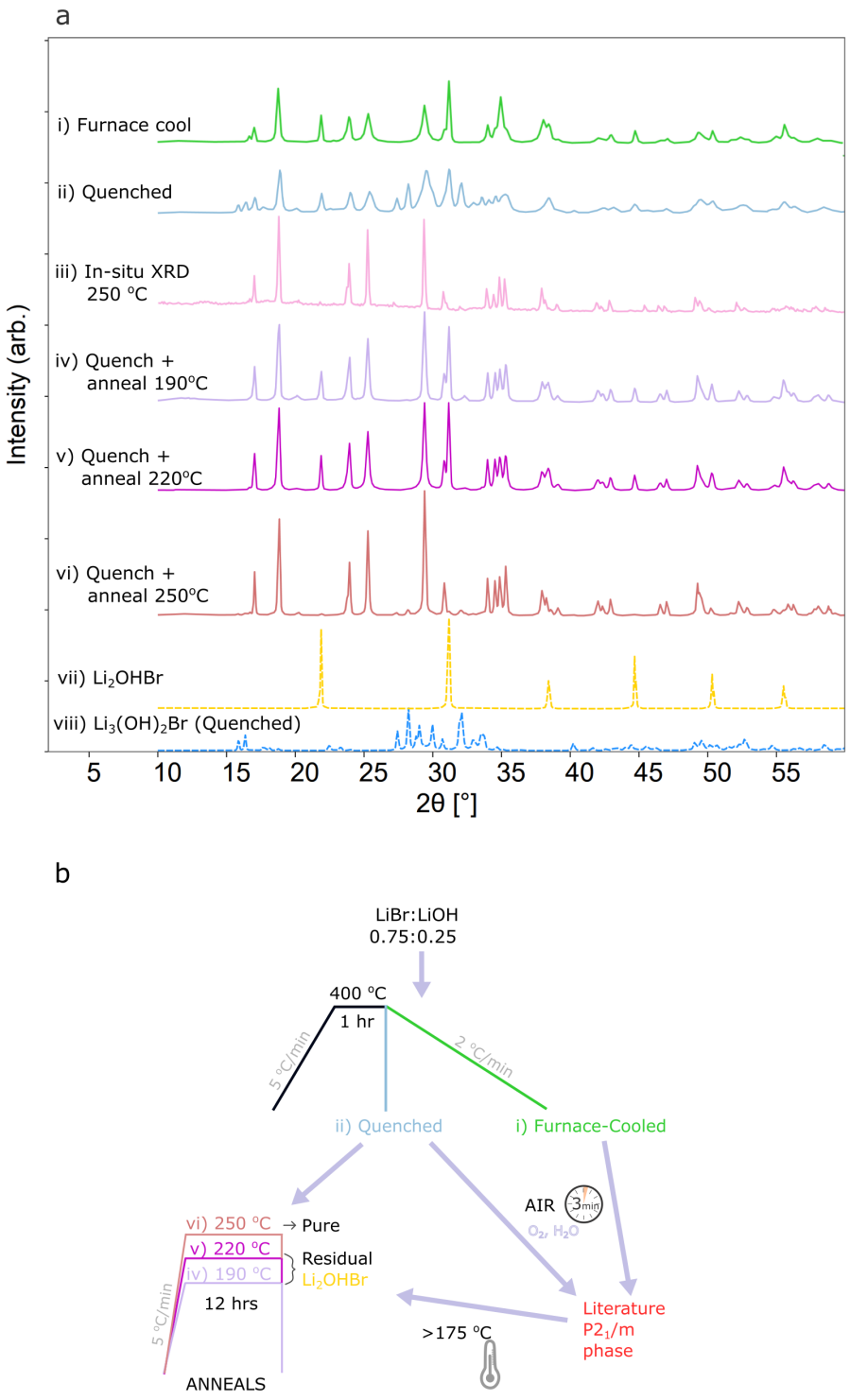

Figure 3.6: *$Li_4(OH)_3Br$ Synthesis Investigations. a) X-ray diffraction patterns obtained for $Li_4(OH)_3Br$ synthesised under a variety of conditions. The synthesis conditions are found to have a big impact on the phase-purity of the obtained samples. For ease of comparison, the diffraction patterns of (vii) Li_2OHBr and (viii) metastable quenched $Li_3(OH)_2Br$ are included, to highlight conditions under which residual impurities remain. b) Schematic showing the relationship between these different synthesis conditions. The diagram is colour-coded to match the diffraction patterns shown in a.*

The samples were found to be very air sensitive. A furnace-cooled sample was exposed to air for 3 minutes, before returning to the glovebox and recording XRD patterns under inert atmosphere. The new diffraction pattern displayed a different set of peaks, which correspond to the $P2_1/m$ crystal structure commonly reported in literature. A Pawley refinement for this $P2_1/m$ structure, shown in Figure 3.7a, gives a unit cell of $a = 5.4594(3)$ Å, $b = 7.5922(3)$ Å, $c = 6.5090(3)$ Å, $\beta = 93.841(2)°$, in excellent agreement with literature[127]. These findings indicate that the previously reported $P2_1/m$ phase corresponds to a hydrated state, and not the true $Li_4(OH)_3Br$ phase. When quenching $Li_4(OH)_3Br$ samples to room temperature from the liquid state at 400 °C, a different diffraction pattern was found, as shown in Figure 3.6aii. Nevertheless, the same $P2_1/m$ peaks were observed to form from quenched samples upon air exposure (Figure 3.7b), further supporting that the phase reported in literature is hydrated. It is likely that XRD setups employed in previous literature were not sufficiently air-tight to avoid hydration, explaining why Mahroug *et al.* believed they had obtained pure $Li_4(OH)_3Br$ regardless of cooling rate[8].

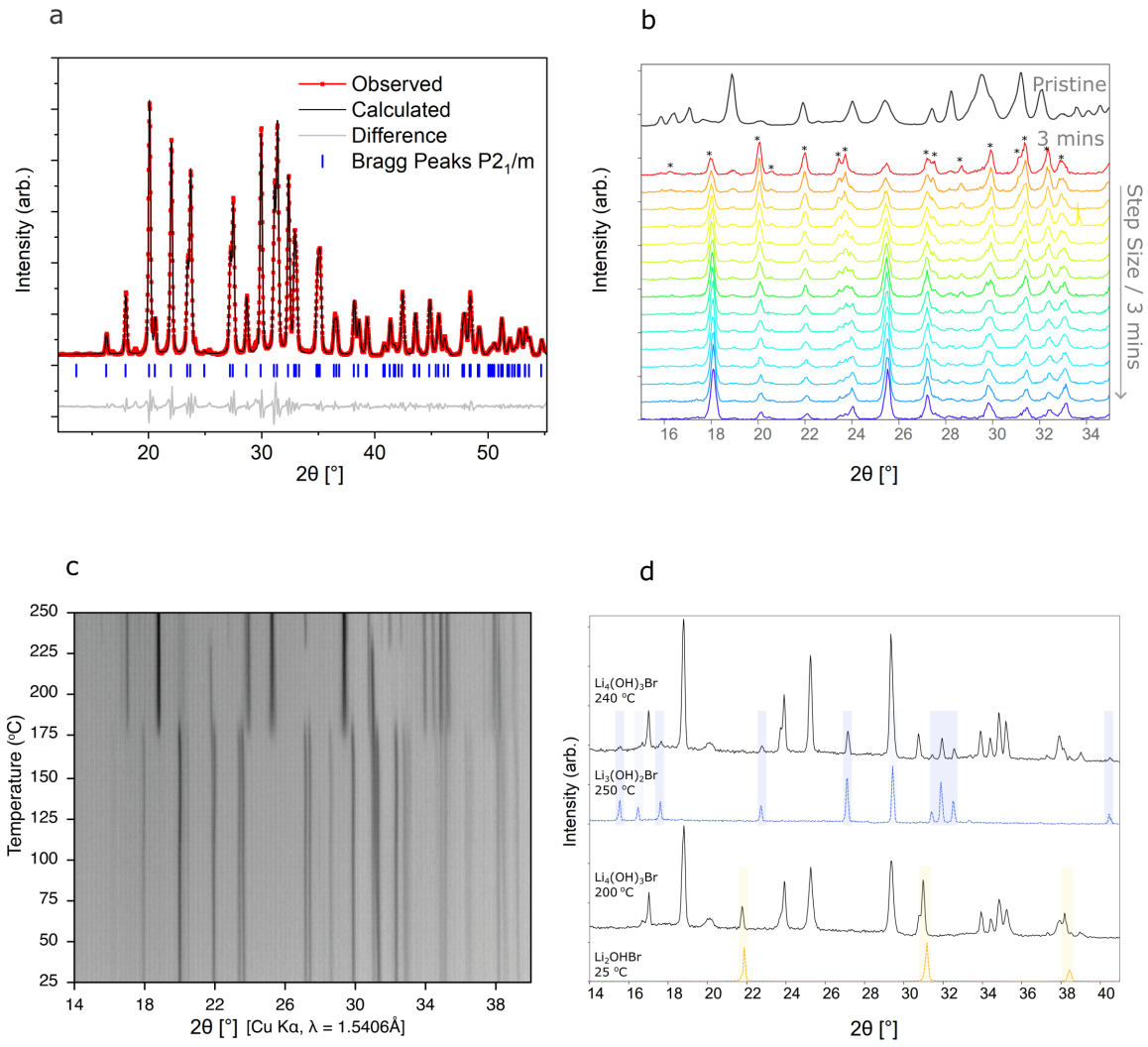

Figure 3.7: *Hydrated $Li_4(OH)_3Br$ studies. a) Powder XRD pattern of air-exposed $Li_4(OH)_3Br$ and corresponding Pawley refinement (R_{wp} = 7.0 %) to the $P2_1/m$ crystal structure reported in literature, with a difference plot included beneath*[127]*. The Bragg peak positions corresponding to the $P2_1/m$ phase are indicated with ticks. b) Diffraction patterns demonstrating the instability of quenched $Li_4(OH)_3Br$ in air. The top 'pristine' pattern shows a diffraction pattern taken under inert conditions. Subsequent patterns correspond to continuous XRD scans with a duration of 3 minutes taken on samples in air. A large reduction in the starting phase, and the formation of peaks corresponding to the $P2_1/m$ phase reported in literature (labelled with asterisks) are observed in as little as 3 minutes exposure, after which further degradation occurs. c) VT-XRD patterns of air-exposed $P2_1/m$ $Li_4(OH)_3Br$ heated from room temperature to 250 °C, displayed on a film plot. Reformation of the non-air-exposed diffraction pattern occurs at ∼ 175 °C. The disappearance and appearance of Li_2OHBr and $Li_3(OH)_2Br$ respectively can be seen upon further heating at ∼ 230 °C. d) XRD patterns of $Li_4(OH)_3Br$ at 200 °C and 240 °C extracted from the film plot in part c, along with diffraction patterns of $Li_3(OH)_2Br$ and Li_2OHBr references. Li_2OHBr impurity is present at 200 °C, which is replaced by $Li_3(OH)_2Br$ in the pattern at 240 °C. Note that there is a slight peak shift between pure Li_2OHBr and impurity Li_2OHBr due to the different measurement temperatures.*

To understand what happens to the $P2_1/m$ phase upon heating, VT-XRD was conducted on a cold-pressed pellet of $Li_4(OH)_3Br$ powder with the air-exposed $P2_1/m$ phase, heated at 1 °C min^{-1} under argon flow. As shown in the film plot in Figure 3.7c, the $P2_1/m$ diffraction peaks disappear between 170 °C and 190 °C. Significantly, this means that the impressive enthalpies of melting predicted from calculations based on this phase do not apply. The diffraction pattern which forms at 170 °C resembles the anhydrous furnace-cooled phase. At $\sim$ 230 °C, some peaks disappear and new peaks appear, corresponding to the antiperovskite Li_2OHBr and high-temperature $Li_3(OH)_2Br$ phases respectively. Diffraction patterns extracted at 200 °C and 240 °C illustrate this clearly in Figure 3.7d. During an *in-situ* anneal for 1 hour at 250 °C, the intensity of the $Li_3(OH)_2Br$ peaks decreased, leaving the diffraction pattern shown in Figure 3.6aiii. These same peaks are observed above $\sim$ 220 °C in synchrotron VT-XRD of unexposed (anhydrous) samples quenched from the melt and reheated *in-situ* (Figure A.2). Hence, it can be implied that these remaining peaks correspond to the true $Li_4(OH)_3Br$ phase. Although there appears to be some reversibility of the hydration process upon heating, it is worth noting that the hydrated $P2_1/m$ phase was not stable in air, and continued evolving into new decomposition products upon continued air exposure (Figure 3.7b).

To see whether phase-pure samples of anhydrous $Li_4(OH)_3Br$ could be obtained directly from the melt through an alternative route, samples were quenched to room-temperature by removing from the furnace at 400 °C. By providing a large undercooling, it was hoped that direct nucleation of $Li_4(OH)_3Br$ would take place, rather than formation through peritectic reaction or peritectic transformation. This has been previously reported for other peritectic materials[133–137]. As has been mentioned, the resulting diffraction pattern (Figure 3.6aii) does not match that of the furnace-cooled sample (Figure 3.6ai), or of phase-pure $Li_4(OH)_3Br$ (Figure 3.6aiii). This could indicate the presence of a lower temperature phase field containing another $Li_4(OH)_3Br$ polymorph, for example, as is suggested on Mahroug's phase diagram below 230 °C (Figure 1.11c). Upon heating quenched samples, a series of changes occur starting from $\sim$ 80 °C. These can be observed in VT-XRD and DSC measurements shown in Figure 3.8a,b. As such, the quenched state is not stable to 230 °C as the polymorph indicated on the phase diagram is. The large number of independently occurring changes implies the presence of several phases, and likely correspond to a series of metastable steps. From XRD and Raman spectroscopy comparisons shown in Figure 3.8c and d, it can be seen that the quenched sample contains a mixture of phases:

Li_2OHBr, LiOH, metastable $Li_3(OH)_2Br$ quenched from 400 °C, and the thermodynamically-stable $Li_4(OH)_3Br$ phase (as will be synthesised subsequently). This indicates that the direct nucleation of the $Li_4(OH)_3Br$ phase does not occur upon quenching as it had been hoped. Instead, some $Li_3(OH)_2Br$ appears to nucleate at high temperatures, and the high cooling rate means the kinetics are not sufficiently fast for transformation to $Li_4(OH)_3Br$ upon cooling, as was seen previously for quenched $Li_3(OH)_2Br$. As such, it is believed that quenched samples do not represent the equilibrium room-temperature state, and there is only one $Li_4(OH)_3Br$ phase between 250 °C and room temperature.

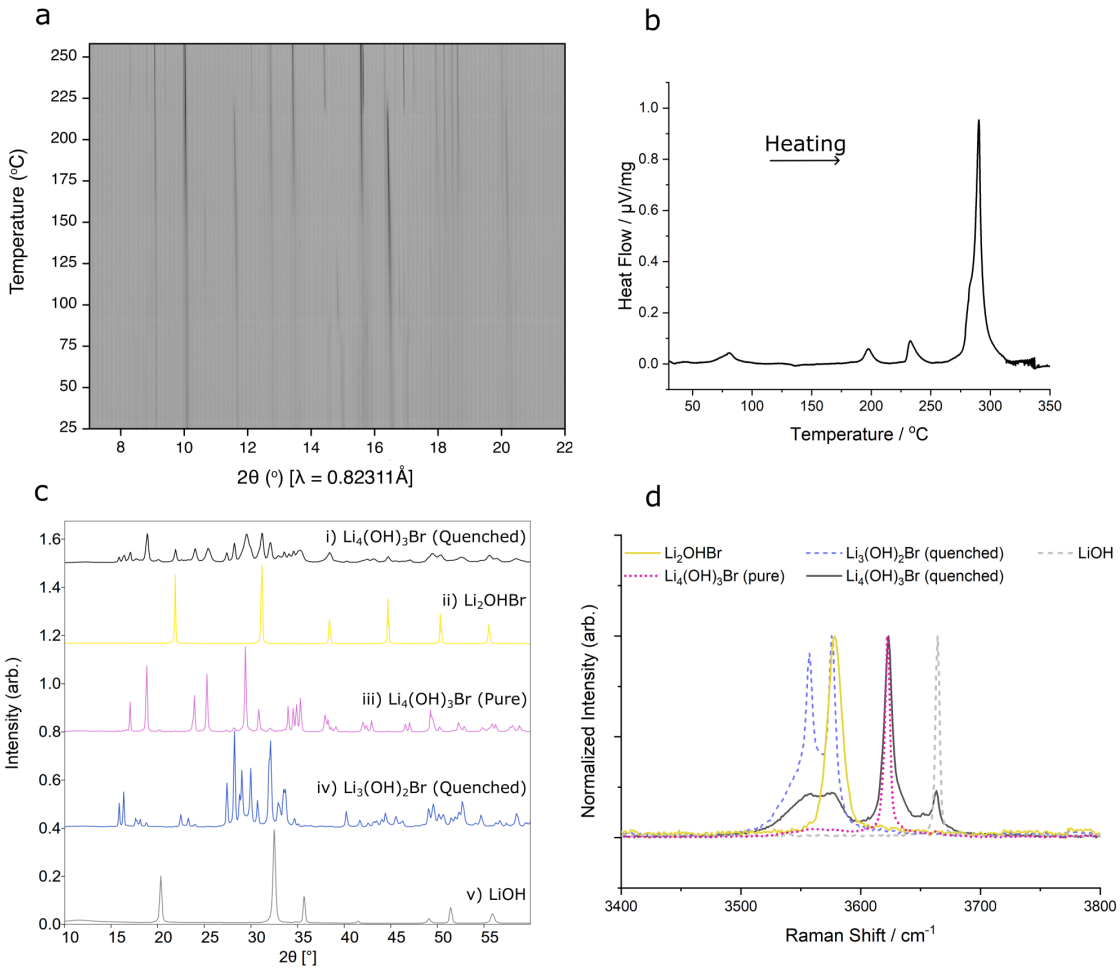

Figure 3.8: *Quenched $Li_4(OH)_3Br$. a) Synchrotron VT-XRD patterns (λ = 0.82311 Å) of quenched $Li_4(OH)_3Br$ showing a series of changes upon heating at 6 °C min^{-1}. b) Heating DSC of quenched $Li_4(OH)_3Br$ at a rate of 5 °C min^{-1} demonstrating a series of small endothermic peaks prior to melting at 300 °C. c) XRD measurements comparing quenched $Li_4(OH)_3Br$ with the phase-pure compounds Li_2OHBr, $Li_4(OH)_3Br$, LiOH and metastable $Li_3(OH)_2Br$ quenched from 400 °C. The quenched $Li_4(OH)_3Br$ consists of a combination of these phases. d) Raman spectroscopy measurements comparing the same compounds as in c.*

Since pure room-temperature $Li_4(OH)_3Br$ could not be produced directly from the melt, a series of anneals and quenches were carried out on different samples quenched from the liquid state. The corresponding XRD patterns for these samples are shown in Figure 3.6aiv - vi. Quenched samples have fine microstructures, maximising the contact area between reacting phases and reducing diffusion distances, and so were chosen for the starting material. Approximately 0.5 g of ground sample was annealed for 12 hours at the stated temperature, and then quenched back to room-temperature to try and 'freeze-in' the phase formed during the anneal, as shown schematically in Figure 3.6b. In anneals below 250 °C, a large amount of antiperovskite Li_2OHBr was found in samples, likely due to insufficient kinetics to obtain equilibrium at these temperatures.

Annealing at 250 °C produced nearly single-phase $Li_4(OH)_3Br$. Minor impurity peaks resembling the diffraction pattern observed for metastable quenched $Li_3(OH)_2Br$ were found to form (Figure 3.6vi), irrespective of the cooling rate employed following the anneal. Employing the same quench and anneal procedure on 80 mol % LiOH composition yielded samples containing a large fraction of LiOH, in addition to the same impurity peaks and $Li_4(OH)_3Br$, indicating that the composition cannot be compensated in this way (Figure 3.9a). It is possible that the phase's stoichiometry doesn't lie exactly on the binary phase diagram, perhaps explaining the difficulty in making completely phase-pure samples from LiBr and LiOH precursors through this approach. Nevertheless, only a minor fraction of impurity exists in $Li_4(OH)_3Br$ produced from the annealed 75 mol % LiOH samples, supported further by Raman spectroscopy measurements (Figure 3.9b). The Raman spectrum shows one sharp peak for the $Li_4(OH)_3Br$ phase, suggesting that the OH groups are in similar or equivalent environments, leading to overlapping modes.

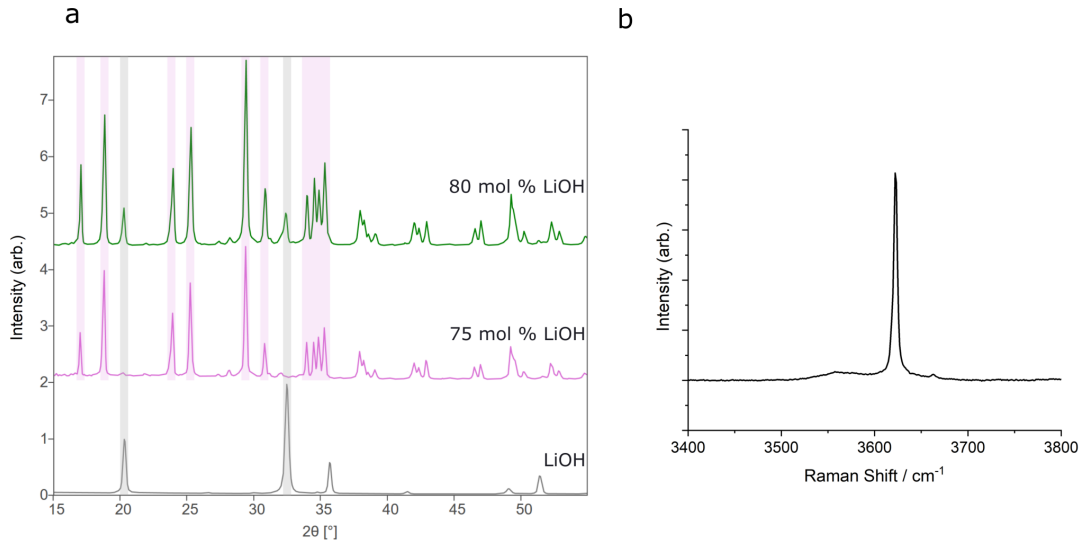

Figure 3.9: *a) Comparison of 75 mol % LiOH and 80 mol % LiOH samples, quenched from* 400 °C *to room temperature and reheated to* 250 °C *for 12 hours, followed by quenching to room temperature again. 75 mol % LiOH samples exhibit the* $Li_4(OH)_3Br$ *phase, whereas an excess of LiOH is also present in the 80 mol % LiOH samples. Minor impurity peaks can be seen in both. b) Raman spectroscopy of the -O-H bond stretching vibration region of room-temperature* $Li_4(OH)_3Br$ *after annealing at* 250 °C*. A strong signal at 3622* cm^{-1} *arises from the* $Li_4(OH)_3Br$ *phase, with only minor impurity peaks, supporting the conclusion that the sample has a high phase purity.*

The complex relationship between processing route (Figure 3.6b) and phase-purity (Figure 3.6a) found in this work highlight the importance of $Li_4(OH)_3Br$ synthesis conditions. Previous reports have not synthesised pure $Li_4(OH)_3Br$, and so the properties have yet to be established.

3.3.6 Characterising the True $Li_4(OH)_3Br$ Phase

To determine the crystal structure of the $Li_4(OH)_3Br$ phase, XRD peak indexing and space group searching was conducted using TOPAS-ACADEMIC software[161]. Peaks corresponding to the residual $Li_3(OH)_2Br$ were excluded from analysis. The diffraction pattern at 250 °C could be accounted for by an orthorhombic unit cell $\sim$ 10.4 Å $\times$ 5.3 Å $\times$ 5.3 Å. Systematic absences were consistent with the *Pmnm* space group symmetry. A Pawley refinement carried out using this space group setting gave an excellent fit to the data and a refined unit cell metric of a = 10.4099(3) Å, b = 5.30384(15) Å, c = 5.27776(13) Å.

Independently, AIRSS was employed by Dr James Quirk to find low-energy structures for $Li_4(OH)_3Br$, and optimised using a CHGNet machine-learned force field fine-tuned for the Li-O-H-Br phase space. Full details of the computational methods are provided in Appendix A.2. A possible layered crystal structure aligning well with the experimentally-determined unit cell was consistently identified, shown in Figure A.4 and detailed in Table A.5. The agreement between the data-driven and physics-based approaches support the robustness of these findings.

A constrained Rietveld refinement was then implemented in which the atom coordinates of the AIRSS solution were combined with the Pawley cell metric to give a structural model for $Li_4(OH)_3Br$. Subsequent refinement of this model involved allowing variation in cell metric, peak-shape parameters, background parameters and the positional coordinates of Br. The positions of Li, O and H within the unit cell were not refined as a consequence of their low X-ray scattering cross-sections. The resulting crystal structure and Rietveld refinement corresponding to the 250 °C annealed room-temperature sample are shown in Figure 3.10, and the crystallographic parameters detailed in Table 3.2. A refinement for the *in-situ* measurements at 250 °C is provided in Figure A.2 (Tables A.2, A.3). An increase in lattice parameter was seen between the room-temperature and *in-situ* 250 °C samples, particularly along the a-axis (Table 3.3). To clarify further information on the crystal structure, complementary techniques such as neutron diffraction should be employed in future work.

Aside from applications in TES, it is interesting to evaluate the lithium-ion dynamics in $Li_4(OH)_3Br$ in case of superionic conductivity which could make it of interest in solid electrolyte research, as with the closely-related compound Li_2OHBr[109,180,181]. To establish the ionic conductivity of $Li_4(OH)_3Br$, EIS measurements were taken on cold-pressed pellets with Ni foil blocking electrodes in 10 °C intervals from 20 - 100 °C. Despite conductivities of Li_2OHBr being easily obtained by this method at room temperature, no measurements were possible for $Li_4(OH)_3Br$ in this temperature range, suggesting a much lower ionic conductivity. To confirm this, MD simulations were performed on the crystal structure proposed in this work, in which negligible Li-ion mobility was observed.

In 1981, Hartwig *et al.* reported the ionic conductivity of $Li_4(OH)_3Br$ to be comparable to that of the antiperovskite Li_2OHBr[126]. These early measurements were only possible at 200 °C, giving values of 5×10^{-5} S cm^{-1} for both $Li_4(OH)_3Br$ and Li_2OHBr. No diffraction patterns

were reported in the work by Hartwig, raising uncertainty as to what was being measured. The findings reported herein indicate that *Pmnm* $Li_4(OH)_3Br$ is a much worse ionic conductor than Li_2OHBr, and should not be pursued as a candidate solid-state electrolyte. In addition, care should be taken to avoid the formation of $Li_4(OH)_3Br$ impurities in Li_2OHBr synthesis, for example by using an excess of LiOH as has been reported in the chloride homologue, Li_2OHCl[120].

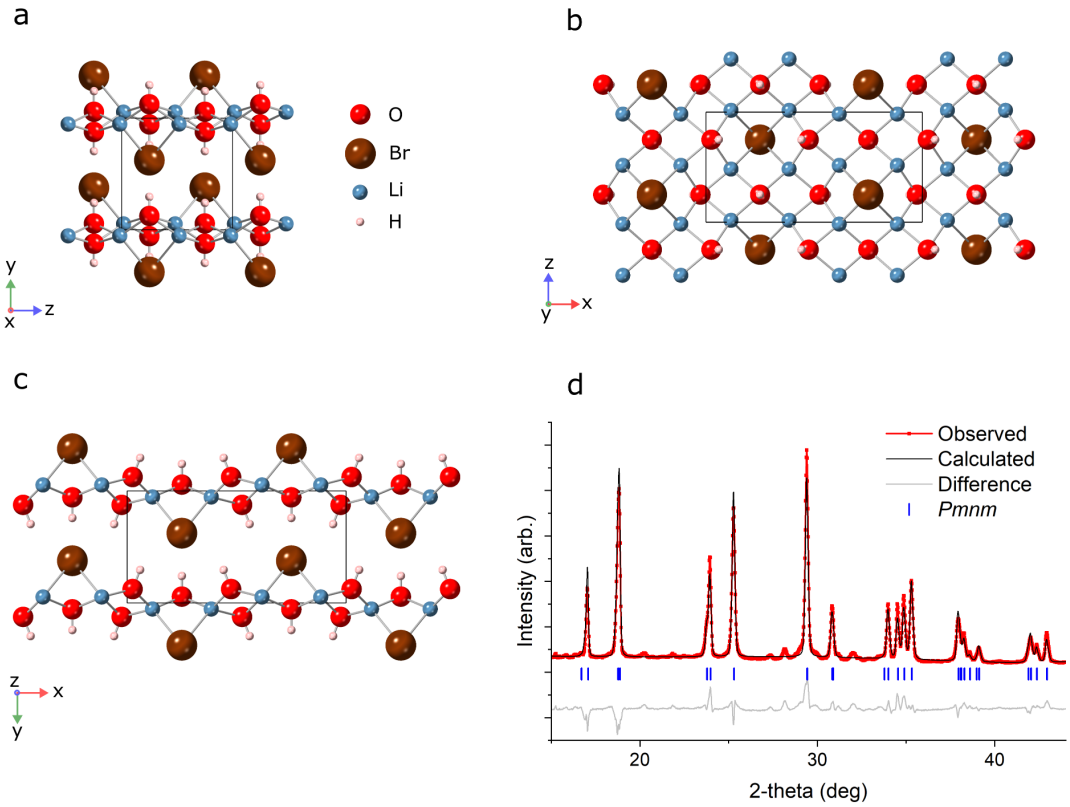

Figure 3.10: *$Li_4(OH)_3Br$ Crystal Structure. Pmnm structural model for $Li_4(OH)_3Br$ viewed along a) [100], b) [010] and c) [001]. The unit cell is indicated with a black box superimposed on the crystal structure. d) Powder XRD pattern of room-temperature $Li_4(OH)_3Br$ produced through the 250 °C annealing route and corresponding Rietveld refinement using the predicted crystal structure. The resulting difference plot is provided beneath the data. A R_{wp} of 11.6 % is obtained using the crystallographic information provided in Table 3.2 for the refinement. Bragg peaks arising from the Pmnm crystal structure are indicated with ticks. The unrefined minority peaks likely correspond to metastable quenched $Li_3(OH)_2Br$.*

3.3.7 Latent Heat of $Li_4(OH)_3Br$

DSC was employed to study the thermal behaviour of $Li_4(OH)_3Br$. The 75 mol % LiOH samples undergoing the 250 °C anneal were chosen as the purest samples. For comparison, samples exhibiting the hydrated $P2_1/m$ phase were also investigated. In each instance, a small amount of

Table 3.2: Crystallographic parameters for the *Pmnm* structure of $Li_4(OH)_3Br$ at room temperature produced via the 250 °C anneal route, from the fit shown in Figure 3.10d. Refined parameters are indicated with errors in parentheses.

a (Å)	10.3761(11)				
b (Å)	5.3028(5)				
c (Å)	5.2681(5)				
V (Å^3)	289.86(5)				
Atom	Wyckoff position	x	y	z	Occupancy
Br1	2b	0.25	0.3727(8)	0.75	1
O1	4f	-0.02508	0.12415	0.25	1
O2	2a	0.25	-0.05675	0.25	1
Li1	8g	0.61587	-0.053665	0.5171	1
H1	4f	-0.05934	0.2956	0.25	1
H2	2a	0.25	0.75881	0.25	1

Table 3.3: Lattice parameters determined from Rietveld refinements of $Li_4(OH)_3Br$ at room temperature and 250 °C. Errors are provided in parentheses.

	Room temperature	250 °C (*in-situ*)
a (Å)	10.3761(11)	10.41106(17)
b (Å)	5.3028(5)	5.30442(7)
c (Å)	5.2681(5)	5.27854(7)

powder (< 2.5 mg) was hermetically sealed in an aluminium pan in an argon glovebox, and samples were measured heating and cooling between 25 °C and 400 °C at 5 °C min^{-1}. Measurements are shown in Figure 3.11. The DSC behaviour for the hydrated sample aligns with that seen in the VT-XRD: a small endothermic peak corresponding to dehydration is observed at $\sim$ 175 °C (Figure 3.11a), resulting in samples containing a mixture of $Li_4(OH)_3Br$ and Li_2OHBr. At $\sim$ 230 °C, the Li_2OHBr converts to $Li_3(OH)_2Br$, indicated by another endothermic peak (Figure 3.11b). The signal around 280 °C appears to be a superposition of endothermic peaks. In Section 3.3.1, it was shown that experimentally $Li_3(OH)_2Br$ bypasses the formation of $Li_4(OH)_3Br$ shown on the phase diagram above 280 °C, instead melting directly, and so the DSC peaks occurring around 280 °C may correspond to melting of the remaining $Li_3(OH)_2Br$, and melting of the $Li_4(OH)_3Br$.

In DSC of the *Pmnm* $Li_4(OH)_3Br$ (Figure 3.11bii), the peaks corresponding to the formation and decomposition of $Li_3(OH)_2Br$ only appear very weakly in the first heating cycle. If fully pure $Li_4(OH)_3Br$, these peaks would not be expected to occur at all. Instead, the minor impurity phase observed in the annealed $Li_4(OH)_3Br$ samples likely transforms to $P6_3/mmc$ Li_3OH_2Br between $\sim$ 230 °C and $\sim$ 280 °C, giving rise to the small peaks seen.

The enthalpies associated with the combined collection of peaks between 275 °C and 295 °C are reported for each heating run in Table 3.4, consistent with the approach taken in literature. An enthalpy of 263 ±3 J g^{-1} is measured for the melting of the anhydrous *Pmnm* samples, surpassing values reported previously ($\leq$ 250 J g^{-1})[6,8,9]. Previous calculations which predicted a melting enthalpy of 804 J g^{-1} were based off incorrect phases, explaining the discrepancy with the value reported here. The theoretical melting enthalpy for the crystal structure proposed here-within was estimated to be 260 J g^{-1} (Figure A.5), which is in excellent agreement with experimental findings. However, once the *Pmnm* $Li_4(OH)_3Br$ has been melted and is cooled at 5 °C min^{-1} in the DSC, the sample undergoes non-equilibrium solidification, and the subsequent heating cycle gives rise to much stronger peaks associated with the non-equilibrium processes. Consequently, the measured enthalpy change decreases considerably, as the fraction of material undergoing the high-enthalpy $Li_4(OH)_3Br \rightarrow$ Liquid + LiOH transition decreases. This contrast between the first and second heating cycle is apparent in the difference in enthalpy values reported in Table 3.4. Although this suggests higher enthalpies than previously reported may be obtainable, this is not practically relevant without an approach to ensure in-use equilibrium solidification.

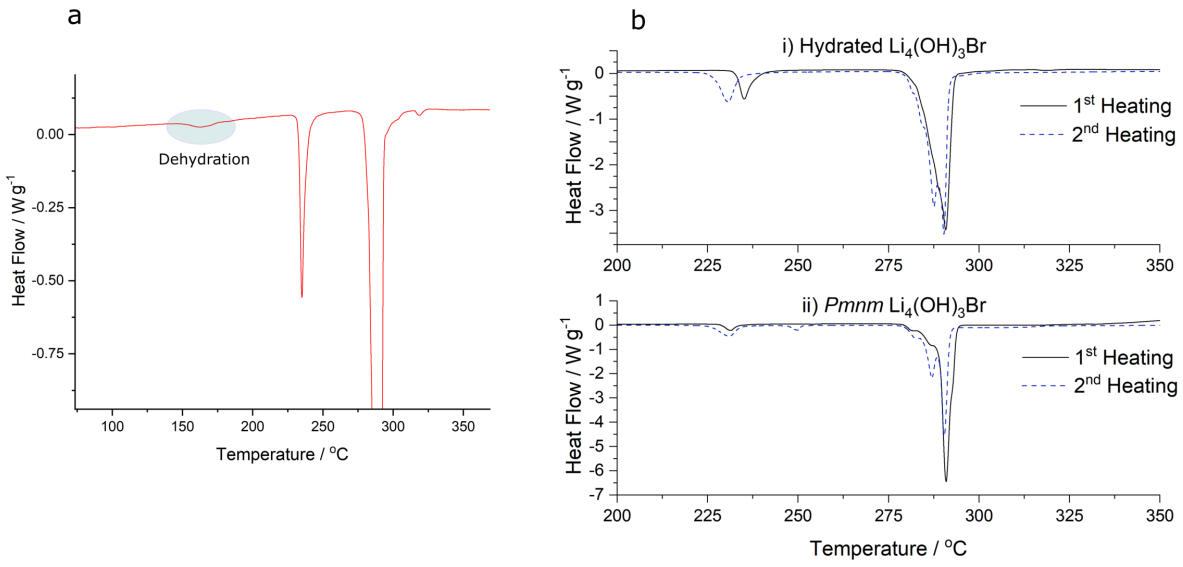

Figure 3.11: *Latent Heat Storage of $Li_4(OH)_3Br$. a) Magnification of DSC of the first heating cycle of hydrated $Li_4(OH)_3Br$, showing a small peak corresponding to dehydration between* 150 °C *and* 175 °C. *b) DSC heating profiles of i) hydrated $Li_4(OH)_3Br$, and ii) Pmnm $Li_4(OH)_3Br$, showing various endothermic processes occurring between* 200 °C *and* 350 °C. *Two heating cycles are shown in each case. The 2nd heating cycle of the Pmnm $Li_4(OH)_3Br$ varies from the 1st due to the non-equilibrium solidification which occurs after the 1st heating cycle.*

Table 3.4: Phase transition enthalpies for the $Li_4(OH)_3Br$ samples shown in Figure 3.11. Errors of 1% are expected for the reported enthalpy values.

Sample		**Enthalpy of phase transition / J g^{-1}**	
		230 °C	275 - 295 °C
Hydrated	1st Heating	31	231
	2nd Heating	39	229
Pmnm	1st Heating	12	263
	2nd Heating	29	200

3.3.8 Phase Diagram Implications

A final important consideration is the implications of this chapter's findings on the proposed LiBr-LiOH phase diagram.

Mahroug *et al.* used DSC peaks to propose a phase diagram in which undefined phase transitions occur at $\sim$ 230 °C and $\sim$ 280 °C for compositions with 75 mol % LiOH or higher[9]. The inclusion of these phase fields implies polymorphs of $Li_4(OH)_3Br$ exist, although this is not something explicitly discussed in their study. This work in this thesis, however, indicates that the phase transition at 230 °C does not belong on the phase diagram, as the DSC peak which provides the basis of its inclusion, arises as a result of non-equilibrium solidification. Specifically, the DSC peak occurs upon heating when $Li_3(OH)_2Br$ forms from the $Li_4(OH)_3Br$-Li_2OHBr mixture found in furnace-cooled samples. Li_2OHBr is also present in furnace-cooled samples of 80 mol % LiOH samples (Figure 3.12), supporting this conclusion for other compositions where this transition is plotted.

It might similarly be expected that the phase boundary Mahroug included at 280 °C is also a result of non-equilibrium processes appearing in DSC measurements. In this instance, the DSC peaks might be associated with the melting of the $Li_3(OH)_2Br$ present in samples above 230 °C, which occurs around 280 °C. However, further consideration may be required for the high-temperature portion of the phase diagram. Notably, diffraction patterns from furnace-cooled 75 mol % and 80 mol % LiOH samples cannot be fitted using solely the $Li_4(OH)_3Br$, Li_2OHBr and LiOH phases, due to unexplained intensity remaining. This may suggest that another phase field exists, or alternatively could be a further consequence of non-equilibrium solidification. Studying this high temperature polymorph region ($\sim$ 280 °C - 290 °C) is more challenging than the other phase field due to the narrow temperature range available prior to melting. To try and mitigate

impacts of non-equilibrium solidification, anneals of quenched 75 mol % and 80 mol % LiOH samples were carried out at 284 °C for 24 hours, followed by quenching to room temperature, to try and retain the indicated phase field to room temperature. The resulting diffraction patterns differed from those of samples annealed at 250 °C, indicating the possibility of a polymorph or another phase field in this region (Figure 3.12). Any additional phase transitions here, whether equilibrium or non-equilibrium processes, will also impact the observed melting enthalpy of $Li_4(OH)_3Br$. In the DSC profiles in Figure 3.11b, it is possible to see a third, minor peak in addition to the 2 main peaks assigned to the melting of $Li_3(OH)_2Br$ and melting of $Li_4(OH)_3Br$. It is possible that this third peak corresponds to a phase transition associated with these findings. However, the narrow temperature range and slow solid-state kinetics suggest that the extent of the transformation occurring within the timescale of DSC heating measurements prior to melting is limited. Thus, the melting enthalpy reported in this work represents a close approximation to the true melting enthalpy of the *Pmnm* $Li_4(OH)_3Br$ phase. To understand the full impact of a potential polymorph, further investigation into the high-temperature portion of the phase diagram will be necessary.

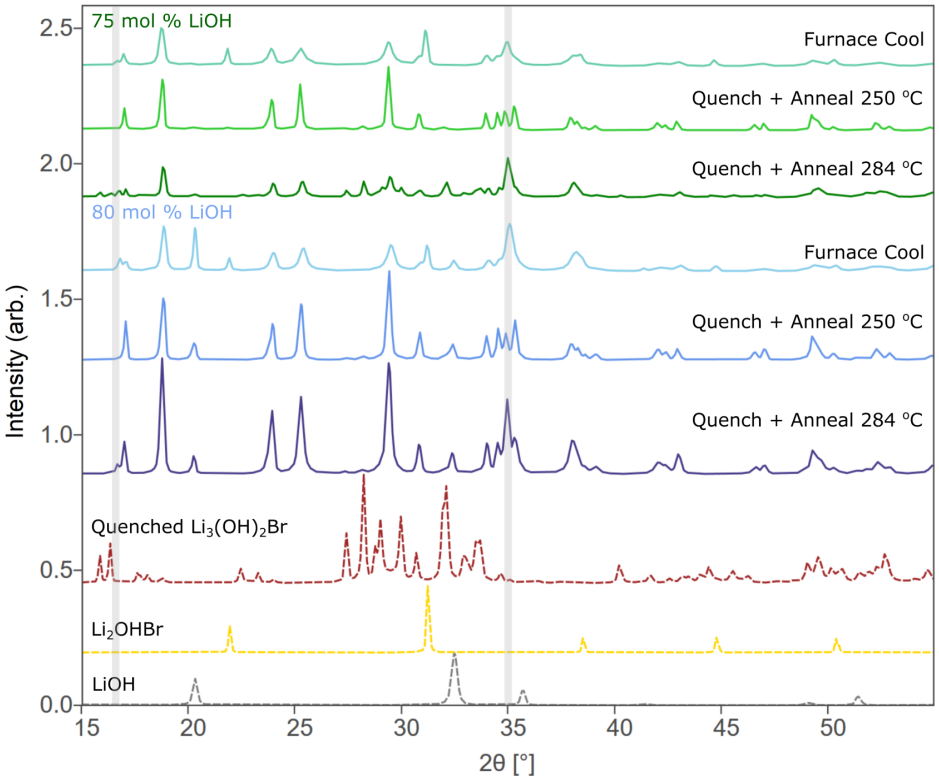

Figure 3.12: *Comparison of XRD patterns for samples undergoing different heat treatments. Unexplained peaks (highlighted) observed in furnace-cooled samples may be a result of non-equilibrium solidification, however their presence in samples annealed at* 284 °C *indicates that another phase field may exist. Further investigation will be required to fully understand this region of the phase diagram.*

3.4 Summary and Outlook

In this chapter, the peritectic phase $Li_4(OH)_3Br$ and high-temperature phase $Li_3(OH)_2Br$ have been investigated. In doing so, previous misconceptions have been clarified, and the first proper characterisations provided. Diffraction studies suggest that $Li_3(OH)_2Br$ forms a phase with a hexagonal unit cell belonging to the $P6_3/mmc$ space group between $\sim$ 225 °C and $\sim$ 275 °C, and lattice parameters of $a = b = 6.572$ Å and $c = 10.746$ Å at 250 °C. MD indicates that the structure contains cage-like structures of lithium, in which intra-cage diffusion is facile. A macroscopic ionic conductivity of 0.12 S cm^{-1} is measured at 250 °C, which would extrapolate to 5×10^{-4} S cm^{-1} upon retention to room temperature. However, attempts to stabilise this phase were not successful, resulting in a different metastable state with worse ionic conductivity.

It is found that the crystal structure for $Li_4(OH)_3Br$ established in literature in fact

corresponds to a metastable hydrated state, which ceases to exist upon heating to $\sim 175\,^{\circ}\mathrm{C}$. Samples of the thermodynamically-stable $Li_4(OH)_3Br$ phase were synthesised via annealing and investigated with respect to their application in TES. An orthorhombic crystal structure with lattice parameters of a = 10.38 Å, b = 5.30 Å, c = 5.27 Å and the *Pmnm* space group is found through diffraction studies, and a potential crystal structure is suggested with the help of theoretical modelling. These findings indicate that previous calculations for the melting enthalpy of $Li_4(OH)_3Br$ are not applicable. An experimental melting enthalpy of 263 ± 3 J g^{-1} is found for $Li_4(OH)_3Br$, in good agreement with calculations for the proposed $Li_4(OH)_3Br$ crystal structure reported herein. Discrepancies with previous experimental reports for the melting enthalpy of $Li_4(OH)_3Br$ ($\leq 250\,^{\circ}\mathrm{C}$ J g^{-1}) arise due to the tendency of peritectic compounds to undergo non-equilibrium solidification, exemplified by the presence of other phases in samples prior to anneals. Although the experimentally-observed latent heats still represent substantial energy storage capabilities, phase segregation could pose challenges to the long-term cycling of $Li_4(OH)_3Br$. This issue may need to be addressed through mitigating strategies such as periodic annealing, stirring or encapsulation.

If $Li_4(OH)_3Br$ is to be considered further as a candidate PCM for TES, future work should focus on better understanding the high-temperature portion of the phase diagram, such that solidification can be understood better and potentially controlled. Approaches to promote equilibrium solidification, perhaps through the use of nucleating agents or optimised cooling conditions could be explored, and further characterisation of the $Li_4(OH)_3Br$ phase, such as its thermal conductivity, will be necessary.

Chapter 4

Microstructure and Purity Control of Antiperovskite Solid Electrolytes

Contents

4.1 Introduction

The impact of grain boundaries on conductivity is a topic often at the centre of discussions on antiperovskite electrolytes[52,65,86,107,108,124,182,183]. Although most studies investigate cold-pressed pellets of antiperovskite powders, a few studies have tried to exploit the larger grain sizes formed in a melt-casting synthesis[86,107]. Zheng *et al.* compared samples of Li_2OHBr which had been cold-pressed, hot-pressed and melt-cast, and attempted to deconvolute the bulk and

grain boundary contributions to conductivity by fitting two semicircles to Nyquist plots[107]. A similar activation energy of ~ 0.54 eV was found for the bulk component in all samples. The grain boundary contribution was least detrimental in the melt-cast samples, with an activation energy of 0.82 eV. Zheng *et al.* concluded that the ionic conductivity of Li_2OHBr is limited by its grain boundaries at room temperature, and the bulk conductivity only becomes limiting at elevated temperatures. Lee *et al.* compared melt-cast samples quenched to room temperature with samples cooled at $1\,^{\circ}C\ min^{-1}$, and found a conductivity 1.5 times higher in the latter case, believed to result from bigger grains[86]. Only the purity of the quenched samples was considered in this work. Nonetheless, these findings suggest that further improvements to ionic conductivity may be possible through complete removal of grain boundaries. One approach to tackle this problem is through the synthesis of single crystal Li_2OHBr. In addition to establishing the bulk conductivity of Li_2OHBr, this would enable investigation into the impact of Li_2OHBr grain boundaries on cycling performance, for example through a CCD study. With access to low porosity single crystals, it would also be possible to conduct an investigation into the impacts of surface defects and solid electrolyte-lithium anode interface quality on lithium growth, without the influence of other microstructural features. Furthermore, the production of high-quality single crystals would open up the possibility of using single-crystal neutron diffraction and single-crystal NMR techniques to address fundamental questions about the crystal structure (occupancy and local ordering) and dynamics (defect mobility) in antiperovskites. One of the aims of this work was therefore to produce centimetre-scale single crystals of Li_2OHBr.

Single crystal growth techniques can broadly be separated into 4 categories:

- Melt growth methods in which the material is melted and crystallised in a controlled manner
- Solution growth methods in which the desired material is initially dissolved in a solvent at high temperatures, followed by cooling or evaporation of the solvent to crystallise the material
- Vapour growth methods in which the material is sublimed and condensed as single crystals
- Epitaxial growth methods in which thin films are typically deposited on a substrate with a similar lattice structure

In order to produce large centimetre-scale crystals, melt growth techniques are typi-

cally required. Melt growth methods typically involve controlled growth of a small seed crystal. In Czochralski growth, a small seed crystal is dipped into molten material and slowly pulled out whilst rotating the crystal, allowing for the growth of large crystals from materials with high melting points. For materials with lower melting points or challenging crystal structures, Bridgman-style growths are often required. In this instance, the material is melted in a crucible with a temperature gradient, and slowly cooled such that crystal growth progresses from one end of the crucible to the other. Bridgman growths are more appropriate for materials containing lithium, as the enclosed system prevents the loss of volatile lithium which would lead to composition changes and potential impurities.

In a 2019 Bachelor's thesis from the Massachusetts Institute of Technology, Eiler attempted to synthesise Li_2OHCl single crystals through various Bridgman growths using a laser diode optical floating zone furnace[184]. Opaque white samples containing large craters down the centre were produced in each instance. In spite of the unpromising appearance, some diffraction spots were observed in Laue diffraction measurements, suggesting large crystallites are present, and that single crystal growth may be possible with further optimisation. It was speculated that this may be achievable by using even slower cooling rates.

Single crystal growth of incongruently-melting samples, in which the sample does not directly melt into a single liquid phase, is challenging using melt growth techniques. Proposed LiBr-LiOH phase diagrams would suggest that this is the case for Li_2OHBr. The minor DSC prepeak observed prior to melting of Li_2OHBr (Figure 4.2a) is attributed to a phase transition, indicating a narrow phase field between $\sim 246\,^{\circ}C$ and $\sim 251\,^{\circ}C$ (Figure 1.11d). Sangster proposes a "LiBr + $Li_4(OH)_3Br$" phase field, whereas Mahroug suggests "LiBr + $Li_3(OH)_2Br$". Although the speculated phase field differs between the two, both would have Li_2OHBr as a peritectoid phase. However, direct evidence of a high temperature phase field has not been reported, and other work has claimed direct melting of Li_2OHBr[107]. Given the other inaccuracies in the phase diagram established in Chapter 3, and the absence of more than DSC measurements to support the proposals, conclusive statements cannot be made.

There has been alternative speculation to the origin of this DSC prepeak in lithium bromide antiperovskites[86,114,185]. These theories are centred on the presence of an order-disorder transition, termed "sub-lattice melting", as has been reported for thermal transitions observed in

other antiperovskite materials[101,186,187]. In this instance, no phase change would be expected to occur in this temperature region, and single crystal growth of Li_2OHBr may be expected to be less problematic. The high and narrow temperature range in which this transition occurs means it is challenging to establish which, if any, scenario is correct.

In this chapter, initial attempts at single crystal growth by directional solidification are presented, followed by investigations into purity and microstructure control of Li_2OHBr. Using this improved understanding, a synthesis protocol is designed which produces large grains of Li_2OHBr with a porous dendritic microstructure. Incongruent solidification makes producing good quality single crystals challenging. Finally, the synthesis and behaviour of the related antiperovskite, $Li_5(OH)_2Br_3$, is briefly investigated. Although theoretically lying in the LiBr-LiOH binary system, synthesis of $Li_5(OH)_2Br_3$ has not previously been understood, which is also found to arise from challenges associated with incongruent solidification.

4.2 Experimental Methods

4.2.1 XRD and Refinements

Most XRD measurements were taken using the powder-XRD method outlined in Section 2.2.1. For XRD measurements of Li_2OHBr pellets in Figure 4.6, sample surfaces were aligned with the top of a SS recession holder using grease and a glass slide.

For the refinements of $Li_5(OH)_2Br_3$, the structural model proposed by Koedtruad *et al.* in reference[141] was used, which omits hydrogen due to its poor X-ray scattering ability. The occupancies were fixed to give a precise stoichiometry of $LiBr(Li_2OBr)_2$. Only the unit cell parameters were allowed to refine from the starting structural model.

4.3 Results and Discussion

4.3.1 Horizontal Directional Solidification of Li_2OHBr

Prior to investigations into the LiBr-LiOH phase diagram, a horizontal directional solidification (HDS) approach was investigated for growing antiperovskite single crystals. Also know as Bagdasarov growth, this is a variation of the Bridgman method in which the crucible is oriented horizontally. As shown schematically in Figure 4.1a, the crucible contains a pointed end designed to act as a single nucleation site from which a single crystal seeds. The molten material is solidified from the seed end by moving a controlled temperature gradient horizontally across the sample. This may be achieved by either moving the crucible through a furnace, or by adjustment of zones in a multizone furnace.

A homemade HDS set-up was made using a tube furnace placed on rails (Figure 4.1b,c). In order to load the samples avoiding air exposure, the furnace tubing had to be cut to a length able to fit inside of glovebox antechambers. The sample was then loaded in the glovebox atmosphere and the tube ends sealed using swagelock attachments. The tube could then be taken out of the glovebox and connected to an argon supply once in the furnace. The tube furnace was mounted on wheels and placed on railings such that it could be move along 1 dimension. The furnace was attached to a motor via a pulley system which moved the furnace over the tube. Slow pull rates (0.1-10 mm hr^{-1}) are necessary to ensure gradual growth with a stable solid-liquid interface, avoid additional nucleation and minimise thermal stresses. As shown in Figure 4.1d, the setup used here produced a pull rate of $\sim$ 1 mm h^{-1}. Since a multizone furnace was not available, the growth relies on the natural temperature gradient which exists in tube furnaces between the centre and ends. The shortened length of quartz tube, required for glovebox sample loading, meant that it was important to accurately determine the temperature gradient in the furnace and find conditions such that a sample is able to go from the molten state to solidified within the range of furnace movement available. The temperature gradient in the tube was measured using a temperature probe by moving the furnace in 5 mm increments with a 5 minute stabilisation period between each measurement. The temperature measured as a function of distance from the furnace centre is plotted for a furnace set to 265 °C in Figure 4.1e. The sample growth was then conducted in the shaded region, so that it passed through its melting point (determined from DSC) during the HDS process. Combining the furnace speed and temperature

gradient gives an average cooling rate of 0.42 °C hr^{-1}. The heating procedure is shown in Figure 4.1f. Prior to solidification, the sample was melted for 2 hours to ensure homogeneity.

Several crucibles were explored for this work. Crucibles are often made from foils of refractory materials which offer the advantages of customisable shapes and easy removal after crystal growth. Crucibles made by folding molybdenum foil were trialled, but led to leakage of the molten material (Figure 4.1g). In attempts to solve this problem, an Inconel crucible was 3D printed (Figure 4.1h). The inside of the crucible was polished using SiC grinding papers to try and remove surface roughness which may act as nucleation sites.

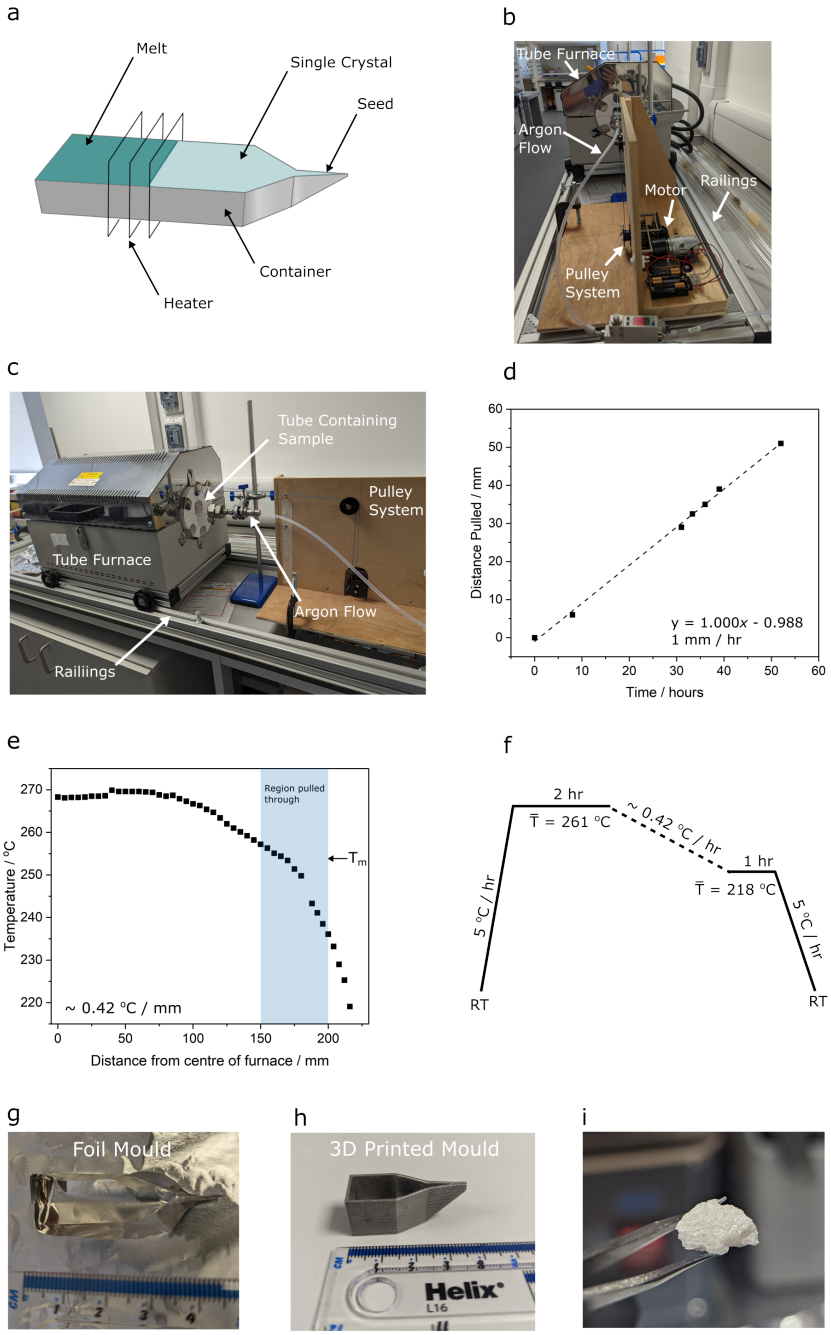

Figure 4.1: *Horizontal Directional Solidification. a) Diagram of HDS growth. A single crystal is grown horizontally, starting from a single seed point. b) Side view of the HDS setup used in this work. c) Front view of the HDS setup. d) Rate of furnace movement produced by the setup. e) Temperature gradient in the furnace during growth. f) Temperature profile of the sample during HDS growth. Note that the average temperature experienced by the 4 cm crucible is shown, since there is spatial variation in the furnace temperature. g) Molybdenum foil crucible tested as a mould. h) 3D printed Inconel crucible tested as a mould. i) Example sample after HDS growth. The opaqueness indicates polycrystallinity.*

Several variations in the HDS setup were tested, without success. Opaque white samples

of polycrystalline Li_2OHBr were produced. In spite of the attempts to polish the crucible surface, it is likely that the surface of the 3D printed crucible contained nucleation sites due to the surface porosity inherent in 3D printed metals. It is also believed that the temperature gradient offered by the tube furnace was insufficient, and more success would be found using a multizone furnace as conventionally used in Bridgman growths. A steeper temperature gradient would produce a more stable solid-liquid interface which is important to growing defect-free crystals. Additionally, if the phase diagrams suggested by Sangster or Mahroug are correct, then single crystal growth may not be successful due to the incongruent melting of Li_2OHBr, as growing peritectoid single crystals from two-phase fields is expected to be extremely challenging.

4.3.2 Cooling Rate and Phase Purity of Li_2OHBr

Sangster believed Li_2OHBr to form via the peritectoid reaction $2LiBr + Li_4(OH)_3Br \rightarrow 3Li_2OHBr$ upon cooling, whereas Mahroug *et al.* incorporated $Li_3(OH)_2Br$ into their phase diagram and suggested an alternative reaction, $LiBr + Li_3(OH)_2Br \rightarrow 2Li_2OHBr$. The work in this thesis demonstrates the existence of $Li_3(OH)_2Br$, and so favours the second of these scenarios. Regardless, Li_2OHBr is proposed to be a peritectoid phase, and so is expected to suffer from the slow kinetics of solid-solid reactions, which could lead to incomplete transformation of the starting phases when synthesised via this two-phase field. If true, the phase-purity of obtained samples will depend on cooling conditions, and the synthesis procedure chosen will be pivotal to avoiding impurities. Despite the prevalence of Li_2OHBr research in the battery community, the importance of synthesis conditions does not seem to be acknowledged in literature. In some reports, synthesis routes allow samples to cool naturally from the molten state[107,118], others pour molten sample onto foils to cool quickly[97,108], and in some instances cooling rates are completely omitted[103].

Evidence of minor impurity phases can frequently be seen in reported Li_2OHBr XRD patterns[97,105,108], the potential impacts of which could be wide-ranging. Furthermore, the effects of amorphous impurities, which may be undetectable by laboratory X-ray diffractometers, is often underappreciated, as was recently demonstrated for the sodium-based antiperovskite Na_3OBr[188]. A large range of experimental room-temperature ionic conductivities have been reported for Li_2OHBr (1×10^{-7} S cm^{-1} – 6×10^{-6} S cm^{-1} [86,97,102–106,108]). This large variation has often

been attributed to the presence of grain boundaries in samples, but may also be impacted by the presence of less (or more) conducting secondary phases, and increased tortuosity of conduction pathways. The inclusion of secondary particles will also be expected to have an effect on the mechanical properties of the solid electrolyte, which becomes important when considering crack initiation and lithium filament growth which can lead to the failure of batteries[47,189,190]. As such, it is important that efforts are made to ensure phase purity of electrolytes.

Directly verifying and studying a potential high-temperature phase field is very challenging due to its narrow temperature window. To try and understand the impact of cooling rate and identify additional phase fields, samples synthesised using three different cooling procedures were investigated. In the first scenario, molten sample was removed from the furnace (at 350 °C) to cool to room temperature quickly ($\sim 100\,^{\circ}\mathrm{C\ min^{-1}}$), termed "air-quenched" samples herein. The expected temperature range in which the LiBr + $Li_3(OH)_2Br$ phasefield occurs is very narrow ($\leq 5\,^{\circ}\mathrm{C}$), above which there is a narrow ($\sim 30\,^{\circ}\mathrm{C}$) window in which L + $Li_3(OH)_2Br$ exist, before becoming fully liquid at $\sim 280\,^{\circ}\mathrm{C}$. By cooling from the liquid state at high rates, it is hypothesised that sufficient undercooling can be achieved such that the Li_2OHBr phase nucleates directly from the melt, bypassing the two-phase solid region entirely. From this, pure Li_2OHBr samples would be expected. At the other extreme, a sample was cooled slowly from 350 °C to 200 °C over a 20 hour period ($0.125\,^{\circ}\mathrm{C\ min^{-1}}$), before allowing to furnace cool to room temperature ($\sim 5\,^{\circ}\mathrm{C\ min^{-1}}$). Significant formation of LiBr and $Li_3(OH)_2Br$ would be expected to occur during the extended period spent in the corresponding phase field, meaning it should be possible to identify in samples. Between these two scenarios, a sample was allowed to cool naturally in the furnace after heating ($\sim 5\,^{\circ}\mathrm{C\ min^{-1}}$), termed a furnace-cooled sample. DSC measurements were taken at a range of rates encompassing typical furnace cooling rates. In the DSC measurements, shown in Figure 4.2a, the DSC prepeak attributed to the two-phase solid field is observed in all instances, indicating that this transition will affect furnace-cooled samples.

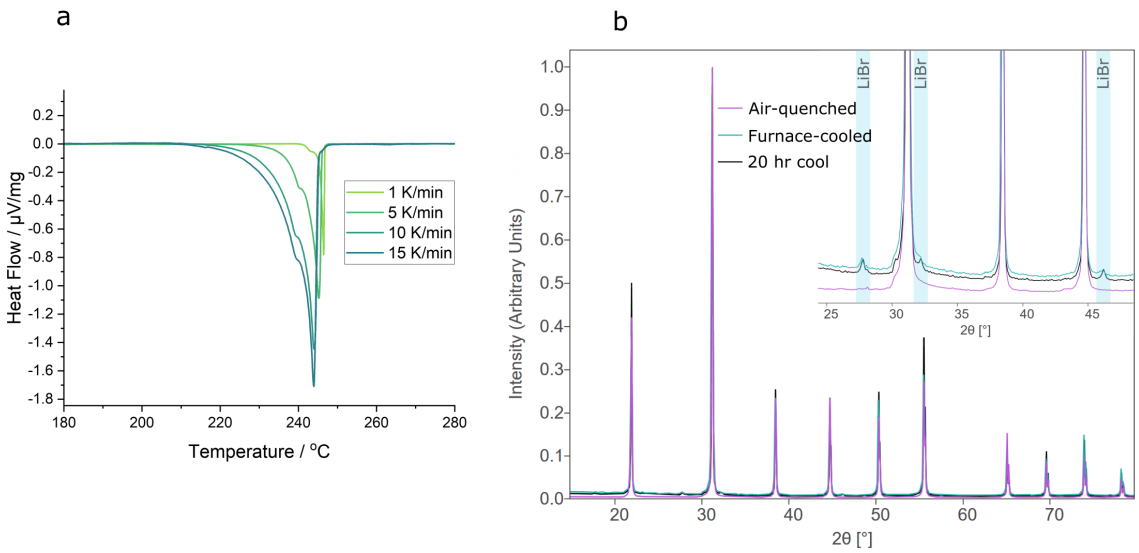

Figure 4.2: *Li_2OHBr synthesis. a) DSC curves of Li_2OHBr at different cooling rates between 1 and 15 °C min^{-1}. b) XRD spectra of Li_2OHBr synthesised using different cooling rates, with an inset showing the presence of LiBr impurity in the furnace and 20 hour cooled samples.*

As shown in the XRD patterns in Figure 4.2b, small impurity peaks corresponding to crystalline LiBr are present in the 20 hour and furnace-cooled samples of Li_2OHBr. On the contrary, the air-quenched samples nominally appear phase-pure in XRD. SEM images were taken of the bottom surface of pellets quenched in SS coin cell cases (Figure 4.3a-d). In some locations, a fine microstructure containing multiple phases can be seen, possibly corresponding to LiBr and $Li_3(OH)_2Br$ compositions. In the bulk, the microstructure appears single phase (Figure 4.4e). This may indicate that initial heterogeneous nucleation of the impurity phases occur on the mould surface during the brief time they are stable. As the sample quickly cools to a greater undercooling where Li_2OHBr is stable, Li_2OHBr grains nucleate which grow to make up most of the sample. The impurity phases do not appear in the XRD of quenched samples as they only have a low volume fraction.

In the 20 hour cooled samples, a coarse microstructure is produced, enabling EDX mapping and analysis to be carried out. This is shown in Figure 4.3e. As was also determined in the XRD, LiBr is found, forming blocky particles dispersed in the microstructure. Additionally, a dark branched phase which is rich in oxygen and deficient in bromine is observed, which could correspond to the $Li_3(OH)_2Br$ phase expected to form with the LiBr between $\sim$ 246 °C and $\sim$ 251 °C. The ratio of O:Br in these regions is 2.17 ± 0.34:1, close to the theoretical ratio of 2:1. A finer eutectic structure can also be seen between these primary particles. There is no direct

evidence of $Li_3(OH)_2Br$ in the XRD patterns, which could be due to that small amount of phase becoming amorphous at room temperature (as a consequence of being unstable at room temperature, and experiencing high levels of strain due to constraints from surrounding material). The presence of amorphous $Li_3(OH)_2Br$ might be expected to have negative implications on the conductivity of samples, as was indicated by the electrochemical measurements of metastable $Li_3(OH)_2Br$ in Chapter 3. To verify that impurities were not due to reactions with the crucible, both alumina and SS crucible syntheses were tested, which yielded the same behaviour. Compositions surrounding the Li_2OHBr stoichiometry were also investigated, examples of which are provided in Appendix B.1. The relationship between cooling conditions and impurity formation indicate that Li_2OHBr does not melt congruently and support speculations that it may be a peritectoid phase, leading to non-equilibrium solidification.

As such, these results demonstrate the importance of synthesis conditions on sample purity. A reliable approach to ensuring phase purity when synthesising Li_2OHBr from the melt is through the employment of high cooling rates. It may also be desirable to use subsequent heat treatments just below the peritectoid transformation temperature ($\sim 246\,^{\circ}C$), providing thermal energy and increased diffusion for equilibrium conditions to be achieved. The fine microstructure produced by fast cooling means that only short diffusion distances are required. Alternatively, it may be possible to mechanically remove impurity, such as by polishing the faces of samples, since impurity nucleation was observed to predominantly occur heterogeneously on the mould walls during cooling. A different approach to avoiding the complications of the peritectoid reaction is a room-temperature ball milling synthesis as demonstrated by Sugumar *et al.*[104], although this may not be desirable due to the detrimental nature of grain boundaries on performance[86,108,180,191].

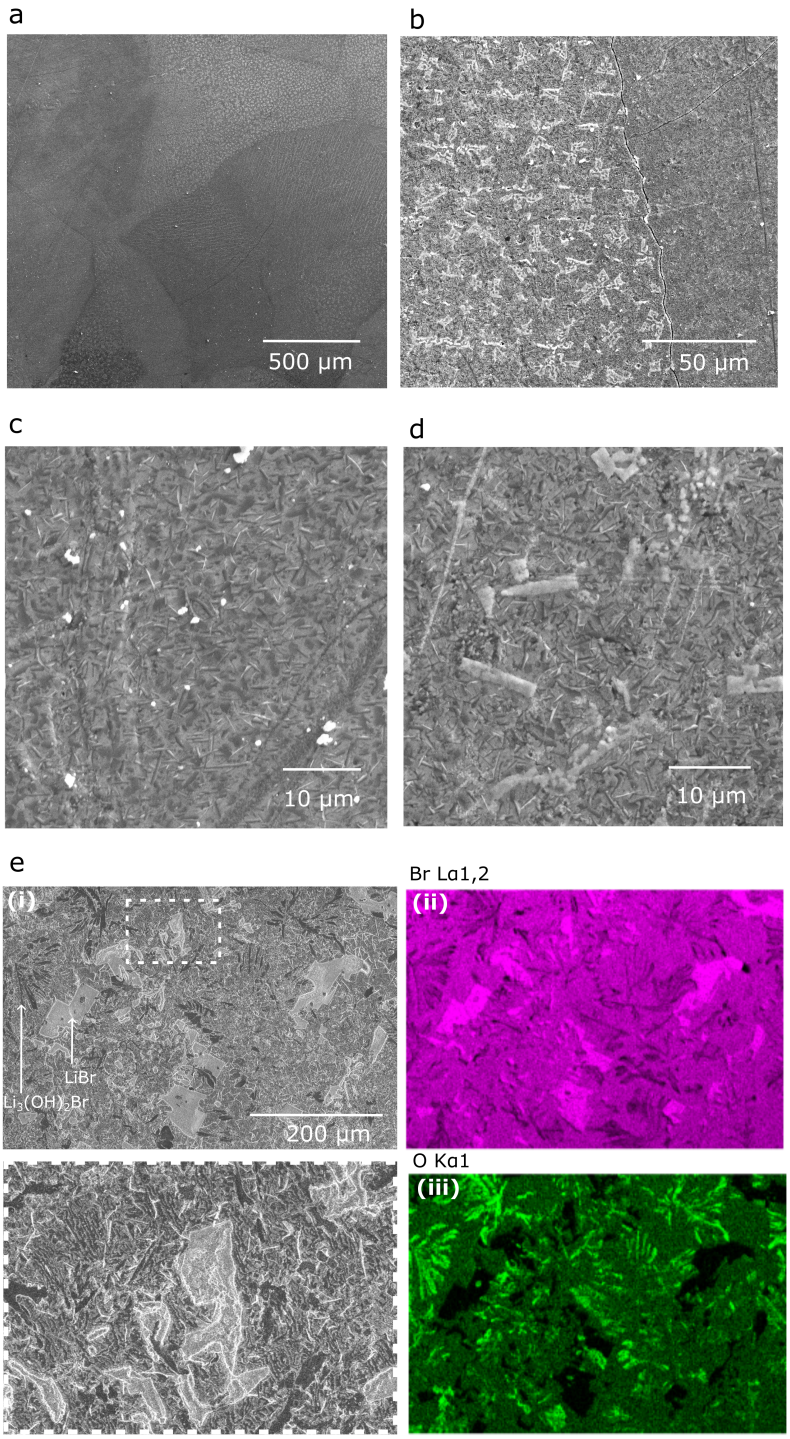

Figure 4.3: *Li_2OHBr microstructure. a-d) SEM images of the bottom surface of fast-cooled Li_2OHBr pellets at a range of magnifications. White particles are believed to be LiBr. In (c) and (d) a fine-scale dark phase is also visible. e) SEM image and corresponding EDX mapping of the bottom of a 20-hour cooled Li_2OHBr pellet showing oxygen-rich and oxygen-free phases. The inset shows a close-up in which a eutectic microstructure matrix is visible.*

4.3.3 Microstructure Control of Li_2OHBr

In the previously-mentioned Li_2OHBr grain size studies by Lee and by Zheng, SEM images of fracture surfaces were used to indicate grain size in melt-cast Li_2OHBr samples[86,107]. Zheng *et al.* showed features of $\sim 50\ \mu m$ diameter, whereas Lee *et al.* claimed a much smaller grain size of $2-3\ \mu m$ in fast-cooled samples. These sizes differ substantially from the grain structure visible in the fast-cooled samples reported here, shown in optical and SEM images in Figure 4.4a-f. To verify the grain size, EBSD of a polished sample is shown in Figure 4.4g, confirming that the observed features correspond to grains with diameters around 1 mm. This grain size is large compared to desirable solid electrolyte thicknesses, and so grain boundaries are likely to have a minimal detrimental impact on ionic conductivity in these samples. It is possible that features previously attributed as grain boundaries, which were not studied by EBSD, in fact correspond to dendrite arms. Dendritic and cellular solidification was seen in the samples in this work, with arm spacings more comparable to previous grain size reports (Appendix B.2). Although different to grain boundaries, these interfaces may also impact the conductivity of samples. In previous computational work[52,65,86], common grain boundary angles typically observed in perovskites are modelled, which will not be applicable in the case of dendrite arm interfaces.

The ionic conductivity of a polished pellet, measured in a pouch cell with sputtered nickel contacts, was 1.39×10^{-6} S cm^{-1} (Figure B.5). This is in good agreement with previous reports for melt-cast Li_2OHBr. However, the pellets were very fragile and prone to breaking in cell preparation. Cracks can be seen along grain boundaries in SEM images, such as in Figure 4.4e, which can be expected to have detrimental impacts on cycling performance.

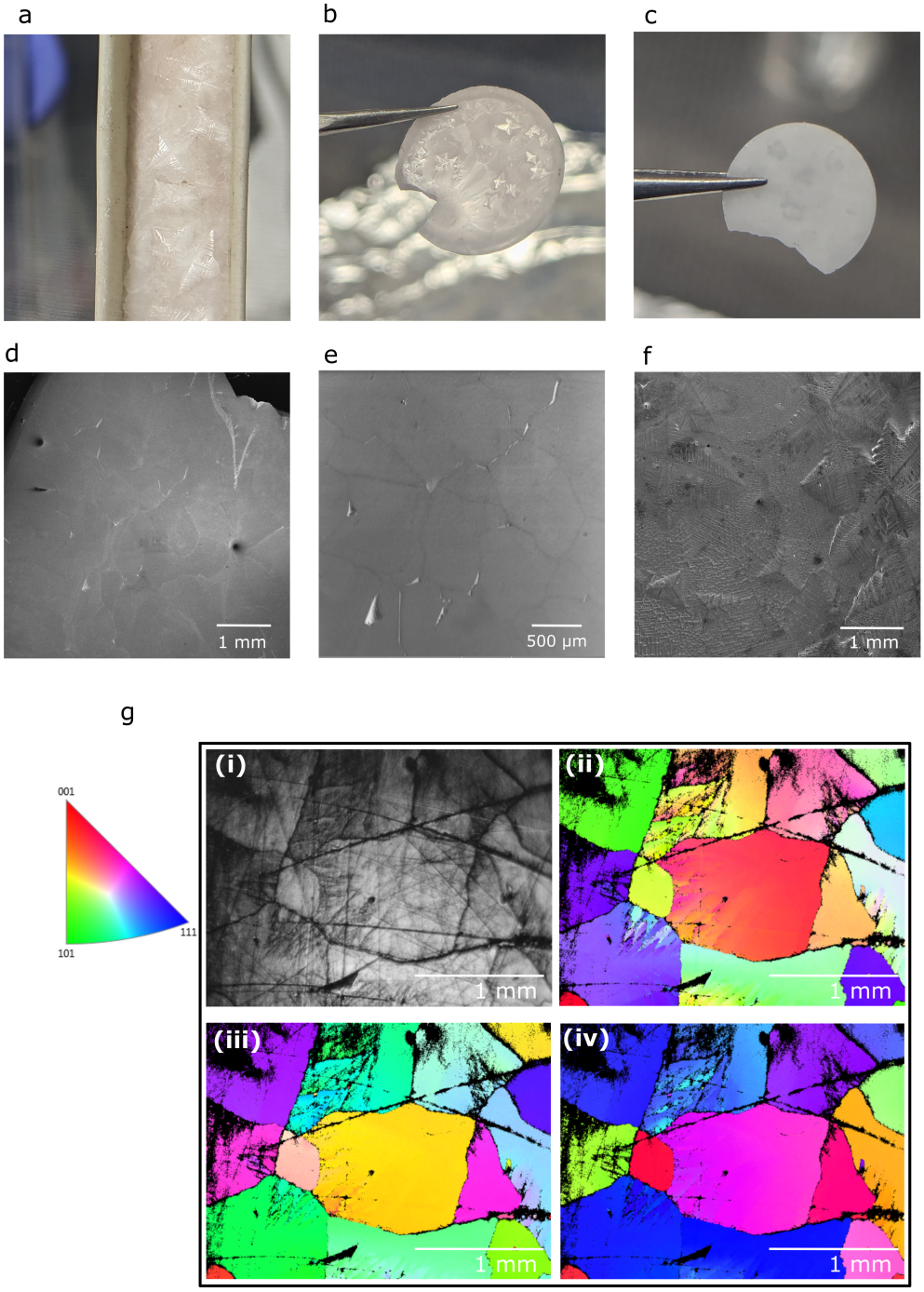

Figure 4.4: *Grain size in fast-cooled Li_2OHBr. Surface of samples produced in a) an alumina, and b) a SS crucible. c) The bottom surface of a pellet produced in a SS crucible. d,e) SEM images of polished pellets. f) SEM of the surface of a pellet. g) EBSD mapping of a polished pellet.*

To see whether the microstructure of samples could be improved, two synthesis ap-

proaches were tried where samples were grown in quartz tubes. Stoichiometric ratios of LiBr and LiOH were ground together, pressed into pellets and sealed in a quartz tube under vacuum, as shown in Figure 4.5a. Both a fast and slow-cooling protocol were investigated, the temperature profiles of which are shown in Figures 4.5b and 4.6a respectively. Samples were first homogenised at 350 °C (significantly above the liquidus temperature), cooled using the appropriate protocol, and finally annealed in the Li_2OHBr phase field to ensure phase purity and reduce defects.

In the slow-cooled sample, it was hoped that by minimising heterogeneous nucleation sites, it might be possible to slowly undercool the sample into the Li_2OHBr phase field to grow a single crystal without prior LiBr and $Li_3(OH)_2Br$ nucleation events. Quartz tubes offer several advantages over the alumina and SS moulds previously used, which may make this possible. First, the interior of the quartz tubes are smooth and without corners, reducing the risk of heterogeneous nucleation on the tube walls. Quartz is also very chemically inert, eliminating potential risks of impurities or nucleation sites arising from corrosion, for example. Finally, the samples were sealed under vacuum, which limits side reactions which may lead to impurities promoting nucleation. One end of the quartz tube was sealed to a sharp point to act as a seed site for a single nucleation event. The sharp tip is also able to dissipate heat more easily than the rest of the tube, mimicking directional solidification, with growth occurring from one end. Zone refinement of impurities may also occur. The use of a static setup minimises disturbances and vibrations which may cause unwanted nucleation. The slow cooling rate minimises thermal gradients which may induce crystallisation. After cooling to room temperature, the samples were removed by breaking the quartz tubing.

In the fast-cooled and annealed quartz tube sample, the grain structure is immediately evident (Figure 4.5c). A central shrinkage pipe formed down a large portion of the sample, making much of the rod unusable. Pellets of the non-hollow portion of the sample were cut using a slow saw and polished for EBSD, shown in Figure 4.5d,e. As with the original fast-cooled samples which had been cast in a mould and not undergone the subsequent annealing step, the samples had a $\sim$ 1 mm grain size and were still very fragile.

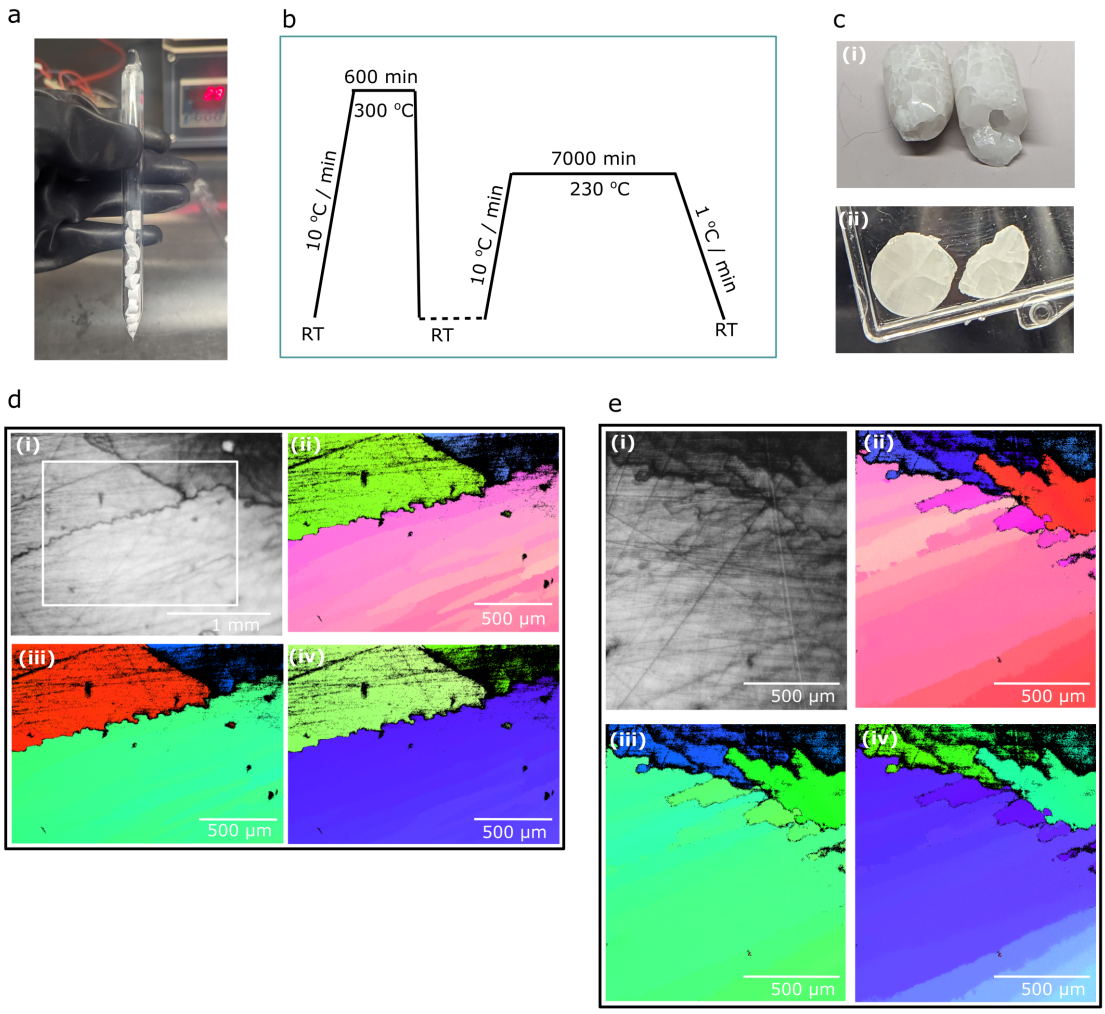

Figure 4.5: *Fast-cooled and annealed quartz growths. a) Pellets of LiBr-LiOH sealed in a quartz tube under vacuum, prepared for quartz growth attempts. b) Heating profile of fast-cooled and annealed quartz growth attempts. c) Sample (i) rod and (ii) pellets produced from the synthesis. d,e) EBSD maps of pellet surfaces showing large grains.*

For the slow-cooled and annealed quartz tube samples, robust rods of translucent Li_2OHBr were produced, with no visible grain boundaries (Figure 4.6b). The samples were cut into pellets and polished to 2500 grit using SiC papers, to produce transparent pellets as shown in Figure 4.6c. It was challenging to assess the grain structure of these slow-cooled samples using EBSD, as the transparent nature of the samples meant that aligning the sample for PECS could not be done using the laser mounting system. Additionally, the small area (d = 2.5 mm) prepared by the polishing would not enable characterisation of the entire pellet (d = 9 mm) without substantial preparation, and could not be applied to other geometries of sample.

A technique often used to identify and orientate single crystals is Laue diffraction. Here,

a polychromatic X-ray source probes a stationary crystal to quickly create a diffraction pattern of spots. Laue diffraction measurements were taken on pieces of sample from initial single crystal growth attempts at the University of Warwick with the help of Dr Daniel Mayoh. To protect the samples from air exposure under which the machine operates, samples were covered in a thin layer of Vaseline. Sharp diffraction spots were found, indicating a highly crystalline sample. By rastering over the surface of crystals, it was possible to see that large single crystals were being produced from the consistent diffraction pattern observed in each location. The sample could be oriented in the diffractometer to a specific crystallographic direction, and is shown in Figure 4.6d oriented along the [100] direction. The Vaseline was unable to protect samples from air exposure for long, leading to visible degradation of the crystal. Therefore, beyond proof of concept, Laue diffraction could not be used to verify each crystal in this work.

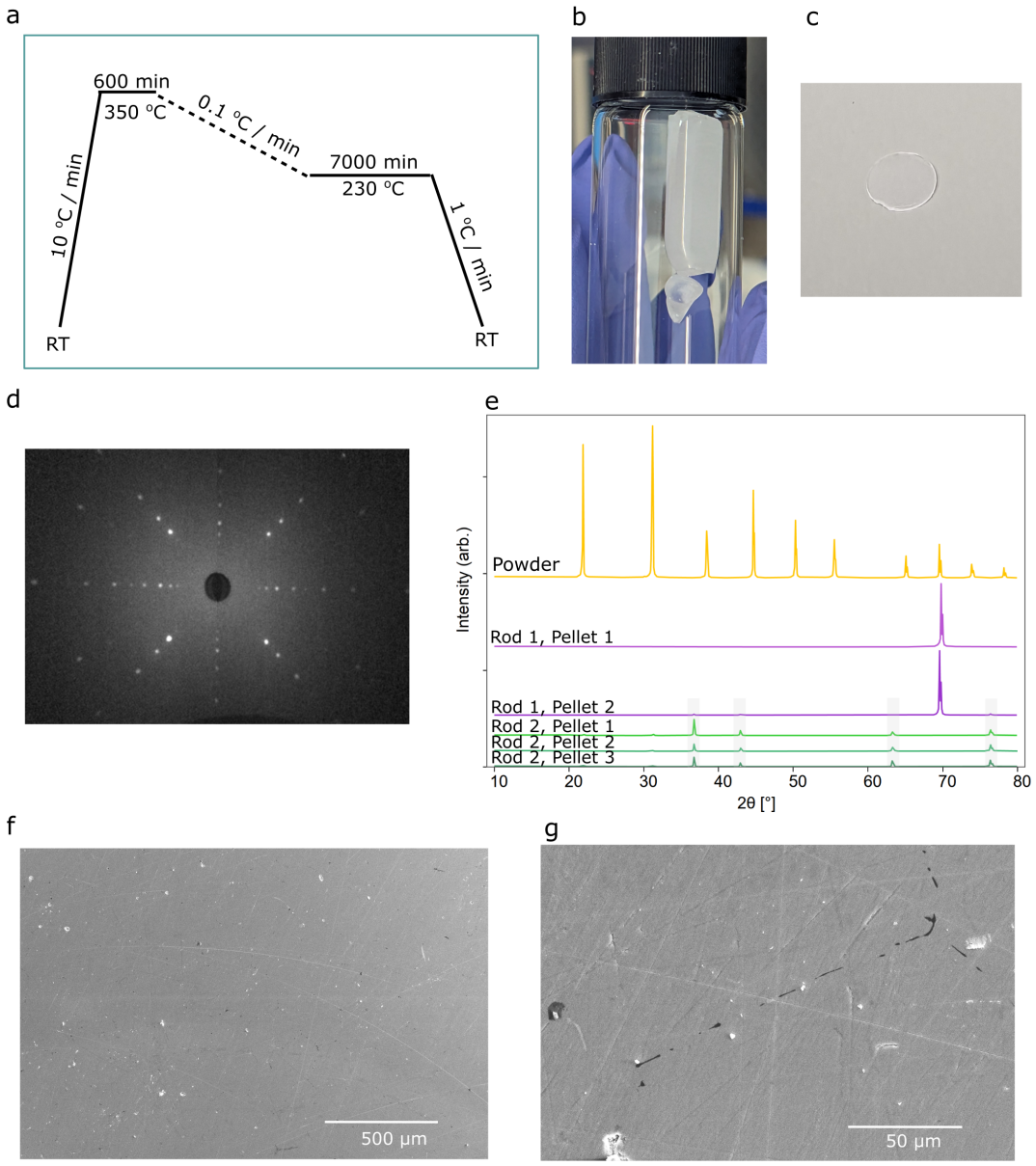

Figure 4.6: *Slow-cooled and annealed quartz growths. a) Heating profile of slow-cooled and annealed quartz growths. b) Rods of material produced from this protocol. c) Transparent polished pellet cut from the rod in (b). d) Laue diffraction pattern of large crystal of Li_2OHBr oriented along the [100] direction, showing sharp crystalline spots. e) XRD pattern of crushed sample showing no impurities, and XRD patterns of pellets from two different growths. Both pellets from rod 1 are aligned along the [112] direction, whereas the orientation of rod 2 does not result in any Bragg peaks. Note that the small highlighted peaks correspond to the SS recession holder the samples were measured in. f,g) SEM images of polished pellets, (g) showing a region with porosity.*

Theta-two theta XRD measurements taken under nitrogen atmosphere are shown in Figure 4.6e. As can be seen in the top powder XRD pattern of the crushed sample, the material

is phase pure, indicating that previous purity concerns have been avoided using this synthesis protocol. XRD measurements of several pellets cut from two different crystal growths are also shown. In the first sample, the [112] peak appears, indicating that this particular sample grew along an axis very close to the [112] direction. In the second sample, no peaks satisfy the Bragg conditions and so no antiperovskite peaks appear, indicating that the growth direction is not consistent between samples and there is no favourable crystal growth axis. An alternative diffraction setup, such as Laue diffraction, EBSD or using a four-circle XRD, would be required to determine the orientation of this sample.

Supporting that these samples are phase pure, SEM images from a polished pellet show a single-phase microstructure (Figure 4.6f,g). At high magnifications, fine dark features making up a broken network can be seen in some locations. This is believed to be porosity, responsible for the translucent rather than fully transparent appearance of the rods. This may correspond to shrinkage occurring during dendritic solidfication of the antiperovskite. This porosity was particularly bad towards the top of the rod and was assessed further using absorption contrast tomography (ACT). For this, a small piece of sample was attached to a tomography stub and coated with a thin layer of UV resin to protect from air exposure during measurements (Figure 4.7a). ACT was carried out by Dr Gareth Douglas at the University of Leicester, and analysed by Dr Pranay Shrestha at the University of Oxford. The 3D reconstruction, shown in Figure 4.7b and c, demonstrates the interconnected porosity network more clearly, revealing much larger pores than observed in the 2D cross-section of the previous sample. Although the porosity was only quantified as 4.4%, pore sizes of the same scale as desirable solid electrolyte thicknesses are present, making these samples impractical. EIS measurements of a sample in a pouch cell configuration yielded an ionic conductivity of 1.31×10^{-6} S cm^{-1}, indicating that no improvement to ionic conductivity was gained over the fast-cooled samples, as was hypothesised (Figure B.5).

The dendritic solidification, and hence porosity, may be a result of the high undercooling which was targeted to nucleate the Li_2OHBr phase without LiBr and $Li_3(OH)_2Br$ formation. Excessive undercooling can destabilise the solid-liquid interface, promoting dendritic rather than planar solidification. By employing a steep spatial temperature gradient in a directional solidification, it may be possible to suppress the growth of perturbations at the solid-liquid interface. Therefore, a better microstructure may be achievable using a Bridgman furnace, whereby both a slow cooling rate and a steep temperature gradient can simultaneously be applied. A Bridg-

man furnace was not available to test this hypothesis, and so the microstructure could not be improved further in this work.

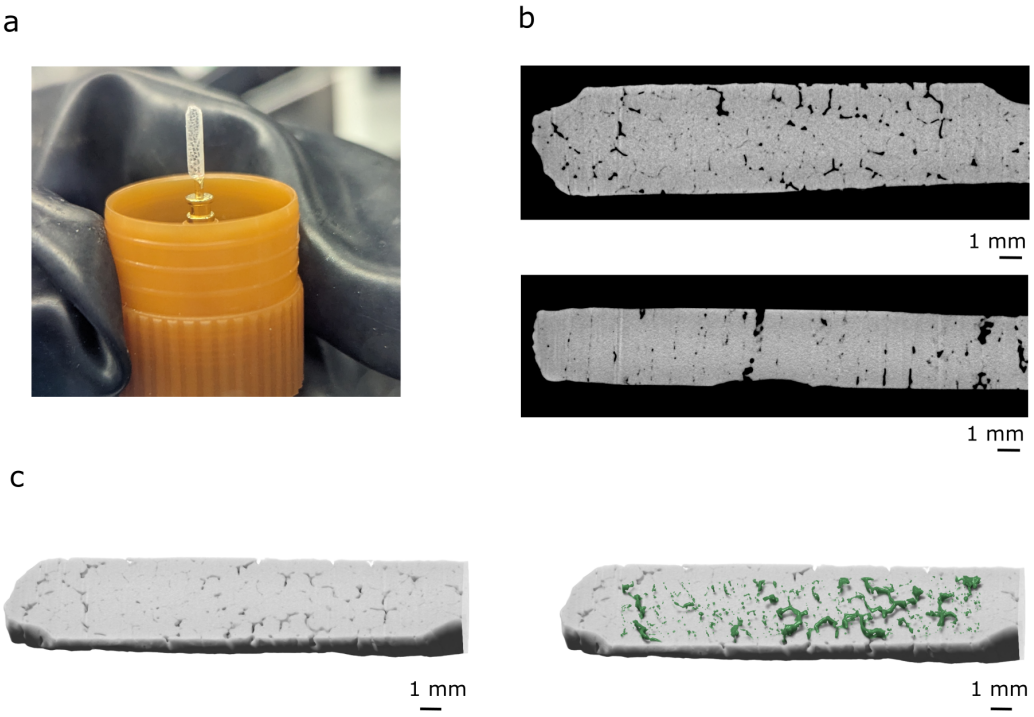

Figure 4.7: *ACT measurements. a) Sample prepared for ACT measurements. b) 2D slices of the 2 longitudinal sides of the sample. c) 3D rendering of the sample, on the right with segmented pores.*

4.3.4 $Li_5(OH)_2Br_3$ and the LiBr-LiOH system

The final part of this chapter considers the layered antiperovskite $Li_5(OH)_2Br_3$, and where it fits into the current understanding of the LiBr-LiOH system. Even with large grains, Li_2OHBr demonstrates suboptimal ionic conductivity. It is possible that $Li_5(OH)_2Br_3$ may exhibit superior properties and so is interesting to investigate[141–145]. Previous attempts to synthesise $Li_5(OH)_2Br_3$ using stoichiometric LiBr and LiOH have produced samples containing high fractions of LiBr and Li_2OHBr[140,141]. This may indicate that $Li_5(OH)_2Br_3$ is not an equilibrium phase, but could also be a result of peritectic or peritectoid reactions which kinetically hinder formation of $Li_5(OH)_2Br$ upon cooling from the melt, as has been observed for other LiBr-LiOH phases in this thesis.

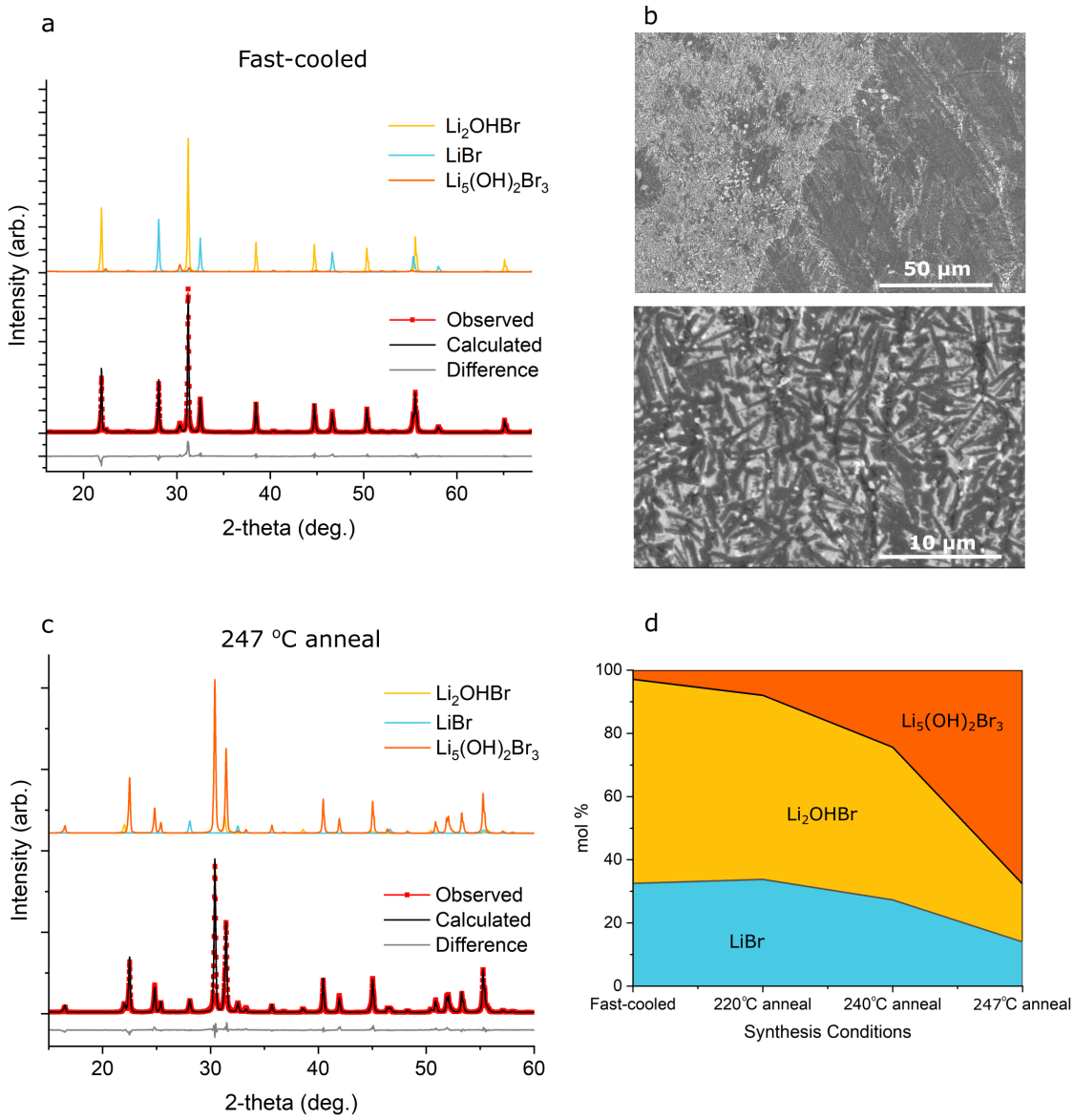

Figure 4.8: *$Li_5(OH)_2Br_3$ synthesis. a) X-ray diffraction pattern, corresponding Rietveld refinement (bottom) and deconvolution into constituent phases (top) of fast-cooled 40 mol % LiOH sample, showing only a small fraction of the $Li_5(OH)_2Br_3$ phase. b) SEM images of fast-cooled 40 mol % LiOH sample showing a fine two-phase microstructure believed to be LiBr (pale) and Li_2OHBr (dark). c) X-ray diffraction pattern, corresponding Rietveld refinement (bottom) and deconvolution into constituent phases (top) of 40 mol % LiOH fast-cooled sample after a 4 hour anneal at* 247 °C*. The primary phase is $Li_5(OH)_2Br_3$ (68 mol %). d) Relationship between annealing temperature and phase composition of 40 mol % LiOH samples as determined by XRD Rietveld refinements.*

Samples of the theoretical stoichiometric ratio, 40 mol % LiOH to 60 mol % LiBr, were melted at 350 °C and either fast-cooled by removing from the furnace, or furnace-cooled at 5 °C min^{-1}. Rietveld refinements were carried out on XRD spectra of the samples using structural models of Li_2OHBr, LiBr and $Li_5(OH)_2Br_3$, which can give estimates of the relative

phase fractions. These refinements indicated that fast-cooled samples contained a mixture of 32 mol % LiBr, 65 mol % Li_2OHBr and 3 mol % $Li_5(OH)_2Br_3$ (Figure 4.8a). This predominantly two-phase microstructure is shown to form a eutectic in SEM images (Figure 4.8b). In the furnace-cooled samples, a higher proportion of 21 mol % $Li_5(OH)_2Br_3$ is formed, but still with 22 mol % LiBr and 57 mol % Li_2OHBr (Figure B.7).

Fast-cooled samples were ground into a fine powder using a mortar and pestle and annealed for 4 hours at a selection of temperatures before quenching back to room temperature. The proportion of $Li_5(OH)_2Br_3$ increased with annealing temperature to a maximum of 68 mol % $Li_5(OH)_2Br_3$ at a 247 °C anneal with 14 mol % LiBr and 18 mol % Li_2OHBr (Figure 4.8c,d, Tables B.1 and B.2). This purity was not improved with longer anneals. Electrochemical measurements of cold-pressed pellets of this sample gave an ionic conductivity of 1.8×10^{-7} S cm^{-1} at 30 °C and an activation energy of 0.63 eV (Figure B.6). Although not phase pure, these values suggest that potential improvements to conductivity offered by this Ruddlesden-Popper variation of the antiperovskite are likely to be insignificant. These measurements also align with values of 1.3×10^{-7} S cm^{-1} and 0.57 eV reported by Koedtruad *et al.* on "$Li_5(OH)_2Br_3$" synthesised from Li_2O, LiBr and LiOH with the stoichiometry $LiBr(Li_{2.5}OH_{0.5}Br)$. DC CA measurements indicated an electronic conductivity of 1.1×10^{-11} S cm^{-1}, supporting that $Li_5(OH)_2Br_3$ is predominantly an ionic conductor.

From DSC measurements, the melting point of the sample is determined to be ~ 254 °C, below which there is another endothermic peak at ~ 251 °C (Figure 4.9a). In anneals above 247 °C, the phase fraction of $Li_5(OH)_2Br_3$ reduced again, as shown in Figure 4.9b. The sample remained solid in each instance, but variation in the obtained diffraction patterns is observed. This is likely due to furnace inaccuracies and slight spatial temperature differences impacting the formed phases in this highly sensitive region of the phase diagram. Mahroug's phase diagram includes a "LiBr + $Li_3(OH)_2Br$" phase field here, but $Li_5(OH)_2Br_3$ has not yet been considered in any proposals.

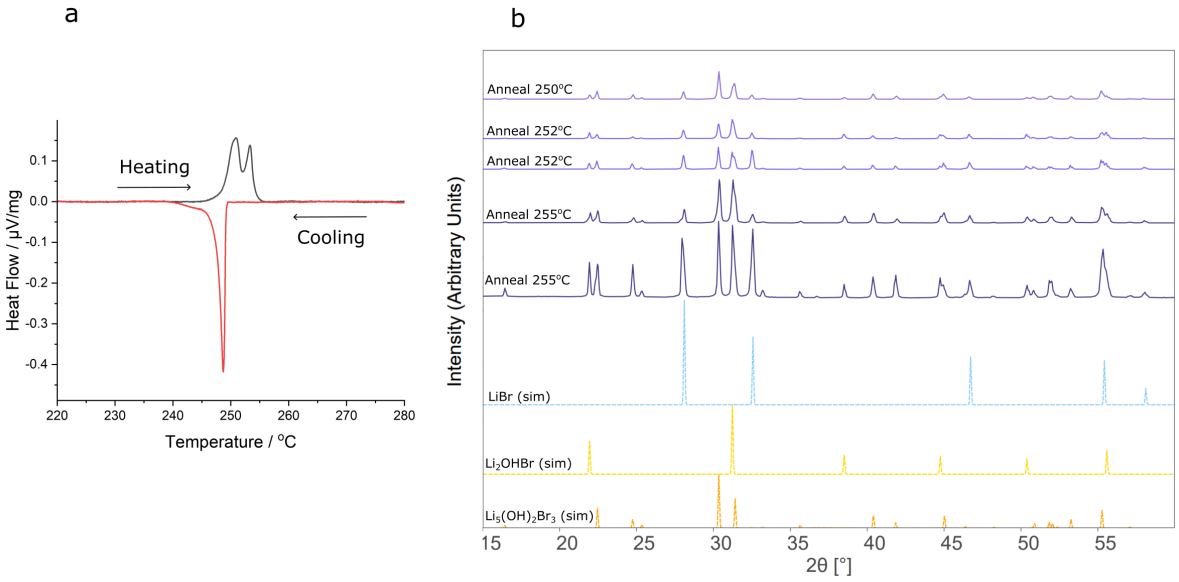

Figure 4.9: *a) DSC taken on fast-cooled 40 mol % LiOH samples at* 5 °C min^{-1}*, showing two endothermic peaks on heating. b) XRD patterns of 40 mol % LiOH samples annealed at similar temperatures between* 250 °C *and* 255 °C*, exhibiting different phase compositions. Simulated diffraction patterns for LiBr, Li_2OHBr and $Li_5(OH)_2Br_3$ are shown at the bottom for comparison.*

Based on this chapter's findings, it can be speculated if and how the $Li_5(OH)_2Br_3$ phase should be incorporated into the LiBr-LiOH equilibrium phase diagram. The Gibbs phase rule first needs to be considered. The Gibbs phase rule defines the degrees of freedom of a system, that is to say, the number of thermodynamic variables which can be independently varied without impacting the number of phases in equilibrium. This places limitations on the addition of new phases to the phase diagram. The Gibbs phase rule states that $F = C - P + 2$ where F is the degrees of freedom, C is the number of components (i.e. LiBr and LiOH), and P is the number of phases. The independent variables, temperature and pressure, are accounted for in the '+2' term. However, since pressure remains constant in a binary phase diagram, and $C = 2$, the equation simplifies to $F = 3 - P$. An implication of this is that four phases can never coexist as it would require $F = -1$.

The phase diagram previously proposed by Mahroug is shown again in Figure 4.10a. The anneals in this work indicate that $Li_5(OH)_2Br_3$ may be stable at elevated temperatures below the "LiBr + $Li_3(OH)_2Br$" field. For a $Li_5(OH)_2Br_3$ field to be introduced here at 40 mol % LiOH, a "LiBr + $Li_5(OH)_2Br_3$" field would be introduced to its left and a "$Li_5(OH)_2Br_3$ + Li_2OHBr" field to its right. However, the "$Li_5(OH)_2Br_3$ + Li_2OHBr" field created would not be permitted

in accordance with the Gibbs phase rule due to the presence of the "LiBr + $Li_3(OH)_2Br$" region above it. A possible solution to this problem is sketched in Figure 4.10b. The existence of a narrow "LiBr + Li_2OHBr" region placed above $Li_5(OH)_2Br_3$ would satisfy equilibrium conditions without disrupting any of the previous findings. Since the fast-cooled samples contain a mixture of LiBr and Li_2OHBr, it is likely that the $Li_5(OH)_2Br_3$ phase field does not extend down to room temperature, and hence LiBr + Li_2OHBr nucleate instead of the $Li_5(OH)_2Br_3$ phase at high cooling rates where larger undercoolings are achieved. At slower cooling rates, sufficient time is spent in the $Li_5(OH)_2Br_3$ phase field for some nucleation of $Li_5(OH)_2Br_3$ to occur. However, since the $Li_5(OH)_2Br_3$ phase does not nucleate directly from the liquid state, the phase cannot be easily synthesised phase pure upon cooling. Verifying the phase diagram is challenging given the close proximity of the proposed phase transitions and the propensity to non-equilibrium behaviour. Nonetheless, preliminary evidence may support this proposal, discussed in Appendix B.5.

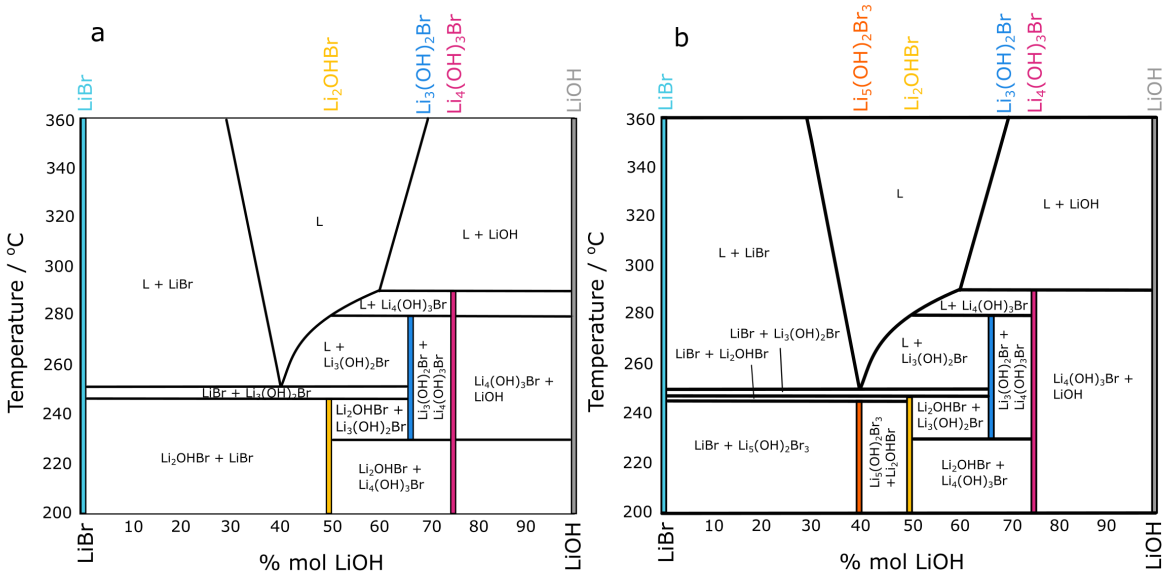

Figure 4.10: *a) Sketch of the phase diagram proposed by Mahroug et al. previously shown in Figure 1.11d, reproduced here for ease of comparison. b) Speculative LiBr-LiOH phase diagram incorporating $Li_5(OH)_2Br_3$ at 40 mol % LiOH. Only the high temperature portion is shown, and $Li_5(OH)_2Br_3$ may not be the equilibrium phase down to room temperature. The unidentified phase transitions plotted by Mahroug for greater than 75 mol % LiOH at* 230 °C *and* 280 °C *have not been included based on the findings of Chapter 3.*

4.4 Conclusions and Future Work

In this chapter, synthesis of the antiperovskite and Ruddlesden-Popper antiperovskite phases Li_2OHBr and $Li_5(OH)_2Br_3$ were investigated. Findings indicate that neither melt congruently, which results in phase impurities forming when the cooling conditions chosen for synthesis aren't optimal. In spite of extensive speculation about the detrimental impact of grain boundaries on ionic conductivity in Li_2OHBr, it was found that mm-scale grains are formed in melt-cast samples. Although the low grain boundary density in these samples means that grain boundaries will have a minimal impact on ionic conductivity, the samples were found to be very fragile and prone to breaking intergranularly. Various strategies were explored in attempts to grow single crystals of Li_2OHBr. Large crystals could be produced through growths in quartz tubes, but dendritic solidification resulted in undesirable porous microstructures. A directional solidification utilising a slow cooling rate and steep temperature gradient may be a possible avenue to overcoming this problem in future work. By cutting thin pellets from high quality single crystals, for example using a femtosecond pulse laser or laser-FIB, solid electrolytes with minimal defects could be investigated as an approach to improving cycling performance.

Chapter 5

Li_2OHBr Glass Electrolytes

Contents

5.1 Introduction

So far in this thesis, the focus has been on crystalline LiBr-LiOH compounds. It had been hoped that some improvement to the macroscopic ionic conductivity of Li_2OHBr could be achieved through the removal of grain boundaries. However, for practical application as a solid electrolyte, it appears that this alone is insufficient, and the bulk ionic conductivity needs to be

enhanced. In spite of suboptimal ionic conductivites, the lithium hydroxyhalide antiperovskites still host a wealth of advantages making them of interest for solid electrolytes, including stability with lithium metal, being relatively inexpensive, non-toxic, relatively low density and having low electronic conductivity. A potential approach to retaining these desirable properties whilst simultaneously attempting to increase the ionic conductivity, is to make glassy samples.

Although the exact definition of a glass can be debated, a sufficient description for most instances is a homogeneous, isotropic and non-crystalline material, free from any internal phase boundaries[192]. Instead of conduction mechanisms relying on intrinsic or extrinsically-doped mobile defects, glasses typically incorporate a large amount of free volume in their structure, which is available as sites for migrating ions to hop into, and may result in improved ionic conductivity. Additionally, the homogeneous nature of glasses mean that ionic conduction is isotropic over a long length scale and bulk samples avoid the detrimental impacts of grain boundaries. Other potential advantages proposed for glass electrolytes include improved resistance to lithium filament growth, better capacity retention, and enhanced rate performance compared to their crystalline counterparts[191,193–195]. Glass electrolytes have been a topic of interest since the 1980s, with extensive research into LPS glasses[91,196–202] and LiPON glasses[194,195,203–207]. Recently, interest into novel glass electrolytes has continued, with exciting reports of amorphous electrolytes exhibiting impressive superionic conductivities[208–211].

In principle, any material system can be vitrified by quenching from the molten state to below its glass transition temperature, T_g, whilst suppressing nucleation of crystals[212]. As such, glasses can be described as a kinetically-locked state. However, unlike LiPON and LPS which derive from more conventional glasses, comprising network formers (PO_4^{3-} and PS_4^{3-} respectively) and lithium modifiers, the antiperovskites do not contain any natural network formers and are not conducive to satisfying the random network theory rules proposed by Zachariasen back in 1932[213]. Additionally, despite the energy and cathode co-processing advantages offered by the low melting points of these antiperovskites ($\leq 300\,^{\circ}C$), the low temperatures can cause challenges in producing the high cooling rates necessary for quenching as is traditionally done to kinetically lock the glass phase in. As such, producing antiperovskite-derived glasses is expected to be challenging.

Between 2014 and 2017, and more recently in 2024, Braga *et al.* published a series of

papers claiming to have made "glassy antiperovskite" electrolytes based on a lightly-doped Li_3OCl composition, using an unconventional wet synthesis approach[146–150]. An ionic conductivity of 25 mS cm^{-1} at 25 ^oC was reported for $Li_{2.99}Ba_{0.005}OCl$, the highest of any solid electrolyte at the time[146]. In the reported synthesis, water is added to LiCl, $Ba(OH)_2$ and LiOH precursors to create a paste, which is then dried at high temperatures. This is followed by manipulation in air which is claimed to be necessary to promote formation of the glassy phase. The work received notable attention due to its impressive claims. However, criticism soon followed, and the work is now regarded as controversial[112,151]. Notably, Hanghofer *et al.* conducted a study to investigate the reported synthesis procedure[112]. In their work, degradation of the supposed "Li_3OCl" to Li_2CO_3 and $LiCl{\cdot}xH_2O$ was found. Hydrated lithium chloride is amorphous, matches the DSC results observed by Braga *et al.*, and exhibits a high ionic conductivity, explaining the results found by Braga and rendering the glass reports unreliable.

Nevertheless, the claims made by Braga *et al.* inspired several computational studies into related antiperovskite-derived glasses[152–154]. Heenen *et al.* modelled glassy Li_3OCl through simulated quenches from 1200 K to 300 K and calculated resulting ionic conductivities using an MD approach[152]. Ionic conductivities of 1 - 10 mS cm^{-1} were found for the glassy Li_3OCl, much higher than that of the crystalline form, and an activation energy of 0.42 eV. This improvement in ionic conductivity was attributed to a predicted 13 % volume increase in the glassy state, and a shift from vacancy conduction to Li-ion migration. The structure was predicted to consist of subnanoscale LiCl and Li_2O domains, in which the transference number is sub-optimal (0.84) due to surprising Cl^- migration through the LiCl domains. Another computational study looked at sodium analogues, predicting glassy Na_3OCl to have an excellent ionic conductivity of $\sim$ 16 mS cm^{-1} at 300 K[154]. This was improved further by the creation of glassy Na_2OHCl, thanks to the introduction of an -OH paddlewheel mechanism. Unlike in the Li_3OCl glass model, no phase separation was observed in the predicted Na_3OCl and Na_2OHCl structures. Smith and Siegel also proposed that advantageous paddlewheel mechanisms could activate at low temperatures in glasses with limited network-forming ability[155], a prediction which could be expected to apply to Li_2OHX (X = Cl, Br) antipervoskites as well. These computational findings suggest that, despite the controversial reports surrounding experimental lithium oxyhalide glasses, the lithium-ion dynamics in an Li_2OHX (X = Cl, Br) glass may be desirable and should be investigated.

In this chapter, the synthesis of glassy Li_2OHBr, Li_2OHCl and $Li_2OHCl_{0.5}Br_{0.5}$ are

investigated using a melt-quench approach. This study aims to resolve the controversies arising from earlier reports of antiperovskite glasses by synthesising real antiperovskite glasses, and assessing whether they exhibit improved lithium-ion dynamics compared to their crystalline counterparts. Diffraction and thermoanalytical techniques are employed to confirm the glassy state of successful samples. Subsequent chemical and structural characterisation is utilised to understand more about these novel glasses. Lithium-ion dynamics in Li_2OHBr glasses are probed through SLR-NMR spectroscopy measurements, to establish whether any improvement is observed over the crystalline antiperovskite phase. In spite of promising findings, the inherent instability of these glasses against crystallisation may limit their practical application in solid-state batteries, and future work should therefore focus on strategies to enhance their stability.

5.2 Experimental Methods

5.2.1 DSC

For DSC measurements, a TA Instruments DSC25 was used. A known mass (2 - 5 mg) of sample was hermetically-sealed in an aluminium pan under argon atmosphere to avoid air exposure. For measurements, a ramp rate of $5\,^{\circ}\text{C}\ \text{min}^{-1}$ was used to conduct 3 heating-cooling cycles from $-40\,^{\circ}\text{C}$ to $400\,^{\circ}\text{C}$.

5.2.2 Density Measurements

The density of Li_2OHBr glass flakes was measured using a sink-float method. 3 ml of anhydrous acetone ($\geq$ 99.8 % Sigma-Aldrich, 0.7847 g/ml) and 3 ml of diiodomethane (99 % Sigma-Aldrich, 3.325 g/ml) were initially mixed together in a vial at 25 ^{o}C using a magnetic stirring rod to produce a homogeneous liquid. A glass flake was added which sinks to the bottom, and diiodomethane added in 0.05 ml increments using a pipette. The vial cap was replaced between additions to avoid volatisation of the acetone, and the sample stirred for $\sim$ 30 seconds. The miscibility of diiodomethane in acetone is high, and so homogeneous solutions are attained easily. The density of the glass flake can be calculated from the ratio of acetone to diiodomethane at the point when the glass flake transitions from sinking to floating. Measurements were taken on 4 glass flakes. No visible reaction occurred to the glass flakes during measurements, and

flakes added at the end of the measurement behaved the same as those in solution for the whole measurement, suggesting that no reactions are affecting the measurements.

5.2.3 NMR

NMR measurements in this chapter were taken by Dr Gregory Rees and Dr Hua Guo. Static solid-state ^{7}Li NMR was completed at $\upsilon_0(^7\text{Li}) = 155.53$ MHz (9.45 T) using a 5 mm solution-state probe, the temperature was calibrated using $KBr_{(s)}$ and all samples are referenced to $LiCl_{(aq)}$ at 0 ppm.[214,215] The spin-lock $T_{1\rho}$ relaxometry experiments utilised a 10 kHz B_{1eff}-field that was varied from 1 μs to 100 ms. The data was fitted to $S(t) = I_0[1 - e^{\frac{-t}{T_{1\rho}}}]$, with errors of < 0.5 %, R^2 of 0.99 with normal residual distributions. For MAS ^{7}Li NMR measurements, the magic angle spinning frequency was 10 kHz using a Bruker 4 mm double air bearing probe.

5.3 Results and Discussion

5.3.1 Glass Synthesis

In attempting to synthesise glasses, both the bromide (Li_2OHBr) and chloride (Li_2OHCl) antiperovskite compositions were investigated. Additionally, a mixed halide composition with the stoichiometry $Li_2OHBr_{0.5}Cl_{0.5}$ was investigated, with the anticipation that the increased disorder resulting from the mixed-anion site may aid in glass-forming ability. XRD measurements were used as an initial indication of crystallinity in samples to assess the effectiveness of each synthesis approach. Peak broadening is indicative of a reduction in crystallite size. Better yet, an absence of peaks would indicate a total loss of long-range order.

Stoichiometric ratios of LiBr, LiOH and LiCl were ground together using a mortar and pestle and heated to the liquid state at 350 °C in an alumina crucible for 45 minutes under a glovebox argon atmosphere. The crucibles were removed from the furnace to quickly cool to room temperature, and the resulting sample ground into a powder using a mortar and pestle. These samples constitute the crystalline antiperovskites referred to in this chapter, and the precursors for glass synthesis attempts.

In-house Quenching

A conventional quenching approach was taken on remelted antiperovskites to try and kinetically-lock in the glass phase. Initial quenching attempts involved transferring molten sample from the furnace to a thermoelectric cooler ($\sim$ 5 °C) in a thin SS coin cell case. Quenching was also attempted by sealing small masses of antiperovskite in quartz tubes under vacuum, which could then be quenched into a bath of liquid nitrogen outside of the glovebox following melting. This approach has previously been conducted in sulphide glass research[196–198,216]. Small masses of sample ($\sim$ 100 mg) were used in each instance, to ensure heat transfer through the sample occurred quickly. Nonetheless, highly crystalline antiperovskites were found to form from the resulting XRD patterns.

Additionally, there was no apparent difference between samples cooled through the thermoelectric cooler and liquid nitrogen approach. It is probable that the thermal transfer through the walls of the quartz tube dampened the cooling rate of the antiperovskite samples significantly. As such, subsequent attempts used the thermoelectric cooler, which required less preparation and resources.

The next iteration investigated was to incorporate a small fraction of a traditional glass former into the sample, with the ambition that it would aid in 'confusing' the structure of the material. Anhydrous boron oxide (99.999 %, Alfa Aesar) was used since its glass transition temperature ($\sim$ 307 °C) is similar to the melting points of the antiperovskites (250 - 300 °C). The effect of 3.5 wt% B_2O_3 was investigated for Li_2OHBr, Li_2OHCl and $Li_2OHCl_{0.5}Br_{0.5}$ antiperovskites, synthesised using the thermoelectric cooler. A higher B_2O_3 content of 7 wt% was also synthesised for the Li_2OHCl sample. Diffraction patterns, presented in Figure 5.1a, showed highly crystalline peaks in each instance. New peaks, with intensity proportional to the B_2O_3 content are also observed in the samples. This suggests an unknown reaction between the antiperovskites and B_2O_3 has occurred. To ensure the boron oxide was fully dry, it was dried in a Buchi under vacuum at 120 °C for 96 hours, and confirmed to be amorphous using XRD. The synthesis was unaffected by this, indicating that the reactions observed were not a result of hydration.

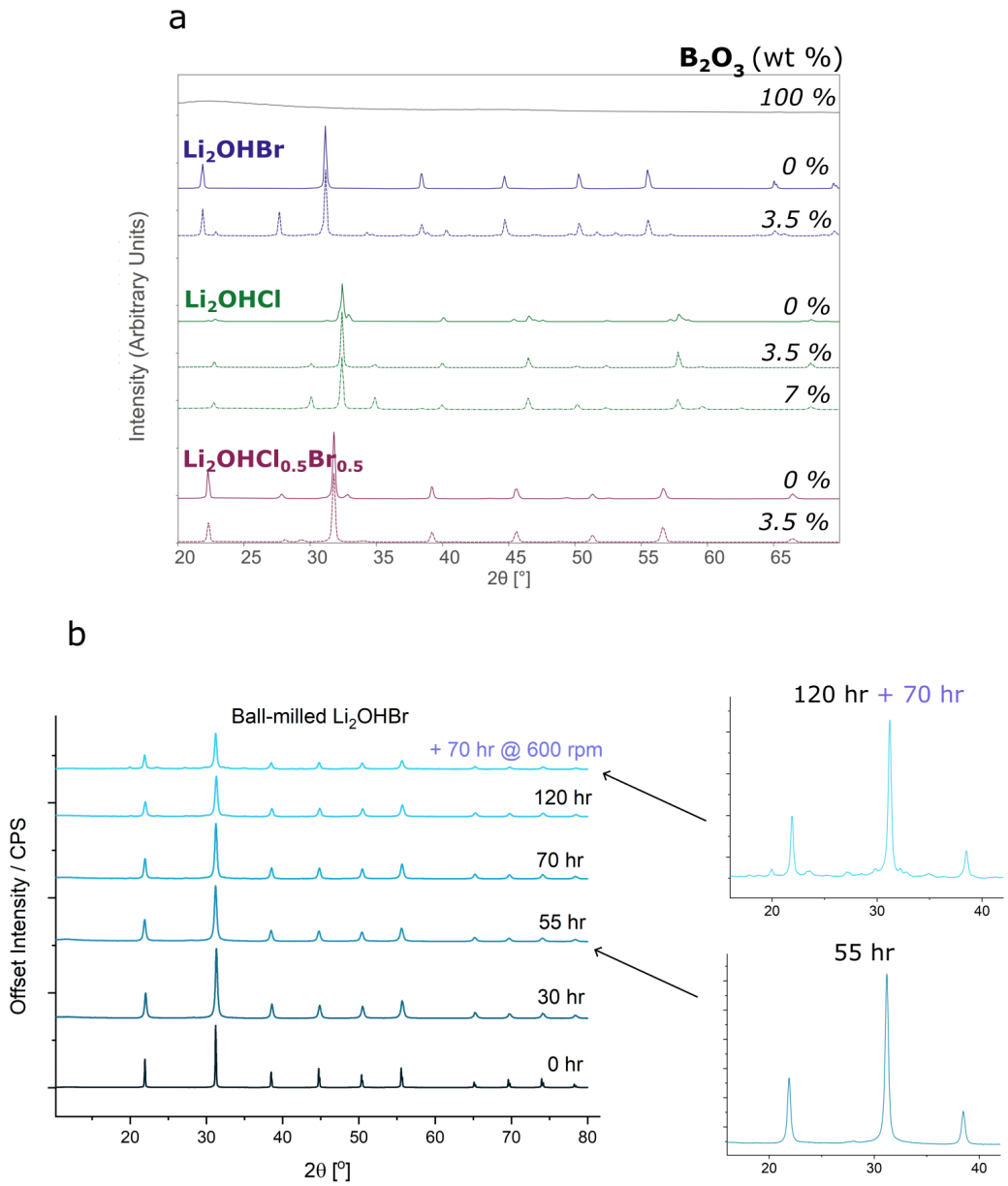

Figure 5.1: *Failed Glass Synthesis Attempts. a) The impact of B_2O_3 doping on the different antiperovskite compositions. Highly crystalline samples were produced in each instance. Some new peaks formed, indicating there may be reactions occurring between the B_2O_3 and antiperovskites. b) XRD patterns taken on a Li_2OHBr sample at different stages of ball milling at 500 rpm, starting from 0 hours at the bottom. A final milling step at 600 rpm resulted in increased impurity formation but little reduction in crystallinity, shown in the insets. Note that the peak intensity of the 0 hr sample was normalised to that of the 30 hr sample, but the rest are unchanged.*

Ball Milling

In addition to quenching attempts, ball milling was investigated as an alternative route to amorphisation, disrupting long-range periodicity through a combination of mechanical strain and localised heat induced by the high-impact collisions. This approach became popular in sulphide glass research to enable synthesis of compositions with poor glass-forming ability[91,200,217–219]. It was hoped that ball milling might be useful in the antiperovskite compositions, which are similarly challenging to vitrify by alternative methods. Although ball milling has the advantage of being a room temperature process, it is very slow and removes the possibility of producing bulk samples.

Milling was carried out in a planetary ball mill (Fritsch Pulverisette 7 Premium) under argon atmosphere using 1 g of Li_2OHBr and zirconia balls in a ball-to-powder ratio of 13:1. Cycles of 3 minutes milling at 500 rpm followed by 7 minutes rest were used to allow dissipation of heat built up during the milling steps. XRD measurements were taken on sample after 30, 55, 70 and 120 hours effective milling (Figure 5.1b). During the milling, surprisingly little peak broadening was observed after the initial 30 hours milling. Following 120 hours milling at 500 rpm, an increased milling rate of 600 rpm was carried out for 70 hours to see whether the increased energy could aid in amorphisation. However, excessive energy can also lead to rapid heat generation and unwanted side effects. As can be seen in the inset of Figure 5.1b, some impurity formation occurred during this stage.

Although the peak full width half maximums (FWHM)s indicate the crystal size is fairly constant, a progressive decrease in intensity with increased milling was observed. This may indicate that the fraction of crystalline material in the sample is decreasing, although care must be taken in interpreting the intensities of XRD signal, even when taken under the same conditions. Regardless, ball milling appears to be an unsuccessful approach to synthesising antiperovskite glasses and so was not investigated further.

Twin-roll Quench

Successful glass synthesis was finally achieved through a collaboration with Professor Steve Feller (Coe College, Iowa), an expert in the field of novel glasses. Using a twin-roll quencher inside

a nitrogen-filled glovebox, sufficient quenching rates for glass production were possible. This is a technique which was also employed in LPS glass electrolyte research prior to the focus on ball milling[199,217,220,221]. In this approach, the molten sample is poured over the face of two spinning steel rollers, each 10 cm diameter in this setup. Powerful motors force the material through the gap between the rollers into a collection bin beneath. The twin-roll quenching approach achieves significantly higher cooling rates ($\sim 10^5$ K s^{-1}) than conventional quenching through a combination of the thin sheet geometry of the material produced, which provides a high surface-area-to-volume ratio, and the direct contact between the molten material and actively cooled rollers, enabling highly efficient heat extraction. The conditions can be optimised through control of the roller separation (0 - 100 microns) and rotation rate (up to 3600 rpm).

Batches of antiperovskites were synthesised, sealed in vacuum pouches, and sent to Coe College, where Professor Feller's students would remelt the samples in platinum crucibles and carry out the twin-roll quench process. Professor Feller's students worked on optimising the synthesis of glasses by adjusting these parameters and the melting temperature used. Flakes of material with varying crystallinity were produced from this process, which were then sent back for manual sorting. Polycrystalline samples are expected to be opaque due to the scattering of light by defects such as grain boundaries, and so optically-transparent flakes were separated as promising samples. Photographs showing examples of these transparent and opaque flakes can be seen in Figure 5.2a and b.

5.3.2 Confirmation of the Glassy State

From optimisation of the twin-roll quench conditions, fully transparent flakes of Li_2OHBr and Li_2OHCl could be obtained, with greater success from the bromide compositions. Glasses should not contain long-range order, and so XRD measurements were taken on crushed samples to ascertain whether this was the case. The crystalline samples exhibit Bragg peaks corresponding to the cubic antiperovskite phase, with additional peaks observed in the crystalline Li_2OHCl corresponding to the orthorhombic antiperovskite, as is expected for the chloride composition below $\sim 35\,^{\circ}C$[102,118,222]. As shown in Figure 5.2c, no Bragg peaks are observed in the completely transparent Li_2OHBr and Li_2OHCl flakes. These findings support that the transparent samples do not have a crystalline structure.

Another important feature of melt-quench glasses is that they exhibit an endothermic second-order transition known as the glass transition temperature, T_g. This manifests as discontinuities in derivative thermodynamic properties such as heat capacity and thermal expansion [192]. The glass transition arises as a result of the rapid decrease in viscosity and corresponding increase in mobility of the atoms in a structure as the temperature is increased above its T_g ($\nu \approx 10^{12}$ Pa.s [192]). A crystallisation temperature, T_c, is typically found above this temperature, at which point the material undergoes an exothermic transition from the disordered state to the thermodynamically-preferable crystalline state. It is worth noting though, that spontaneous crystallisation is possible below these temperatures, particularly in unstable glasses such as these.

DSC was conducted on transparent Li_2OHBr and Li_2OHCl samples to observe whether glass transitions occur upon heating, shown in Figure 5.2d. In both instances, features indicative of a glass transition can be seen in the samples' responses, confirming the presence of a glass phase. These features are absent in measurements taken on crystalline samples.

In Li_2OHCl, a small endothermic peak corresponding to the orthorhombic-to-cubic phase transition can be seen in the crystalline sample at $\sim 30\,^{\circ}C$ [102,118,222]. This is absent in the glass samples since they do not contain any orthorhombic Li_2OHCl. In the glass, a small exothermic hump occurs just above $150\,^{\circ}C$, visible in the zoomed-in region shown in inset iii of Figure 5.2d. This corresponds to sub-T_g relaxation, whereby some structural rearrangements to a more stable environment occur. Around $225\,^{\circ}C$, a small endothermic slope signifies the onset of the glass transition. This is immediately followed by exothermic responses corresponding to subsequent rearrangement and crystallisation occurring. Multiple exothermic events appear to occur, which may be indicative of multiple glass phases existing, or could be a result of a series of crystallisation steps occurring from a single glass phase. Above this temperature, the material behaves as the crystalline Li_2OHCl, albeit with a small shift to lower temperatures ($\approx 5\,^{\circ}C$).

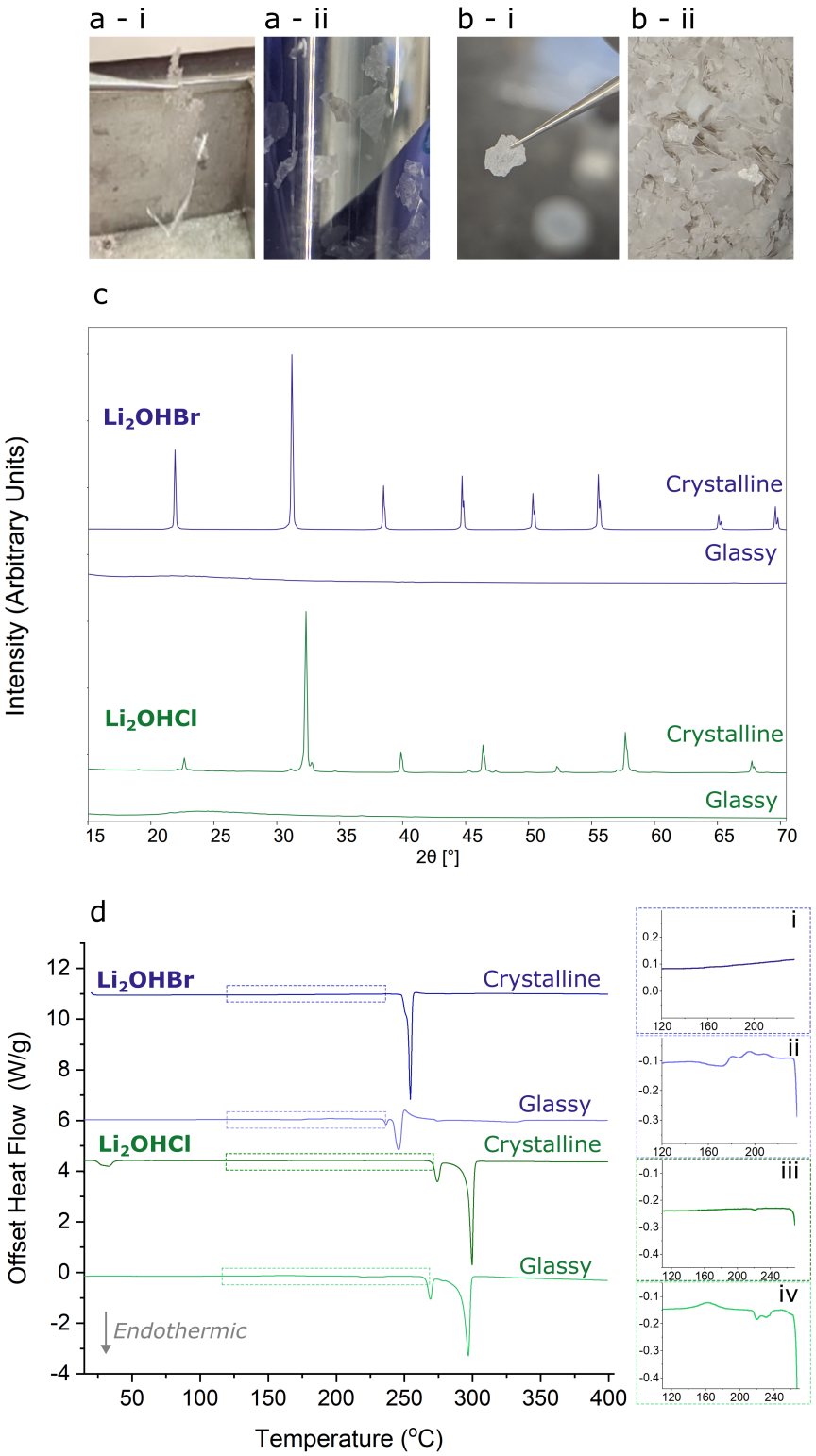

Figure 5.2: *Proof of Glass Synthesis. a) Photographs of transparent 'glassy' Li_2OHBr flakes i) held by tweezers, and ii) stored in a vial. b) Similar photographs, this time showing opaque examples of flakes. c) XRD patterns of Li_2OHBr and Li_2OHCl glasses showing the absence of the characteristic Bragg peaks seen in the crystalline homologues. d) DSC measurements of crystalline and glassy Li_2OHBr and Li_2OHCl on the first heating cycle. The insets (i-iv) show glass transition events are present only in the glassy samples.*

As in the chloride glass, features indicative of a glass transition are seen in measurements of the bromide glass samples from $\sim 150\,^{\circ}\mathrm{C}$. Similarly, various exothermic crystallisation responses appear to be occurring above the glass transition. The absence of a 'working range' between the glass transition and crystallisation temperatures eliminates any possibility of processing these glasses in the viscous state, as has been previously demonstrated for other glass electrolytes[208,223,224]. For the bromide glass, the behaviour of the profile after crystallisation is noticeably different to that of the pristine crystalline material: the endothermic peak observed at $254\,^{\circ}\mathrm{C}$ in crystalline measurements is replaced with endothermic peaks at $237\,^{\circ}\mathrm{C}$ and $246\,^{\circ}\mathrm{C}$. It was not possible to capture what is happening through *ex-situ* experiments, due to the narrow temperature ranges of interest. Nevertheless, the samples are no longer glassy on subsequent heating and cooling cycles, apparent from the disappearance of the glass transition (Figure 5.3).

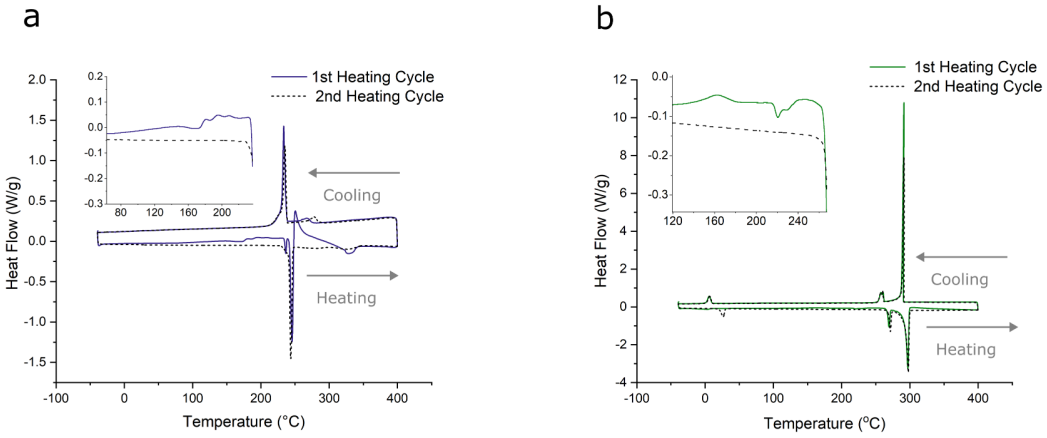

Figure 5.3: *Loss of the Glassy State. Two DSC heating-cooling cycles of glassy a) Li_2OHBr and b) Li_2OHCl, showing the disappearance of the glass transition after the initial heating*

Glass Ceramics

The flakes produced from the twin-roll quench process varied in appearance. The flakes were separated into opaque (Figure 5.2b), transparent with some white specs (Figure 5.4a) and fully transparent (Figure 5.2a). Based on appearance, it is difficult to know whether the partially transparent flakes appear transparent due to the presence of defects such as pores, or due to some crystallisation in the glass. XRD patterns of samples showed Bragg peaks corresponding to the antiperovskite phase with reduced intensity compared to measurements of homologue crystalline samples taken under the same conditions (Figure 5.4d-f). TEM electron diffraction of a crushed partially-transparent Li_2OHBr flake showed a mixture of amorphous and crystalline

regions (Figure 5.4b,c). As such, these samples appear to correspond to a mixture of glassy and crystalline material, termed here as a glass-ceramic.

Although it was possible to obtain pure Li_2OHBr and Li_2OHCl glass samples, it was typical for there to be some crystalline material in the samples, even after optimisation of the synthesis conditions. For the $Li_2OHCl_{0.5}Br_{0.5}$ samples, it was only possible to produce these mixed phase 'glass-ceramics' rather than pure glasses. Using an internal standard method, the amorphous fraction in these samples was estimated to be around 70 % (see Appendix C.1), although this will vary between batches.

Synthesis was most successful using the Li_2OHBr composition. Nevertheless, even after optimisation of the synthesis conditions, the amorphous content of different yields was found to vary vastly. A relationship is found in metallic glasses, whereby glass-forming ability improves with a higher 'reduced glass transition temperature', equivalent to T_g/T_l where T_l is the liquidus temperature[225]. Since T_g typically varies slowly with composition, this can be achieved with eutectic, or near-eutectic, stoichiometries. The eutectic composition on the LiBr-LiOH phase diagram (40 mol % LiOH) was investigated to see whether improved glass forming could be achieved, however a noticeable improvement was not observed. Consequently, to try and obtain measurements for pure glasses in subsequent characterisation, the best quality Li_2OHBr glass flakes were selected based on appearance. It is likely that a small amount of crystalline phase may be present.

5.3.3 Structural and Chemical Characterisation

SEM images of the surface and cross-section (prepared using a PFIB) of Li_2OHBr glass flakes were taken, however no phase contrast was observed (Figure 5.5a and b). Corresponding EDX spectroscopy mapping was conducted to see whether any chemical segregation could be identified. For example, a mixture of two glass phases, or the possibility to distinguish between crystalline and glassy regions. The elemental concentrations were found to be homogeneous, indicating that no significant variations in stoichiometry occur (Figure C.1).

Glasses typically incorporate free space into their structure, and so the antiperovskite glasses are expected to have a lower density than their crystalline counterparts. The density of

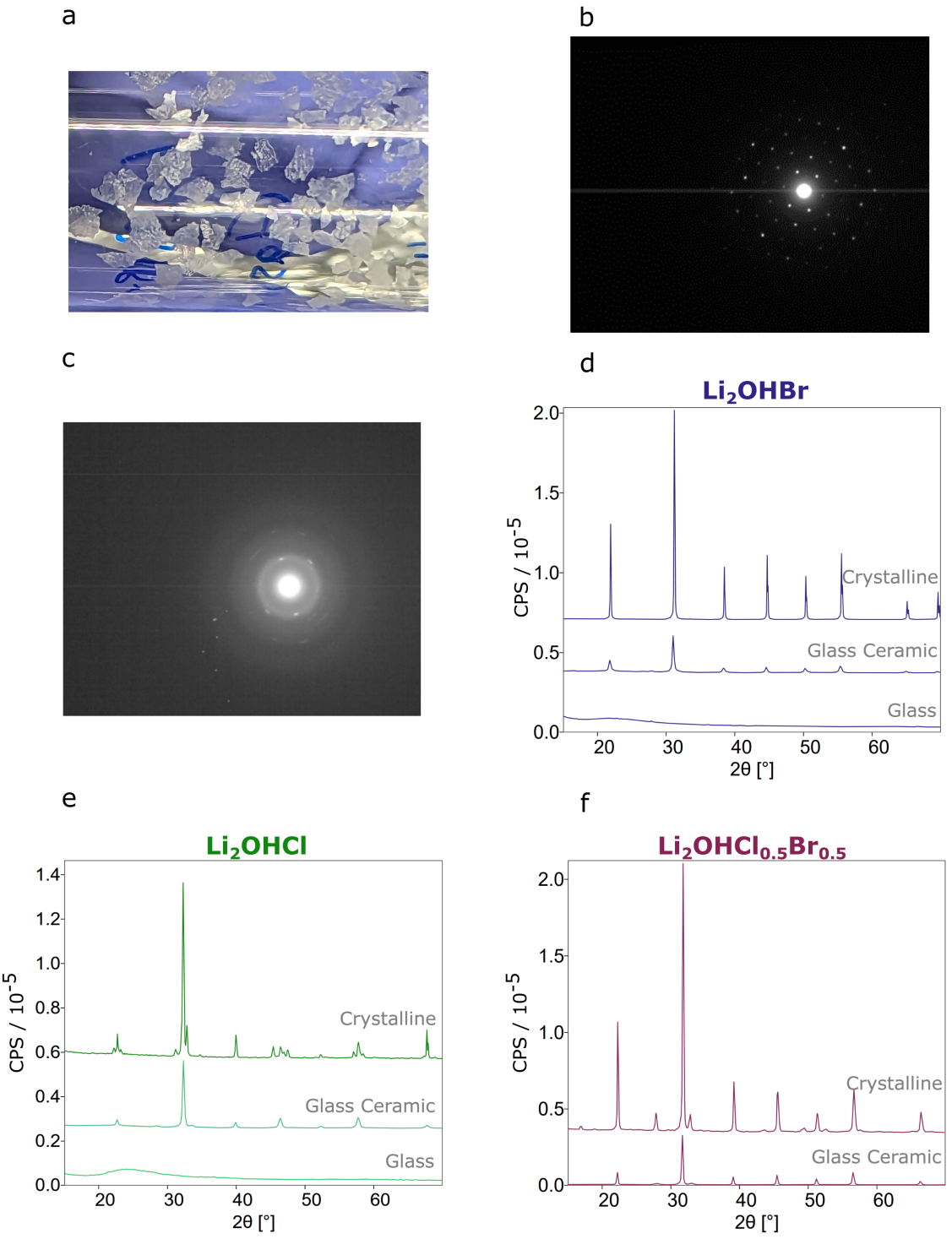

Figure 5.4: *Glass-Ceramics. a) Photograph of partially-transparent glass-ceramic samples, stored in a vial. b) TEM electron diffraction pattern of a crystalline region of an Li_2OHBr flake showing sharp discreet spots. c) TEM electron diffraction pattern of a glassy region of an Li_2OHBr flake showing diffuse rings, indicative of an amorphous structure. d-f) XRD patterns showing varying crystallinity in (d) Li_2OHBr, (e) Li_2OHCl and (f) $Li_2OHCl_{0.5}Br_{0.5}$ flakes respectively.*

pure Li_2OHBr glass flakes was measured using a sink-float method. Very little porosity can be seen in PFIB cross-sections of transparent glass flakes, as were selected for these measurements (Figure C.2). As such, the porosity can be assumed to be negligible. The measurements indicate a density of 2.31 g cm^{-3} $\pm$ 0.05 g cm^{-3} for the Li_2OHBr glass. This is 83 % of the theoretical density of crystalline Li_2OHBr (2.78 g cm^{-3}). This impressive observed decrease in density may be beneficial to the lithium dynamics in the material, since the increased free volume can act as potential sites for lithium ions to hop into during migration. Relationships between decreased glass density and increased ionic conductivity have been reported previously[226–228], and in Heenen's computational study of Li_3OCl glasses, enhanced ion mobilities were observed in ensembles quenched to lower densities[152].

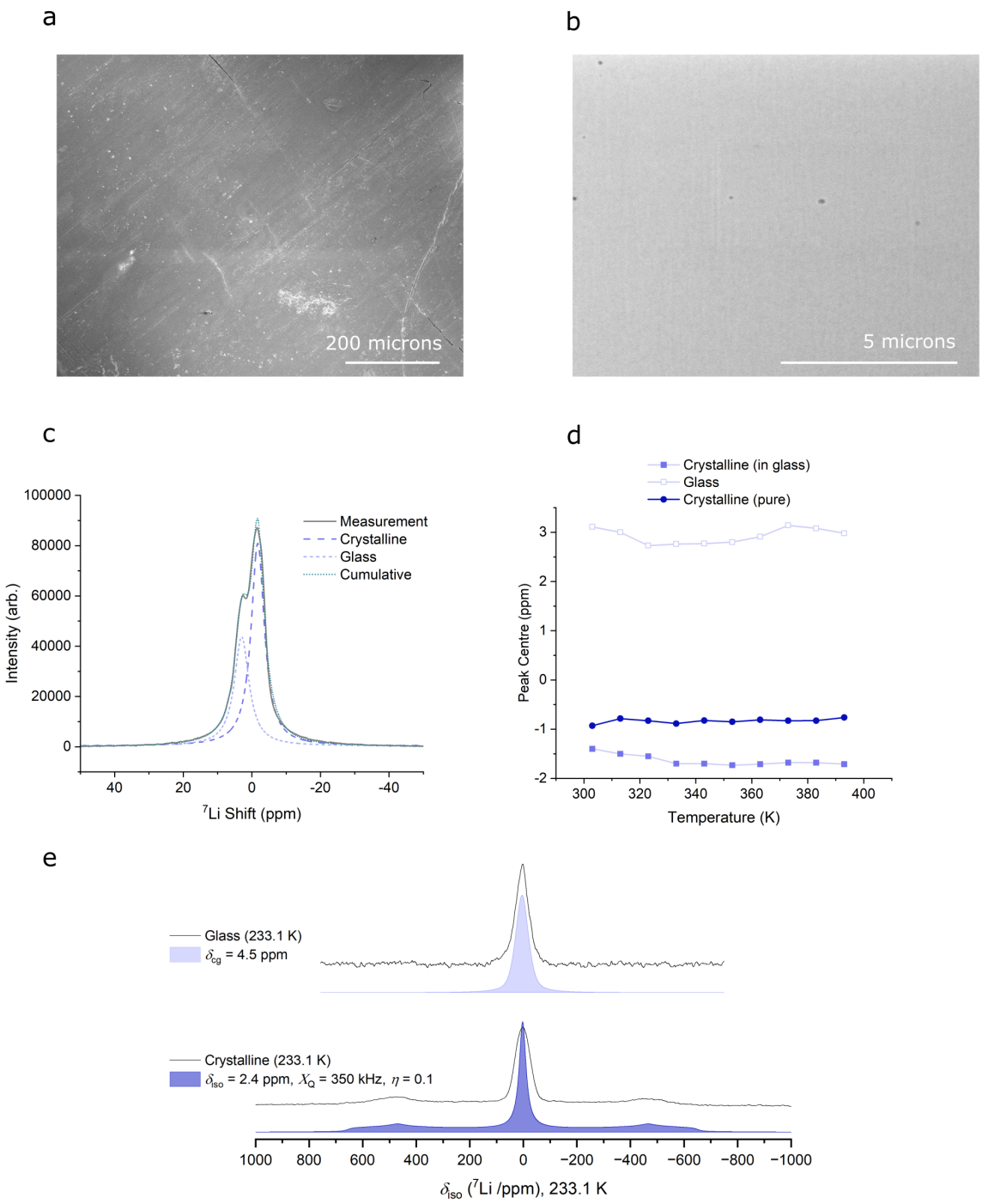

Figure 5.5: *Structural and chemical characterisation. a) Surface SEM image of a Li_2OHBr glass flake. The rolling direction of the twin-roll quench process can be seen to go from bottom left to top right. Small cracks can be seen in various locations. Small amounts of surface contamination appear as bright specs. b) SEM image of a cross-section of a Li_2OHBr glass flake prepared using a PFIB. Small isolated pores can be seen in various locations. c) ^7Li MAS-NMR lineshape obtained from glass-ceramic Li_2OHBr at 393 K, showing a glass peak centred on 2.9 ppm and a crystalline peak at -1.6 ppm. d) Peak centres plotted as a function of temperature. Curve fitting was carried out using 2 Gaussian-Lorentzian peaks. A small shift in position of the crystalline peak is seen between the glass-ceramic and pure crystalline sample due to the differing environment. e) Static ^7Li NMR of glass and crystalline Li_2OHBr. Satellites are only observed in the crystalline material due to its high symmetry local structure.*

^{7}Li MAS NMR spectroscopy measurements of Li_2OHBr glass-ceramic samples were taken at a range of temperatures between 303 K and 393 K. Peaks corresponding to the crystalline and glassy phase can be deconvoluted, especially apparent at higher temperatures due to the motional narrowing that occurs (Figure 5.5c,d). The peak corresponding to the crystalline phase, assigned using a pure crystalline sample, occurs at a more negative shift than the glass peak (Figure C.3). The more positive shift in the glass phase could be an indication of longer bond lengths. The increased shielding, and reduced ionic interaction implied from this, may be beneficial to lithium mobility in the glassy state.

Low temperature (233.1 K) static ^{7}Li NMR of glass and crystalline samples were taken (Figure 5.5e). ^{7}Li is a spin-3/2 nucleus and therefore has a nuclear quadrupole moment, which interacts with the local electric field gradient (EFG) at the lithium site. In the crystalline material, the high-symmetry local structure creates well-defined EFGs, leading to second-order quadrupolar interactions, and hence the appearance of satellite peaks in the NMR spectrum. The presence of well-resolved quadrupolar features confirms the ordered local environment in the crystalline phase. This is modelled using the isotropic chemical shift δ_{iso}, quadrupolar coupling constant X_Q and asymmetry parameter η. In the glass, there is a distribution of local environments. This leads to a wide range of chemical shifts and quadrupolar coupling constants, which causes the quadrupolar interactions to broaden and average out. As a result, the satellite peaks are merged into the baseline. For this spectrum, a single centre-of-gravity shift δ_{cg} is fitted. This observation further supports that the sample measured correspond to a glassy, disordered state.

5.3.4 Lithium Mobility

The potential for improved ionic conductivity was the original motivation for synthesising the antiperovskite glasses. To obtain an indication of the lithium dynamics in the Li_2OHBr glass, SLR-NMR measurements were taken as a function of temperature.

The $R_{1\rho}$ rate peaks for glass and crystalline Li_2OHBr are plotted in Figure 5.6. In both instances, two peaks ($R_{1\rho(max)}$) of very similar activation energy can be seen, as was observed for crystalline Li_2OHCl by Wilkening *et al.*[121]. These may be attributed to bulk Li-ion diffusion through the antiperovskite, and the onset of the hydroxyl-ion paddlewheel rotations, which has been the topic of extensive investigation, and is believed to help facilitate lithium ion

motion[113,118,120–122].

In the glass, a high-temperature flank activation energy of ~ 0.29 eV is seen for both mobility processes, which is substantially lower than in the crystalline material (~ 0.4 eV). The disorder in the glass flattens the energy landscape, making ion mobility more facile. In addition, the two peaks in the glass ($R_{1\rho(max)}$) appear at lower temperatures than in the crystalline material, suggesting that the glass has faster Li-ion dynamics. This is because ion hopping is thermally activated, and a lower temperature peak implies faster hopping at lower thermal energy.

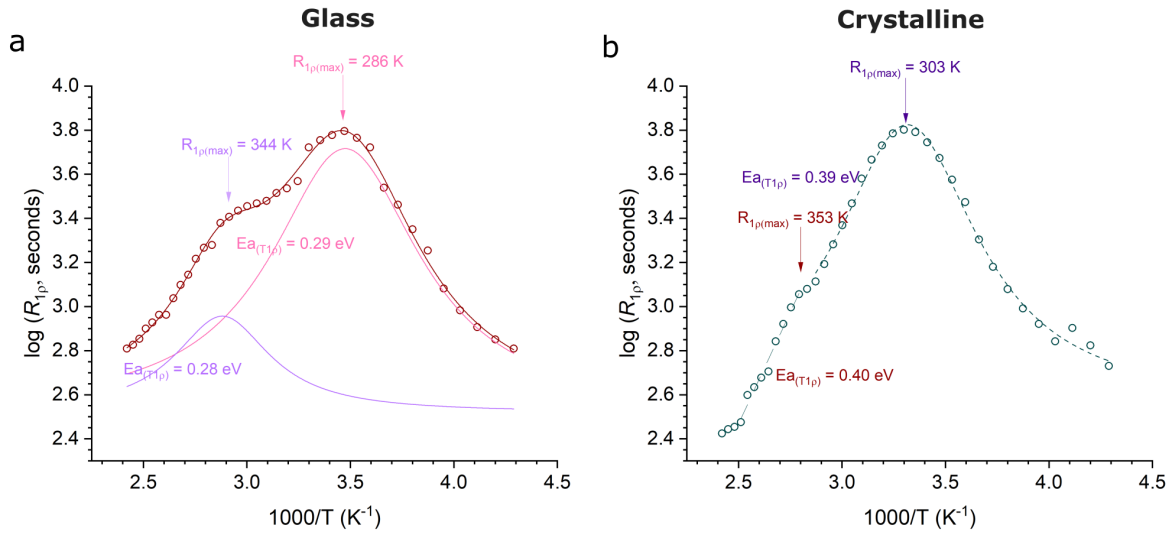

Figure 5.6: *Lithium ion Mobility. $T_{1\rho}$ SLR measurements and activation energies comparing a) glass and b) crystalline Li_2OHBr samples. Activation energies of 0.29 eV are seen for the processes in the glass, whereas a higher energy of 0.39 eV for the crystalline sample. The temperatures of these rate peaks also occur at lower temperatures in the glass sample.*

The Meyer-Neldel compensation law is an empirical relationship affecting thermally-activated processes, often observed in disordered materials. Specifically, the rule suggests that the activation energy (E_a) and the pre-exponential factor (σ_0) in an Arrhenius-type expression for conductivity are correlated, such that an increase in one is compensated by an increase in the other, thereby meaning a reduction in activation energy would not necessarily translate to an improvement in conductivity. The findings here indicate both a reduction in activation energy and increased hopping rate in glass samples. These observations suggest that in the case of Li_2OHBr antiperovskites, enhancements to the Li-ion conductivity are gained from vitrification.

T_1 SLR measurements were also taken on glass-ceramic Li_2OHBr samples, and are discussed in Appendix C.3. To eliminate any impacts from relaxation and crystallisation of the

glass phase which may be occurring upon heating, samples were limited to 150 °C and measured on 2 heating cycles. No changes were observed after heating, indicating that the glasses are stable in this range (Figure C.4).

5.3.5 Electrochemical Performance

Although the SLR-NMR measurements indicate improved lithium dynamics in the glassy state, these measurements only probe short-range motions and information about its ionic conductivity is unknown. In order to establish a macroscopic ionic conductivity, EIS measurements are desirable.

Direct Measurement

The ideal scenario would be to measure the ionic conductivity and activation energy directly from a glass flake. This would ensure the measurement is of the bulk glass, rather than any boundaries or interfaces found in pressed pellets, which are expected to be detrimental to the performance.

As such, the first approach taken was to sputter nickel contacts directly onto glass flakes, with a known area defined on both sides of the flake by a Kapton tape mask. For sufficiently large pieces, partially-transparent flakes had to be used. Photographs of this process are shown in Figures 5.7a and b. As shown in Figure 5.7c, a mostly homogeneous and conformal nickel film could be deposited on the glass surface this way. However, it was not possible to obtain measurements from these samples using copper foil contacts, due to their small size and extremely fragile nature. Post-mortem SEM images of samples showed fractured flakes, and in many instances delamination down the centre-line of the flake was seen (Figure 5.7d,e). This may contribute to why these flakes were not fully transparent. PFIB cross-sections showed the same phenomenon occurring in the centre of flakes, away from fracture sites, as pictured in Figure 5.7f. This presence of weak interfaces in the flakes is an unsurprising result of the twin-roll quench process used to manufacture them. These findings explain the inability to measure ionic conductivity through this method, and mean that an alternative approach is necessary.

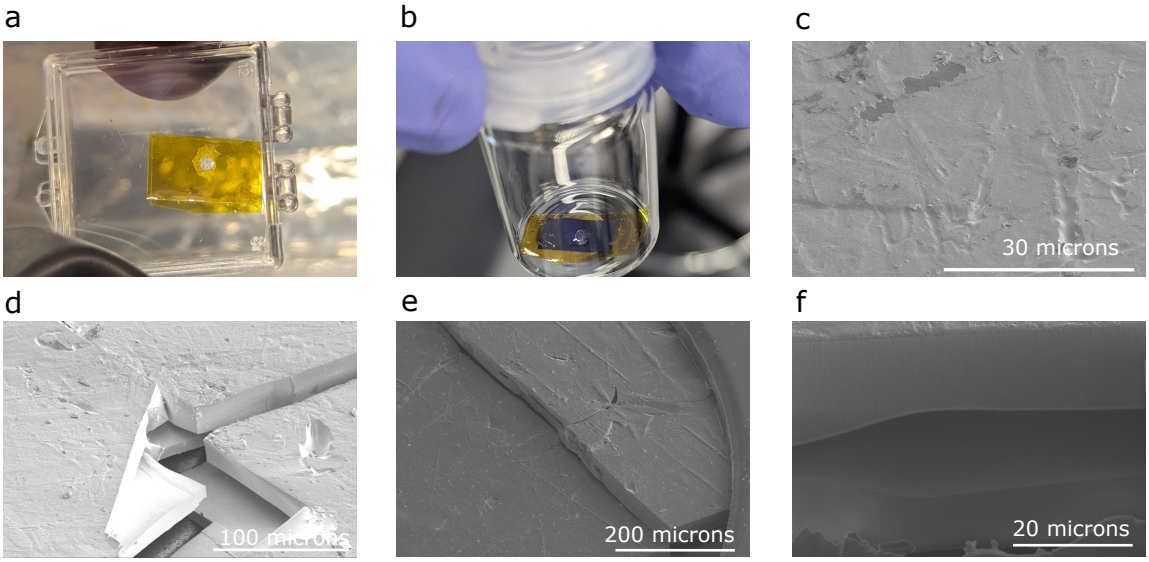

Figure 5.7: *Direct Electrochemical Measurement Attempts. a) A Glass-Ceramic Li_2OHBr flake with a Kapton tape mask defining a circular area on both sides of the flake. b) Flake after nickel sputtering. c) SEM image showing a homogeneous and conformal nickel layer on the flake. A small area appears to have lost its coating, potentially due to handling. d) SEM image of a fractured flake showing significant separation down the centre of the flake's cross-section. e) Another fracture surface showing the presence of an interface, with lesser delamination than the previous example. f) An SEM image of a PFIB cross-section in the centre of a flake, suggesting that these weak interfaces occur throughout the flakes.*

Cold-pressed Pellets

Subsequently, a conventional cold-pressing approach was taken to press pellets. High pressures are typically required to reduce impacts from particle interfaces. Solid electrolyte pellets of glass and crystalline Li_2OHBr samples were prepared in PEEK cells using a pressure of 370 MPa for 3 minutes. PFIB cross-sections indicated that the densification behaviour was comparable in both (Figure 5.8a), and EIS and CA measurements were taken to calculate values of ionic conductivity, activation energy and electronic conductivity. As can be seen in the Arrhenius plots and IV trends shown in Figure 5.8b and c, little variation was seen between the two samples. DSC was taken on a pressed Li_2OHBr glass pellet and didn't exhibit the glass transition behaviour observed in the pristine glass powder, indicating that crystallisation of the samples is occurring under pressure during the pellet pressing stage (Figure 5.8d). This means that the electrochemical performance of the glass phase is not being measured. The minor variations in performance might be due to slightly different porosities and grain sizes between the samples.

This meant that it was not possible to measure an ionic conductivity of the glasses. The

unstable nature of these glasses may make them impractical for any potential application as an electrolyte, regardless of their performance. Future work may focus on determining whether bulk samples can be produced without crystallisation, potentially by using lower pressing pressures, by optimising twin-roll quenching conditions to produce larger ribbons, or by exploring alternative synthesis routes such as thin-film techniques. Alternatively, efforts could be directed towards improving the crystallisation stability of these glasses, for example, by further exploring doping with traditional glass formers.

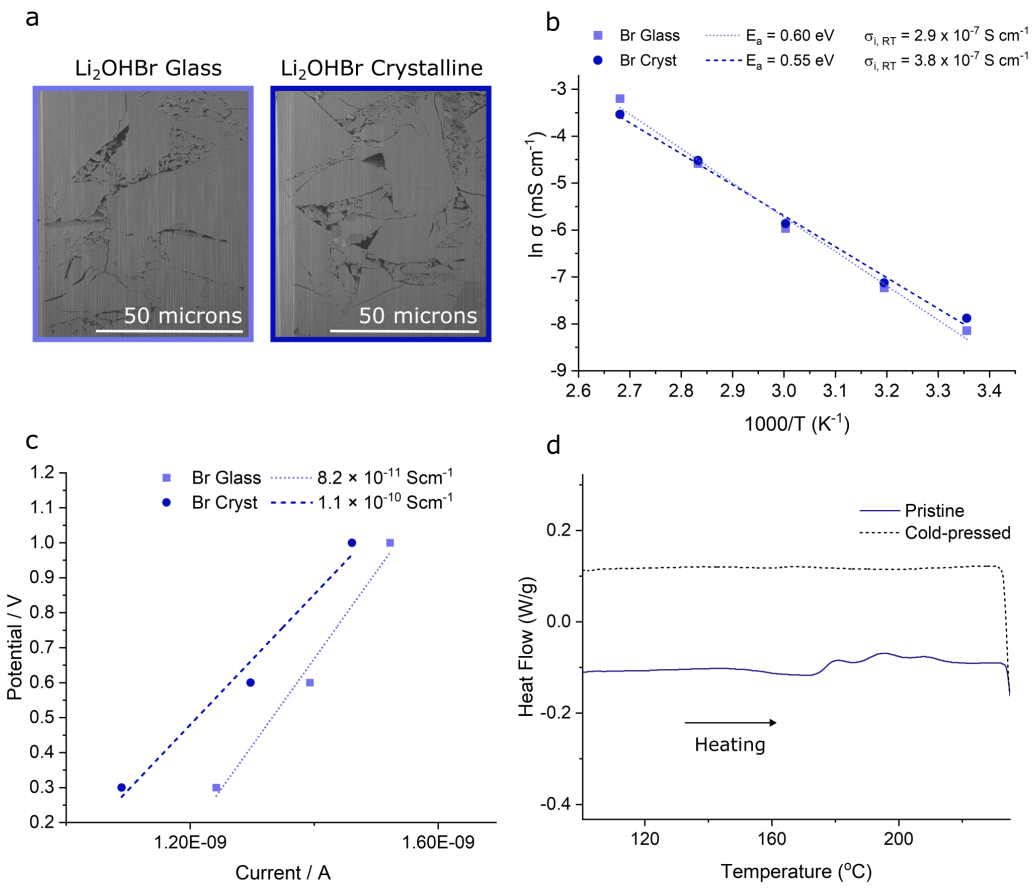

Figure 5.8: *Cold-Pressed Pellets. a) SEM images of PFIB cross-sections of cold-pressed glass and crystalline Li_2OHBr pellets. b) Comparison of their ionic conductivity with temperature. c) Comparison of their IV plots. d) Magnified DSC curve showing that the glass transition has been lost in glassy Li_2OHBr upon cold-pressing.*

5.4 Summary and Outlook

In this chapter, glassy Li_2OHBr, Li_2OHCl and $Li_2OHCl_{0.5}Br_{0.5}$ were synthesised. Pure glasses appear optically transparent, contain no XRD peaks, and exhibit a glass transition on their first heating cycle. These glasses were found to be challenging to synthesise, requiring extreme cooling rates achievable only by a twin-roll quench process. Synthesis was most successful with the Li_2OHBr composition. SLR-NMR measurements revealed a lower activation energy and higher hopping frequency in the glassy samples, indicating improved lithium dynamics when compared to the crystalline state. This improvement in dynamics may be due to the increased free volume in the glassy structure ($\frac{\rho_{glass}}{\rho_{cryst}} = 0.83$). It may also be attributable to a reduced ionic interaction of lithium ions with the glass structure, indicated by the more positive peak shift in ^{7}Li NMR measurements. In spite of these findings suggesting improvements to lithium dynamics may be gained from the vitrification of Li_2OHBr, cold-pressing pellets for EIS was found to result in their crystallisation. In further work, it would be beneficial to establish processing conditions for bulk glass electrolyte samples.

Chapter 6

Conclusions and Future Outlook

Energy storage is a critical area of research in the transition toward a sustainable future. This thesis has explored materials in the LiBr-LiOH binary system with potential applications in solid-state batteries and for TES. This material system is complicated by peritectic and peritectoid transformations, which has led to confusion in TES literature on $Li_4(OH)_3Br$, and may present limitations to the practical use of cast Li_2OHBr electrolyte pellets. Furthermore, the presence of previously uncharacterised high-temperature phase fields has hindered a complete understanding of this system.

The existence of a high-temperature $Li_3(OH)_2Br$ phase was verified and characterised using a combination of diffraction and NMR techniques, supported further with theoretical modelling. A hexagonal crystal structure belonging to the $P6_3/mmc$ space group was proposed, within which lithium experiences facile hopping. It would be desirable to retain this phase to room-temperature for use as a superionic conductor, however attempts to do so result in decomposition of the phase into either a combination of $Li_4(OH)_3Br$ and Li_2OHBr (as expected at equilibrium), or an alternative metastable state which exhibits poor lithium dynamics. Future research could investigate doping strategies, such as halide substitution, to stabilise $Li_3(OH)_2Br$ at lower temperatures. During these investigations, it was also revealed that previous reports on the crystal structure and characterisation of $Li_4(OH)_3Br$ have been impacted by air exposure effects. The thermodynamically-stable anhydrous phase is studied and a layered crystal structure belonging to the $Pmnm$ space group is proposed. It would be worthwhile to establish whether similar issues exist for the chloride analogue, $Li_4(OH)_3Cl$, where an equivalent crystal structure

has been reported as the literature $Li_4(OH)_3Br$. The latent heat of fusion of the revised crystal structure results in much lower melting enthalpies (263 J g^{-1}) than previously predicted (804 J g^{-1}). Additionally, the tendency of peritectic phases to undergo non-equilibrium solidification typically lowers this experimental value further ($\leq$ 250 J g^{-1}). Strategies to promote equilibrium solidification, such as with nucleating agents or encapsulation to prevent segregation, may present an interesting direction for future work. Several findings in this chapter highlighted inconsistencies with existing proposed LiBr–LiOH phase diagrams. These discrepancies suggest that a more accurate phase diagram may require the systematic application of *in-situ* diffraction techniques across the full composition range. Previous phase diagram proposals have predominantly relied on thermoanalytical methods, which are prone to capturing non-equilibrium transitions and may misrepresent true phase stability. Additionally, conventional approaches for phase diagram determination, such as "freezing-in" phases after annealing at different temperatures, proved problematic in this system. Specifically, involvement of the high-temperature $Li_3(OH)_2Br$ phase resulted in the formation of complex metastable products upon quenching. By employing *in-situ* methods to monitor phase evolution as a function of temperature, complications associated with quenching and the misidentification of metastable phases could be avoided.

Following this, the synthesis and microstructure of the antiperovskite Li_2OHBr was explored. Due to the peritectoid solidification of Li_2OHBr, the purity of samples cooled quickly was generally better than of those cooled at slower rates. However, by minimising nucleation sites and employing slow growth rates, it was possible to undercool into the Li_2OHBr phase field and directly nucleate single crystals. Although this method enabled the formation of large grains without the impurity concerns, it also led to substantial interconnected porosity which would make samples unsuitable for use as solid electrolytes. Future work might be able to address this issue by promoting planar growth via directional solidification using a Bridgman furnace. Access to high-quality Li_2OHBr single crystals would enable fundamental diffraction and NMR studies into the crystal structure and conductivity mechanisms in antiperovskites, as well as investigations into the impact of grain boundaries and defects on cell cycling performance and failure mechanisms. In Chapter 4, the related antiperovskite $Li_5(OH)_2Br_3$ was also studied, but offered no advantages in conductivity nor ease of synthesis over the conventional Li_2OHBr antiperovskite.

The final part of this work looked at whether the conductivity of antiperovskite elec-

trolytes could be improved through vitrification. Li_2OHX (X = Br, Cl) glasses were synthesised through a melt-quench approach using a twin-roll quencher. XRD, DSC and NMR were used to confirm the glassy state of these samples. SLR-NMR measurements indicated improved lithium dynamics in these samples, likely due to the increased free volume in the glassy state. However, the glasses were found to be unstable against crystallisation, with cold-pressing inducing unwanted crystallisation. Practical use of these materials will require either improved synthesis approaches (for example, forming bulk glass ribbons) or chemical stabilisation (for example, doping to enhance stability).

Chapter 7

Appendices

Appendix A

Appendix for Chapter 3

The following appendix provides additional information relevant to Chapter 3.

A.1 Additional Refinement Information

Table A.1: XRD peak positions (CuKα) corresponding to the $Li_3(OH)_2Br$ phase at 250 °C, used to search for the lattice parameters and space group of the $Li_3(OH)_2Br$ phase.

Peak Position / $2\theta(^o)$
15.6
16.5
17.6
22.7
27.1
29.4
31.4
31.9
32.5
33.3

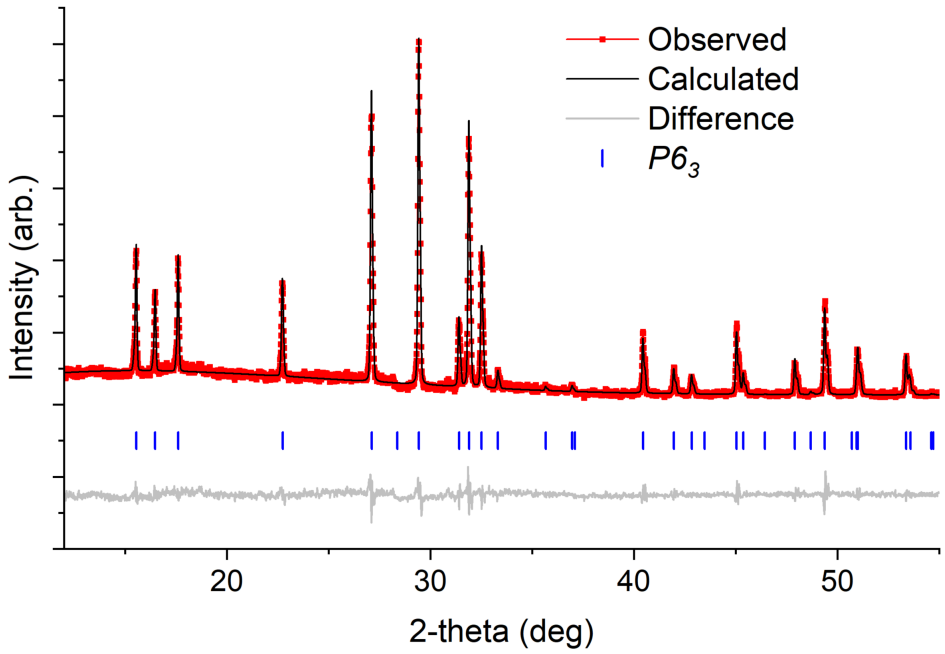

Figure A.1: *XRD pattern of $Li_3(OH)_2Br$ at 250 °C and corresponding Pawley refinement ($R_{wp} = 10.5\%$) for the $P6_3$ space group. The corresponding difference curve is offset below the data. Bragg peak positions expected from the space group symmetry are shown with ticks.*

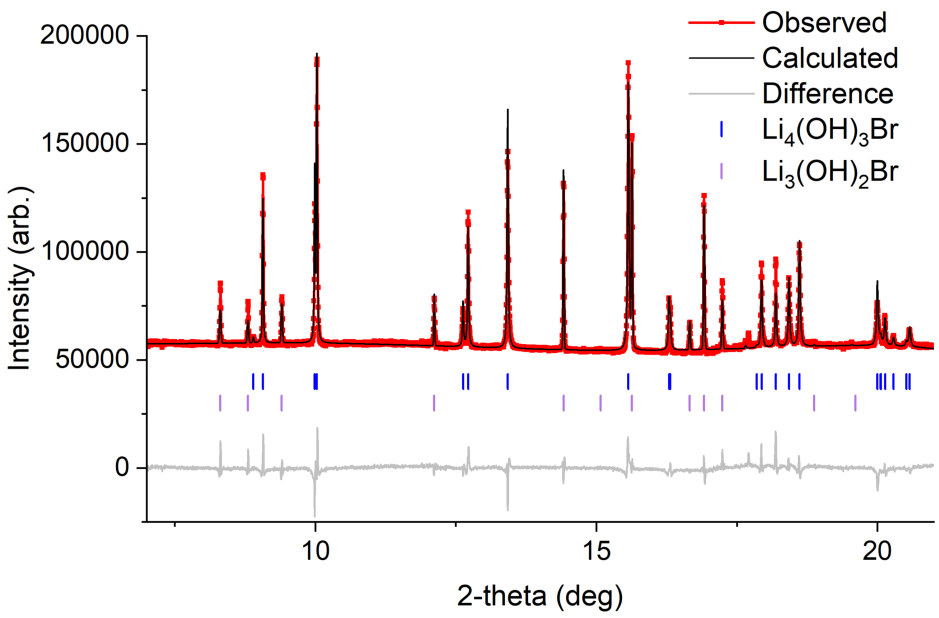

Figure A.2: *Synchrotron powder XRD pattern of a 75 mol % LiOH sample at* 250 °C *and corresponding Rietveld refinement (R_{wp} = 1.5 %) for Pmnm $Li_4(OH)_3Br$ and $P6_3/mmc$ $Li_3(OH)_2Br$, the Bragg peak positions of which are indicated with ticks. The resulting difference curve is offset beneath the data. Samples were quenched to room temperature from* 400 °C *and reheated at* 6 °C*/min. The sample contains a large fraction of $P6_3/mmc$ $Li_3(OH)_2Br$ due to the high heating rate employed meaning equilibrium conditions are not attained. Refinement details are provided in Tables A.2 and A.3.*

Table A.2: Crystallographic parameters for the *Pmnm* structure of $Li_4(OH)_3Br$ *in-situ* at 250 °C, from the fit shown in Figure A.2. Refined parameters are indicated with errors in parentheses.

a (Å)	10.41180(17)					
b (Å)	5.30463(7)					
c (Å)	5.27890(7)					
V (Å^3)	291.557(7)					
Atom	Wyckoff position	x	y	z	Occupancy	U_{iso} (Å^2)
Br1	2b	0.25	0.3675(4)	0.75	1	0.006(2)
O1	4f	-0.02508	0.12415	0.25	1	0.006(2)
O2	2a	0.25	-0.05675	0.25	1	0.006(2)
Li1	8g	0.61587	-0.053665	0.5171	1	0.006(2)
H1	4f	-0.05934	0.2956	0.25	1	0.006(2)
H2	2a	0.25	0.75881	0.25	1	0.006(2)

Table A.3: Unit cell parameters for the $P6_3/mmc$ structure of $Li_3(OH)_2Br$ present in the diffraction pattern in Figure A.2 *in-situ* at 250 °C. Errors are given in parentheses.

Unit Cell	
$a = b$ (Å)	6.55948(6)
c (Å)	10.72619(14)
V (Å^3)	399.682(9)

A.2 Computational Modelling Details

The computational modelling reported in this thesis was carried out by Dr James Quirk and Professor James Dawson from Newcastle University. The details of the computational approach used, provided by Dr Quirk, are outlined here.

A preliminary AIRSS[229] run was performed on several hundred geometries for $Li_3(OH)_2Br$ and $Li_4(OH)_3Br$ using the pre-trained CHGNet foundation model. Then, a CHGNet model was fine-tuned for Li-O-H-Br systems by training against a set of MD trajectories. The systems were: solid Li_2OHBr, $Li_3(OH)_2Br$, and $Li_4(OH)_3Br$ at 900 K with *NPT* ensemble; and molten Li_2OHBr, $Li_3(OH)_2Br$, and $Li_4(OH)_3Br$ at 2000 K with *NVT* ensemble. The fine-tuned model was then used for the final AIRSS to determine the stable structures in this work and all further MD runs. Due to the importance of H-bonding in materials containing OH species, dispersion was treated using the DFT-D3 method[230] using the implementation in `torch-dftd`.[231]

For modelling of the $Li_3(OH)_2Br$, analysis of the MD trajectories was performed with `Pymatgen`[232] and `Gemdat`,[233] which allows for decomposition of activation energies into distinct hops between atomic sites. Fully-occupied unit cells were produced by the structure searching. Then, a supercell was constructed and equilibrated at 250 °C. Partially occupied sites were determined by wrapping the trajectory back into the unit cell to determine stable sites. Because Li diffuses so readily in the structure, the convergence of site occupancies is poor. For simplicity, the occupation of the determined stable sites was normalized to give the correct number of Li per unit cell.

All geometry optimisations were carried out until forces on ions were less than 0.05 eV/Å. The time-step for MD was 0.5 fs to ensure numerical stability when integrating equations of motion due to the small mass and rapid acceleration of protons. The computational activation energy was fitted to temperatures of 220 °C, 230 °C, 230 °C, 235 °C, 240 °C 245 °C, 250 °C, 260 °C, and 270 °C. All trajectories are at least 250 ps long. For fitting to the Einstein relation, the trajectories were split into 5 parts to calculate mean-squared displacements in order to reduce errors arising from deviations from linearity in long trajectories.[234] Simulated NMR and ab-initio MD for fine-tuning was performed in VASP. Exchange-correlation was treated with the PBE functional.[235] Projector-augmented wave (PAW) pseudopotentials[236,237] were employed in

which the following electrons were treated as valence: $1s^1$ for H, $1s^2 2s^1$ for Li; $2s^2 2p^4$ for O; and $4s^2 4p^5$ for Br. The plane wave basis used a cutoff energy of 500 eV.

For modelling of $Li_4(OH)_3Br$, analysis of the MD trajectories was performed with `Pymatgen`[232] and the Atomic Simulation Environment[238]. All geometry optimizations were carried out until forces on ions were less than 0.05 eV/Å. The time-step for molecular dynamics was 0.5 fs to ensure numerical stability when integrating equations of motion due to the small mass and rapid acceleration of protons. All MD calculations used a supercell that was a $2 \times 4 \times 4$ expansion of the unit cell. Enthalpy of melting is determined using the same procedure as Alvarez et. al[239]. The structure was melted and equilibrated at 1200 K for a total of 50 ps. For temperatures between 230 °C and 260 °C in increments of 10 °C, MD was performed on the solid material and the liquid material, for at least 100 ps with 25 ps of equilibration to allow the material to come to the correct temperature. The mean enthalpy across each run was taken then, by fitting straight lines to the solid and the liquid branch, the enthalpy of melting can be determined from the difference between the two lines.

A.3 Additional Computational Results

Table A.4: Crystallographic parameters from the computationally-determined $P6_3$ $Li_3(OH)_2Br$ crystal structure, shown in Figure A.3.

Space Group	$P6_3$				
$a = b$ (Å)	6.437163				
c (Å)	10.617548				
V (Å^3)	381.017				
Atom	Wyckoff position	x	y	z	Occupancy
Br1	2b	1/3	2/3	0.913445	1
Br2	2b	1/3	2/3	0.282528	1
O1	6c	0.147307	0.804925	0.592446	1
O2	2a	1	0	0.814739	1
Li1	6c	0.529535	0.470658	0.0354630	0.214
Li2	6c	0.5496650	0.449422	0.174301	0.214
Li3	2b	2/3	1/3	0.027143	0.214
Li4	2b	2/3	1/3	0.146215	0.214
Li5	6c	0.770769	0.707472	0.917378	0.214
Li6	6c	0.941172	0.709313	0.919614	0.214
Li7	6c	0.111691	0.899328	0.984623	0.214
Li8	6c	0.180061	0.354849	0.091703	0.214
Li9	6c	0.872638	0.709476	0.258420	0.214
Li10	6c	0.818558	0.905321	0.193865	0.214
Li11	2a	0	0	0.525085	0.214
Li12	2a	0	0	0.661937	0.214

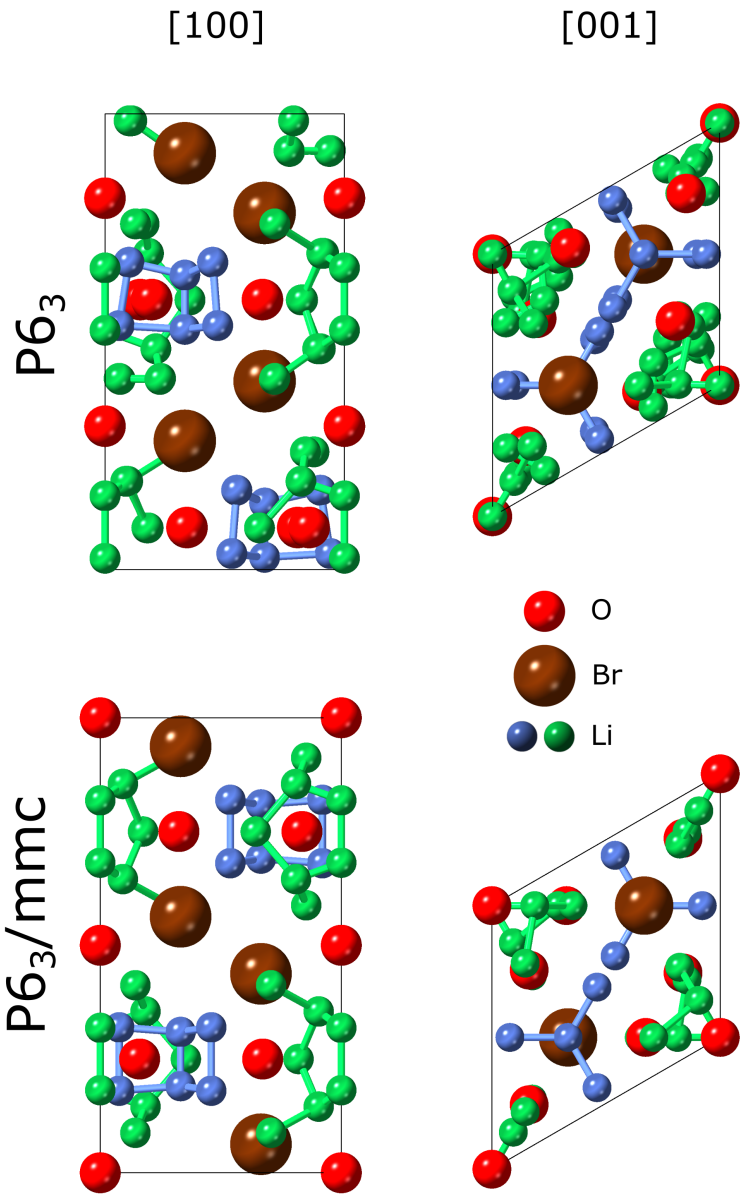

Figure A.3: *Comparison of the computationally-determined $P6_3$ model for $Li_3(OH)_2Br$ (top) and the final refined $P6_3/mmc$ structure (bottom), viewed along [100] and [001]. Note that the origin of the $P6_3/mmc$ unit cell is shifted along the c-axis relative to the $P6_3$ structure to satisfy the additional symmetry constraints. Lithium sites are depicted as fully occupied for easier visualisation, but are expected to correspond to 0.214 in the $P6_3$ structure and 0.24 in the $P6_3/mmc$ structure.*

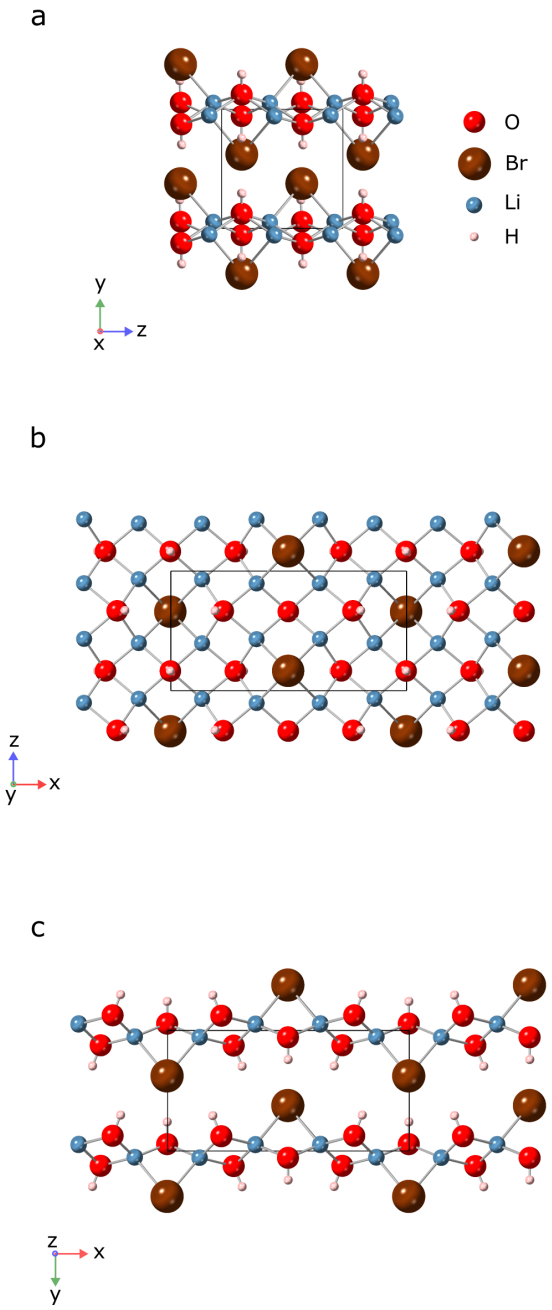

Figure A.4: *Computationally-predicted crystal structure for $Li_4(OH)_3Br$ found using AIRSS and optimisation, viewed along a) [100], b) [010] and c) [001]. Atomic positions are detailed in Table A.5.*

Table A.5: Crystallographic parameters from the computationally-determined $Li_4(OH)_3Br$ crystal structure, shown in Figure A.4

a (Å)	10.585518		
b (Å)	5.281199		
c (Å)	5.370332		
V (Å^3)	300.224241		
Atom	x	y	z
Br1	-0.002293	0.376336	0.660738
Br2	0.497465	0.622271	0.165855
Li1	0.363473	0.943347	0.430843
Li2	0.132275	0.055429	-0.068900
Li3	0.863662	0.052760	-0.067498
Li4	0.632133	0.941236	0.433144
Li5	0.132208	0.054273	0.396716
Li6	0.363737	0.949365	-0.103164
Li7	0.631353	0.948983	-0.101322
Li8	0.864054	0.049794	0.398415
O1	0.222310	0.877160	0.665833
O2	0.273436	0.124696	0.163587
O3	0.723143	0.122543	0.165993
O4	0.772337	0.873474	0.667914
O5	-0.001979	0.942669	0.164455
O6	0.498076	0.056167	0.662108
H1	0.186982	0.705983	0.668619
H2	0.308211	0.296109	0.163812
H3	0.689276	0.293827	0.167676
H4	0.805416	0.701549	0.671058
H5	-0.001788	0.758156	0.164731
H6	0.498654	0.240542	0.653282

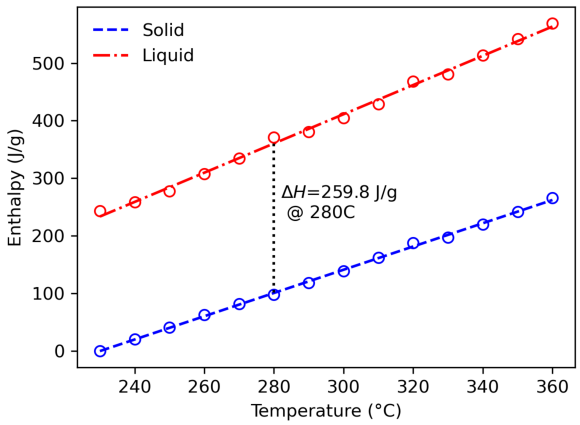

Figure A.5: *Plot used to theoretically estimate the enthalpy of melting of $Li_4(OH)_3Br$ from the computationally-predicted crystal structure. A value of 259.8 J g^{-1} is found from the difference between the solid and liquid lines at* 280 °C.

A.4 Additional $Li_3(OH)_2Br$ EIS

Identical samples of 67 mol % LiOH stoichiometry, cooled to room temperature from 350 °C at 3 °C/min and ground into a powder, were measured by EIS. In both cases, samples were held at the desired temperature for 30 minutes prior to measurement, followed by a 15 minute ramp period to the next temperature. Sample 1 (shown in the main text) was measured at the following temperatures consecutively: 25 °C, 100 °C, 150 °C, 200 °C, 210 °C, 220 °C, 230 °C, 240 °C, 250 °C, 260 °C. Sample 2 underwent additional cooling steps at 250 °C, 240 °C, 230 °C, 220 °C and 210 °C following the heating measurements. Arrhenius plots of the total conductivities obtained from these measurements are shown in Figure A.6. Note that the heating measurement at 240 °C on sample 2 failed, and so does not appear in the plot.

In both cases, a step in conductivity is seen between the low temperature regime and the $Li_3(OH)_2Br$ phase, and this change was reversible upon cooling. A slight increase in ionic conductivity can be seen between the heating and cooling cycles. This is likely due to the additional sintering and grain growth occurring during the extended periods at elevated temperatures.

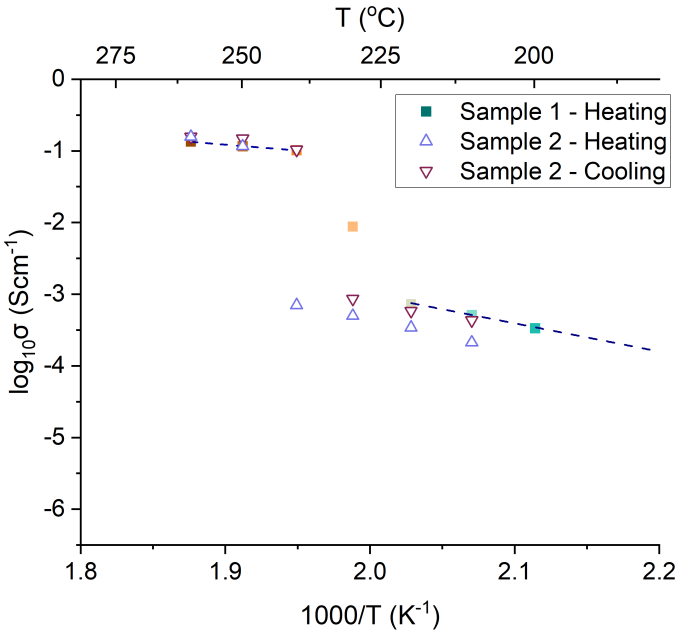

Figure A.6: *Arrhenius plot showing the ionic conductivity of cold-pressed $Li_3(OH)_2Br$ samples upon heating and cooling, to establish whether microstructural changes occurring upon heating impact the measurements. The conductivity measurements in the $Li_3(OH)_2Br$ phase field are very similar upon heating and cooling.*

Appendix B

Appendix for Chapter 4

The following appendix provides additional information relevant for Chapter 4.

B.1 Further Li_2OHBr impurity investigations

To verify that the purity of Li_2OHBr could not be improved by adjusting the stoichiometry, slightly off stoichiometries were investigated. As the LiOH content was increased, the LiBr impurity disappeared. Diffraction peaks matching those of the quenched $Li_3(OH)_2Br$ phase became visible in fast-cooled samples with excess LiOH, as the anticipated $Li_3(OH)_2Br$ content increases. Impurities in slow-cooled samples became particularly complicated, and peaks in XRD could not be identified. This is perhaps not surprising given the complexity proposed in this region of the phase diagram, and the inaccuracies indicated in Chapter 3. Examples from these investigations are given in Figures B.1 and B.2.

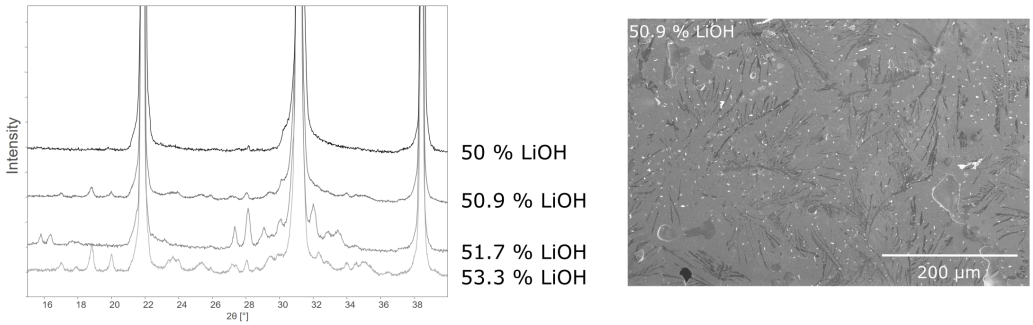

Figure B.1: *Fast-cooled samples of Li_2OHBr with stoichiometries with small LiOH excesses. Left: XRD patterns showing impurity formation as the LiOH content is increased. Some impurity peaks correspond to those observed for quenched $Li_3(OH)_2Br$. Right: SEM image of polished fast-cooled sample with composition 50.9 mol % LiOH. The dark branched minority phase might correspond to impurity with the $Li_3(OH)_2Br$ stoichiometry.*

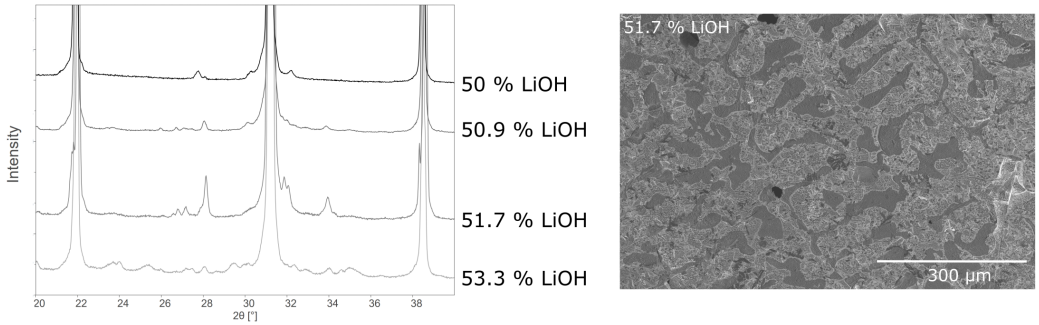

Figure B.2: *20-hour cooled samples of Li_2OHBr with stoichiometries with small LiOH excesses. Left: XRD patterns showing impurity formation as the LiOH content is increased. The LiBr peaks disappear and new impurities form. Right: SEM image of polished 20-hour cooled sample with composition 51.7 mol % LiOH.*

B.2 Li_2OHBr Solidification Microstructure

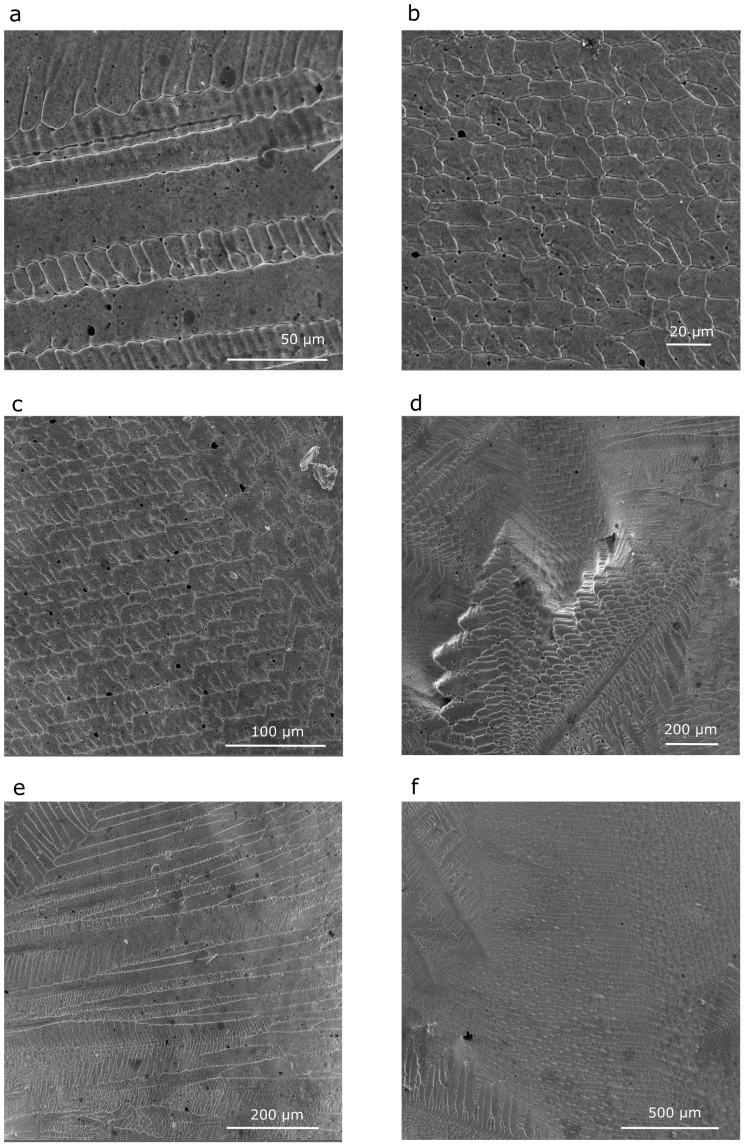

Figure B.3: *Selection of SEM images showing the surface of fast-cooled Li_2OHBr pellets. Dendritic and cellular microstructures are observed. A range of feature sizes as small as $\sim 10\mu m$ are seen.*

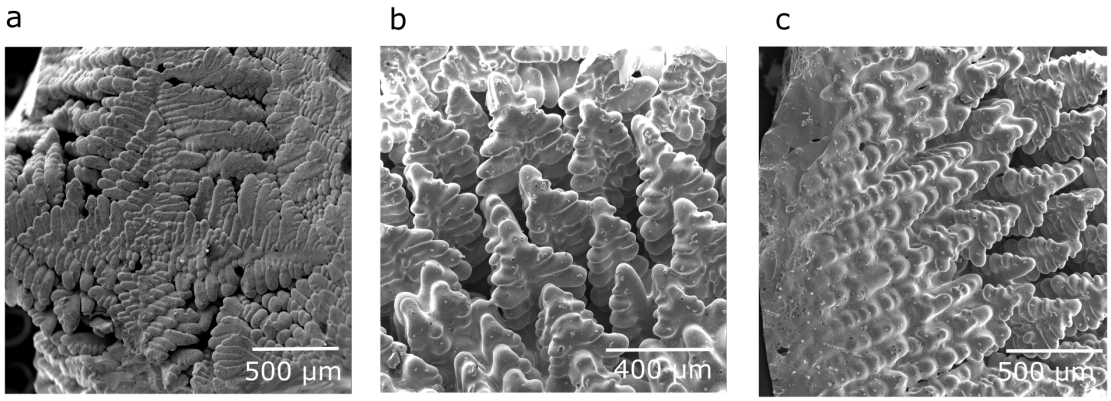

Figure B.4: *SEM images of the surface of 20-hour cooled Li_2OHBr pellets showing very coarse dendrites.*

B.3 Li_2OHBr and $Li_5(OH)_2Br_3$ Electrochemistry

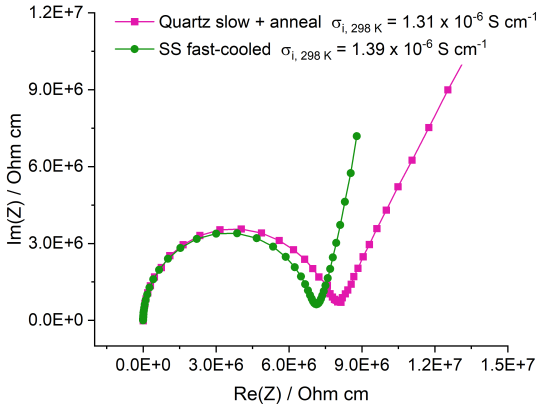

Figure B.5: *Nyquist plots of EIS measurements on pouch cells of pellets of Li_2OHBr prepared by the fast-cooled approach in a SS mould, and by the quartz tube slow cool and anneal route. Data is normalised by pellet area and thickness. A very similar ionic conductivity is measured in both.*

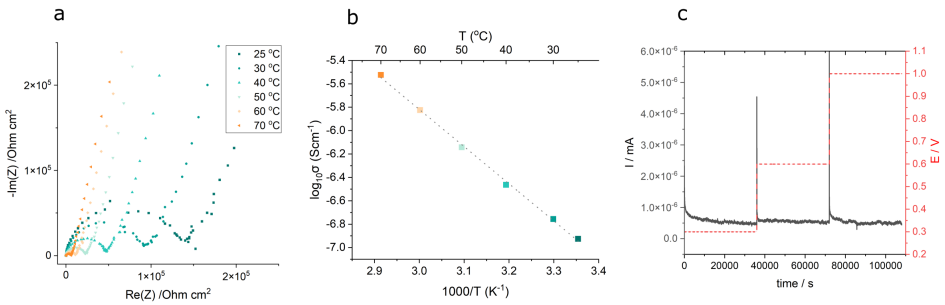

Figure B.6: *$Li_5(OH)_2Br_3$ electrochemistry. a) Nyquist plots from EIS measurements of cold-pressed pellets of $Li_5(OH)_2Br_3$ at temperatures between 25 °C and 70 °C. b) Temperature-dependent ionic conductivity of $Li_5(OH)_2Br_3$ calculated using total resistances measured in (a). c) DC CA measurements on cold-pressed pellets of $Li_5(OH)_2Br_3$ used to calculated electronic conductivity of the sample.*

B.4 Additional $Li_5(OH)_2Br_3$ Refinements

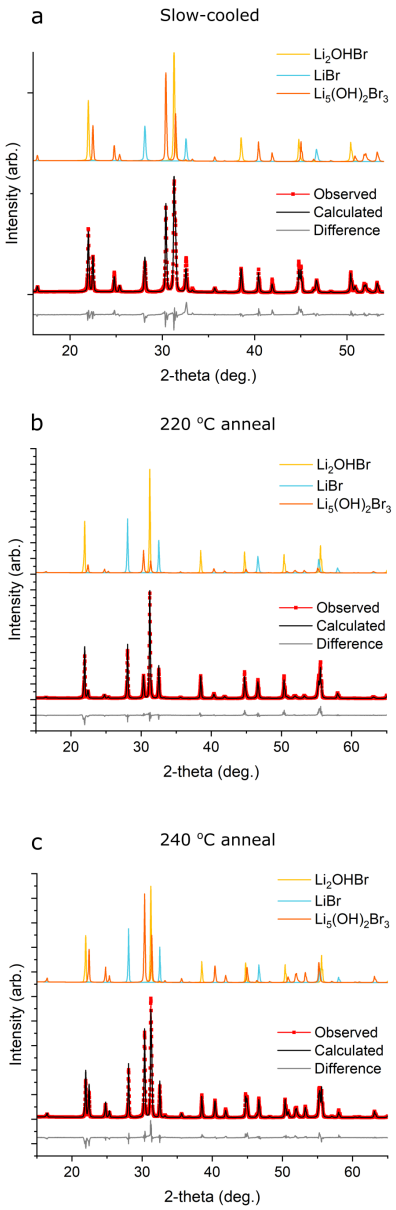

Figure B.7: *Rietveld refinements of 40 mol % LiOH samples (a) furnace-cooled, and samples quenched followed by annealing at (b)* 220 °C *and (c)* 240 °C.

Table B.1: Structural information for the $Li_5(OH)_2Br_3$ phase from the Rietveld refinement in Figure 4.8c (R_{wp} = 8.4 %). The structural model was taken from reference[141] and the unit cell allowed to refine. Errors are indicated in parentheses.

Space group	$I4/mmm$				
a (Å)	4.03085(7)				
b (Å)	4.03085(7)				
c (Å)	21.5711(4)				
Atom	Wyckoff position	x	y	z	Occupancy
Br1	2b	0	0	0.5	1
Br2	4e	0	0	0.31113	1
Li1	2a	0	0	0	0.68
Li2	4e	0	0	0.1861	1
Li3	8g	0	0.5	0.09	0.59
O1	4e	0	0	0.0964	1

Table B.2: Unit cell of $Li_5(OH)_2Br_3$ produced under different synthesis conditions determined by Rietveld refinements. Errors on values are indicated in parentheses.

Phase	Quenched	220 °C	240 °C	247 °C	Furnace-cooled
$Li_5(OH)_2Br_3$					
$a = b$ (Å)	4.0360(6)	4.0345(2)	4.03319(12)	4.03085(7)	4.0280(2)
c (Å)	21.527(4)	21.5602(17)	21.5585(8)	21.5711(4)	21.5706(13)
Li_2OHBr					
$a = b = c$ (Å)	4.04886(6)	4.05075(8)	4.04991(8)	4.04875(17)	4.0483(2)
LiBr					
$a = b = c$ (Å)	5.50327(11)	5.50773(13)	5.50764(13)	5.5146(2)	5.5033(3)
R_{wp}	10.5	11.5	11.0	8.4	12.8

B.5 $Li_5(OH)_2Br_3$ and the LiBr-LiOH Phase Diagram

In Chapter 4 it was suggested that two narrow phase fields may exist between 250 °C and 255 °C in the 0 - 50 mol % LiOH range. This differs from the single field previously suggested, in order to accommodate for the $Li_5(OH)_2Br_3$ phase. It is difficult to verify the existence of these two intermediate phase fields due to their narrow temperature windows and close proximity. Nonetheless, in DSC measurements taken on 30 mol % LiOH and 47 mol % LiOH samples (Figure B.8a,b), the signal appears to be a convolution of three different peaks, which could indicate three phase transitions as proposed here. This can also be seen in DSC measurements

taken for 29 mol % LiOH and 43 mol % LiOH by Mahroug *et al.*, although the authors did not discuss this in their work[9].

SEM images and EDX mapping of 40 mol % LiOH samples cooled from 350 °C to 240 °C at 0.2 °C/min, annealed for 4 hours and then quenched to room temperature, were taken (Figure B.8c). In these images, 4 different phases can be seen: dark oxygen-rich regions thought to be $Li_3(OH)_2Br$, pale oxygen-free regions corresponding to LiBr, and low-contrast intergrown regions believed to be Li_2OHBr and $Li_5(OH)_2Br_3$. Although a non-equilibrium microstructure, the presence of each of these phases is consistent with a sample which has been cooled through the phase fields proposed in the phase diagram in Figure 4.10b.

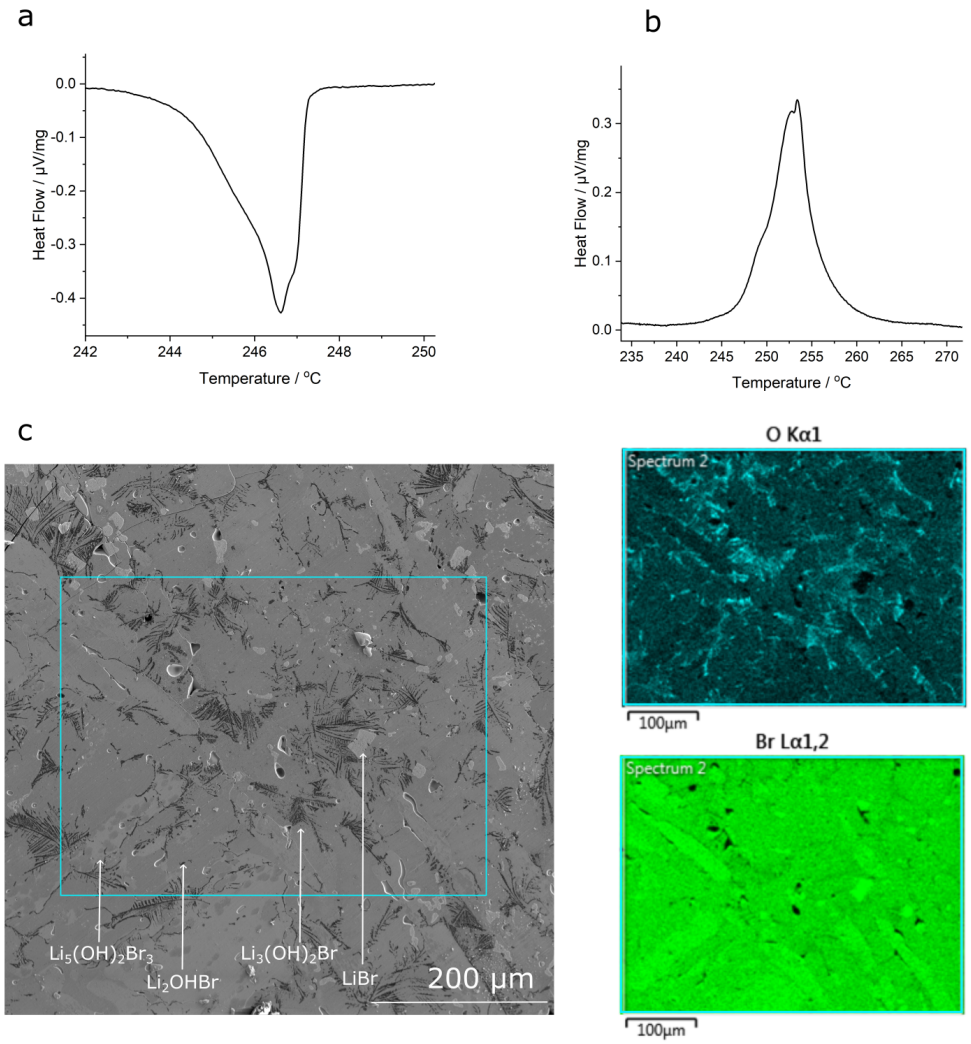

Figure B.8: *a) DSC cooling curve for 30 mol % LiOH sample, taken at* $5\,^{\circ}\mathrm{C}/\mathrm{min}$*. The asymmetric line shows two shoulders, suggesting a convolution of three peaks. b) DSC heating curve of 47 mol % LiOH sample, similarly showing evidence of three peaks. c) SEM image and EDX mapping insets of a 40 mol % LiOH sample cooled from* $350\,^{\circ}\mathrm{C}$ *to* $240\,^{\circ}\mathrm{C}$ *at* $0.2\,^{\circ}\mathrm{C}/\mathrm{min}$*, annealed for 4 hours and quenched to room temperature. A four-phase microstructure is obtained.*

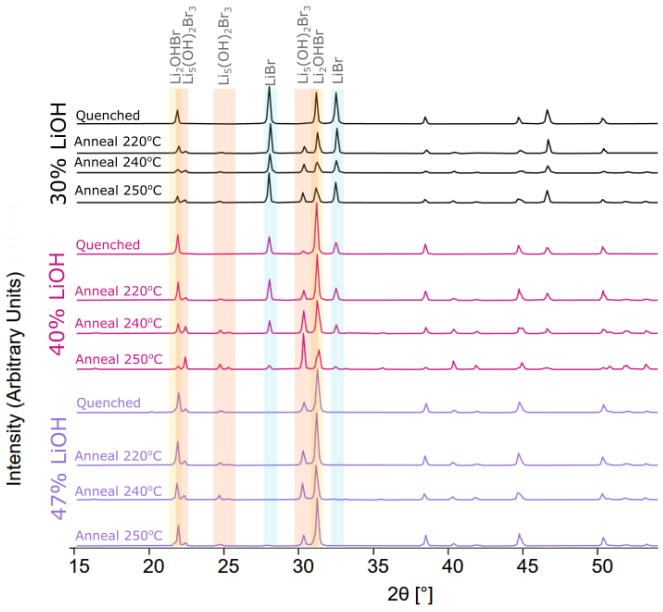

Figure B.9: *XRD patterns of samples with compositions of 30, 40 and 47 mol % LiOH synthesised under a variety of conditions. Samples to the left of the $Li_5(OH)_2Br_3$ field contain LiBr excesses, whereas those to the right contain Li_2OHBr, as expected.*

Appendix C

Appendix for Chapter 5

The following appendix provides additional information for Chapter 5.

C.1 Glass Fraction Estimation in $Li_2OHCl_{0.5}Br_{0.5}$ Glass-Ceramics

To estimate the amorphous fraction in samples, an internal standard method was used[240]. A known mass of an internal standard was mixed into the sample and the XRD pattern measured. Background subtraction and peak integration was carried out using PDXL2 software. The amorphous fraction in the sample can be estimated by considering the observed relative intensities of the phases in the XRD pattern (i.e. the crystalline response) to the known ratio of the two samples. Equations C.1 and C.2 can be used to this outcome:

$$\left(\frac{I_{sample}}{I_{standard}}\right) \times \text{wt fraction standard} = F_{cryst} \tag{C.1}$$

$$F_{amorph} = 1 - F_{cryst} \tag{C.2}$$

Both a silicon nanopowder and LiCl granule were explored as a standard for this process. These materials have few XRD peaks, distinct from the antiperovskite peaks, and did not react with the samples upon mixing. The low masses of glasses available for testing meant that

homogeneous mixtures could not be easily produced when using the LiCl granules, even using a mortar and pestle for the mixing process. The fine nature of the nanopowder meant that this was not a problem with the silicon standard. However, the nanopowder contains a large fraction of amorphous material, which needed to be accounted for. Consequently, the crystalline fraction in the silicon nanopowder was estimated through an internal standard method with LiCl. The availability of these materials meant that larger batches with better mixing could be done. As shown in Table C.1, this gave an amorphous fraction of 68 % ± 5 % in the silicon nanopowder, which could then be accounted for in the glass internal standard calculations by multiplying $I_{standard}$ by $\frac{100}{100-68}$. This gave amorphous contents between 64 % and 71 % for the $Li_2OHCl_{0.5}Br_{0.5}$ glass ceramics (Table C.2).

Table C.1: Intensities determined from XRD of Si-LiCl mixtures, used to establish the amorphous content in silicon nanopowder. "Standard" refers to LiCl and the "sample" to silicon.

Sample	**Wt % Standard**	**Sample Intensity / CPS**	**Standard Intensity / CPS**	**Sample Amorphous Content %**
1	35.24	21382	30223	64.8
2	55.46	17663	34111	71.3
Average				**68.0 ± 4.6**

Table C.2: Intensities determined from XRD of $Li_2OHCl_{0.5}Br_{0.5}$ - Si mixtures, along with the 'corrected' standard intensity accounting for the 68 % amorphous content in the silicon nanopowder. Estimations of the amorphous content in glass-ceramic samples are calculated using the outlined approach.

Sample	**Wt % Standard**	**Intensity**			**Sample Amorphous Content %**
		Sample / CPS	**Standard / CPS**	**Corrected Standard / CPS**	
1	9.05	63124	6459	20184	71.7
2	18.57	74275	12352	38624	64.3
3	11.10	50061	5372	16799	66.9

C.2 Supplementary Glass SEM and EDX

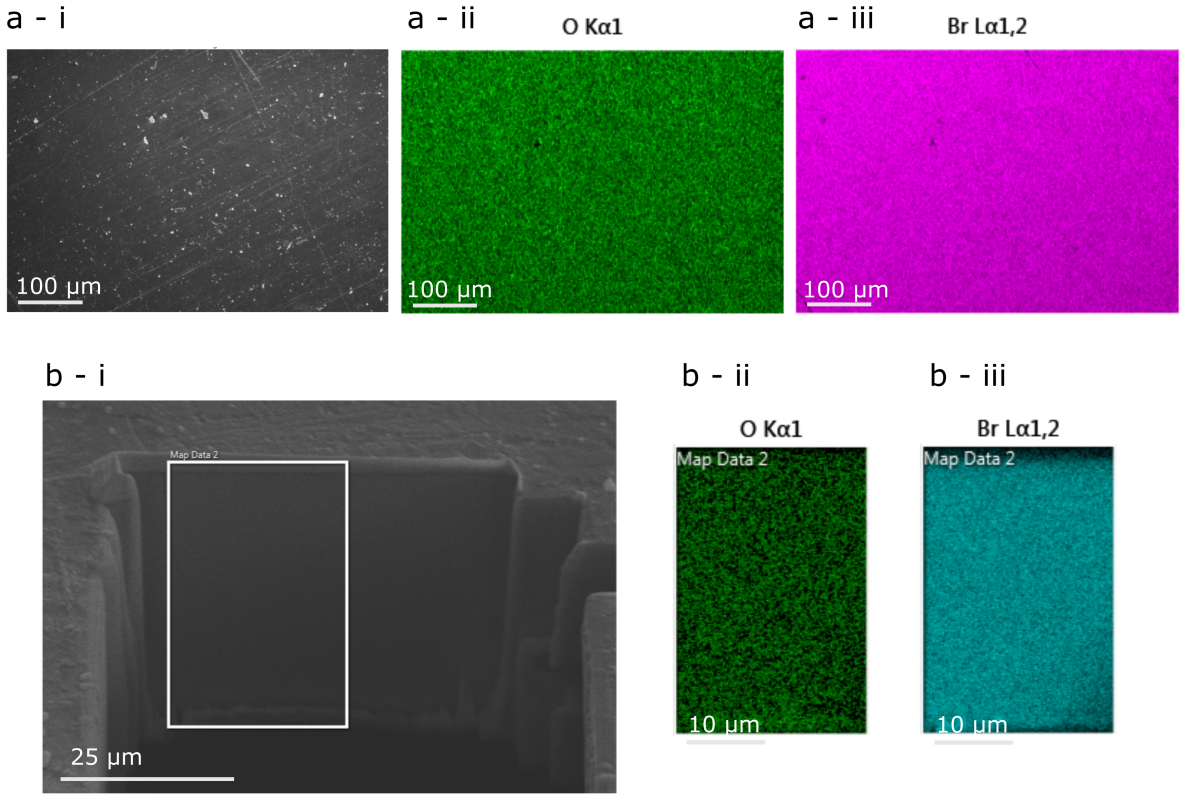

Figure C.1: *SEM images and corresponding EDX mapping of the a) surface, and b) PFIB cross-section, of a glass Li_2OHBr flake. Note that white specs in a-i correspond to surface contamination.*

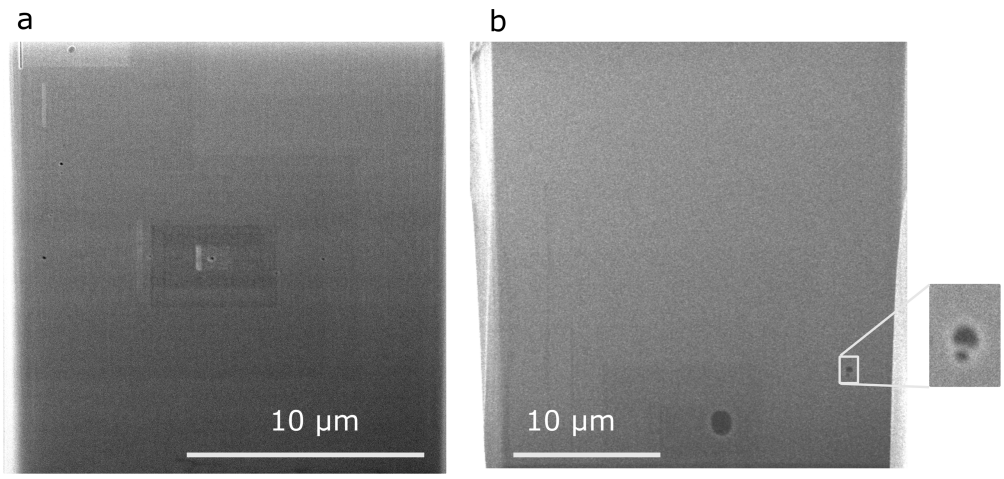

Figure C.2: *Cross-sectional PFIB images of Li_2OHBr glass flakes, showing low porosity in each case. a) The same region as shown in Figure 5.5b. Here clear halos can be seen around the pores, supporting that the features are pores, opposed to inclusions of another phase. Note that the boxes present correspond to regions of beam damage arising from imaging. b) A different flake, showing a few larger pores, but still a high relative density.*

C.3 Glass-Ceramic NMR

Figure C.3a shows another example glass-ceramic MAS ^{7}Li spectrum taken at 313 K and deconvoluted into glass and crystalline components. Figure C.3b is an equivalent measurement on a pure crystalline sample. The spectra were fitted at each temperature to give the peak positions and FWHMs plotted in Figure C.3c and d respectively. The onset of motional narrowing of peaks can often be used to estimate an activation energy for thermal processes, however this narrowing onsets below the measured temperature range here. Additionally, peak broadening in glasses also arises due to the broader range of chemical environments present, and so can also influence interpretation. Nonetheless, the shape of the crystalline contributions appear similar in the pure and glass-ceramic samples, supporting the assignment of the crystalline peaks in this model.

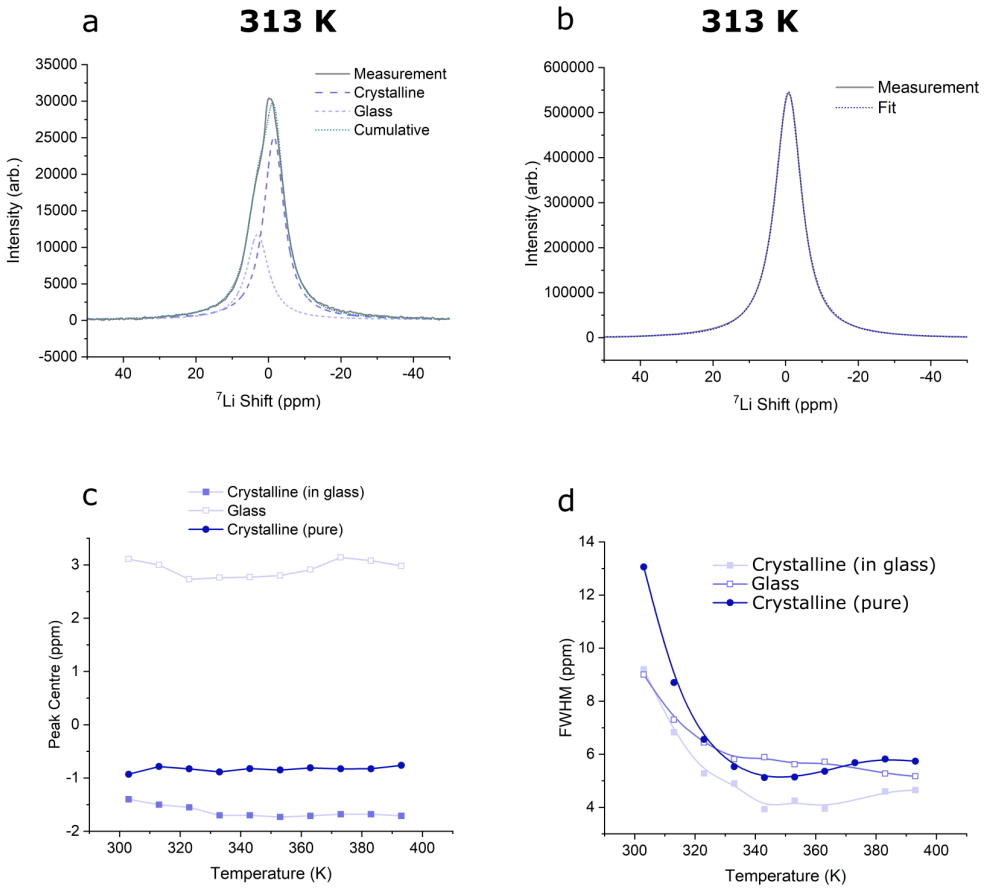

Figure C.3: *Peak model applied to the ^{7}Li MAS-NMR spectra. a) Glass-ceramic at 313 K, b) Crystalline sample at 313 K. c) Peak centres plotted as a function of temperature. Curve fitting was carried out using 2 Gaussian-Lorentzian peaks. A small shift in position of the crystalline peak is seen between the glass-ceramic and pure crystalline sample due to the differing environment. d) FWHMs of the peaks in the peak model as a function of temperature. Motional narrowing occurs as the temperature increases.*

T_1 SLR measurements were also taken on some glass-ceramic Li_2OHBr samples, shown in Figure C.4a. Since T_1 measurements probe faster molecular motions than $T_{1\rho}$ measurements, only the low temperature flank of the rate peak is visible in the available temperature range. This means that a comparison of the hopping frequencies in the samples (from the peak tops) cannot be made. Nonetheless, an Arrhenius fit can be used to estimate an activation energy for lithium hopping, and gives a value of 0.39 eV for the crystalline samples (in excellent agreement with the $T_{1\rho}$ measurements). The apparent activation energies for the glass ceramic samples (0.34 eV, 0.36 eV) lie between that of the pure crystalline material (0.39 eV) and the T_1 activation energy of the pure glass material (0.29 eV), as would be anticipated. Since these T_1 measurements correspond to the low temperature flank of the rate peak, disorder is expected to affect the

apparent activation energy such that they appear higher than the true value, and so the activation energies of the glass-ceramics are likely to be overestimated here.

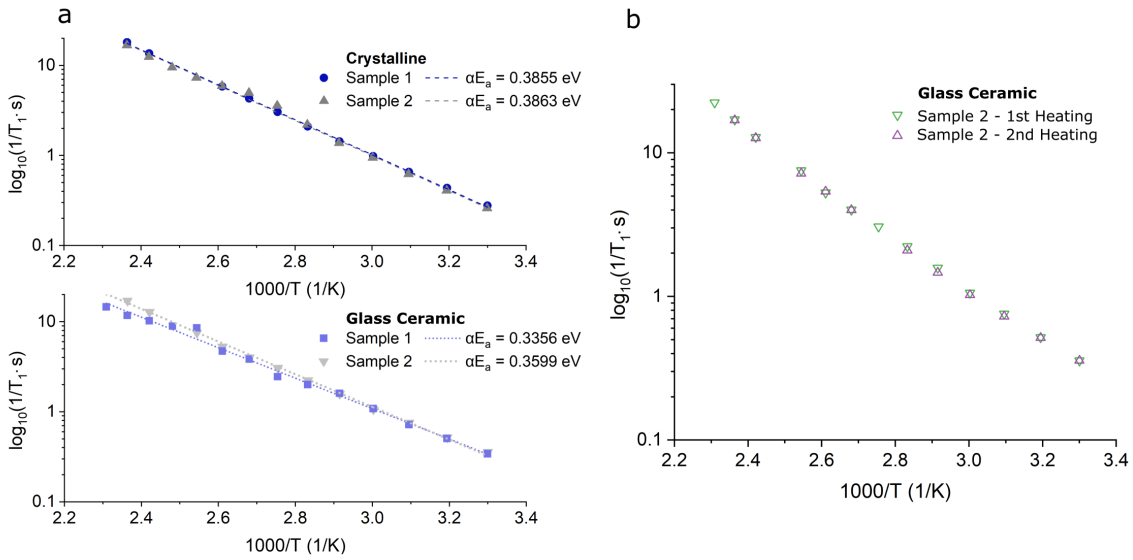

Figure C.4: *Additional SLR measurements. a) T_1 SLR measurements of 2 crystalline and 2 glass-ceramic Li_2OHBr samples. The activation energy for the crystalline samples is accurately reproducible. Slight variation in the glass-ceramic samples could be due to differences in crystalline content. b) T_1 SLR measurement on a glass-ceramic sample upon 2 heating cycles, confirming that no irreversible changes such as crystallisation are occurring upon heating in this temperature range on short timescales.*

Bibliography

[1] A Mucha-Geppert, A Agosta, A Weiss, A Mohammad, B Heid, B Stackhouse, C Ding, D Hernandez Diaz, E Furnari, F van der Marel, Liebach F, G Boccara, G Pinheiro, G Kudar, H Tai, I Nadeem, J Noffsinger, R Gonzalez J, L Di Fiori, M Prieto, M Patel, M Waardenburg, M Smith, M Foucart, M Van Hoey, M Nivard, N Sharma, N Zanardi, P Ovidio, P Chen, R Majiti, R Clune, S de Sa, T Grunewald, T Hundertmark, T Moller, T Naucler, U Weihe, and V Agarwal. Global energy perspective 2024, 2024. URL https://www.mckinsey.com/industries/energy-and-materials/our-insights/global-energy-perspective.

[2] T Kousksou, P Bruel, A Jamil, T El Rhafiki, and Y Zeraouli. Energy storage: Applications and challenges. *Solar Energy Materials and Solar Cells*, 120:59–80, 2014. ISSN 09270248. doi: 10.1016/j.solmat.2013.08.015.

[3] J Gasia, L Miró, and L F Cabeza. Review on system and materials requirements for high temperature thermal energy storage. Part 1: General requirements. *Renewable and Sustainable Energy Reviews*, 75:1320–1338, 2017. ISSN 18790690. doi: 10.1016/j.rser.2016.11.119.

[4] G Wei, G Wang, C Xu, X Ju, L Xing, X Du, and Y Yang. Selection principles and thermophysical properties of high temperature phase change materials for thermal energy storage: A review. *Renewable and Sustainable Energy Reviews*, 81:1771–1786, 1 2018. ISSN 18790690. doi: 10.1016/j.rser.2017.05.271.

[5] M M Kenisarin. High-temperature phase change materials for thermal energy storage. *Renewable and Sustainable Energy Reviews*, 14(3):955–970, 4 2010. ISSN 13640321. doi: 10.1016/j.rser.2009.11.011.

[6] F Achchaq, E Palomo Del Barrio, E Lebraud, S Péchev, and J Toutain. Development of a

new LiBr/LiOH-based alloy for thermal energy storage. *Journal of Physics and Chemistry of Solids*, 131:173–179, 2019. doi: 10.1016/j.jpcs.2019.04.001.

[7] P Legros, E Lebraud, M Duquesne, and F Achchaq. Li4Br(OH)3 microstructure monitoring over its synthesis to tackle the lithium-based salts exploitation challenges as advanced phase change materials for storage technologies. *Materials and Design*, 196:109160–109170, 11 2020. ISSN 18734197. doi: 10.1016/j.matdes.2020.109160.

[8] I Mahroug, S Doppiu, J L Dauvergne, M Echeverria, J Toutain, and E Palomo del Barrio. Study of peritectic compound Li4(OH)3Br for high temperature thermal energy storage in solar power applications. *Solar Energy Materials and Solar Cells*, 230:111259–111261, 9 2021. ISSN 09270248. doi: 10.1016/j.solmat.2021.111259.

[9] I Mahroug, S Doppiu, J L Dauvergne, J Toutain, and E P del Barrio. Extended investigation of LiOH–LiBr binary system for high-temperature thermal energy storage applications. *Journal of Thermal Analysis and Calorimetry*, 147(22):12455–12465, 11 2022. ISSN 15882926. doi: 10.1007/s10973-022-11468-4.

[10] I Mahroug, L González-Fernández, Y Grosu, S Doppiu, and E Palomo. Compatibility of container materials with peritectic phase change material for high-temperature thermal energy storage. *Journal of Energy Storage*, 73:108892–108905, 12 2023. ISSN 2352152X. doi: 10.1016/j.est.2023.108892.

[11] C Prieto, L F Cabeza, M C Pavón-Moreno, and E Palomo. Thermal energy storage for direct steam generation concentrating solar power plants: Concept and materials selection. *Journal of Energy Storage*, 83:110618–110627, 4 2024. ISSN 2352152X. doi: 10.1016/j.est.2024.110618.

[12] N Nitta, F Wu, J T Lee, and G Yushin. Li-ion battery materials: Present and future. *Materials Today*, 18(5):252–264, 6 2015. ISSN 18734103. doi: 10.1016/j.mattod.2014.10.040.

[13] J Fleischmann, M Hanicke, E Horetsky, D Ibrahim, S Jautelat, M Linder, P Schaufuss, L Torscht, and A van de Rijt. Battery 2030: Resilient, sustainable, and circular, 2023. URL https://www.mckinsey.com/industries/automotive-and-assembly/our-insights/battery-2030-resilient-sustainable-and-circular.

[14] R A Huggins. *Advanced Batteries: Materials Science Aspects*. Springer, 2009.

[15] J Janek and W G Zeier. A solid future for battery development. *Nature Energy*, 1(9):1–4, 2016. ISSN 20587546. doi: 10.1038/nenergy.2016.141.

[16] J B Goodenough and K S Park. The Li-Ion Rechargeable Battery: A Perspective. *Journal of the American Chemical Society*, 135(4):1167–1176, 1 2013. ISSN 0002-7863. doi: 10.1021/ja3091438.

[17] J Liu, Z Bao, Y Cui, E J Dufek, J B Goodenough, P Khalifah, Q Li, B Y Liaw, P Liu, A Manthiram, Y S Meng, V R Subramanian, M F Toney, V V Viswanathan, M S Whittingham, J Xiao, W Xu, J Yang, X Q Yang, and J G Zhang. Pathways for practical high-energy long-cycling lithium metal batteries. *Nature Energy*, 4(3):180–186, 3 2019. ISSN 20587546. doi: 10.1038/s41560-019-0338-x.

[18] D Lu, Y Shao, T Lozano, W D Bennett, G L Graff, B Polzin, J Zhang, M H Engelhard, N T Saenz, W A Henderson, P Bhattacharya, J Liu, and J Xiao. Failure mechanism for fast-charged lithium metal batteries with liquid electrolytes. *Advanced Energy Materials*, 5(3):1400993–1400993, 2 2015. ISSN 16146840. doi: 10.1002/aenm.201400993.

[19] B Wu, J Lochala, T Taverne, and J Xiao. The interplay between solid electrolyte interface (SEI) and dendritic lithium growth. *Nano Energy*, 40:34–41, 10 2017. ISSN 22112855. doi: 10.1016/j.nanoen.2017.08.005.

[20] E J Cheng, A Sharafi, and J Sakamoto. Intergranular Li metal propagation through polycrystalline Li6.25Al0.25La3Zr2O12 ceramic electrolyte. *Electrochimica Acta*, 223:85–91, 1 2017. ISSN 00134686. doi: 10.1016/j.electacta.2016.12.018.

[21] C Fang, J Li, M Zhang, Y Zhang, F Yang, J Z Lee, M H Lee, J Alvarado, M A Schroeder, Y Yang, B Lu, N Williams, M Ceja, L Yang, M Cai, J Gu, K Xu, X Wang, and Y S Meng. Quantifying inactive lithium in lithium metal batteries. *Nature*, 572(7770):511–515, 8 2019. ISSN 14764687. doi: 10.1038/s41586-019-1481-z.

[22] J R Dahn, J C Burns, and D A Stevens. Importance of Coulombic Efficiency Measurements in R&D Efforts to Obtain Long Lived Li-Ion Batteries. *The Electrochemical Society Interface*, 25(75):75–78, 2016. doi: 10.1149/2.F07163if.

[23] C M MacLaughlin. Innovations in Lithium Ion Battery Technologies: A Conversation with

Will West, Nancy Dudney, and Andrew Westover. *ACS Energy Letters*, 4(3):786–788, 3 2019. ISSN 2380-8195. doi: 10.1021/acsenergylett.9b00358.

[24] C Monroe and J Newman. The Impact of Elastic Deformation on Deposition Kinetics at Lithium/Polymer Interfaces. *Journal of The Electrochemical Society*, 152(2):A396, 2005. ISSN 00134651. doi: 10.1149/1.1850854.

[25] T Famprikis, P Canepa, J A Dawson, M S Islam, and C Masquelier. Fundamentals of inorganic solid-state electrolytes for batteries. *Nature Materials*, 18(12):1278–1291, 12 2019. ISSN 14764660. doi: 10.1038/s41563-019-0431-3.

[26] M Pasta, D Armstrong, Z L Brown, J Bu, M R Castell, P Chen, A Cocks, S A Corr, E J Cussen, E Darnbrough, V Deshpande, C Doerrer, M S Dyer, H El-Shinawi, N Fleck, P Grant, G L Gregory, C Grovenor, L J Hardwick, J T S Irvine, H J Lee, G Li, E Liberti, I McClelland, C Monroe, P D Nellist, P R Shearing, E Shoko, W Song, D Spencer-Jolly, C I Thomas, S J Turrell, M Vestli, C K Williams, Y Zhou, and P G Bruce. 2020 roadmap on solid-state batteries. *Journal of Physics: Energy*, 2(3):032008, 7 2020. ISSN 25157655. doi: 10.1088/2515-7655/ab95f4.

[27] L Fan, S Wei, S Li, Q Li, and Y Lu. Recent Progress of the Solid-State Electrolytes for High-Energy Metal-Based Batteries. *Advanced Energy Materials*, 8(11):1702657, 4 2018. ISSN 16146840. doi: 10.1002/aenm.201702657.

[28] T Inoue and K Mukai. Are all-solid-state lithium-ion batteries really safe?verification by differential scanning calorimetry with an all-inclusive microcell. *ACS Applied Materials and Interfaces*, 9(2):1507–1515, 1 2017. ISSN 19448252. doi: 10.1021/acsami.6b13224.

[29] J C Bachman, S Muy, A Grimaud, H Chang, N Pour, S F Lux, O Paschos, F Maglia, S Lupart, P Lamp, L Giordano, and Y Shao-Horn. Inorganic Solid-State Electrolytes for Lithium Batteries: Mechanisms and Properties Governing Ion Conduction. *Chemical Reviews*, 116(1):140–162, 1 2016. ISSN 0009-2665. doi: 10.1021/acs.chemrev.5b00563.

[30] K M Diederichsen, E J McShane, and B D McCloskey. Promising Routes to a High Li + Transference Number Electrolyte for Lithium Ion Batteries. *ACS Energy Letters*, 2(11): 2563–2575, 11 2017. ISSN 2380-8195. doi: 10.1021/acsenergylett.7b00792.

[31] F Han, A S Westover, J Yue, X Fan, F Wang, M Chi, D N Leonard, N J Dudney, H Wang, and C Wang. High electronic conductivity as the origin of lithium dendrite formation within solid electrolytes. *Nature Energy*, 4(3):187–196, 3 2019. ISSN 20587546. doi: 10.1038/s41560-018-0312-z.

[32] W D Richards, L J Miara, Y Wang, J C Kim, and G Ceder. Interface Stability in Solid-State Batteries. *Chemistry of Materials*, 28(1):266–273, 1 2016. ISSN 15205002. doi: 10.1021/acs.chemmater.5b04082.

[33] A Manthiram, X Yu, and Shaofei Wang. Lithium battery chemistries enabled by solid-state electrolytes. *Nature Reviews Materials*, 2(4):1–16, 2017. ISSN 20588437. doi: 10.1038/natrevmats.2016.103.

[34] M Dirican, C Yan, P Zhu, and X Zhang. Composite solid electrolytes for all-solid-state lithium batteries. *Materials Science and Engineering R: Reports*, 136:27–46, 4 2019. ISSN 0927796X. doi: 10.1016/j.mser.2018.10.004.

[35] M A Ratner and D F Shriver. Ion Transport in Solvent-Free Polymers. *Chemical Reviews*, 88:109–124, 1988. doi: 10.1021/cr00083a006.

[36] X Yang, M Jiang, X Gao, D Bao, Q Sun, N Holmes, H Duan, S Mukherjee, K Adair, C Zhao, J Liang, W Li, J Li, Y Liu, H Huang, L Zhang, S Lu, Q Lu, R Li, C Veer Singh, and X Sun. Determining the limiting factor of the electrochemical stability window for PEO-based solid polymer electrolytes: Main chain or terminal -OH group? *Energy and Environmental Science*, 13(5):1318–1325, 2020. ISSN 17545706. doi: 10.1039/d0ee00342e.

[37] C Sun, J Liu, Y Gong, D P Wilkinson, and J Zhang. Recent advances in all-solid-state rechargeable lithium batteries. *Nano Energy*, 33:363–386, 3 2017. ISSN 22112855. doi: 10.1016/j.nanoen.2017.01.028.

[38] N Kamaya, K Homma, Y Yamakawa, M Hirayama, R Kanno, M Yonemura, T Kamiyama, Y Kato, S Hama, K Kawamoto, and A Mitsui. A lithium superionic conductor. *Nature Materials*, 10(9):682–686, 2011. ISSN 14764660. doi: 10.1038/nmat3066.

[39] W Zhao, J Yi, P He, and H Zhou. Solid-State Electrolytes for Lithium-Ion Batteries: Fundamentals, Challenges and Perspectives. *Electrochemical Energy Reviews*, 2(4):574–605, 12 2019. ISSN 25208136. doi: 10.1007/s41918-019-00048-0.

[40] E J Cussen. Structure and ionic conductivity in lithium garnets. *Journal of Materials Chemistry*, 20(25):5167, 2010. ISSN 0959-9428. doi: 10.1039/b925553b.

[41] P Hartmann, T Leichtweiss, M R Busche, M Schneider, M Reich, J Sann, P Adelhelm, and J Janek. Degradation of NASICON-type materials in contact with lithium metal: Formation of mixed conducting interphases (MCI) on solid electrolytes. *Journal of Physical Chemistry C*, 117(41):21064–21074, 10 2013. ISSN 19327447. doi: 10.1021/jp4051275.

[42] W Zhang, D Schröder, T Arlt, I Manke, R Koerver, R Pinedo, D A Weber, J Sann, W G Zeier, and J Janek. (Electro)chemical expansion during cycling: Monitoring the pressure changes in operating solid-state lithium batteries. *Journal of Materials Chemistry A*, 5 (20):9929–9936, 2017. ISSN 20507496. doi: 10.1039/c7ta02730c.

[43] B Wu, S Wang, W J Evans, D Z Deng, J Yang, and J Xiao. Interfacial behaviours between lithium ion conductors and electrode materials in various battery systems. *Journal of Materials Chemistry A*, 4(40):15266–15280, 2016. ISSN 20507496. doi: 10.1039/c6ta05439k.

[44] F Han, J Yue, C Chen, N Zhao, X Fan, Z Ma, T Gao, F Wang, X Guo, and C Wang. Interphase Engineering Enabled All-Ceramic Lithium Battery. *Joule*, 2(3):497–508, 3 2018. ISSN 25424351. doi: 10.1016/j.joule.2018.02.007.

[45] E Kazyak, R Garcia-Mendez, W S LePage, A Sharafi, A L Davis, A J Sanchez, K H Chen, C Haslam, J Sakamoto, and N P Dasgupta. Li Penetration in Ceramic Solid Electrolytes: Operando Microscopy Analysis of Morphology, Propagation, and Reversibility. *Matter*, 2 (4):1025–1048, 4 2020. ISSN 25902385. doi: 10.1016/j.matt.2020.02.008.

[46] J Kasemchainan, S Zekoll, D Spencer-Jolly, Z Ning, G O Hartley, J Marrow, and P G Bruce. Critical stripping current leads to dendrite formation on plating in lithium anode solid electrolyte cells. *Nature Materials*, 18:1105–1111, 10 2019. ISSN 1476-1122. doi: 10.1038/s41563-019-0438-9.

[47] L Porz, T Swamy, B W Sheldon, D Rettenwander, T Frömling, H L Thaman, S Berendts, R Uecker, W C Carter, and Y M Chiang. Mechanism of Lithium Metal Penetration through Inorganic Solid Electrolytes. *Advanced Energy Materials*, 7(20):1701003–1701014, 10 2017. ISSN 16146840. doi: 10.1002/aenm.201701003.

[48] R Raj and J Wolfenstine. Current limit diagrams for dendrite formation in solid-state electrolytes for Li-ion batteries. *Journal of Power Sources*, 343:119–126, 2017. ISSN 03787753. doi: 10.1016/j.jpowsour.2017.01.037.

[49] J Wolfenstine, J L Allen, J Sakamoto, D J Siegel, and H Choe. Mechanical behavior of Li-ion-conducting crystalline oxide-based solid electrolytes: a brief review. *Ionics*, 24(5): 1271–1276, 5 2018. ISSN 18620760. doi: 10.1007/s11581-017-2314-4.

[50] M Ohring. *Chapter 11: Interdiffusion, Reactions, and Transformations in Thin Films. Materials Science of Thin Films*. Elsevier, 2002. doi: 10.1016/B978-0-12-524975-1.X5000-9.

[51] Y Mishin and C Herzig. Grain boundary diffusion: recent progress and future research. *Materials Science and Engineering*, 260:55–71, 1999. doi: 10.1016/S0921-5093(98)00978-2.

[52] J A Dawson, P Canepa, T Famprikis, C Masquelier, and M S Islam. Atomic-Scale Influence of Grain Boundaries on Li-Ion Conduction in Solid Electrolytes for All-Solid-State Batteries. *Journal of the American Chemical Society*, 140(1):362–368, 1 2018. ISSN 15205126. doi: 10.1021/jacs.7b10593.

[53] Xujie Lü, John W. Howard, Aiping Chen, Jinlong Zhu, Shuai Li, Gang Wu, Paul Dowden, Hongwu Xu, Yusheng Zhao, and Quanxi Jia. Antiperovskite Li3 OCl superionic conductor films for solid-state li-ion batteries. *Advanced Science*, 3(3), 3 2016. ISSN 21983844. doi: 10.1002/advs.201500359.

[54] X Lü, G Wu, J W Howard, A Chen, Y Zhao, L L Daemen, and Q Jia. Li-rich anti-perovskite Li3OCl films with enhanced ionic conductivity. *Chemical Communications*, 50 (78):11520–11522, 9 2014. ISSN 1364548X. doi: 10.1039/c4cc05372a.

[55] J Zhu, S Li, Y Zhang, J W Howard, X Lü, Y Li, Y Wang, R S Kumar, L Wang, and Y Zhao. Enhanced ionic conductivity with Li7O2Br3 phase in Li3OBr anti-perovskite solid electrolyte. *Applied Physics Letters*, 109(10), 9 2016. ISSN 00036951. doi: 10.1063/1.4962437.

[56] C Ma, K Chen, C Liang, C W Nan, R Ishikawa, K More, and M Chi. Atomic-scale origin of the large grain-boundary resistance in perovskite Li-ion-conducting solid electrolytes. *Energy and Environmental Science*, 7(5):1638–1642, 2014. ISSN 17545706. doi: 10.1039/c4ee00382a.

[57] J F Wu and X Guo. Origin of the low grain boundary conductivity in lithium ion conducting perovskites: Li3xLa0.67-xTiO3. *Physical Chemistry Chemical Physics*, 19(8):5880–5887, 2017. ISSN 14639076. doi: 10.1039/c6cp07757a.

[58] S K Tiku and F A Kroger. Effects of Space Charge Grain-Boundary Segregation and Mobility Differences Between Grain Boundary and Bulk on the Conductivity of Polycrystalline Al2O3. *Journal of the American Ceramic Society*, 63(3-4):183–189, 1980. doi: 10.1111/j.1151-2916.1980.tb10688.x.

[59] A Tschope. Grain size-dependent electrical conductivity of polycrystalline cerium oxide II: Space charge model. *Solid State Ionics*, 139:267–280, 2001. doi: 10.1016/S0167-2738(01)00677-4.

[60] X Guo and Y Ding. Grain Boundary Space Charge Effect in Zirconia. *Journal of The Electrochemical Society*, 151(1):J1, 2004. ISSN 00134651. doi: 10.1149/1.1625948.

[61] O J Durá, M A López De La Torre, L Vázquez, J Chaboy, R Boada, A Rivera-Calzada, J Santamaria, and C Leon. Ionic conductivity of nanocrystalline yttria-stabilized zirconia: Grain boundary and size effects. *Physical Review B - Condensed Matter and Materials Physics*, 81(18), 5 2010. ISSN 10980121. doi: 10.1103/PhysRevB.81.184301.

[62] C Kjølseth, H Fjeld, Ø Prytz, P I Dahl, C Estournès, R Haugsrud, and T Norby. Space-charge theory applied to the grain boundary impedance of proton conducting BaZr0.9Y0.1O3 - δ. *Solid State Ionics*, 181(5-7):268–275, 3 2010. ISSN 01672738. doi: 10.1016/j.ssi.2010.01.014.

[63] S Yu and D J Siegel. Grain Boundary Contributions to Li-Ion Transport in the Solid Electrolyte Li7La3Zr2O12 (LLZO). *Chemistry of Materials*, 29(22):9639–9647, 11 2017. ISSN 15205002. doi: 10.1021/acs.chemmater.7b02805.

[64] J A Dawson, P Canepa, M J Clarke, T Famprikis, D Ghosh, and M S Islam. Toward Understanding the Different Influences of Grain Boundaries on Ion Transport in Sulfide and Oxide Solid Electrolytes. *Chemistry of Materials*, 31(14):5296–5304, 7 2019. ISSN 15205002. doi: 10.1021/acs.chemmater.9b01794.

[65] J A Quirk and J A Dawson. Design Principles for Grain Boundaries in Solid-State Lithium-

Ion Conductors. *Advanced Energy Materials*, 13(32):2301114, 8 2023. ISSN 16146840. doi: 10.1002/aenm.202301114.

[66] A Kuhn, V Duppel, and B V Lotsch. Tetragonal Li10GeP2S12 and Li 7GePS8-exploring the Li ion dynamics in LGPS Li electrolytes. *Energy and Environmental Science*, 6(12): 3548–3552, 12 2013. ISSN 17545692. doi: 10.1039/c3ee41728j.

[67] P Bron, S Dehnen, and B Roling. Li10Si0.3Sn0.7P2S12 – A low-cost and low-grain-boundary-resistance lithium superionic conductor. *Journal of Power Sources*, 329:530–535, 10 2016. ISSN 03787753. doi: 10.1016/j.jpowsour.2016.08.115.

[68] M Duchardt, U Ruschewitz, S Adams, S Dehnen, and B Roling. Vacancy-Controlled Na+ Superion Conduction in Na11Sn2PS12. *Angewandte Chemie - International Edition*, 57 (5):1351–1355, 1 2018. ISSN 15213773. doi: 10.1002/anie.201712769.

[69] T Krauskopf, S P Culver, and W G Zeier. Local Tetragonal Structure of the Cubic Superionic Conductor Na3PS4. *Inorganic Chemistry*, 57(8):4739–4744, 4 2018. ISSN 1520510X. doi: 10.1021/acs.inorgchem.8b00458.

[70] P Albertus, S Babinec, S Litzelman, and A Newman. Status and challenges in enabling the lithium metal electrode for high-energy and low-cost rechargeable batteries. *Nature Energy*, 3(1):16–21, 1 2018. ISSN 20587546. doi: 10.1038/s41560-017-0047-2.

[71] S Hao, J J Bailey, F Iacoviello, J Bu, P S Grant, D J L Brett, and P R Shearing. 3D Imaging of Lithium Protrusions in Solid-State Lithium Batteries using X-Ray Computed Tomography. *Advanced Functional Materials*, 31(10), 3 2021. ISSN 16163028. doi: 10.1002/adfm.202007564.

[72] K Fu, Y Gong, B Liu, Y Zhu, S Xu, Y Yao, W Luo, C Wang, S Lacey, J Dai, Y Chen, Y Mo, E Wachsman, and L Hu. Toward garnet electrolyte-based Li metal batteries: An ultrathin, highly effective artificial solid-state electrolyte/metallic Li interface. *Science Advances*, 3, 2017. doi: 10.1126/sciadv.1601659.

[73] V Thangadurai, S Narayanan, and D Pinzaru. Garnet-type solid-state fast Li ion conductors for Li batteries: Critical review. *Chemical Society Reviews*, 43(13):4714–4727, 7 2014. ISSN 14604744. doi: 10.1039/c4cs00020j.

[74] S Yu and D J Siegel. Grain Boundary Softening: A Potential Mechanism for Lithium Metal Penetration through Stiff Solid Electrolytes. *ACS Applied Materials and Interfaces*, 10(44):38151–38158, 11 2018. ISSN 19448252. doi: 10.1021/acsami.8b17223.

[75] Z Liu, S Ma, J Liu, S Xiong, Y Ma, and H Chen. High Ionic Conductivity Achieved in Li3Y(Br3Cl3) Mixed Halide Solid Electrolyte via Promoted Diffusion Pathways and Enhanced Grain Boundary. *ACS Energy Letters*, 6(1):298–304, 1 2021. ISSN 23808195. doi: 10.1021/acsenergylett.0c01690.

[76] Y T Chen, A Jena, W K Pang, V K Peterson, H S Sheu, H Chang, and R S Liu. Voltammetric Enhancement of Li-Ion Conduction in Al-Doped Li7-xLa3Zr2O12 Solid Electrolyte. *Journal of Physical Chemistry C*, 121(29):15565–15573, 7 2017. ISSN 19327455. doi: 10.1021/acs.jpcc.7b04004.

[77] K Minami, F Mizuno, A Hayashi, and M Tatsumisago. Lithium ion conductivity of the Li2S-P2S5 glass-based electrolytes prepared by the melt quenching method. *Solid State Ionics*, 178(11-12):837–841, 5 2007. ISSN 01672738. doi: 10.1016/j.ssi.2007.03.001.

[78] E Rangasamy, J Wolfenstine, and J Sakamoto. The role of Al and Li concentration on the formation of cubic garnet solid electrolyte of nominal composition Li 7La 3Zr 2O 12. *Solid State Ionics*, 206:28–32, 1 2012. ISSN 01672738. doi: 10.1016/j.ssi.2011.10.022.

[79] G Li and C W Monroe. Dendrite nucleation in lithium-conductive ceramics. *Physical Chemistry Chemical Physics*, 21(36):20354–20359, 2019. ISSN 14639076. doi: 10.1039/c9cp03884a.

[80] L Cheng, C H Wu, A Jarry, W Chen, Y Ye, J Zhu, R Kostecki, K Persson, J Guo, M Salmeron, G Chen, and M Doeff. Interrelationships among Grain Size, Surface Composition, Air Stability, and Interfacial Resistance of Al-Substituted Li7La3Zr2O12 Solid Electrolytes. *ACS Applied Materials and Interfaces*, 7(32):17649–17655, 8 2015. ISSN 19448252. doi: 10.1021/acsami.5b02528.

[81] D K Singh, A Henss, B Mogwitz, A Gautam, J Horn, T Krauskopf, S Burkhardt, J Sann, F H Richter, and J Janek. Li6PS5Cl microstructure and influence on dendrite growth in solid-state batteries with lithium metal anode. *Cell Reports Physical Science*, 3(9), 9 2022. ISSN 26663864. doi: 10.1016/j.xcrp.2022.101043.

[82] C L Tsai, V Roddatis, C V Chandran, Q Ma, S Uhlenbruck, M Bram, P Heitjans, and O Guillon. Li7La3Zr2O12 Interface Modification for Li Dendrite Prevention. *ACS Applied Materials and Interfaces*, 8(16):10617–10626, 4 2016. ISSN 19448252. doi: 10.1021/acsami.6b00831.

[83] B Wu, S Wang, J Lochala, D Desrochers, B Liu, W Zhang, J Yang, and J Xiao. The role of the solid electrolyte interphase layer in preventing Li dendrite growth in solid-state batteries. *Energy and Environmental Science*, 11(7):1803–1810, 7 2018. ISSN 17545706. doi: 10.1039/c8ee00540k.

[84] A Sharafi, C G Haslam, R D. Kerns, J Wolfenstine, and J Sakamoto. Controlling and correlating the effect of grain size with the mechanical and electrochemical properties of Li7La3Zr2O12 solid-state electrolyte. *Journal of Materials Chemistry A*, 5(40):21491–21504, 2017. ISSN 20507496. doi: 10.1039/c7ta06790a.

[85] Y Kim, H Jo, J L Allen, H Choe, J Wolfenstine, and J Sakamoto. The Effect of Relative Density on the Mechanical Properties of Hot-Pressed Cubic Li 7 la 3 Zr 2 O 12. *Journal of the American Ceramic Society*, 99(4):1367–1374, 4 2016. ISSN 15512916. doi: 10.1111/jace.14084.

[86] H J Lee, B Darminto, S Narayanan, M Diaz-Lopez, A W Xiao, Y Chart, J H Lee, J A Dawson, and M Pasta. Li-ion conductivity in Li 2 OHCl 1 x Br x solid electrolytes: grains, grain boundaries and interfaces. *Journal of Materials Chemistry A*, 10:11574–11586, 2022. ISSN 2050-7488. doi: 10.1039/d2ta01462a.

[87] Z Huang, L Chen, B Huang, B Xu, G Shao, H Wang, Y Li, and C A Wang. Enhanced Performance of Li6.4La3Zr1.4Ta0.6O12Solid Electrolyte by the Regulation of Grain and Grain Boundary Phases. *ACS Applied Materials and Interfaces*, 12(50):56118–56125, 12 2020. ISSN 19448252. doi: 10.1021/acsami.0c18674.

[88] L Cheng, W Chen, M Kunz, K Persson, N Tamura, G Chen, and M Doeff. Effect of surface microstructure on electrochemical performance of garnet solid electrolytes. *ACS Applied Materials and Interfaces*, 7(3):2073–2081, 1 2015. ISSN 19448252. doi: 10.1021/am508111r.

[89] M Biesuz and V M Sglavo. Flash sintering of ceramics. *Journal of the European Ceramic Society*, 39(2-3):115–143, 2 2019. ISSN 1873619X. doi: 10.1016/j.jeurceramsoc.2018.08.048.

[90] J V Campos, I R Lavagnini, V M Zallocco, E B Ferreira, Eliria, M J A Pallone, and A C M Rodrigues. Flash sintering with concurrent crystallization of Li 1.5 Al 0.5 Ge 1.5 (PO 4) 3 glass. *Acta Materialia*, 244:118593, 2023. doi: 10.1016/j.actamat.2022.118593.

[91] Y Seino, T Ota, K Takada, A Hayashi, and M Tatsumisago. A sulphide lithium super ion conductor is superior to liquid ion conductors for use in rechargeable batteries. *Energy and Environmental Science*, 7(2):627–631, 2014. ISSN 17545706. doi: 10.1039/c3ee41655k.

[92] C H Lee, K H Joo, J H Kim, S G Woo, H J Sohn, T Kang, Y Park, and J Y Oh. Characterizations of a new lithium ion conducting Li 2 O-SeO 2-B 2 O 3 glass electrolyte. *Solid State Ionics*, 149:59–65, 2002. doi: 10.1016/S0167-2738(02)00137-6.

[93] K Kataoka, H Nagata, and J Akimoto. Lithium-ion conducting oxide single crystal as solid electrolyte for advanced lithium battery application. *Scientific Reports*, 8(1), 12 2018. ISSN 20452322. doi: 10.1038/s41598-018-27851-x.

[94] G Schwering, A Honnerscheid, L Van Wüllen, and M Jansen. High Lithium Ionic Conductivity in the Lithium Halide Hydrates Li3-n(OHn)Cl (0.83n2) and Li3-n(OHn)Br (1n2) at Ambient Temperatures. *ChemPhysChem*, 4(4):343–348, 2003. doi: 10.1002/cphc.200390060.

[95] Y Zhao and L L Daemen. Superionic conductivity in lithium-rich anti-perovskites. *Journal of the American Chemical Society*, 134(36):15042–15047, 9 2012. ISSN 00027863. doi: 10.1021/ja305709z.

[96] Z D Hood, H Wang, A Samuthira Pandian, J K Keum, and C Liang. Li2OHCl Crystalline Electrolyte for Stable Metallic Lithium Anodes. *Journal of the American Chemical Society*, 138(6):1768–1771, 2016. ISSN 15205126. doi: 10.1021/jacs.5b11851.

[97] R L Sacci, T H Bennett, H Fang, K Sung Han, M Lames, V Murugesan, P Jena, and J Nanda. Halide sublattice dynamics drive Li-ion transport in antiperovskites. *Journal of Materials Chemistry A*, 10(29):15731–15742, 7 2022. ISSN 20507496. doi: 10.1039/d2ta02598a.

[98] A S Bhalla, R Guo, and R Roy. The perovskite structure - A review of its role in ceramic science and technology. *Materials Research Innovations*, 4(1):3–26, 2000. ISSN 14328917. doi: 10.1007/s100190000062.

[99] T He, Q Huang, A P Ramirez, Y Wang, K A Regan, N Rogado, M A Hayward, M K Haas, J S Slusky, K Inumara, H W Zandbergen, N P Ong, and R J Cava. Superconductivity in the non-oxide perovskite MgCNi3. *Nature*, 411(6833):54–56, 5 2001. ISSN 0028-0836. doi: 10.1038/35075014.

[100] R Huang, L Li, F Cai, X Xu, and L Qian. Low-temperature negative thermal expansion of the antiperovskite manganese nitride Mn3CuN codoped with Ge and Si. *Applied Physics Letters*, 93(8), 8 2008. ISSN 0003-6951. doi: 10.1063/1.2970998.

[101] J Zheng, H Fang, L Fan, Y Ren, P Jena, and Y Wu. Antiperovskite K3OI for K-Ion Solid State Electrolyte. *Journal of Physical Chemistry Letters*, 12(30):7120–7126, 8 2021. ISSN 19487185. doi: 10.1021/acs.jpclett.1c01807.

[102] A Y Song, Y Xiao, K Turcheniuk, P Upadhya, A Ramanujapuram, J Benson, A Magasinski, M Olguin, L Meda, O Borodin, and G Yushin. Protons Enhance Conductivities in Lithium Halide Hydroxide/Lithium Oxyhalide Solid Electrolytes by Forming Rotating Hydroxy Groups. *Advanced Energy Materials*, 8(3):1700971–1700981, 1 2018. ISSN 16146840. doi: 10.1002/aenm.201700971.

[103] Z Deng, M Ou, J Wan, S Li, Y Li, Y Zhang, Z Deng, J Xu, Y Qiu, Y Liu, C Fang, Q Li, L Huang, J Zhu, S Han, J Han, and Y Zhao. Local structural changes and inductive effects on ion conduction in antiperovskite solid electrolytes. *Chemistry of Materials*, 32 (20):8827–8835, 2020. ISSN 15205002. doi: 10.1021/acs.chemmater.0c02173.

[104] M K Sugumar, T Yamamoto, M Motoyama, and Y Iriyama. Room temperature synthesis of anti-perovskite structured Li2OHBr. *Solid State Ionics*, 349:115298, 6 2020. ISSN 01672738. doi: 10.1016/j.ssi.2020.115298.

[105] A Koedtruad, M A Patino, N Ichikawa, D Kan, and Y Shimakawa. Crystal structures and ionic conductivity in Li2OHX (X = Cl, Br) antiperovskites. *Journal of Solid State Chemistry*, 286:121263–121267, 6 2020. ISSN 1095726X. doi: 10.1016/j.jssc.2020.121263.

[106] K Yoshikawa, T Yamamoto, M K Sugumar, M Motoyama, and Y Iriyama. Room Temperature Operation and High Cycle Stability of an All-Solid-State Lithium Battery Fabricated by Cold Pressing Using Soft Li2OHBr Solid Electrolyte. *Energy and Fuels*, 35(15):12581–12587, 8 2021. ISSN 15205029. doi: 10.1021/acs.energyfuels.1c01190.

[107] J Zheng, J Elgin, J Shao, and Y Wu. Differentiating grain and grain boundary ionic conductivities of Li-ion antiperovskite electrolytes. *eScience*, 2(6):639–645, 11 2022. ISSN 26671417. doi: 10.1016/j.esci.2022.10.002.

[108] K S Han, J D Bazak, R L Sacci, Y Chen, T H Bennett, J Nanda, and V Murugesan. Halide Substitution Effects on Lithium-Ion Diffusion in Protonated Antiperovskites. *Journal of Physical Chemistry C*, 127(9):4451–4458, 3 2023. ISSN 19327455. doi: 10.1021/acs.jpcc.2c09097.

[109] J A Dawson, T Famprikis, and K E Johnston. Anti-perovskites for solid-state batteries: recent developments, current challenges and future prospects. *Journal of Materials Chemistry A*, 9:18746–18772, 2021. ISSN 2050-7488. doi: 10.1039/d1ta03680g.

[110] M Dondelinger, J Swanson, G Nasymov, C Jahnke, Q Qiao, J Wu, C Widener, A M Numan-Al-Mobin, and A Smirnova. Electrochemical stability of lithium halide electrolyte with antiperovskite crystal structure. *Electrochimica Acta*, 306:498–505, 5 2019. ISSN 00134686. doi: 10.1016/j.electacta.2019.03.074.

[111] Y Li, W Zhou, S Xin, S Li, J Zhu, L Xujie, Z Cui, Q Jia, J Zhou, Y Zhao, and J B Goodenough. Fluorine-Doped Antiperovskite Electrolyte for All-Solid-State Lithium-Ion Batteries. *Angewandte Chemie - International Edition*, 55(34):9965–9968, 8 2016. ISSN 15213773. doi: 10.1002/anie.201604554.

[112] I Hanghofer, G J Redhammer, S Rohde, I Hanzu, A Senyshyn, H M R Wilkening, and D Rettenwander. Untangling the Structure and Dynamics of Lithium-Rich Anti-Perovskites Envisaged as Solid Electrolytes for Batteries. *Chemistry of Materials*, 30(22):8134–8144, 11 2018. ISSN 15205002. doi: 10.1021/acs.chemmater.8b02568.

[113] M B Effat, J Liu, Z Lu, T H Wan, A Curcio, and F Ciucci. Stability, Elastic Properties, and the Li Transport Mechanism of the Protonated and Fluorinated Antiperovskite Lithium Conductors. *ACS Applied Materials and Interfaces*, 12(49):55011–55022, 12 2020. ISSN 19448252. doi: 10.1021/acsami.0c17975.

[114] Y Zhang, Y Zhao, and C Chen. Ab initio study of the stabilities of and mechanism of superionic transport in lithium-rich antiperovskites. *Physical Review B - Condensed Matter and Materials Physics*, 87(13), 4 2013. ISSN 10980121. doi: 10.1103/PhysRevB.87.134303.

[115] A Emly, E Kioupakis, and A Van Der Ven. Phase stability and transport mechanisms in antiperovskite Li 3OCl and Li3OBr superionic conductors. *Chemistry of Materials*, 25(23): 4663–4670, 12 2013. ISSN 08974756. doi: 10.1021/cm4016222.

[116] K Kim, Y Li, P C Tsai, F Wang, S B Son, Y M Chiang, and D J Siegel. Exploring the Synthesis of Alkali Metal Anti-perovskites. *Chemistry of Materials*, 34(3):947–958, 2 2022. ISSN 15205002. doi: 10.1021/acs.chemmater.1c02150.

[117] M H Chen, A Emly, and A Van der Ven. Anharmonicity and phase stability of antiperovskite Li3OCl. *Physical Review B*, 91(21):214306–214313, 6 2015. ISSN 1098-0121. doi: 10.1103/PhysRevB.91.214306.

[118] J A Dawson, T S Attari, H Chen, S P Emge, K E Johnston, and M S Islam. Elucidating lithium-ion and proton dynamics in anti-perovskite solid electrolytes. *Energy and Environmental Science*, 11(10):2993–3002, 2018. ISSN 17545706. doi: 10.1039/c8ee00779a.

[119] S Li, J Zhu, Y Wang, J W Howard, X Lü, Y Li, R S Kumar, L Wang, L L Daemen, and Y Zhao. Reaction mechanism studies towards effective fabrication of lithium-rich antiperovskites Li3OX (X = Cl, Br). *Solid State Ionics*, 284:14–19, 1 2016. ISSN 01672738. doi: 10.1016/j.ssi.2015.11.027.

[120] F Wang, H A Evans, K Kim, L Yin, Y Li, P C Tsai, J Liu, S H Lapidus, C M Brown, D J Siegel, and Y M Chiang. Dynamics of Hydroxyl Anions Promotes Lithium Ion Conduction in Antiperovskite Li2OHCl. *Chemistry of Materials*, 32(19):8481–8491, 10 2020. ISSN 15205002. doi: 10.1021/acs.chemmater.0c02602.

[121] J Spychala, A Wilkening, and H M R Wilkening. The Batteries' New Clothes: Li and H Dynamics in Poorly Conducting Li2OHCl Directly Probed by Nuclear Spin Relaxation. *Journal of Physical Chemistry C*, 127(15):7433–7444, 4 2023. ISSN 19327455. doi: 10.1021/acs.jpcc.2c08815.

[122] A Y Song, K Turcheniuk, J Leisen, Y Xiao, L Meda, O Borodin, and G Yushin. Understanding Li-Ion Dynamics in Lithium Hydroxychloride (Li2OHCl) Solid State Electrolyte via Addressing the Role of Protons. *Advanced Energy Materials*, 10(8):1903480–1903488, 2 2020. ISSN 16146840. doi: 10.1002/aenm.201903480.

[123] Z Jiang, S Wang, X Chen, W Yang, X Yao, X Hu, Q Han, and H Wang. Tape-Casting Li0.34La0.56TiO3 Ceramic Electrolyte Films Permit High Energy Density of Lithium-Metal Batteries. *Advanced Materials*, 32(6), 2 2020. ISSN 15214095. doi: 10.1002/adma.201906221.

[124] M Dixit, N Muralidharan, A Bisht, C J Jafta, C T Nelson, R Amin, R Essehli, M Balasubramanian, and I Belharouak. Tailoring of the anti-perovskite solid electrolytes at the grain-scale. *ACS Energy Letters*, 8:2356–2364, 5 2023. ISSN 23808195. doi: 10.1021/acsenergylett.3c00265.

[125] G Scarpa. Atti Accad. Naz. Lincei Rend. *Classe di Scienze Fisiche, Matematiche e Naturali. Serie V*, 24:476, 1915.

[126] P Hartwig, A Rabenau, and W Weppner. Lithium hydroxide halides: Phase equilibria and ionic conductivities. *Journal of the Less-Common Metals*, 78:227–233, 1981. doi: 10.1016/0022-5088(81)90132-6.

[127] A Hönnerscheid, J Nuss, C Mühle, and M Jansen. Die kristallstrukturen der hydroxyhalogenide Li4(OH)3Br und Li4(OH)3I. *Zeitschrift fur Anorganische und Allgemeine Chemie*, 629(2):317–320, 2003. ISSN 00442313. doi: 10.1002/zaac.200390050.

[128] J Sangster. Thermodynamics and phase diagrams of 32 binary common-ion systems of the group Li,Na,K,Rb,Cs//F,Cl,Br,I,OH,NO3. *Journal of Phase Equilibria*, 21:241–268, 2000. doi: https://doi.org/10.1361/105497100770340048.

[129] F Achchaq and E P Del Barrio. A proposition of peritectic structures as candidates for thermal energy storage. *Energy Procedia*, 139:346–351, 2017. ISSN 18766102. doi: 10.1016/j.egypro.2017.11.219.

[130] C W Bale, E Bélisle, P Chartrand, S A Decterov, G Eriksson, A E Gheribi, K Hack, I H Jung, Y B Kang, J Melançon, A D Pelton, S Petersen, C Robelin, J Sangster, P Spencer, and M A Van Ende. FactSage thermochemical software and databases, 2010–2016. *Calphad: Computer Coupling of Phase Diagrams and Thermochemistry*, 54:35–53, 12 2016. ISSN 03645916. doi: 10.1016/j.calphad.2016.07.004.

[131] C Mcmillan, R Boardman, M Mckellar, P Sabharwall, M Ruth, and S Bragg-Sitton. Generation and Use of Thermal Energy in the U.S. Industrial Sector and Opportunities to

Reduce its Carbon Emissions. Technical report, National Renewable Energy Lab (NREL), Golden, CO (United States), 2016. URL www.nrel.gov/publications.

[132] W D Steinmann and R Tamme. Latent heat storage for solar steam systems. *Journal of Solar Energy Engineering, Transactions of the ASME*, 130(1):0110041–0110045, 2 2008. ISSN 01996231. doi: 10.1115/1.2804624.

[133] H Fredriksson and T Nylén. Mechanism of peritectic reactions and transformations. *Metal Science*, 16(6):283–294, 1982. doi: 10.1179/030634582790427370.

[134] G Phanikumar, K Biswas, O Funke, D Holland-Moritz, D M Herlach, and K Chattopadhyay. Solidification of undercooled peritectic Fe-Ge alloy. *Acta Materialia*, 53(13):3591–3600, 8 2005. ISSN 13596454. doi: 10.1016/j.actamat.2005.03.053.

[135] W Löser, M Leonhardt, H G Lindenkreuz, and B Arnold. Phase selection in undercooled binary peritectic alloy melts. *Materials Science and Engineering: A*, 375-377:534–539, 7 2004. ISSN 09215093. doi: 10.1016/j.msea.2003.10.138.

[136] W Zhai and B Wei. Direct nucleation and growth of peritectic phase induced by substantial undercooling condition. *Materials Letters*, 108:145–148, 2013. ISSN 0167577X. doi: 10.1016/j.matlet.2013.06.084.

[137] P. Lü and H. P. Wang. Direct formation of peritectic phase but no primary phase appearance within Ni83.25Zr16.75 peritectic alloy during free fall. *Scientific Reports*, 6, 3 2016. ISSN 20452322. doi: 10.1038/srep22641.

[138] M A Orozco, K Acurio, F Vásquez-Aza, J Martínez-Gómez, and A Chico-Proano. Thermal storage of nitrate salts as phase change materials (PCMs). *Materials*, 14(23):7223–7240, 12 2021. ISSN 19961944. doi: 10.3390/ma14237223.

[139] N A Reshetnikov and G M Unzhakov. Izv Fiz-Khim Nauch-Issled Inst Irkutsk Gosud Univ. 2:23, 1953.

[140] K Friese, A Hönnerscheid, and M Jansen. Crystal structure determination of systematically intergrown compounds: Li5(OH)2Br3 and Li2(OH)Br. *Zeitschrift für Kristallographie - Crystalline Materials*, 218(8):536–541, 2003. doi: 10.1524/zkri.218.8.536.20686.

[141] A Koedtruad, M A Patino, Y C Chuang, W T Chen, D Kan, and Y Shimakawa. Ruddlesden-Popper phases of lithium-hydroxide-halide antiperovskites: Two dimensional

Li-ion conductors. *RSC Advances*, 10(68):41816–41820, 11 2020. ISSN 20462069. doi: 10.1039/d0ra07803d.

[142] C Li, S Lian, C Kang, J Ren, and M Chen. Insights on transport performance, thermodynamic properties, and mechanical properties of Ruddlesden-Popper antiperovskite LiBr(Li2OHBr)2 and LiBr(Li3OBr)2. *The Journal of chemical physics*, 159(2), 7 2023. ISSN 10897690. doi: 10.1063/5.0158411.

[143] D Ni, J Qi, Z Deng, R Xiao, Y Sun, S Li, and Y Zhao. First-Principles Study on a Layered Antiperovskite Li7O2Br3 Solid Electrolyte. *The Journal of Physical Chemistry Letters*, 15 (7):1879–1886, 2 2024. ISSN 1948-7185. doi: 10.1021/acs.jpclett.4c00043.

[144] Z Lu, J Liu, and F Ciucci. Superionic conduction in low-dimensional-networked antiperovskites. *Energy Storage Materials*, 28:146–152, 6 2020. ISSN 24058297. doi: 10.1016/j.ensm.2020.03.005.

[145] A C Coutinho Dutra, G E Rudman, K E Johnston, and J A Dawson. Defect chemistry and ion transport in low-dimensional-networked Li-rich anti-perovskites as solid electrolytes for solid-state batteries. *Energy Advances*, 2023. ISSN 27531457. doi: 10.1039/d3ya00075c.

[146] M H Braga, J A Ferreira, V Stockhausen, J E Oliveira, and A El-Azab. Novel Li3ClO based glasses with superionic properties for lithium batteries. *Journal of Materials Chemistry A*, 2(15):5470–5480, 2014. ISSN 20507496. doi: 10.1039/c3ta15087a.

[147] M H Braga, A J Murchison, J A Ferreira, P Singh, and J B Goodenough. Glass-amorphous alkali-ion solid electrolytes and their performance in symmetrical cells. *Energy and Environmental Science*, 9(3):948–954, 2016. ISSN 17545706. doi: 10.1039/c5ee02924d.

[148] M H Braga, N S Grundish, A J Murchison, and J B Goodenough. Alternative strategy for a safe rechargeable battery. *Energy and Environmental Science*, 10(1):331–336, 2017. ISSN 17545706. doi: 10.1039/c6ee02888h.

[149] M H Braga, J A Ferreira, A J Murchison, and J B Goodenough. Electric Dipoles and Ionic Conductivity in a Na + Glass Electrolyte . *Journal of The Electrochemical Society*, 164(2):A207–A213, 2017. ISSN 0013-4651. doi: 10.1149/2.0691702jes.

[150] J Ou, V Tatagari, I Senevirathna, S Luitel, C Segre, L Shaw, and M H Braga. On the formation and properties of amorphous and crystalline Li3-yBay/2OCl elec-

trolytes. *Journal of Power Sources*, 609:234685–234692, 7 2024. ISSN 03787753. doi: 10.1016/j.jpowsour.2024.234685.

[151] D A Steingart and V Viswanathan. Comment on "Alternative strategy for a safe rechargeable battery" by M. H. Braga, N. S. Grundish, A. J. Murchison and J. B. Goodenough, Energy Environ. Sci., 2017, 10, 331-336, 1 2018. ISSN 17545706.

[152] H H Heenen, J Voss, C Scheurer, K Reuter, and A C Luntz. Multi-ion Conduction in Li3OCl Glass Electrolytes. *The Journal of Physical Chemistry Letters*, 10:2264–2269, 2019. doi: 10.1021/acs.jpclett.9b00500.

[153] Y W Choi, C M Araujo, and R Lizárraga. Amorphisation-induced electrochemical stability of solid-electrolytes in Li-metal batteries: The case of Li3ClO. *Journal of Power Sources*, 521:230916–230923, 2 2022. ISSN 03787753. doi: 10.1016/j.jpowsour.2021.230916.

[154] T L Pham, M Guerboub, A Bouzid, M Boero, C Massobrio, Y H Shin, and G Ori. Unveiling the structure and ion dynamics of amorphous Na3xOHxCl antiperovskite electrolytes by first-principles molecular dynamics. *Journal of Materials Chemistry A*, 11(42):22922–22940, 9 2023. ISSN 20507496. doi: 10.1039/d3ta01373a.

[155] J G Smith and D J Siegel. Low-temperature paddlewheel effect in glassy solid electrolytes. *Nature Communications*, 11(1):1483–1493, 12 2020. ISSN 20411723. doi: 10.1038/s41467-020-15245-5.

[156] E Gaffet, C Louison, M Harmelin, and F Faudot. Metastable phase transformations induced by ball-milling in the cu-w system. *Materials Science and Engineering, A*, 134:1380–1384, 1991.

[157] M Oehring, Z H Yan, T Klassen, and R Bormann. Competition between stable and metastable phases during mechanical alloying and ball milling. *physica status solidi (a)*, 131:671–689, 1992. ISSN 1521396X. doi: 10.1002/pssa.2211310237.

[158] G J Fan, M X Quan, and Z Q Hu. Metastable phases formation induced by mechanical alloying. *JOURNAL OF MATERIALS SCIENCE*, 30:4847–4851, 1995.

[159] V V Boldyrev. Mechanochemistry and mechanical activation of solids. *Russian Chemical Reviews*, 75:177–189, 3 2006. ISSN 0036-021X. doi: 10.1070/rc2006v075n03abeh001205.

[160] W H Bragg and W L Bragg. The Reflection of X-rays by Crystals. *Proceedings of the Royal Society A: Mathematical, Physical and Engineering Sciences*, 88:428–438, 1913. doi: 10.1098/rspa.1913.0040.

[161] A A Coelho. TOPAS and TOPAS-Academic: an optimization program integrating computer algebra and crystallographic objects written in C++. *Journal of Applied Crystallography*, 51(1):210–218, 2 2018. doi: 10.1107/S1600576718000183.

[162] B Reif, S E Ashbrook, L Emsley, and M Hong. Solid-state NMR spectroscopy. *Nature Reviews Methods Primers*, 1(2), 2021. ISSN 26628449. doi: 10.1038/s43586-020-00002-1.

[163] T Polenova, R Gupta, and A Goldbourt. Magic angle spinning NMR spectroscopy: A versatile technique for structural and dynamic analysis of solid-phase systems. *Analytical Chemistry*, 87(11):5458–5469, 6 2015. ISSN 15206882. doi: 10.1021/ac504288u.

[164] P B Kingsley. Methods of measuring spin-lattice (T1) relaxation times: An annotated bibliography. *Concepts in Magnetic Resonance*, 11(4):243–276, 1999. ISSN 10437347. doi: 10.1002/(SICI)1099-0534(1999)11:4<243::AID-CMR5>3.0.CO;2-C.

[165] R Freeman, H D W Hill, and R Kaptein. An Adaptive Scheme for Measuring NMR Spin-Lattice Relaxation Times. *Journal of Magnetic Resonance*, 7:82–98, 1972. doi: 10.1016/0022-2364(72)90148-5.

[166] A Kuhn, M Kunze, P Sreeraj, H D Wiemhöfer, V Thangadurai, M Wilkening, and P Heitjans. NMR relaxometry as a versatile tool to study Li ion dynamics in potential battery materials. *Solid State Nuclear Magnetic Resonance*, 42:2–8, 4 2012. ISSN 09262040. doi: 10.1016/j.ssnmr.2012.02.001.

[167] P Heitjans, A Schirmer, and S Indris. *NMR and β-NMR Studies of Diffusion in Interface-Dominated and Disordered Solids*. Springer, Berlin, Heidelberg, 2005.

[168] G Pagès, V Gilard, R Martino, and M Malet-Martino. Pulsed-field gradient nuclear magnetic resonance measurements (PFG NMR) for diffusion ordered spectroscopy (DOSY) mapping. *Analyst*, 142(20):3771–3796, 10 2017. ISSN 13645528. doi: 10.1039/c7an01031a.

[169] SEM Resolution, 2022. URL https://www.thermofisher.com/uk/en/home/materials-science/learning-center/applications/sem-resolution.html.

[170] The Difference Between SEM and Optical Microscopy, 2022. URL https://www.thermofisher.com/uk/en/home/materials-science/learning-center/applications/sem-optical-microscopes-difference.

[171] A C Lazanas and M I Prodromidis. Electrochemical impedance spectroscopy: A tutorial. *ACS Measurement Science Au*, 3(3):162–193, 6 2023. ISSN 2694250X. doi: 10.1021/acsmeasuresciau.2c00070.

[172] Basics of electrochemical impedance spectroscopy, 2022. URL https://www.gamry.com/application-notes/EIS/basics-of-electrochemical-impedance-spectroscopy/.

[173] A Lasia. The origin of the constant phase element. *Journal of Physical Chemistry Letters*, 13(2):580–589, 1 2022. ISSN 19487185. doi: 10.1021/acs.jpclett.1c03782.

[174] K Hashi, S Ohki, Y Mogami, A Goto, and T Shimizu. High-Temperature Pulsed-Field-Gradient 7Li-NMR Measurements of Li2CO3 over 700 K. *Analytical Sciences*, 37(10): 1477–1479, 2021. ISSN 13482246. doi: 10.2116/analsci.21A001.

[175] B Deng, P Zhong, K Jun, J Riebesell, K Han, C J Bartel, and G Ceder. Chgnet as a pretrained universal neural network potential for charge-informed atomistic modelling. *Nature Machine Intelligence*, 5:1031—-1041, 2023. doi: 10.1038/s42256-023-00716-3.

[176] A Kuhn, S Narayanan, L Spencer, G Goward, V Thangadurai, and M Wilkening. Li self-diffusion in garnet-type Li7La3Zr 2O12 as probed directly by diffusion-induced Li7 spin-lattice relaxation NMR spectroscopy. *Physical Review B - Condensed Matter and Materials Physics*, 83(9):94302, 3 2011. ISSN 10980121. doi: 10.1103/PhysRevB.83.094302.

[177] P Bottke, D Rettenwander, W Schmidt, G Amthauer, and M Wilkening. Ion Dynamics in Solid Electrolytes: NMR Reveals the Elementary Steps of Li+ Hopping in the Garnet Li6.5La3Zr1.75Mo0.25O12. *Chemistry of Materials*, 27(19):6571–6582, 9 2015. ISSN 15205002. doi: 10.1021/acs.chemmater.5b02231.

[178] G A Blengini, C E L Latunussa, U Eynard, C Torres de Matos, D Wittmer, K Georgitzikis, C Pavel, S Carrara, L Mancini, M Unguru, D Blagoeva, F Mathieux, and D Pennington. Study on the EU's list of Critical Raw Materials (2020) Final Report. Technical report, European Commission, 2020. URL `http://www.europa.eu`.

[179] A Gautam, M Sadowski, M Ghidiu, N Minafra, A Senyshyn, K Albe, and W G Zeier. Engineering the Site-Disorder and Lithium Distribution in the Lithium Superionic Argyrodite Li6PS5Br. *Advanced Energy Materials*, 11(5):2003369, 2021. ISSN 1614-6840. doi: 10.1002/aenm.202003369.

[180] J Zheng, B Perry, and Y Wu. Antiperovskite Superionic Conductors: A Critical Review. *ACS Materials Au*, 1(2):92–106, 11 2021. ISSN 2694-2461. doi: 10.1021/acsmaterialsau.1c00026.

[181] W Xia, Y Zhao, F Zhao, K Adair, R Zhao, S Li, R Zou, Y Zhao, and X Sun. Antiperovskite Electrolytes for Solid-State Batteries. *Chemical Reviews*, 122(3):3763–3819, 2 2022. ISSN 15206890. doi: 10.1021/acs.chemrev.1c00594.

[182] B Chen, C Xu, and J Zhou. Insights into grain boundary in lithium-rich anti-perovskite as solid electrolytes. *Journal of The Electrochemical Society*, 165:A3946–A3951, 2018. ISSN 0013-4651. doi: 10.1149/2.0831816jes.

[183] K Shen, R He, Y Wang, C Zhao, and H Chen. Atomistic Insights into the Role of Grain Boundary in Ionic Conductivity of Polycrystalline Solid-State Electrolytes. *Journal of Physical Chemistry C*, 124(48):26241–26248, 12 2020. ISSN 19327455. doi: 10.1021/acs.jpcc.0c07328.

[184] S L Eiler. Antiperovskite crystal growth. Master's thesis, Massachusetts Institute of Technology, 2019.

[185] J Zhang, L Wang, J Zhu, and Y Zhao. Structural disorder, sublattice melting, and thermoelastic properties of anti-perovskite Li3OBr under high pressure and temperature. *Applied Physics Letters*, 117(8), 8 2020. ISSN 00036951. doi: 10.1063/5.0018714.

[186] F Wang, Y Li, P Tsai, L Yin, H Evens, K Kim, S H Lapidus, D J Siegel, and Y Chiang. Understanding the Structural Disorder Related to Ionic Conductivity Enhancement in Anti-Perovskite Ion Conductors. In *ECS Meeting Abstracts*, volume MA2020-02, page 967. The Electrochemical Society, Inc., 11 2020. doi: 10.1149/MA2020-025967mtgabs.

[187] Y Li, P Tsai, F Wang, S Mair, D Zhang, L Yin, S Lapidus, and Y M Chiang. Non-Arrhenius Ionic Conductivity Transitions in Sodium Antiperovskite Ionic Conductors. In

ECS Meeting Abstracts, volume MA2021-02, page 43. The Electrochemical Society, Inc., 10 2021. doi: 10.1149/MA2021-02143mtgabs.

[188] B Darminto, G J Rees, J Cattermull, K Hashi, M Diaz-Lopez, N Kuwata, S J Turrell, E Milan, Y Chart, C Di Mino, H J Lee, A L Goodwin, and M Pasta. On the Origin of the Non-Arrhenius Na-ion Conductivity in Na3OBr. *Angewandte Chemie - International Edition*, 62(51), 12 2023. ISSN 15213773. doi: 10.1002/anie.202314444.

[189] Z Ning, D Spencer-Jolly, G Li, R De Meyere, S D. Pu, Y Chen, J Kasemchainan, J Ihli, C Gong, B Liu, D L R Melvin, A Bonnin, O Magdysyuk, P Adamson, G O Hartley, C W Monroe, T J Marrow, and P G Bruce. Visualizing plating-induced cracking in lithium-anode solid-electrolyte cells. *Nature Materials*, 20(8):1121–1129, 8 2021. ISSN 14764660. doi: 10.1038/s41563-021-00967-8.

[190] Z Ning, G Li, D L R Melvin, Y Chen, J Bu, D Spencer-Jolly, J Liu, B Hu, X Gao, J Perera, C Gong, S D. Pu, S Zhang, B Liu, G O Hartley, A J Bodey, R I Todd, P S Grant, D E J Armstrong, T J Marrow, C W Monroe, and P G Bruce. Dendrite initiation and propagation in lithium metal solid-state batteries. *Nature*, 618(7964):287–293, 6 2023. ISSN 14764687. doi: 10.1038/s41586-023-05970-4.

[191] E Milan and M Pasta. The role of grain boundaries in solid-state Li-metal batteries. *Materials Futures*, 2(1):013501–013517, 3 2023. ISSN 27525724. doi: 10.1088/2752-5724/aca703.

[192] A Abdelouas, J Adam, A M Agarwal, I Ahmed, M Allix, C Bardin, ..., and J W Zwanziger. *Springer Handbook of Glass*. Springer Cham, 1st edition, 2019. doi: 10.1007/978-3-319-93728-1.

[193] S Wang, W Zhang, X Chen, D Das, R Ruess, A Gautam, F Walther, S Ohno, R Koerver, Q Zhang, W G Zeier, F H Richter, C W Nan, and J Janek. Influence of Crystallinity of Lithium Thiophosphate Solid Electrolytes on the Performance of Solid-State Batteries. *Advanced Energy Materials*, 11(24):1–11, 2021. ISSN 16146840. doi: 10.1002/aenm.202100654.

[194] A S Westover, N J Dudney, R L Sacci, and S Kalnaus. Deposition and Confinement of Li Metal along an Artificial Lipon-Lipon Interface. *ACS Energy Letters*, 4(3):651–655, 3 2019. ISSN 23808195. doi: 10.1021/acsenergylett.8b02542.

[195] S Kalnaus, A S Westover, M Kornbluth, E Herbert, and N J Dudney. Resistance to fracture in the glassy solid electrolyte Lipon. *Journal of Materials Research*, 36(4):787–796, 3 2021. ISSN 20445326. doi: 10.1557/s43578-020-00098-x.

[196] R Mercier, J P Malugani, B Fahys, and G Robert. Superionic Conduction in Li2S-P2S5-LiI Glasses. *Solid State Ionics*, 5:663–666, 1981. doi: 10.1016/0167-2738(81)90341-6.

[197] M Menetrier, A Levasseur, C Delmas, J F Audebert, and P Hagenmuller. New Secondary Batteries for Room Temperature Applications Using a Vitreous Electrolyte. *Solid State Ionics*, 14:257–261, 1984. doi: 10.1016/0167-2738(84)90108-5.

[198] S Kondo, K Takada, and Y Yamamura. New Lithium Ion Conductors Based on Li2S-SiS2 System. *Solid State Ionics*, 56:1183–1186, 1992. doi: 10.1016/0167-2738(92)90310-L.

[199] A Hayashi, M Tatsumisago, and T Minami. Electrochemical Properties for the Lithium Ion Conductive (100 - x) (0.6Li2S . 0.4SiS2).xLi4SiO4 Oxysulfide Glasses. *Journal of The Electrochemical Society*, 146:3472–3475, 1999. doi: 10.1149/1.1392498.

[200] A Hayashi, S Hama, H Morimoto, M Tatsumisago, and T Minami. Preparation of Li 2 S–P 2 S 5 Amorphous Solid Electrolytes by Mechanical Milling. *Journal of the American Ceramic Society*, 84(2):477–479, 2001. doi: 10.1111/j.1151-2916.2001.tb00685.x.

[201] R Zhao, G Hu, S Kmiec, J Wheaton, V M Torres, and S W Martin. Grain-Boundary-Free Glassy Solid Electrolytes based on Sulfide Materials: Effects of Oxygen and Nitrogen Doping on Electrochemical Performance. *Batteries and Supercaps*, 5(11):e202100356–e202100368, 11 2022. ISSN 25666223. doi: 10.1002/batt.202100356.

[202] C E Athanasiou, X Liu, M Y Jin, E Nimon, S Visco, C Lee, M Park, J Yun, N P Padture, H Gao, and B W Sheldon. Rate-dependent deformation of amorphous sulfide glass electrolytes for solid-state batteries. *Cell Reports Physical Science*, 3(4):100845–100861, 4 2022. ISSN 26663864. doi: 10.1016/j.xcrp.2022.100845.

[203] J B Bates, N J Dudney, G R Gruzalski, R A Zuhr, A Choudhury, C F Luck, and J D Robertson. Fabrication and characterization of amorphous lithium electrolyte thin films and rechargeable thin-film batteries. *Journal of Power Sources*, 43(1-3):103–110, 1993. doi: 10.1016/0378-7753(93)80106-Y.

[204] B J Neudecker, N J Dudney, and J B Bates. "Lithium-Free" Thin-Film Battery with In Situ Plated Li Anode. *Journal of The Electrochemical Society*, 147(2):517–523, 2000. doi: 10.1149/1.1393226.

[205] Y Hamon, A Douard, F Sabary, C Marcel, P Vinatier, B Pecquenard, and A Levasseur. Influence of sputtering conditions on ionic conductivity of LiPON thin films. *Solid State Ionics*, 177(3-4):257–261, 1 2006. ISSN 01672738. doi: 10.1016/j.ssi.2005.10.021.

[206] Z Wang, D Santhanagopalan, W Zhang, F Wang, H L Xin, K He, J Li, N Dudney, and Y S Meng. In situ STEM-EELS observation of nanoscale interfacial phenomena in all-solid-state batteries. *Nano Letters*, 16(6):3760–3767, 6 2016. ISSN 15306992. doi: 10.1021/acs.nanolett.6b01119.

[207] D Cheng, T Wynn, B Lu, M Marple, B Han, R Shimizu, B Sreenarayanan, J Bickel, P Hosemann, Y Yang, H Nguyen, W Li, G Zhu, M Zhang, and Y S Meng. A free-standing lithium phosphorus oxynitride thin film electrolyte promotes uniformly dense lithium metal deposition with no external pressure. *Nature Nanotechnology*, 18(12):1448–1455, 12 2023. ISSN 17483395. doi: 10.1038/s41565-023-01478-0.

[208] T Dai, S Wu, Y Lu, Y Yang, Y Liu, C Chang, X Rong, R Xiao, J Zhao, Y Liu, W Wang, L Chen, and Y S Hu. Inorganic glass electrolytes with polymer-like viscoelasticity. *Nature Energy*, 8:1221–1228, 9 2023. ISSN 2058-7546. doi: 10.1038/s41560-023-01356-y.

[209] L Hu, J Wang, K Wang, Z Gu, Z Xi, H Li, F Chen, Y Wang, Z Li, and C Ma. A cost-effective, ionically conductive and compressible oxychloride solid-state electrolyte for stable all-solid-state lithium-based batteries. *Nature Communications*, 14(1):3807–3818, 12 2023. ISSN 20411723. doi: 10.1038/s41467-023-39522-1.

[210] F Li, X Cheng, G Lu, Y C Yin, Y C Wu, R Pan, J D Luo, F Huang, L Z Feng, L L Lu, T Ma, L Zheng, S Jiao, R Cao, Z P Liu, H Zhou, X Tao, C Shang, and H B Yao. Amorphous Chloride Solid Electrolytes with High Li-Ion Conductivity for Stable Cycling of All-Solid-State High-Nickel Cathodes. *Journal of the American Chemical Society*, 145: 27774–27787, 12 2023. ISSN 15205126. doi: 10.1021/jacs.3c10602.

[211] S Zhang, F Zhao, L-Y Chang, Y-C Chuang, Z Zhang, Y Zhu, X Hao, J Fu, J Chen, J Luo, M Li, Y Gao, Y Huang, T K Sham, M D Gu, Y Zhang, G King, and X Sun. Amorphous

Oxyhalide Matters for Achieving Lithium Superionic Conduction. *Journal of the American Chemical Society*, 146(5):2977–2985, 1 2024. ISSN 0002-7863. doi: 10.1021/jacs.3c07343.

[212] Z H Jiang and Q Y Zhang. The structure of glass: A phase equilibrium diagram approach. *Progress in Materials Science*, 61:144–215, 2014. ISSN 00796425. doi: 10.1016/j.pmatsci.2013.12.001.

[213] W H Zachariasen. The Atomic Arrangement in Glass. *Journal of the American Chemical Society*, 54(10):3841–3851, 1932. doi: 10.1021/ja01349a006.

[214] K R Thurber and R Tycko. Measurement of sample temperatures under magic-angle spinning from the chemical shift and spin-lattice relaxation rate of 79Br in KBr powder. *Journal of Magnetic Resonance*, 196(1):84–87, 1 2009. ISSN 10907807. doi: 10.1016/j.jmr.2008.09.019.

[215] R K Harris, E D Becker, S M Cabral De Menezes, R Goodfellow, and P Granger. NMR Nomenclature: Nuclear Spin Properties and Conventions for Chemical Shifts (IUPAC Recommendations 2001). Technical report, 2001. URL `http://www.iupac.org/publications/pac/2001/7311/7311x1795.html`.

[216] J H Kennedy and Y Yang. Glass-Forming Region and Structure in SiS2-Li2S-LX (X = Br, I). *Journal of Solid State Chemistry*, 257:252–257, 1987. doi: 10.1016/0022-4596(87)90081-8.

[217] M Tatsumisago, H Yamashita, A Hayashi, H Morimoto, and T Minami. Preparation and structure of amorphous solid electrolytes based on lithium sulfide. *Journal of Non-Crystalline Solids*, 274:30–38, 2000. doi: 10.1016/S0022-3093(00)00180-0.

[218] S Ujiie, A Hayashi, and M Tatsumisago. Preparation and ionic conductivity of (100-x)(0.8Li2S·0.2P2S5)·xLiI glass–ceramic electrolytes. *Journal of Solid State Electrochemistry*, 17:675–680, 2013. doi: 10.1007/s10008-012-1900-7.

[219] A Yamauchi, A Sakuda, A Hayashi, and M Tatsumisago. Preparation and ionic conductivities of (100-x)(0.75Li2S-0.25P2S5)xLiBH4 glass electrolytes. *Journal of Power Sources*, 244:707–710, 2013. doi: 10.1016/j.jpowsour.2012.12.001.

[220] A Pradel and M Ribes. Electrical Properties of Lithium Conductive Silicon Sulfide

Glasses Prepared by Twin Roller Quenching. *Solid State Ionics*, 19:351–355, 1986. doi: 10.1016/0167-2738(86)90139-6.

[221] N Aotani, K Iwamoto, K Takada, and S Kondo. Synthesis and electrochemical properties of lithium ion conductive glass, Li3PO4-Li2S-SiS2. *Solid State Ionics*, 68:35–39, 1994. doi: 10.1016/0167-2738(94)90232-1.

[222] C Eilbracht, W Kockelmann, D Hohlwein, and H Jacobs. Orientational disorder in perovskite like structures of Li2X(OD) (X = C1, Br) and LiBr. D20. *Physica B: Condensed Matter*, 234-236:48–50, 1997. doi: 10.1016/S0921-4526(96)00874-5.

[223] M Olson, J Wheaton, M Okkema, N Oldham, and S W Martin. Optimized Thin Film Processing of Sodium Mixed Oxy-Sulfide-Nitride Glassy Solid Electrolytes for All-Solid-State Batteries. *ACS Applied Energy Materials*, 6(11):5842–5855, 6 2023. ISSN 25740962. doi: 10.1021/acsaem.3c00294.

[224] J Wheaton, S Kmiec, D Schuler, C Sorensen, and S W Martin. Electrochemical Behavior of Drawn Thin-Film Vitreous Lithium Metaphosphate. *ACS Applied Energy Materials*, 4 (10):10835–10842, 10 2021. ISSN 25740962. doi: 10.1021/acsaem.1c01809.

[225] Z P Lu, H Tan, Y Li, and S C Ng. The Correlation Between Reduced Glass Transition Temperature and Glass Forming Ability of Bulk Metallic Glasses. *Scripta Materialia*, 42 (7):667–673, 2000. doi: 10.1016/S1359-6462(99)00417-0.

[226] J Swenson and L Börjesson. Correlation between Free Volume and Ionic Conductivity in Fast Ion Conducting Glasses. *Physical Review Letters*, 77(17):3569–3572, 1996. doi: 10.1103/PhysRevLett.77.3569.

[227] A V Deshpande and V K Deshpande. Correlation of glass transition temperature and density with electrical conductivity of lithium sulfoborosilicate glasses. *Solid State Ionics*, 177(26-32):2747–2751, 10 2006. ISSN 01672738. doi: 10.1016/j.ssi.2006.07.021.

[228] S S Gundale, V V Behare, and A V Deshpande. Study of electrical conductivity of Li2O-B2O3-SiO2-Li2SO4 glasses and glass-ceramics. *Solid State Ionics*, 298:57–62, 12 2016. ISSN 01672738. doi: 10.1016/j.ssi.2016.11.002.

[229] C J Pickard and R J Needs. Ab initio random structure searching. *Journal of Physics: Condensed Matter*, 23(5):053201, 2011. ISSN 0953-8984. doi: 10.1088/0953-8984/23/5/053201.

[230] S Grimme, J Antony, S Ehrlich, and H Krieg. A consistent and accurate ab initio parametrization of density functional dispersion correction (DFT-D) for the 94 elements H-Pu. *The Journal of Chemical Physics*, 132(15):154104, 2010. ISSN 0021-9606. doi: 10.1063/1.3382344.

[231] So Takamoto, Chikashi Shinagawa, Daisuke Motoki, Kosuke Nakago, Wenwen Li, Iori Kurata, Taku Watanabe, Yoshihiro Yayama, Hiroki Iriguchi, Yusuke Asano, Tasuku Onodera, Takafumi Ishii, Takao Kudo, Hideki Ono, Ryohto Sawada, Ryuichiro Ishitani, Marc Ong, Taiki Yamaguchi, Toshiki Kataoka, Akihide Hayashi, Nontawat Charoenphakdee, and Takeshi Ibuka. Towards universal neural network potential for material discovery applicable to arbitrary combination of 45 elements. *Nature Communications*, 13(1):2991–3001, 12 2022. ISSN 20411723. doi: 10.1038/s41467-022-30687-9.

[232] S P Ong, W D Richards, A Jain, G Hautier, M Kocher, S Cholia, D Gunter, V L Chevrier, K A Persson, and G Ceder. Python Materials Genomics (pymatgen): A robust, open-source python library for materials analysis. *Computational Materials Science*, 68:314–319, 2013. ISSN 0927-0256. doi: 10.1016/j.commatsci.2012.10.028.

[233] V Azizi, S Smeets, A K Lavrinenko, S Ciarella, and T Famprikis. Gemdat. URL `https://gemdat.readthedocs.io`.

[234] X He, Y Zhu, A Epstein, and Y Mo. Statistical variances of diffusional properties from ab initio molecular dynamics simulations. *npj Computational Materials*, 4(1):1–9, 2018. ISSN 2057-3960. doi: 10.1038/s41524-018-0074-y.

[235] J P Perdew, K Burke, and M Ernzerhof. Generalized Gradient Approximation Made Simple. *Physical Review Letters*, 77(18):3865–3868, 1996. doi: 10.1103/PhysRevLett.77.3865.

[236] G Kresse and D Joubert. From ultrasoft pseudopotentials to the projector augmented-wave method. *Physical Review B*, 59(3):1758–1775, 1999. doi: 10.1103/PhysRevB.59.1758.

[237] P E Blöchl. Projector augmented-wave method. *Physical Review B*, 50(24):17953–17979, 1994. doi: 10.1103/PhysRevB.50.17953.

[238] A H Larsen, J J Mortensen, J Blomqvist, I E Castelli, R Christensen, M Dułak, J Friis, M N Groves, B Hammer, C Hargus, E D Hermes, P C Jennings, P B Jensen, J Kermode, J R Kitchin, E L Kolsbjerg, J Kubal, K Kaasbjerg, S Lysgaard, J B Maronsson, T Maxson,

T Olsen, L Pastewka, A Peterson, C Rostgaard, J Schiøtz, O Schütt, M Strange, K S Thygesen, T Vegge, L Vilhelmsen, M Walter, Z Zeng, and K W Jacobsen. The atomic simulation environment—a Python library for working with atoms. *Journal of Physics: Condensed Matter*, 29(27):273002, 2017. ISSN 0953-8984. doi: 10.1088/1361-648X/aa680e.

[239] C M S Alvares, G Deffrennes, A Pisch, and N Jakse. Thermodynamics and structural properties of CaO: A molecular dynamics simulation study. *The Journal of Chemical Physics*, 152(8):084503, 2020. ISSN 0021-9606. doi: 10.1063/1.5141841.

[240] K Yasukawa, Y Terashi, and A Nakayama. Crystallinity Analysis of Glass-Ceramics by the Rietveld Method. *Journal of the American Ceramic Society*, 81(11):2978–2982, 1998. doi: 10.1111/j.1151-2916.1998.tb02723.x.